

**Cooperative
Institute for
Research in
Environmental Sciences**
University of Colorado at Boulder



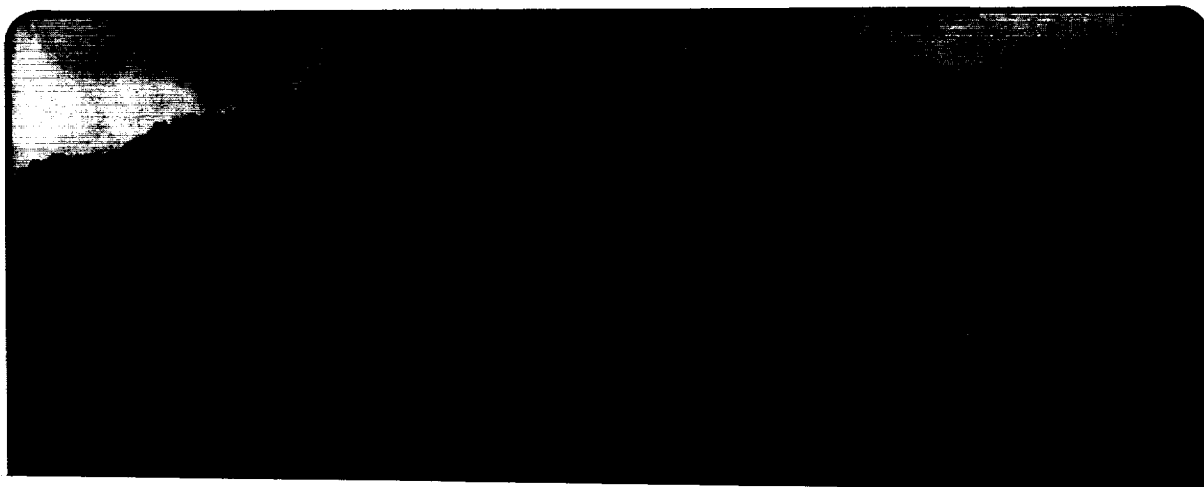
FINAL REPORT

**Cloud Cover Determination in Polar Regions
From Satellite Imagery**

R.G. Barry and J. Key

NAG5-898

*GODDARD
GRANT
IN-47-CR
243198
p. 269*



(NASA-CR-186096) CLOUD COVER DETERMINATION
IN POLAR REGIONS FROM SATELLITE IMAGERY
Final Report (Colorado Univ.) 269 p

N90-13003

CSCL 048

Unclass

G3/47 0243198



University of Colorado



National Oceanic and Atmospheric Administration

**CLOUD COVER DETERMINATION IN POLAR REGIONS
FROM SATELLITE IMAGERY**

NASA Grant: NAG-5-898

FINAL REPORT

R.G. Barry and J. Key

Cooperative Institute for Research in Environmental Sciences

University of Colorado

Boulder, CO 80309-0449

15 December 1989

Contents

Abstract	iv
1.0 Introduction	1
1.1 Difficulties with Satellite Cloud Analysis in Polar Regions	1
1.2 Objectives of this Project	4
2.0 Data	5
3.0 Cloud Detection Algorithms	6
3.1 Classification of Clouds and Surfaces with Fuzzy Sets	8
3.2 Classification of Clouds and Surfaces with Neural Networks	9
3.3 Cloud Detection with Spatial and Temporal Coherence	11
3.4 Cloud Detection Following an ISCCP Methodology	15
4.0 Analysis of Cloud Patterns with Spectral and Textural Measures	18
5.0 Empirical Studies of Arctic Cloud Cover	21
6.0 Comparison of Modeled and Observed Cloud Cover in the Arctic	22
7.0 Concluding Remarks	23
8.0 Future Research	23
9.0 References	25
10.0 Publications Supported by this Project	28
Attachments	29
1: Merging AVHRR and SMMR Data	30
2: Cloud Classification with Fuzzy Sets	36
3: Classification with Neural Networks	76
4: Cloud Cover Analysis: Detection	108
5: Adaption of the ISCCP Cloud Detection Algorithm	158

**CLOUD COVER DETERMINATION IN POLAR REGIONS
FROM SATELLITE IMAGERY**

NASA Grant: NAG-5-898

FINAL REPORT

R.G. Barry and J. Key

Cooperative Institute for Research in Environmental Sciences

University of Colorado

Boulder, CO 80309-0449

15 August 1989

Contents

Abstract	iv
1.0 Introduction	1
1.1 Difficulties with Satellite Cloud Analysis in Polar Regions	1
1.2 Objectives of this Project	4
2.0 Data	5
3.0 Cloud Detection Algorithms	6
3.1 Classification of Clouds and Surfaces with Fuzzy Sets	8
3.2 Classification of Clouds and Surfaces with Neural Networks	9
3.3 Cloud Detection with Spatial and Temporal Coherence	11
3.4 Cloud Detection Following an ISCCP Methodology	15
4.0 Analysis of Cloud Patterns with Spectral and Textural Measures	18
5.0 Empirical Studies of Arctic Cloud Cover	21
6.0 Comparison of Modeled and Observed Cloud Cover in the Arctic	22
7.0 Concluding Remarks	23
8.0 Future Research	23
9.0 References	25
10.0 Publications Supported by this Project	28
Attachments	29
1: Merging AVHRR and SMMR Data	30
2: Cloud Classification with Fuzzy Sets	36
3: Classification with Neural Networks	76
4: Cloud Cover Analysis: Detection	108
5: Adaption of the ISCCP Cloud Detection Algorithm	158

6: Cloud Classification with Spectral and Textural Measures	162
7: Intercomparison of Satellite-derived Cloud Analyses	211
8: Arctic Cloudiness in Spring	233
9: Comparison of Observed and Simulated Cloud Cover	236

Abstract

The objectives of this project are to develop a suitable validation data set for evaluating the effectiveness of the International Satellite Cloud Climatology Project (ISCCP) algorithm for cloud retrieval in polar regions, to identify limitations of current procedures and to explore potential means to remedy them using textural classifiers, and to compare synoptic cloud data from model runs with observations.

Toward the first goal, a polar data set consisting of visible, thermal, and passive microwave data was developed. AVHRR and SMMR data were digitally merged to a polar stereographic projection with an effective pixel size of $(5 \text{ km})^2$. With this data set, two unconventional methods of classifying the imagery for the analysis of polar clouds and surfaces were examined: one based on fuzzy sets theory and another based on a trained neural network. Both were compared to the maximum likelihood procedure and were found to provide additional flexibility in the analysis of polar clouds in that the inherently fuzzy boundaries between cloud and surface classes in spatial and spectral space are acknowledged. However, limitations with statistical classifiers were recognized, and the need for a more standardized approach became apparent.

An algorithm for cloud detection was developed from an early test version of the ISCCP algorithm. This algorithm includes the identification of surface types with passive microwave, then temporal tests at each pixel location in the cloud detection phase. Cloud maps and clear sky radiance composites for 5-day periods are produced. Algorithm testing and validation was done with both actual AVHRR/SMMR data, and simulated imagery. Accurate surface parameterization and the temporal variability of pixels were found to be crucial elements in the identification of polar clouds. From this point in the algorithm, groups of cloud pixels are examined for their spectral and textural characteristics, and a procedure is developed for the analysis of cloud patterns utilizing albedo, IR temperature, and texture. This procedure abandons the traditional method of gridding an image and classifying the grid cells in favor of assigning a local texture value to each

pixel. The spectral and textural characteristics are used in a supervised classification of mesoscale (250 km) cloud patterns without artificially-imposed boundaries.

In a completion of earlier work, empirical analyses of arctic cloud cover were explored through manual interpretations of DMSP imagery and compared to the US Air Force 3D-nephanalysis. Results show that, because of limitations using only visible and thermal data, cloud parameters computed over small geographic areas are subject to error but that broad climatological features can be captured with these methods. Comparisons of observed cloudiness from existing climatologies to patterns computed by the GISS climate model were also made. The GISS results indicate that, while most of the cloud cover would appear to be due to large-scale processes, there is some evidence that reduced ice concentration in summer may give rise to low-level cloud on a limited regional basis.



1. Introduction

The climate of the polar regions is significantly influenced by the extent and thickness of sea ice modulating the oceanic heat loss and surface albedo which, in turn, influence the global climate via the ice-albedo feedback (Budyko, 1969; Sellers, 1969). Many studies have shown that the polar climate, in turn, is sensitive to radiative forcing (e.g., Maykut and Untersteiner, 1971; Robock, 1983). This is particularly true in the Arctic where the ocean surface is covered by sea ice whose thickness depends on the radiative input from the overlying atmosphere. The major influence on this input is cloud which is linked to the sea ice through a series of radiative, dynamical, thermodynamic and hydrological feedbacks (Saltzman and Moritz, 1980; Shine et al., 1984b; MacCracken et al., 1986). For instance, during the Arctic winter the presence of clouds limits radiative cooling at the surface whereas in high summer the absence of stratus cloud facilitates surface snow melt (Scharfen et al., 1987). Paradoxically, surface net radiation in the central Arctic is greater for cloudy conditions than under clear skies, except in July (Herman, 1980; Tsay et al., 1988; Serreze and Bradley, 1987). The radiative interactions with polar clouds and our ability to monitor these clouds is therefore critical to understanding the climate of polar regions.

High latitude response to changes in cloud cover is a key area of uncertainty in evaluating changes in the global climate system. To improve understanding of climate forcing, statistical frameworks for describing the morphology of cloud fields as well as the radiative, dynamical, and microphysical processes determining this morphology are needed (CGC, 1988, pg. 117). The importance of Arctic cloud analysis to the International Geosphere-Biosphere Programme (IGBP) has also been recognized (UCAR, 1988), and one of the program elements of the IGBP is to obtain continuous and systematic observations of Arctic cloud cover from satellites.

1.1 Difficulties with Satellite Cloud Analysis in Polar Regions

The study of polar cloudiness and properties of the underlying surface using satellite data such as that provided by the AVHRR encounters a number of significant difficulties that influence

the reliability of cloud retrieval schemes. Some particularly relevant ones are:

- (i) Low radiance contrasts between cloudy and clear scenes: The small polar temperature lapse rates reduce the infrared radiance contrasts and the snow and ice covered surface limit the solar reflection contrasts (Figure 1). Thus the radiance characteristics in polar regions require sensitive radiance analysis.
- (ii) The complex surface property variations caused by changes in snow and sea ice: Rapid small-scale variations in surface properties, particularly surface reflectance, make it difficult to characterize cloud free scenes based on spatial and temporal variability techniques.
- (iii) The effect of haze on reflected and emitted radiances: The presence of optically thick haze, especially during the spring in the Arctic, may obscure the pack ice and conceal discernible surface features that might otherwise be used to determine the absence of cloud layers (e.g., Shine et al., 1984a; Barry et al., 1988; Curry, 1988; Curry et al., 1989a,b) or used in an automated retrieval scheme.
- (iv) Complex non-linear relationship between radiances and cloud properties: The differences in the angular variations of reflected sunlight between rough surfaces and broken clouds and the occurrences of strong inversions produce complex effects on these relationships. The utility of simple radiance difference techniques is doubtful and cloud retrieval becomes a multi-valued problem.

The impact of these uncertainties on cloud retrieval methods will vary in degree according to location and season. However, some overall assessment of their effects on satellite radiance measurements is sorely needed. Since operational digital imagery over the polar region is only available from polar orbiting meteorological satellites of the NOAA series, assessment of these factors in the context of AVHRR might provide insight to the solution of these problems. We also note, however, that results may also be applicable to existing Defense Meteorological Satellite

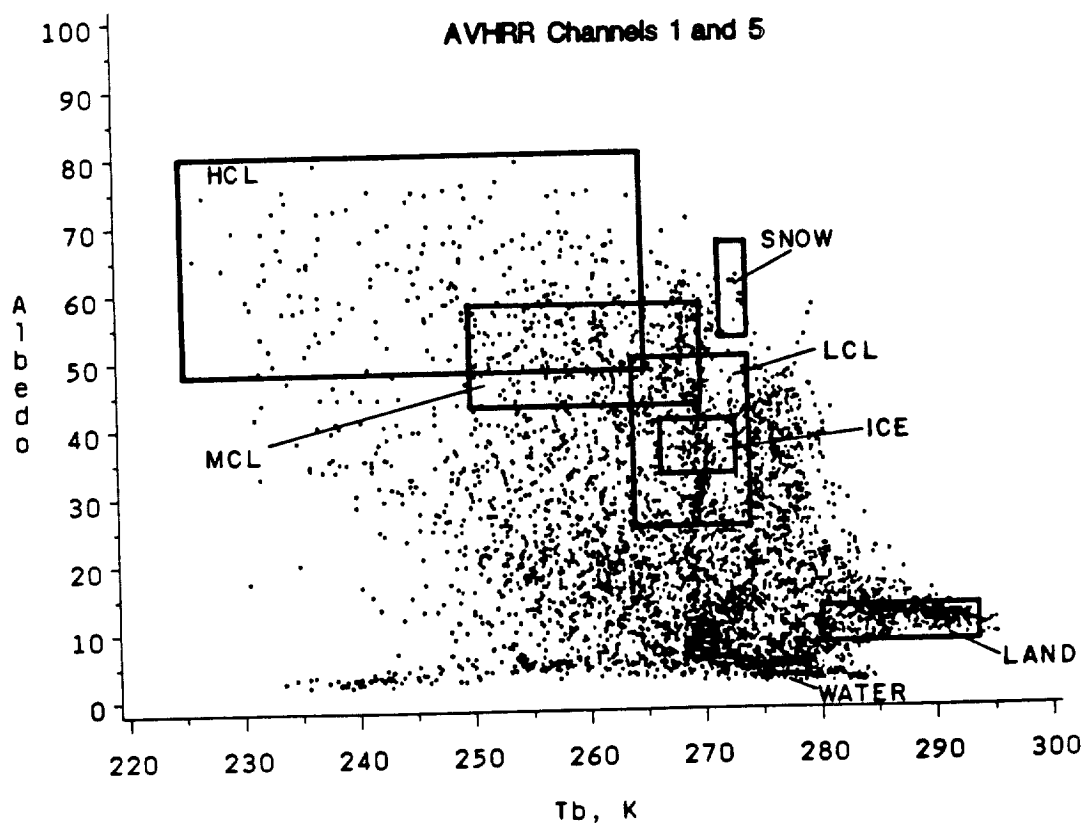
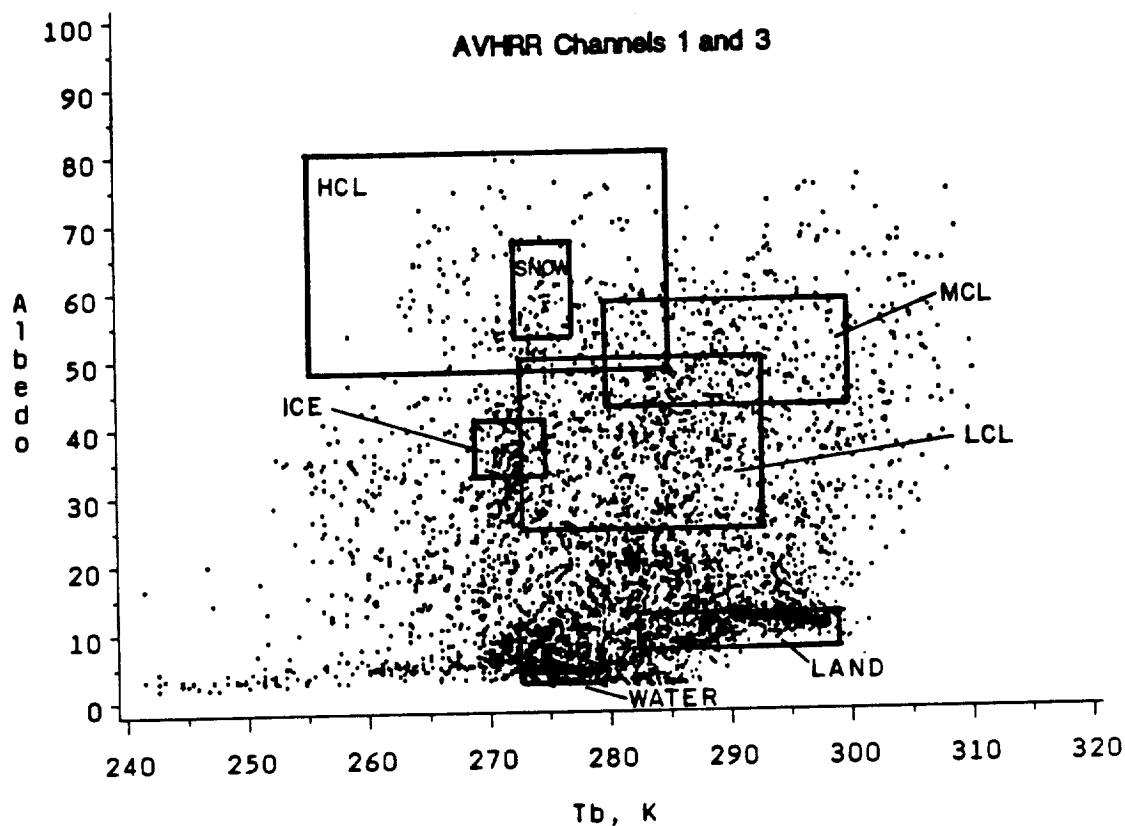


Fig. 1. Relationship between AVHRR channels 1 and 3 (top) and 1 and 5 (bottom) for pixels taken from a summer image near the Kara Sea. Rectangles enclose the mean \pm one standard deviation in each channel for surface and cloud classes (HCL: high cloud, MCL: middle cloud, LCL: low cloud). Data are based on training area statistics. Significant overlap between some classes can be seen in both plots.

Program (DMSP) satellites, and to sensors planned to be part of the Earth Observing System (NASA, n.d.).

1.2 Objectives of this Project

The principal objectives of this project are

- (1) to develop suitable validation data sets to evaluate the effectiveness of the International Satellite Cloud Climatology Project (ISCCP) operational algorithm for cloud retrieval in polar regions and to validate model simulations of polar cloud cover;
- (2) to identify limitations of current procedures for varying atmospheric surface conditions, and to explore potential means to remedy them using textural classifiers;
- (3) to compare synoptic cloud data from a control run experiment of the GISS climate model II with typical observed synoptic cloud patterns.

This report details the investigations that were undertaken to achieve these goals. Prior to any specific analyses, a data set consisting of visible, thermal, and passive microwave data was developed. With this data set, two unconventional methods of classifying the imagery for the analysis of polar clouds and surfaces were examined: one based on fuzzy sets theory and another based on a trained neural network. Recognizing the problems with statistical classifiers, the need for a more standardized approach specific to the geographic area and data set became apparent. An algorithm for cloud detection was developed from an early test version of the ISCCP algorithm for the pixel-scale identification of clouds and surfaces. With cloud maps produced from this algorithm, a procedure was developed for the classification of cloud pixels based on their spectral and local textural characteristics for the analysis of mesoscale cloud patterns. Empirical analyses of cloud cover were also explored through manual interpretations of DMSP imagery and comparisons to the US Air Force 3D-nephanalysis. Finally, comparisons of observed cloudiness and synoptic

pressure patterns to those generated by the GISS model are also made. Each of the following sections gives a brief description of these research topics, and refers to the attached papers for additional detail.

2. Data

A data set has been developed that combines digital AVHRR and Nimbus-7 SMMR passive microwave data. This data set serves as the principal source for radiance measurements in algorithm development. Data includes all AVHRR channels (1: 0.58-0.68 μ m, 2: 0.73-1.0 μ m, 3: 3.55-3.93 μ m, 4: 10.3-11.3 μ m, 5: 11.5-12.5 μ m), as well as channel 3 albedo (approximated). AVHRR data are initially of the Global Area Coverage (GAC) resolution (3x5 km), and are part of an ISCCP test data set. Data are available for January 6-13, 1984 and July 1-7, 1984 covering both the Arctic and Antarctic regions.

The Nimbus-7 Scanning Multichannel Microwave Radiometer (SMMR) measures in five channels: 6.6, 10.7, 18.0, 21.0, and 37.0 GHz. Vertical and horizontal polarizations are available for each channel. Sea ice concentration and ice type are calculated from SMMR data using the operational NASA Team algorithm. A simple gradient ratio threshold is included to reduce the effects of ocean surface spray and foam on ice concentration estimates.

The AVHRR data are merged with the SMMR data onto a polar stereographic projection with a grid cell size of 5 km at 70° N latitude. The data merging procedure is given in Attachment 1.

Visible (0.4-1.1 μ m) and thermal (10.5-12.5 μ m) imagery from the DMSP - a near-polar orbiter with a resolution of 2.7 km for orbital swath format images - is used for manual comparisons of cloud type and amount and surface conditions in cloud-free areas. Other ancillary data include pressures and temperatures from the European Centre for Medium Range Forecasting (ECMWF) and sea ice albedo from Scharfen et al. (1987) which are derived from a combined interpretation of DMSP imagery and the NOAA/Navy ice charts.

In order to test the sensitivity of the various cloud algorithms, a control data set with known characteristics is needed. A synthetic data set has been developed which consists of seven days of AVHRR data (channels 1, 3, 4), three days of SMMR brightness temperature data (every other day; 18 and 37 GHz vertical polarization), SMMR-derived sea ice concentrations, and a land mask. Surface types are snow-covered and snow-free land, open water, and sea ice. Cloud layers are classified as low, middle, and high, where levels are defined by AVHRR channel 4 temperatures. Data are based on class characteristic means and standard deviations computed from training areas. Synthetic data sets are described in Attachment 4.

Three areas of the Arctic are examined (Figure 2). One area is centered on the Kara and Barents Sea extending north to the pole and south to Norway and the Siberian coast. The second area covers most of the Canadian Archipelago and Greenland, and extends north to the pole. The third area extends from the coast of Norway to Ellesmere Island. A seven-day summer series of areas 1 and 2, and a winter series of area 3 were examined. While covering only one-third of the Arctic Basin, they include representative samples of all surface types found in the Arctic: snow-covered and snow-free land, sea ice of varying concentrations, open water, and permanent ice cap. In fact, these areas during the July period present particularly difficult conditions for cloud algorithms to work with; sea ice is moving, snow is melting and ponds form, and the extensive coastlines exhibit mixed temperature regimes.

3. Cloud Detection Algorithms

Several objective methods exist for mapping cloud cover using satellite radiance measurements. Among these are methods that utilize statistical approaches (e.g., Coakley and Bretherton, 1982) and pattern recognition techniques (e.g., Harris and Barrett, 1978; Chin et al., 1987 and others). Other approaches are based on physical relationships determined from some form of radiative transfer scheme (Reynolds and Vonder Haar, 1977; Arking and Childs, 1985; Wu, 1987).

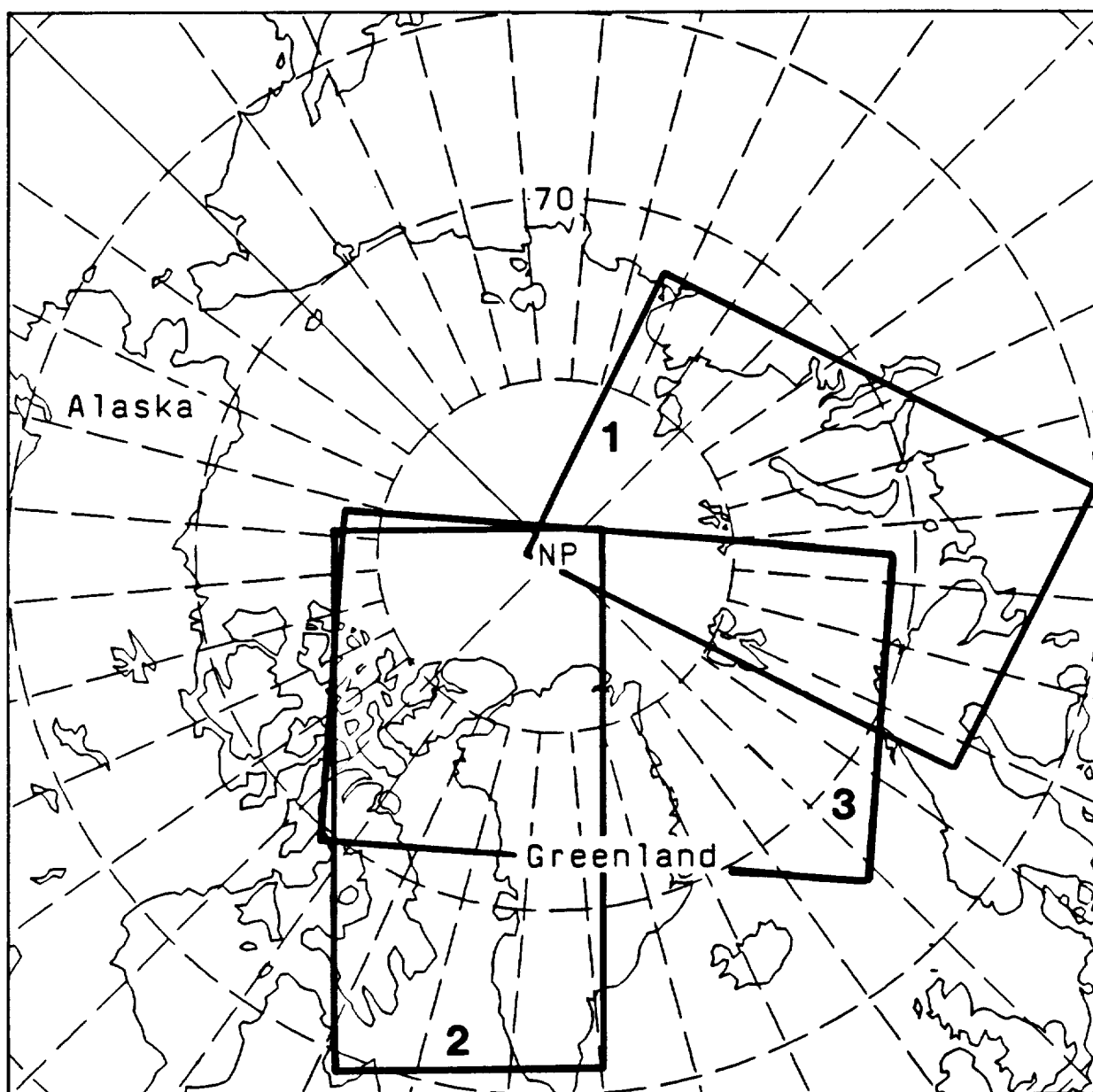


Fig. 2. The three Arctic study areas. Summer data (July 1-7, 1984) were examined for areas 1 and 2; in area 3 winter data (January 6-13, 1984) were employed.

These methods, which are principally based on the use of visible and infrared radiances, generally fail in the polar regions as a result of the problems listed in Section 1. However, the spectral differences of ice, snow and clouds under various conditions permit the use of multichannel techniques to separate clouds from ice and snow covered surfaces. Of particular interest is the potential of existing channels on the AVHRR for this purpose. Near infrared radiances have been used in the methods of Arking and Childs (1985), Wu (1987), Key et al. (1989a,b), and Key and Barry (1989). These radiance data demonstrate great potential for differentiating the phase of water in clouds and the underlying surface. A better understanding of the wavelength variations of the albedo and emissivity of snow and ice-covered surfaces and of the overlying clouds of different microstructure as well as an assessment of the effects of large zenith view angles are all important considerations for polar cloud studies.

Although the AVHRR provides data in a wide range of channels, which collectively provide the ability to distinguish between surface and cloud types, the question remains of how to take advantage of this information in the development of a cloud detection algorithm. We investigate this problem through clustering and classification procedures, spatial and temporal coherence, and the basic methodology followed in the ISCCP algorithm.

3.1 Classification of Clouds and Surfaces with Fuzzy Sets

Where spatial boundaries between phenomena are diffuse, classification methods which construct mutually exclusive clusters seem inappropriate. The Fuzzy c-means (FCM) algorithm assigns each observation to all clusters, with membership values as a function of distance to the cluster center. The FCM algorithm is applied to AVHRR data for the purpose of classifying polar clouds and surfaces. Careful analysis of the fuzzy sets can provide information on which spectral channels are best suited to the classification of particular features, and can help determine likely areas of misclassification. The ability of the fuzzy sets approach to address indistinct spectral classes by calculating class memberships as opposed to the "in-or-out" decision required of hard

classifiers is particularly well suited to the range of albedos and physical temperatures encountered in the analysis of ice and cloud in the polar regions.

Application of the fuzzy sets classifier to an AVHRR image containing sea ice and cloud of varying condition and opacity yielded ten membership sets containing contextually and statistically unique information. Interpretation of intensities in images of these sets demonstrates the ability of the fuzzy sets to describe well-defined classes (such as open water and land) as well as classes that fall in intermediate spectral space (e.g., ice cap, thin stratus over water, or sea ice of varying concentration). Identification of such fuzzy areas in taxonomic space provides information on classes where data in additional spectral regions are required for accurate classification. Future work will use the fuzzy sets approach as a tool to help "tune" hard classifiers such as unsupervised clustering and bispectral threshold methods for cloud and ice mapping in the polar regions. General agreement in the classes identified, as well as cloud fraction, was found between the FCM algorithm, a manual classification, and an unsupervised maximum likelihood (ML) classifier. See Attachment 2 for additional detail.

3.2 Classification of Clouds and Surfaces with Neural Networks

A similar study to that with the fuzzy sets procedure was carried out using a trained neural network to classify a combined AVHRR/SMMR multispectral image. Again, the goal was to examine the advantages and disadvantages of a methodology which allows for fuzzy boundaries in both spatial and spectral space. Four surface and eight cloud classes were examined: snow-free land, snow-covered land/ice cap, open water, and sea ice; low cloud over land, water, and ice; middle cloud over water and ice; and high cloud over land, water, and ice. The data were classified by two procedures: a neural network and a maximum likelihood classifier. The maximum likelihood procedure is supervised, initially using the same training areas as used to train the neural network. The neural network approach to classification is generally less rigid than the traditional maximum likelihood procedure in that 1) there are no assumptions of distributions of variables and

relationships between them, 2) the network is easily trained to learn the relationships between input and output, and 3) the classification produces both a categorical value and a type of membership value for each pixel. It is recognized that there is some loss of information and interpretability with the departure from statistical theory. Additionally, computation time required for training the network is not trivial when compared to the training of the ML classifier (i.e., computation of mean vectors and the covariance matrix), although future hardware architectures should alleviate this problem.

Both numeric and the numeric/symbolic neural network designs were implemented and both extracted correct information from the multispectral images. The differences between the neural network and supervised maximum likelihood classifications were primarily due to the greater flexibility of the neural network to classify indistinct classes, e.g., classes containing pixels with spectral values that differ significantly from those in the training areas, while ignoring assumptions of statistical normality. The two classification approaches illustrate the tradeoffs between human interaction in the selection of training areas and classification accuracy and flexibility. Flexibility similar to that shown by the neural network might be achieved using a maximum likelihood routine by manipulating class membership probabilities and/or by adjusting probability thresholds to relax the membership requirements for individual classes. Such steps would require an *a priori* knowledge of probabilities and may increase classification error.

The ability to interpret weights within the trained network provides a potentially powerful tool for understanding the role of inputs and the geophysical processes they represent in the making of decisions. Through an examination of the connection strengths between input, hidden, and output units, it is possible to identify which inputs influence the classification most, and which are redundant. These relationships are not always clear, and care must be taken in extending their interpretation to physical processes. We emphasize that the data and applications of interest for remote sensing of polar climate is not typical of applications such as land cover mapping, which may be limited to a single image covering relatively small areas with small within-class variance.

This study does not show whether a neural network offers any advantages for the latter type of analyses. The merits and drawbacks of a neural network approach relative to others must therefore be considered based on the particular problem at hand.

3.3 Cloud Detection with Spatial and Temporal Coherence

Clear sky radiance retrieval was examined from the point of view of the spatial and temporal coherence of pixel radiances in AVHRR data. These two methods were then combined into a spatiotemporal coherence analysis method for the determination of clear sky radiances. In all three procedures the basic assumption is that clear sky areas exhibit low spatial and/or temporal structure; i.e., a group of contiguous pixels will, if each is clear, have a low standard deviation. Since visible data are not available during the polar winters, the coherence tests are based on thermal data (AVHRR channel 4) only.

With single-layer, single surface image regions, a plot of cell means against their standard deviations reveals a characteristic arch-shaped distribution where a cluster of points with low deviations indicates clear sky, and another cluster also with low deviations but lower mean temperature indicates cloud-covered areas (Coakley and Bretherton, 1982). These areas exhibit a high degree of spatial coherence. Between these two "feet" are areas with intermediate temperatures and greater variability which can be interpreted as partially cloud-filled fields of view. The assumptions are that only one surface type and one cloud layer are present, and that the cloud is colder than the surface.

In the Arctic, these assumptions are seldom realized, and with isothermal and inversion conditions common, difficulties occur in determining which foot (or feet) of the arch correspond to clear sky cells. Figure 3 illustrates the spatial coherence method as applied to a $(250 \text{ km})^2$ region for each of four consecutive days. The problem of multiple surface types and cloud layers is apparent. To aid further in the determination of clear sky radiances, locations may be examined for their variation in time. Scenes which do not vary significantly from the day before and the day

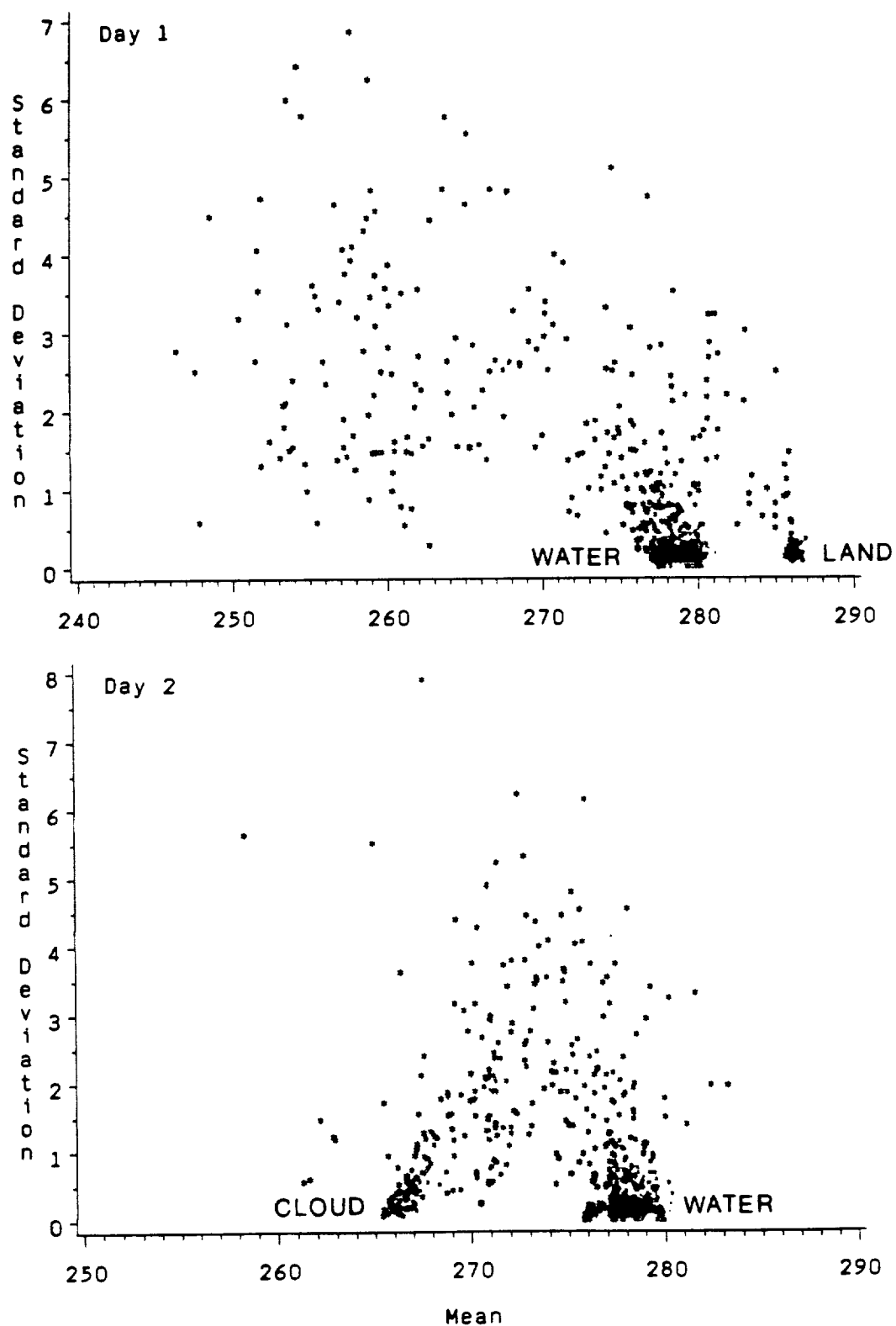


Fig. 3. Spatial coherence plots for four consecutive days. Region size is $(250 \text{ km})^2$, cells are 3×3 pixels.

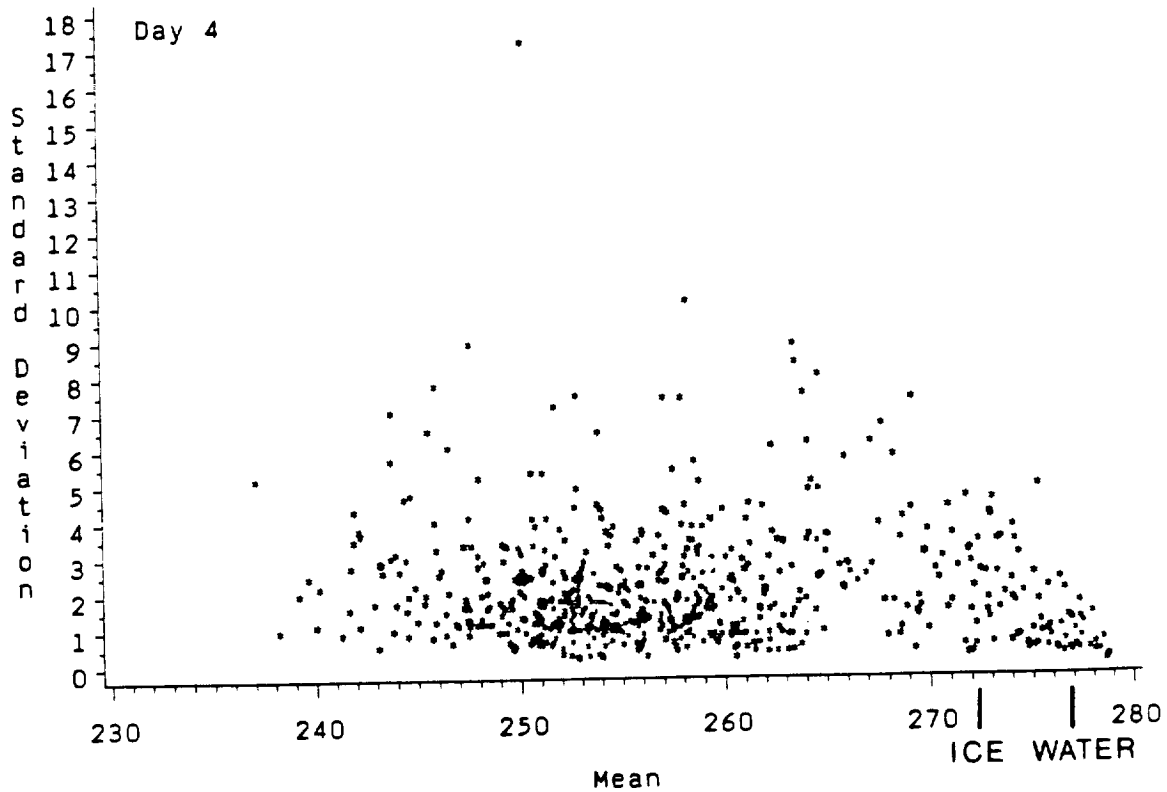
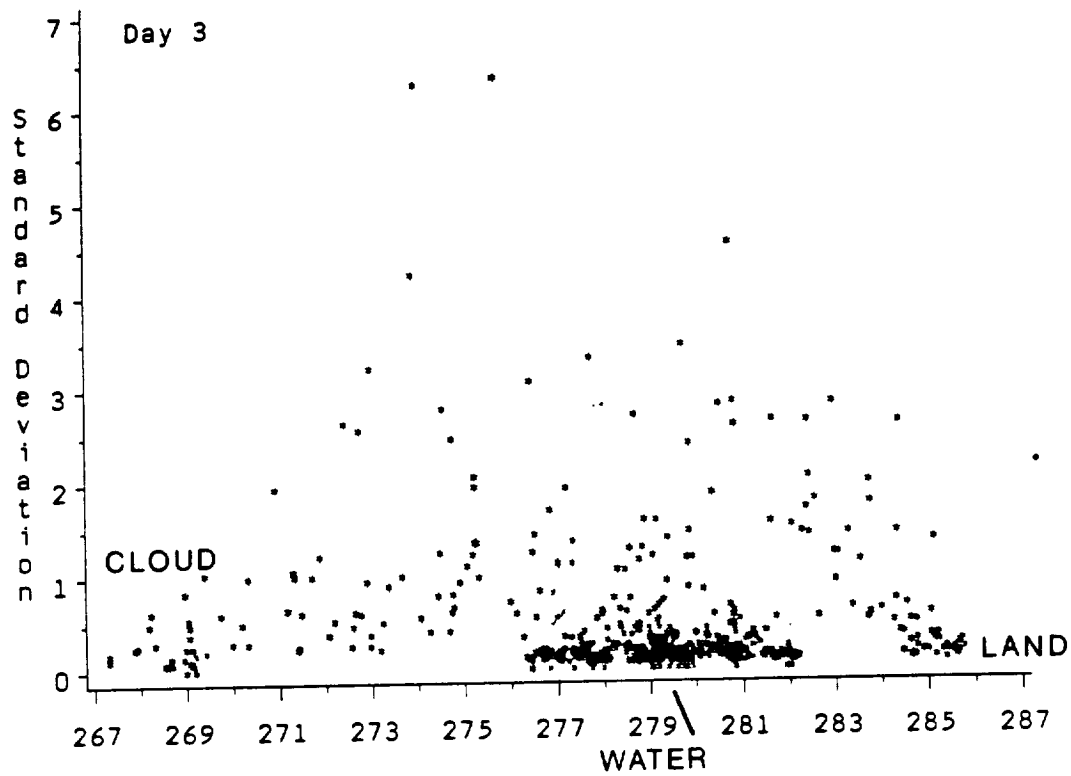


Fig. 3, continued.

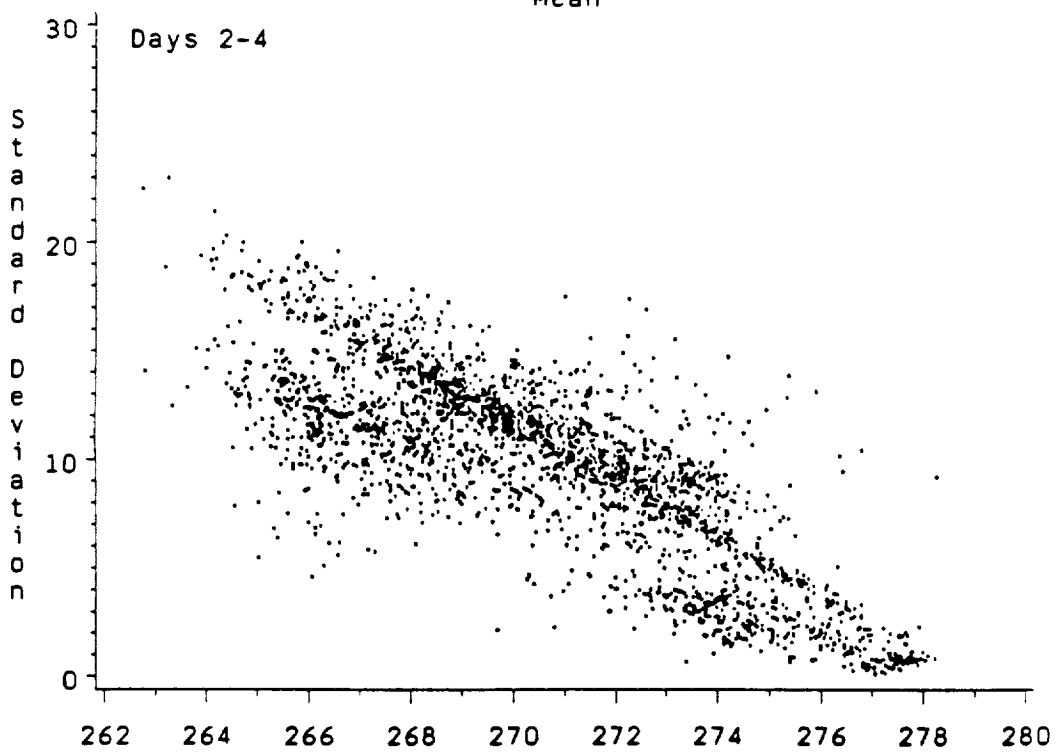
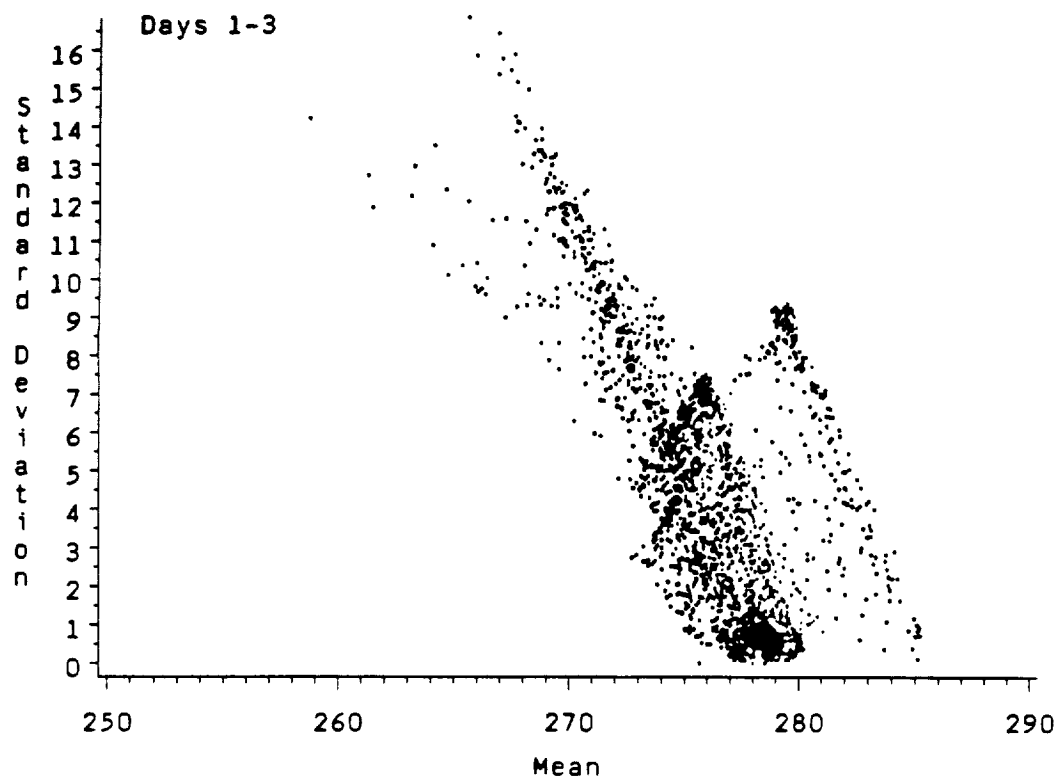


Fig. 4. Temporal coherence plots for days 1-3 and 2-4 (Figure 3).

after are assumed to be clear, although stationary cloud decks will exhibit similar temporal coherence. Figure 4 illustrates the temporal coherence of cells for the same period as in the spatial coherence plots, determined for days 1-3 and 2-4. The first plot in the figure clearly identifies the open water surface (278 K), and also shows the land surface (285 K). In the second 3-day period, land is not evident in the plot.

Spatial and temporal coherence tests were combined for the purpose of identifying which feet of the spatial coherence arch represent clear sky conditions. Results indicate that spatial and temporal tests in combination provide an effective method of identifying clear sky conditions, although requiring low spatial and temporal variability may miss some clear pixels. This information has proven useful in the development of an algorithm that includes spatial and temporal tests, such as that based on ISCCP methodology, described next.

3.4 Cloud Detection Following an ISCCP Methodology

The ISCCP, which began its operational data collection in July 1983, aims to compile a global climatology of cloud cover, cloud top height as pressure and cloud optical thickness. This is to be achieved by using imaging measurements of geostationary satellites which cover the globe from latitudes from 60°N to 60°S. The regions poleward of these latitudes are observed by the polar orbiting NOAA satellites with the AVHRR imager. However few studies have attempted to use these observations to derive cloud properties over the predominantly snow- and ice-covered polar regions. As a basis for developing the ISCCP algorithm, Rossow et al. (1985) compared six cloud algorithms. However, the algorithms were not compared in the polar regions, and a separate study was organized to focus specifically on polar cloudiness (WMO, 1987). In 1990, a joint workshop of radiation/cloud experts, atmospheric modelers, and polar scientists will be organized to examine (1) advances in mapping the surface radiation fluxes over the polar region, (2) the impact of uncertainties in the determination of the time- and space-dependent downward radiation flux on the prediction of the sea ice field, and (3) the quality of model-derived surface radiation fluxes over

sea ice and their validation against observations (WMO, 1988).

The current ISCCP algorithm is composed of a series of steps, each of which is designed to detect some of the clouds present in the scene. The general idea in cloud detection is first to isolate the less variable clear scene radiances in the data and then identify the clouds by their alteration of these radiances (compare to Rossow et al., 1989a). In the basic algorithm, spatial and temporal variation are used in the detection of clear pixels; clear sky composite maps (over five day periods) are then constructed. Finally, each pixel is compared to the clear sky radiances to determine if cloud is present. It has been recognized that reliable detection of cloudiness in the polar regions with the current ISCCP algorithm is particularly difficult, and it has been recommended that the study of clouds over polar regions be continued (WMO, 1988).

This algorithm is applied to Arctic data for January and July conditions. Both AVHRR and SMMR data are utilized. Synthetic AVHRR and SMMR data for a seven-day analysis period are also generated to provide a data set with known characteristics on which to test and validate algorithms. Modifications to the basic algorithm for polar conditions include the use of SMMR and SMMR-derived data sets for the estimation of surface parameters, elimination of the spatial test for the warmest pixel, the use of AVHRR channels 1 ($0.7\mu\text{m}$), 3 ($3.7\mu\text{m}$), and 4 ($11\mu\text{m}$) in the temporal tests and the final multispectral thresholding, and the use of surface class characteristic values when clear sky values cannot be obtained. Additionally, the difference between channels 3 and 4 is included in the temporal test for the detection of optically thin cloud. Figure 5 illustrates the basic steps of this algorithm. Greatest improvement in cloud fraction computed by the modified algorithm is realized over snow and ice surfaces; over open water or snow-free land, all versions perform similarly. Since the inclusion of SMMR for surface analysis and additional spectral channels increases the computational burden, its use may be justified only over snow and ice-covered regions.

The original algorithm, its modification, and testing are described in more detail in Attachments 4 and 5.

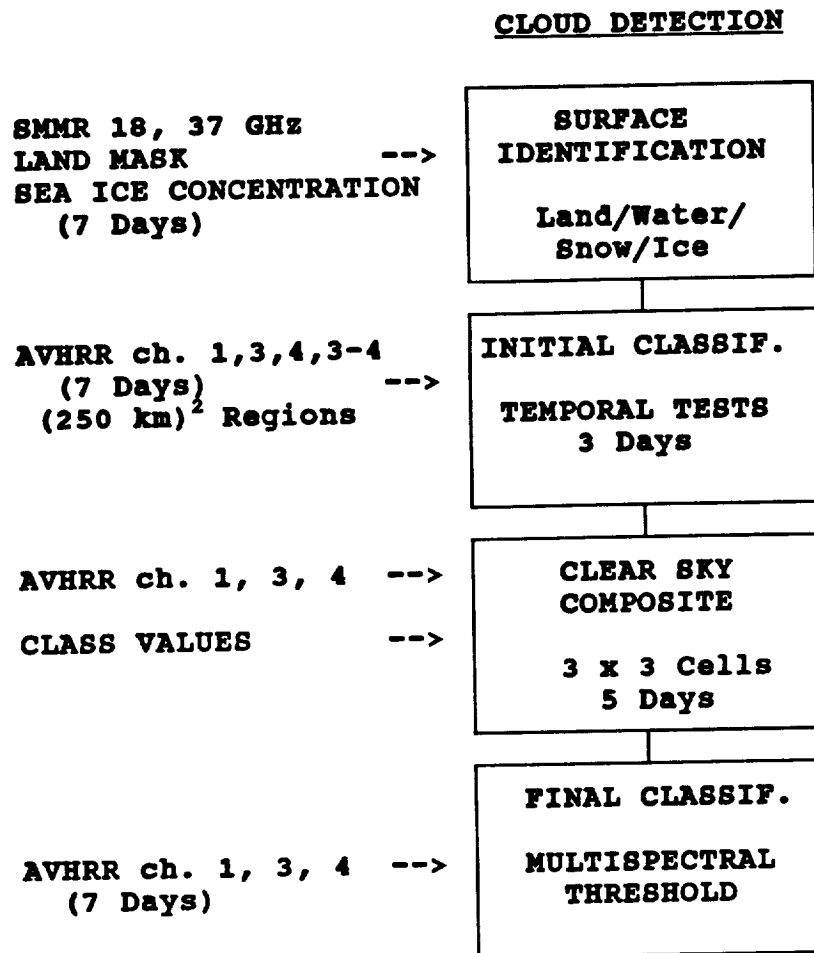


Fig. 5. Major components of the cloud detection algorithm. Inputs are shown on the left.

4. Analysis of Cloud Patterns with Spectral and Textural Measures

High latitude response to changes in cloud cover is a key area of uncertainty in evaluating changes in the global climate system. To improve understanding climate forcing, statistical frameworks for describing the morphology of cloud fields are needed. Major uncertainties exist in current cloud climatologies for polar regions as a result of the problem of discriminating clouds over snow and ice using satellite visible or infrared data. This problem of cloud detection was addressed in the previous section. A methodology for analyzing cloud patterns is presented in this section.

Simulated AVHRR GAC imagery and tests of spatial coherence indicate that in the traditional method of gridding an image, computing spectral and textural features for each cell, and then classifying the cells, those cells small enough to retain a high degree of spatial coherence may be too small to measure texture adequately in the data set. Our method begins with cloud detection on the pixel scale as described in Section 3.4. From this point, two methods of cloud pattern analysis are presented. In one case, simple measures are used to describe cloud types which occur in $(250 \text{ km})^2$ regions with artificially defined boundaries. Such parameters as cloud fraction at three levels, cloud connectivity, and Fourier measures of cloud structure within the regions are computed. These descriptors may be useful for applications which require gridded data; e.g., in climate models.

The second method is presented as an attempt to eliminate the problems inherent in analyses which impose artificial boundaries on cloud and surface patterns, that being the mixture of different classes within a single cell. Rather than compute texture for each cell in a gridded image and then cluster the grid cells, here texture is determined for each pixel. The value assigned to the pixel is the mean texture value computed for all cloudy cells to which it belongs. Cloud pixels are then classified by their spectral and textural features following a maximum likelihood procedure. This procedure is shown in Figure 6.

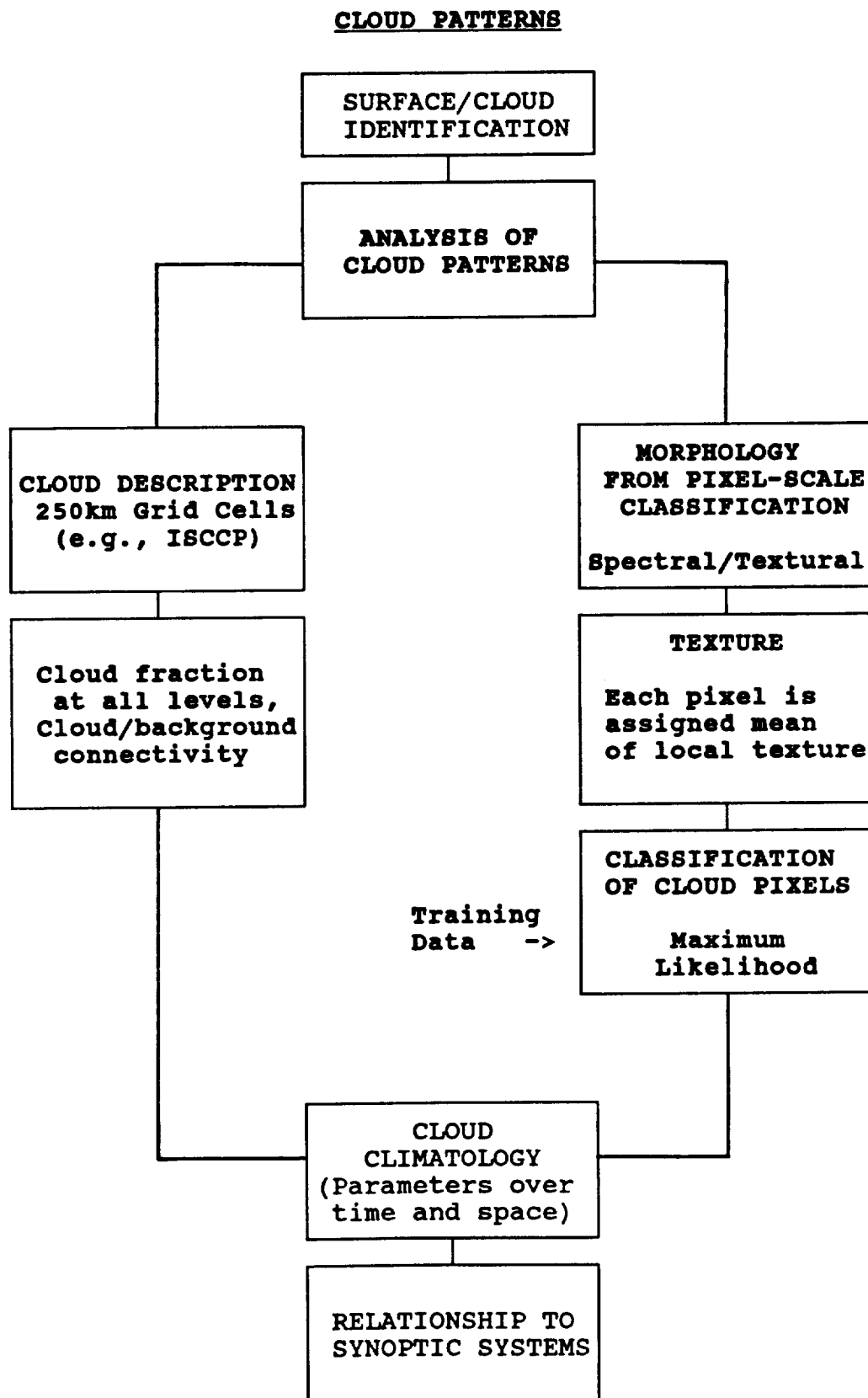


Fig. 6. Major components of cloud pattern analysis. Surface and cloud identification are performed with the algorithm shown in Figure 5. Cloud patterns are described for $(250 \text{ km})^2$ grid cells (left side of figure) or by classifying pixels based on their spectral and local textural characteristics (right side of figure). Future work is shown in the bottom two boxes.

This methodology differs from others which have incorporated cloud texture analyses in two important ways: only the cloudy pixels are examined (surface pixels are identified in the cloud detection step), and texture values are assigned to each pixel rather than to a grid cell. In this manner, training classes can be defined based on texture, and do not need to include mixtures of cloud and/or surface classes. However, the subjectivity inherent in defining cloud types makes an objective assessment of the accuracy of the results difficult. This problem is compounded in the test data, where cloud systems are complex. The spectral and textural measures are determined for the five surface classes defined previously, and for twelve cloud classes which include some of the basic cloud groups and mixtures of these as observed in the data:

1. Low thin cloud over water (stratus);
2. Low thin cloud over ice (stratus);
3. Low thin cloud over land (stratus);
4. Low thick cloud, smooth texture (stratus);
5. Low thick cloud, bumps or broken (stratocumulus);
6. Middle cloud rolls (broken, linear altostratus usually over a stratiform layer);
7. Broken middle cloud, not linear;
8. Middle thick cloud, smooth (altostratus, possibly over stratus);
9. Middle/high bumps (cirrocumulus or altocumulus);
10. High thick cloud with some middle cloud (broken cirrostratus over altostratus);
11. High thick cloud, smooth (cirrus or cirrostratus);
12. Cumulus.

The surface was included in classes 1-3 only because the clouds are thin and differed primarily in albedo. Contributions from surfaces to cloud albedo or temperature in the other classes were not significant enough to justify defining additional classes. Class 7 is similar to class 6, but occurred at a higher level. Correlation between spectral and textural features and the discriminatory capability of each indicates that spectral features are most useful in discriminating between polar surface and cloud classes but that a few texture measures, such as angular second moment, vector strength, entropy, and standard deviation, retrieve structural information of clouds.

A test case resulted in 68% of the cloud pixels being correctly classified when compared to a manual interpretation, although no redefinition of classes or training areas was done to improve this figure. Ebert (1987), in a classification study utilizing fixed grid texture measures on AVHRR

imagery, was able to achieve 84% classification accuracy. However, because of the fixed grid procedure, some of the classes were defined as mixtures of surface and/or cloud types. Additionally, an iterative procedure was used to optimize the training set and the classification algorithm. Therefore, a direct comparison between these two procedures is not appropriate.

The classification results indicate that, as expected, cloud fields are organized into recognizable mesoscale morphologies. An analysis of cloud morphology may in turn give some indication of the physical state of the atmosphere. A detailed examination of the relationship between cloud patterns and synoptic variables requires greater spatial coverage than examined here, as well as a procedure to correlate the cloud patterns to other meteorological data sets. The development of such a procedure is the subject of future research. Additional details are given in Attachment 6.

5. Empirical Studies of Arctic Cloud Cover

The cloud regime over the Arctic Ocean is highly seasonal, with total average cloud cover varying from 40-60 percent in winter to 70-80 or 90 percent in summer (Huschke, 1969; Vowinckel and Orvig, 1970) and a rapid increase from April to May. Geographically, low level cloud in July increases poleward of the Eurasian coastline from about 55-60 percent to an estimated 90 percent around 85°N, 90°E, according to Voskresenskiy and Chukanin (1959). Vowinckel and Orvig (1970) show a similar pattern. However, these two sources differ markedly in their display of low level cloud frequencies in winter. This type of discrepancy highlights our limited knowledge of even mean Arctic cloud conditions, and the need to derive more reliable long term statistics on Arctic cloud cover.

Attachment 7 describes the results of three independent satellite-based analyses of Arctic cloud conditions for selected periods in spring and summer. Cloud cover maps were prepared using two manual analyses and a 3D-nephanalysis (automated algorithm) to identify and classify cloud; all methods utilized DMSP images. A comparison of the cloud information produced by these

methods shows that they are capable of capturing broad climatological features of the cloud cover. For example, the results suggest that in the early part of the spring-summer season cloudiness is strongly influenced by weather systems. The melting of snow cover on the Arctic sea ice is also associated with synoptic weather system activity. However, small-scale parameters such as cloud fraction are subject to error with these methods due to surface effects and the difficulty of discriminating cloud from snow/ice surfaces. It appears that visible and thermal infrared data are insufficient for cloud mapping over some Arctic surfaces on the small scale. This was also shown to be the case with AVHRR data as described in Attachments 4 and 5.

6. Comparison of Modeled and Observed Cloud Cover in the Arctic

A component of a previous NASA project (NAG-5-417) was the analysis of model output from a control run of the Goddard Institute for Space Studies (GISS) general circulation model (Hansen et al., 1983). Five-day pressure fields were classified by the same objective procedure used for the observational data (also for 5-day intervals) and the synoptic variability compared. Overall, the GISS model displays realistic regimes and appropriate seasonal distributions of the principal MSL pressure patterns (Crane and Barry, 1988).

In this project, the GISS model was used to predict cloud cover in the Arctic. Monthly average cloud fractions calculated by the GISS model were evaluated in terms of temporal and spatial distributions, and were compared to observed cloud amounts. The GISS model cloudiness in the Arctic was found to demonstrate the seasonal variability expected based on observational data, but at a much reduced range in the central Arctic. As with the observational data, the zone of maximum cloud cover moves north in the summer, but the calculated amounts are less than expected by about 10-20%. The GISS results indicate that, while most of the cloud cover would appear to be due to large-scale processes, there is evidence that reduced ice concentration in summer may give rise to low-level cloud on a limited regional basis. Attachment 9 provides additional details.

7. Concluding Remarks

The fuzzy sets and neural network classification methods have provided valuable insight into the need for a multispectral approach to cloud detection, and have made clear the ambiguities encountered during the classification process that occur in both spatial and spectral dimensions. This has also been verified by manual interpretations of DMSP imagery. Through spatial and temporal coherence tests, most of this ambiguity can be resolved. This is particularly true if there is knowledge of the types of surfaces and how they are changing underneath the cloud cover - information that can be obtained from the combined AVHRR/SMMR data set.

These investigations provided the impetus to develop a cloud detection scheme utilizing spatial, temporal, and multispectral characteristics of polar clouds and surfaces, as well as surface information. In recognition of the need for a "standardized" procedure, the algorithm follows the basic steps of that used by the ISCCP. The process has been taken even further, where a methodology has been developed for the recognition of mesoscale cloud patterns based on their spectral and textural features. Although additional refinement of the algorithms is still needed, the groundwork has been laid for producing maps of surface and cloud extents, changes, temperatures and albedos, and cloud patterns from polar satellite data.

8. Future Research

Continued work on polar cloud analysis is planned, and a research proposal involving both empirical and modeling studies has been submitted to NASA. Our proposed tasks are to (i) employ radiative transfer and empirical, statistical analyses of satellite-derived data in a coordinated, symbiotic manner to refine our understanding of polar clouds and radiation, (ii) use this information to investigate the potential of AVHRR data in detecting clouds and measuring cloud properties over both polar regions, (iii) further assess the utility of other correlative data, e.g., passive microwave SMMR and SSM/I data, snow cover information, DMSP imagery, along with AVHRR information in cloud retrieval, (iv) investigate the feasibility of using passive microwave data to estimate surface

temperatures over sea ice considering atmospheric effects, ice types, and snow/ice thermal conductivity, (v) assess the effects of haze and ice microphysics on the radiances of AVHRR wavelengths, (vi) utilize this information for the development of a polar-specific cloud detection and analysis algorithm which is expected to follow, at least initially, the major steps of the current ISCCP algorithm. Although emphasis is being placed on passive microwave data from the SMMR, data from the SSM/I instrument on board the DMSP satellites will also be examined. In particular, the 85 GHz channel will be investigated for its potential in cloud detection. SSM/I data are currently being archived at the National Snow and Ice Data Center (Weaver et al., 1987).

Following the further refinement of the cloud detection algorithm, we intend to apply it and some form of the cloud pattern analysis procedures described in Section 4 to a longer time series (e.g., one year, or a single season over a number of years) of AVHRR data for the purpose of compiling a comprehensive set of cloud and surface statistics. With this information, the relationship between cloud morphology and synoptic variables such as pressure and winds can be examined.

9. References

- Arking, A. and J.D. Childs, 1985: Retrieval of Cloud Cover Parameters from Multispectral Satellite Images. *J. Climate Appl. Meteor.*, 24, 322-333.
- Barry, R.G., R.G. Crane, A. Schweiger and J. Newell, 1988: Arctic Cloudiness in Spring from Satellite Imagery: Response. *J. Climatol.*, 8, 539-540.
- Barry, R.G., R.G. Crane, A. Schweiger and J. Newell, 1987: Arctic Cloudiness in Spring from Satellite Imagery. *J. Climatol.*, 7, 423-451.
- Barry, R.G., A. Henderson-Sellers, and K.P. Shine, 1984: Climate Sensitivity and the Marginal Cryosphere. In: J. Hausen and T. Takahasi, eds., *Climate Processes and Climate Sensitivity, Geophys. Monogr.*, 29, Amer. Geophys. Union, 221-237.
- Budyko, M.I., 1969: The Effect of Solar Radiation Variation on the Climate of the Earth. *Tellus*, 21, 611-619.
- Chin, R.T., C. Jau, and J.A. Weinman, 1987: The applications of time series models to cloud field morphology analysis. *J. Climate Appl. Meteor.*, 26, 363-373.
- CGC, 1988: Toward and Understanding of Global Change. Committee on Global Change, National Research Council. Washington, D.C.: National Academy Press.
- Coakley, J.A. and F.P. Bretherton, 1982: Cloud Cover from High-Resolution Scanner Data: Detecting and Allowing for Partially Filled Fields of View. *J. Geophys. Res.*, 87, 4917-4932.
- Crane, R.G. and R.G. Barry, 1984: The Influence of Clouds on Climate with a Focus on High Latitude Interaction. *J. Climatol.*, 4, 71-93.
- Crane, R.G. and Barry, R.G., 1988: Comparison of the MSL synoptic pressure patterns of the Arctic as observed and simulated by the GISS General Circulation Model, *Meteor. Atmos. Physics*, 39, 169-183.
- Curry, J.A., 1988: Arctic Cloudiness in Spring from Satellite Imagery: Some Comments. *J. Climatol.*, 8, 533-538.
- Curry, J.A. et al., 1989a: "Cloudless" ice crystal precipitation in the polar regions. In IRS '88: Current Problems in Atmospheric Radiation (ed. J. LeNoble), Deepak Publ.
- Curry, J.A. et al., 1989b: Arctic ice-crystal haze. *Symposium on the Role of Clouds in Air Chemistry and Climate*, American Meteorological Society, 114-117.
- Ebert, E., 1987: A pattern recognition technique for distinguishing surface and cloud types in the polar regions. *J. Clim. Appl. Meteor.*, 26, 1412-1427.
- Gorschkov, I.G. (ed.), 1983: *World Ocean Atlas, Vol. 3, Arctic Ocean*. Pergamon Press, Oxford (Ministry of Defense, USSR, 1980).
- Hansen, J., et al., 1983: Efficient three dimensional global models for climate studies. *Mon. Wea. Rev.*, 111, 609-662.
- Harris, R. and E.C. Barrett, 1978: Toward an Objective Cloud Analysis. *J. Appl. Meteor.*, 17, 1258-1266.
- Herman, G.F., 1980: Thermal Radiation in Arctic Stratus Clouds. *Quart. J. Roy. Met. Soc.*, 106, 771-780.
- Huschke, R.E., 1969: Arctic Cloud Statistics from Air Calibrated Surface Weather Observations. Mem. RM-6173-PR, Rand Corp., Santa Monica, CA, 79.
- Key, J.R., J.A. Maslanik, and R.G. Barry, 1989a: Cloud Classification Using a Fuzzy Sets Algorithm: A Polar Example. *Int. J. Rem. Sensing*, in press.
- Key, J., J.A. Maslanik, and A.J. Schweiger, 1989b: Classification of merged AVHRR and SMMR data with neural networks. *Photogram. Eng. Rem. Sensing*, in press.
- Key, J. and R.G. Barry, 1989: Cloud cover analysis from AVHRR data, part I: cloud detection. *J. Geophys. Res.*, in press.

- Kukla, G.J. and D.A. Robinson, 1988: Variability of summer cloudiness in the Arctic Basin. *Met. Atmos. Phys.*, 39, 42-50.
- MacCracken, M.C. et al., 1986: Climatic effects of anthropogenic arctic aerosols: an illustration of climatic feedback effects with one- and two-dimensional climate models. *J. Geophys. Res.*, 91 (D13), 14445-14450.
- Maykut, G. and N. Untersteiner, 1971: Some Results from a Time-Dependent Thermodynamic Model of Sea Ice. *J. Geophys. Res.*, 76, 1550-1575.
- McGuffie, K.M., R.G. Barry, J. Newell, A. Schweiger, and D.A. Robinson, 1988: Intercomparison of Satellite-Derived Cloud Analyses for the Arctic Ocean in Spring and Summer. *Int. J. Rem. Sensing*, 9(3), 447-467.
- NASA, (no date): From Pattern to Process: The Strategy of the Earth Observing System. EOS Science Steering Committee Report Vol. II.
- Reynolds, D.W. and T.H. Vonder Haar, 1977: A Bispectral Method for Cloud Parameter Determination. *Mon. Wea. Rev.*, 105, 447-457.
- Robock, A., 1983: Ice and Snow Feedbacks and the Latitudinal and Seasonal Distribution of Climate Sensitivity. *J. Atmos. Sci.*, 40, 986-997.
- Rossow, W.B., F. Moshier, E. Kinsella, A. Arking, M. Desbois, E. Harrison, P. Minnis, E. Ruprecht, G. Seze, C. Simmer, and E. Smith, 1985: ISCCP Cloud Algorithm Intercomparison. *J. Clim. Appl. Meteor.*, 24, 877-903.
- Rossow, W.B., L.C. Garder, and A.A. Lacis, 1989a: Global, seasonal cloud variations from satellite radiance measurements. Part I: sensitivity of analysis. *J. Climate*, 2, 419-458.
- Rossow, W.B., C.L. Brest, and L.C. Garder, 1989b: Global, seasonal surface variations from satellite radiance measurements. *J. Climate*, 2, 214-247.
- Saltzman, B. and R.E. Moritz, 1980: A Time-Dependent Climatic Feedback System Involving Sea-Ice Extent, Ocean Temperature, and CO_2 . *Tellus*, 32, 93-118.
- Scharfen, G., R.G. Barry, D.A. Robinson, G.J. Kukla, and M.C. Serreze, 1987: Large-scale patterns of snow melt on Arctic sea ice mapped from meteorological satellite imagery. *Annals Glacio.*, 9, 200-205.
- Sellers, W.D., 1969: A Global Climatic Model Based on the Energy Balance of the Earth-Atmosphere System. *J. Appl. Meteor.*, 8, 392-400.
- Serreze, M.C. and R.S. Bradley, 1987: Radiation and cloud observations on a high Arctic plateau ice cap. *J. Glacio.*, 33, 162-168.
- Shine, K.P., D.A. Robinson, A. Henderson-Sellers and G. Kukla, 1984a: Evidence of Arctic-Wide Atmospheric Aerosols from DMSP Visible Imagery. *J. Climate Appl. Meteor.*, 23, 1459-1464.
- Shine, K.P., A. Henderson-Sellers, and R.G. Barry, 1984b: Albedo-Climate Feedback: The Importance of Cloud and Cryosphere Variability. In: A. Berger and C. Nicolis, eds., *New Perspectives on Climate Modeling*, Elsevier, 135-155.
- Tsay, S.C., K. Stamnes, and K. Jayaweera, 1988: Radiative Transfer in Stratified Atmospheres: III. Cloudy and Hazy Sky Conditions in the Arctic. Submitted to *J. Atmos. Sci.*
- UCAR, 1988: Arctic interactions, recommendations for an Arctic component in the International Geosphere-Biosphere Programme, Office for Interdisciplinary Earth Studies, UCARR, September 1988.
- Voskresenskiy, A.I. and Chukanin, K.I., 1959: Meteorologicheskie usloviya obled eneniya v oblakov tipa st i sc. *Arkt. Antarkt. Nauch.-Issled. Inst. Trudy*, 228, 124.
- Vowinkel, E. and S. Orvig, 1970: The Climate of the North Polar Basin. *World Survey of Climatology*, 14, *Climates of the Polar Regions*, Elsevier, 129-252.
- Weaver, R., C. Morris, and R.G. Barry, 1987: Passive microwave data for sea ice research: planned products from the DMSP SSM/I system, *EOS*, 68, 769, 776-777.

- WMO, 1987: Report on the International Satellite Cloud Climatology Project (ISCCP) workshop on cloud algorithms in the polar regions. Tokyo, 19-21 August 1986, WCP-131, WMO/TD-No. 170, March 1987.
- WMO, 1988: Report of the third session of the working group on sea ice and climate. Oslo, Norway, 31 May - 3 June 1988, WCRP-18, WMO/TD-No. 272.
- Wu, M-L C., 1987: Determination of cloud ice water content and geometrical thickness using microwave and infrared radiometric measurements. *J. Climate Appl. Meteor.*, 26, 878-884.

10. Publications Supported in Whole or Part by NAG-5-898

PAPERS (Journal/Proceedings)

- Barry, R.G., Crane, R.G., Newell, J., and Schweiger, A., 1988. "Arctic cloudiness in spring from satellite imagery. A response," *J. Climatol.*, 8, 539-540.
- Key, J. and R.G. Barry, 1989. Adaptation of the ISCCP cloud detection algorithm to combined AVHRR and SMMR Arctic data. *IGARSS'89 Proceedings*, Vol. 1, 188-191, July 10-14.
- Key, J., Maslanik, J.A., and Barry, R.G. "Cloud classification using a fuzzy sets algorithm: a polar example," *Int. J. Remote Sensing*, in press.
- Key, J., J.A. Maslanik, and A. Schweiger. Classification of merged AVHRR and SMMR Arctic data with neural networks. *Photogram. Eng. Rem. Sens.*, 55 (9), 1331-1338.
- Key, J. and R.G. Barry. Cloud cover analysis with Arctic AVHRR, part I: cloud detection. *J. Geophys. Res. (Atmospheres)*, in press.
- Key, J. Cloud cover analysis with Arctic AVHRR, part II: classification of with spectral and textural measures. *J. Geophys. Res. (Atmospheres)*, in press.
- Maslanik, J.A., Key, J.R., and Barry, R.G. "Merging AVHRR and SMMR data for sea ice and cloud analysis," *Int. J. Remote Sensing*, in press.
- McGuffie, K., Barry, R.G., Newell, J., Schweiger, A., and Robinson, D., 1988. "Intercomparison of satellite-derived cloud analyses for the Arctic Ocean in spring and summer," *Int. J. Remote Sensing*, 9 (3), 467-477.

THESES

- Key, J.R., 1988. "Cloud analysis in the Arctic with combined AVHRR and SMMR data," unpublished Ph.D. dissertation, University of Colorado, Boulder, 180 pp.

PRESENTATIONS

- 1987 Maslanik, J.A., Barry, R.G., and Crane, R.G., 1987. "Approaches to the interpretation of cloud cover in the polar regions," (abstract). *Clouds in Climate II*. (A WCRP Workshop on Modeling and Observations, Columbia, MD). WCRP, NASA, NSF, NOAA, and DOE, p. 169.
- 1989 Cloud cover retrieval in the Arctic from combined AVHRR and SMMR data. National Center for Atmospheric Research, Advanced Studies Program, March (invited), J. Key.
- 1989 Key, J., J.A. Maslanik, and R.G. Barry, 1989. "Cloud analysis in the Arctic with combined AVHRR and SMMR data." *IAMAP 89, Abstracts Vol. II*, RP-6, Reading, UK, July 31-August 11.

ATTACHMENTS

- 1: Merging AVHRR and SMMR Data
- 2: Cloud Classification with Fuzzy Sets
- 3: Classification with Neural Networks
- 4: Cloud Cover Analysis: Detection
- 5: Adaption of the ISCCP Cloud Detection Algorithm
- 6: Cloud Classification with Spectral and Textural Measures
- 7: Intercomparison of Satellite-derived Cloud Analyses
- 8: Arctic Cloudiness in Spring
- 9: Comparison of Observed and Simulated Cloud Cover

ATTACHMENT 1
MERGING AVHRR AND SMMR DATA

Merging AVHRR and SMMR data for remote sensing of ice and cloud in polar regions

J. A. MASLANIK, J. R. KEY and R. G. BARRY

Cooperative Institute for Research in Environmental Sciences and
Department of Geography, University of Colorado, Boulder,
Campus Box 449 Boulder, Colorado 80309-0449 U.S.A.

(Received 23 June 1988; in final form 22 September 1988)

Abstract. Multispectral data from the Advanced Very High Resolution Radiometer (AVHRR) were digitally processed and merged with Scanning Multichannel Microwave Radiometer (SMMR) imagery. Five channels of AVHRR data, four channels of SMMR brightness temperatures and SMMR-derived ice concentration and ice type were co-registered to a polar stereographic grid. The merged data sets are currently being used in combination with meteorological information for integrated studies of clouds and sea ice.

1. Introduction

The important role that polar processes play in the dynamics of global climate is widely recognized (Polar Research Board 1984). Remote-sensing of the distribution and characteristics of clouds and sea ice is required to monitor climate variability in the Arctic and Antarctic, as well as to provide input to global climatic models.

Optical-wavelength sensors can provide data with a high spatial resolution but are limited by the long periods of winter, darkness poor lighting conditions and persistent cloud cover common in polar regions. Passive microwave sensors operate independently of solar illumination, can view the surface through cloud cover and provide surface information not contained in visible or thermal infrared imagery. However, existing passive microwave sensors yield data with a relatively poor spatial resolution. A combination of digital multispectral data appears to be a logical way of capitalizing on the unique capabilities of each group of sensors, while overcoming some of the problems inherent in remote sensing at high latitudes. Comparison of data from these two sensor groups has been undertaken previously by Choudhury *et al.* (1987) for vegetation studies and d'Entremont and Thomason (1987) for cloud analysis. This work describes a set of merged digital data consisting of visible, near-infrared and thermal infrared imagery from the Advanced Very High Resolution Radiometer (AVHRR) and passive microwave imagery from the Scanning Multichannel Microwave Radiometer (SMMR) combined into a form suitable for the analysis of cloud and sea ice cover.

2. AVHRR and SMMR data

The AVHRR sensors carried on board the NOAA-7 satellite sample the Earth in five spectral channels ($0.58\text{--}0.68\text{ }\mu\text{m}$, $0.725\text{--}1.0\text{ }\mu\text{m}$, $3.55\text{--}3.93\text{ }\mu\text{m}$, $10.3\text{--}11.3\text{ }\mu\text{m}$, $11.5\text{--}12.5\text{ }\mu\text{m}$), with a nadir resolution of 1.1 km . Partial orbits of Global Area Coverage (GAC) data (which is a reduced-resolution product created through on-board satellite processing to yield a nadir resolution of $3\text{ km} \times 4\text{ km}$ for 6–13 January and 1–7 July, 1984 are used in this study. The imagery covers areas in

the Arctic with a permanent ice cap, snow-covered and snow-free land, sea ice and ocean, and a variety of cloud types over each of these surfaces.

First-order calibration of the AVHRR GAC data was performed using the calibration coefficients contained in the image files and the methods described in the NOAA Polar Orbiter Users Guide (NOAA 1984) and in Lauritsen *et al.* (1979). The data values recorded in channels 1 and 2 were converted to spectral albedo in per cent, and channels 3–5 were converted to radiance in milliwatts/(m²-steradians-cm), then to brightness temperature in Kelvin using an approximation of the inverse of the Planck function. The percentage reflectance values produced for channels 1 and 2 by this method are only approximations of albedo and so care is required when comparing these values to broad-band albedos sensed over a wider spectral range (Shine *et al.* 1984).

To mitigate for the effects of solar zenith angle differences along the wide swath of AVHRR, channels 1 and 2 were normalized by dividing the pixel value by the cosine of the solar zenith angle for that pixel as provided in the GAC data records. Since only one zenith angle is given per eight data pixels, the intermediate zenith angles were interpolated linearly. Under the assumption that atmospheric effects can be neglected due to the typically low water vapour content and low temperatures in polar atmospheres, no other adjustments for these effects were made.

A final step in the AVHRR data correction involved extracting the reflected-energy component from the emitted component in channel 3. Brightness temperatures estimated from channel 4 were converted to expected radiances for channel 3 using an inverse calculation of the Planck approximation with channel 3 parameters (the assumption is that emissivity of the surface is constant in these two channels). Subtraction of these radiances from the actual radiances measured in channel 3 yields the component of energy in channel 3 attributable to reflection.

Passive microwave data used in this study were acquired on 6, 8 and 10 January and 2, 4 and 6 July 1984 by the SMMR on Nimbus 7 (Gloersen and Barath 1977). The SMMR collects data in five microwave channels (6.6 GHz, 10.7 GHz, 18.0 GHz, 21.0 GHz and 37.0 GHz), with horizontal and vertical polarizations for each channel. The instantaneous field of view of the sensor varies with channel, ranging from 148 km × 95 km for the 6.6 GHz channel to 55 km × 41 km and 27 km × 18 km for the 18 GHz and 37 GHz channels, respectively. The data stored in these grids are recorded as brightness temperature in Kelvin. No distinction is made between day, night and twilight orbits and data from overlapping orbits are averaged to yield a daily value. SMMR data mapped to polar stereographic grids and archived in the Cryospheric Data Management System (CDMS) of the National Snow and Ice Data Center.

3. Combining AVHRR and SMMR data

Merging of the AVHRR GAC and SMMR data required selection of a common grid size that offered a compromise between spatial resolution and data volume. A polar stereographic projection yielding equal-area pixels true at 70° latitude was selected as the desired map base, with a 5 km grid cell (pixel) size. This pixel size represents a slight degradation of the AVHRR GAC spatial resolution but has the advantage, in terms of data processing, of being an even multiple of SMMR 25 km × 25 km cells used in the CDMS archive. The SMMR data were converted to 5 km cell sizes by simple duplication of pixels, thereby avoiding any artificial increase in spatial resolution. Sea ice concentration and old ice fraction were calculated from

st_w-free land, sea ice and
faces.

was performed using the
methods described in the
Lauritsen *et al.* (1979). The
spectral albedo in per cent.
m²-steradians-cm), then
of the inverse of the
for channels 1 and 2 by
care is required when
for a wider spectral range

ences along the wide swath of
pixel value by the cosine
GAC data records. Since
intermediate zenith angles were
ic effects can be neglected
x temperatures in polar
e made.

ived extracting the reflected-
ar el 3. Brightness tempera-
ected radiances for channel 3
on with channel 3 parameters
st at in these two channels).
s asured in channel 3 yields
reflection.

quired on 6, 8 and 10 January
lc sen and Barath 1977). The
6 GHz, 10.7 GHz, 18.0 GHz.
polarizations for each channel.
s th channel, ranging from
k and 27 km x 18 km for the
ata stored in these grids are
ti. tion is made between day.
o its are averaged to yield a
phic grids and archived in the
e National Snow and Ice Data

re. ired selection of a common
re. lution and data volume. A
pixels true at 70° latitude was
cell (pixel) size. This pixel size
atial resolution but has the
an even multiple of SMMR
SMMR data were converted to
y. oiding any artificial increase
ce. action were calculated from

the SMMR data using the NASA Team Algorithm (Cavalieri *et al.* 1984). This algorithm is based on the normalized difference between vertically- and horizontally-polarized emissivity at 18 GHz and the normalized difference between vertically-polarized data at 18 GHz and 37 GHz.

Nearest-neighbour remapping of the AVHRR data to the polar projection was performed using the ground locations, in latitude and longitude, provided in the GAC records. Since locations are provided only at every eighth pixel, coordinates for the intermediate pixels were interpolated linearly and transformed from latitude/longitude to polar grid coordinates using standard map projection routines. Unfilled grid cells were interpolated by an average of non-zero neighbours. The reduction in ground resolution at the edges of the orbit swath due to the Earth's curvature is handled by pixel duplication so that the grid cell size remains constant across the rectified polar-stereographic image. No adjustments were made to compensate for viewing angle dependencies, as one of the goals of creating this data set is to investigate these effects. Accuracy of the AVHRR navigation using this method is expected to be within 25 km, roughly corresponding to an individual SMMR pixel.

4. An application

Examples of a calibrated and registered AVHRR channel 1 image, centred approximately on Novaya Zemlaya (75°N, 60°E), and covering the Kara and Barents Seas (figure 1), and SMMR 37 GHz data for the same area (figure 2) illustrate the differences in resolution and information content between the two sensors. The colour-composite of AVHRR channels 1 and 4 plus SMMR-derived ice concentration shown in figure 3 demonstrates the ability to map ice concentration and ice edge position beneath cloud cover.

The merged AVHRR—SMMR data sets are proving useful for a variety of applications that benefit from near-simultaneous observations of clouds and surfaces. These data are being used to determine the spectral and textural properties of

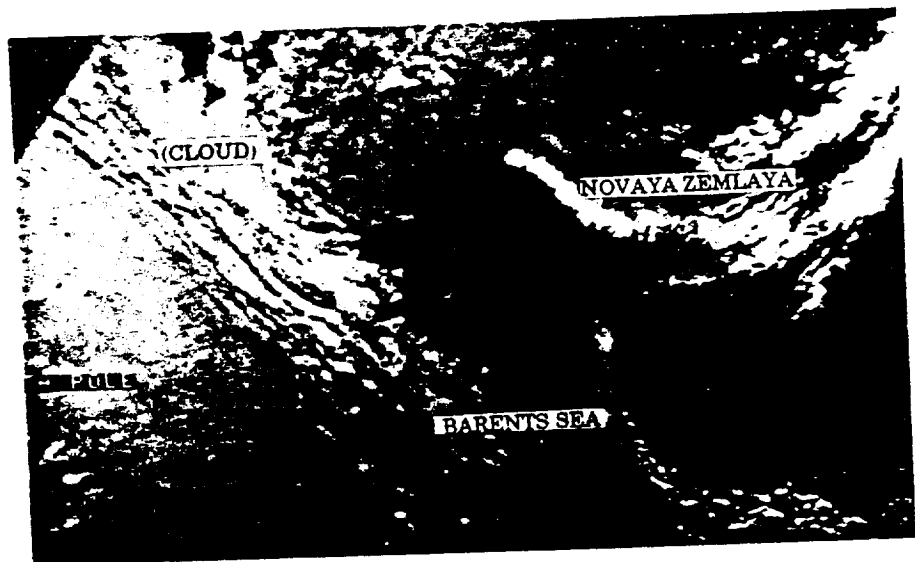


Figure 1. Calibrated and registered AVHRR channel 1 image centred approximately on Novaya Zemlaya and covering the Kara and Barents Seas.

ORIGINAL PAGE
BLACK AND WHITE PHOTOGRAPH

4

J. A. Maslanik et al.

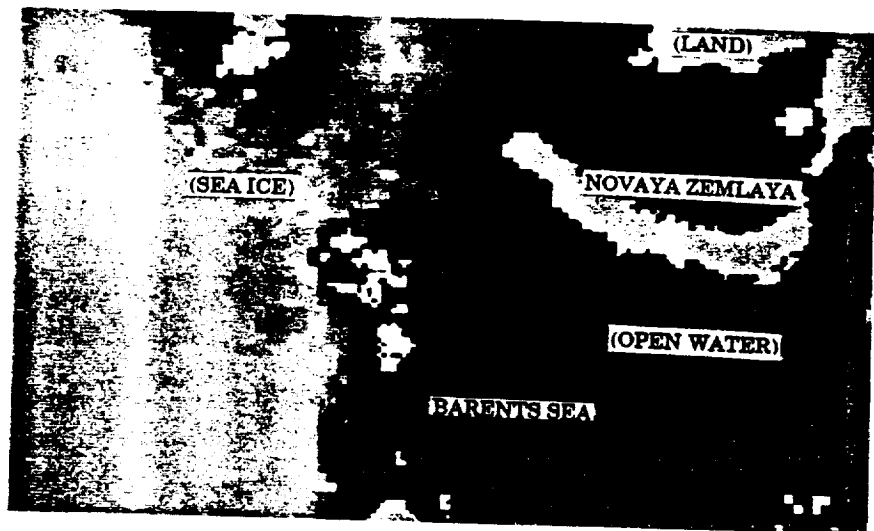
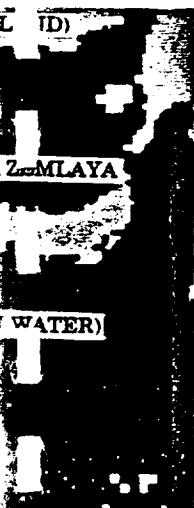


Figure 2. SMMR 37 GHz horizontal polarization data for the same area shown in figure 1.

clouds over snow-covered and snow-free land, permanent ice cap, open water and different concentrations and conditions of sea ice as part of a continuing effort to adapt the International Satellite Cloud Climatology Project (ISCCP) algorithm (Rossow *et al.* 1985) for use in polar regions. The combined data sets allow spatial and temporal thresholds to be chosen based on surface conditions and have shown that the surface often changes within the time periods over which the ISCCP algorithm operates. This situation is illustrated in figure 4, which consists of cloud

Figure 3. A composite of AVHRR channels 1 and 4, and SMMR-derived ice concentration for the areas shown in figure 1.



a shown in figure 1.

can, open water and
a continuing effort to
t (ISCCP) algorithm
data sets allow spatial
tics and have shown
er, which the ISCCP
which consists of cloud

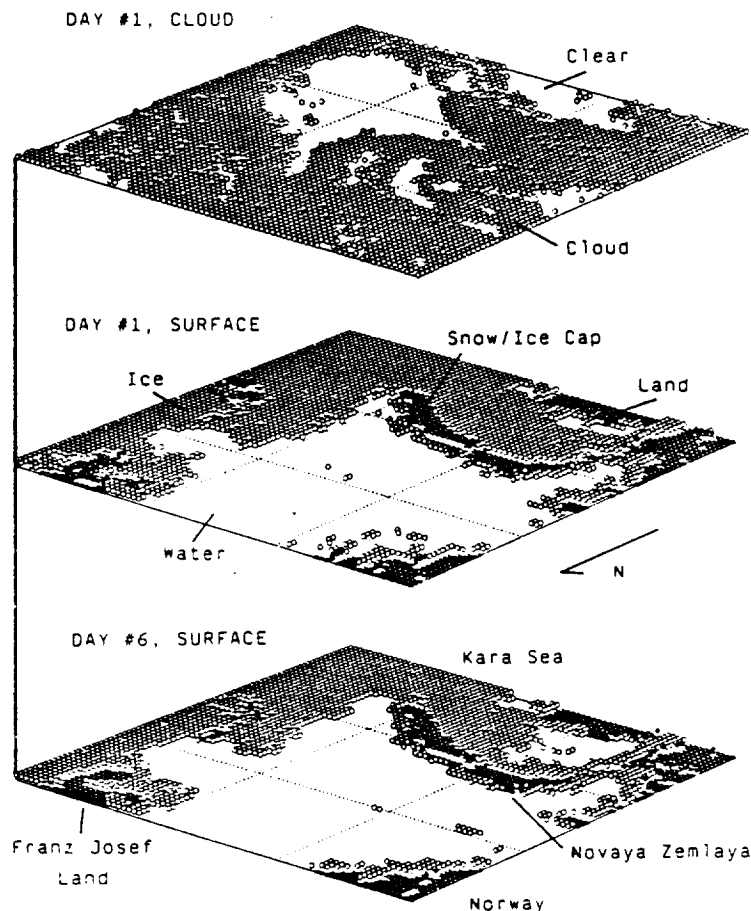


Figure 4. Cloud cover and surface types of a single day and surface types for the same area five days later. Area covered is (1500 km²). The combined AVHRR/SMMR data set provides for the mapping of cloud over varying surfaces, as shown here for changing ice extent north-east and south of Novaya Zemlaya.

mapped with the AVHRR data and surface types identified using SMMR (18 GHz and 37 GHz) and SMMR-derived sea ice concentrations. Cloud cover and surface types are shown for the first day of the seven-day analysis period. Surface types are again shown for the sixth day. The change in ice extent to the north-east and south of Novaya Zemlaya, and the associated change in surface albedo and temperature that will limit the applicability of the ISCCP algorithm in areas with snow and ice cover.

5. Conclusions

The ability to retrieve information on albedo, physical temperature and brightness temperature from spatially and temporally co-located imagery is proving to be a useful aid in comparing the spectral and textural properties of ice and clouds in a broad range of the energy spectrum. The merged data sets capitalize on the unique capabilities of AVHRR and passive microwave data by reducing the inherent limitations of each sensor and provide a means to improve automated cloud mapping

derived ice concentration

in polar regions. Other applications include analysis of directional reflectance and emittance differences, the investigation of the relationship between SMMR-derived ice concentration and AVHRR-measured albedo, comparison of ice concentration and ice-edge position as estimated by AVHRR and SMMR and comparison of AVHRR-derived temperatures with temperatures estimated from SMMR. Future work will investigate the utility of passive microwave data merged with the Level B3 AVHRR product to be archived as part of ISCCP (Schiffer and Rossow 1985) and will assess the potential contribution of such merged data sets to extend the time period of multisensor data available from SSM/I and OLS on DMSP platforms and sensor combinations proposed for the Earth Observing System (EOS).

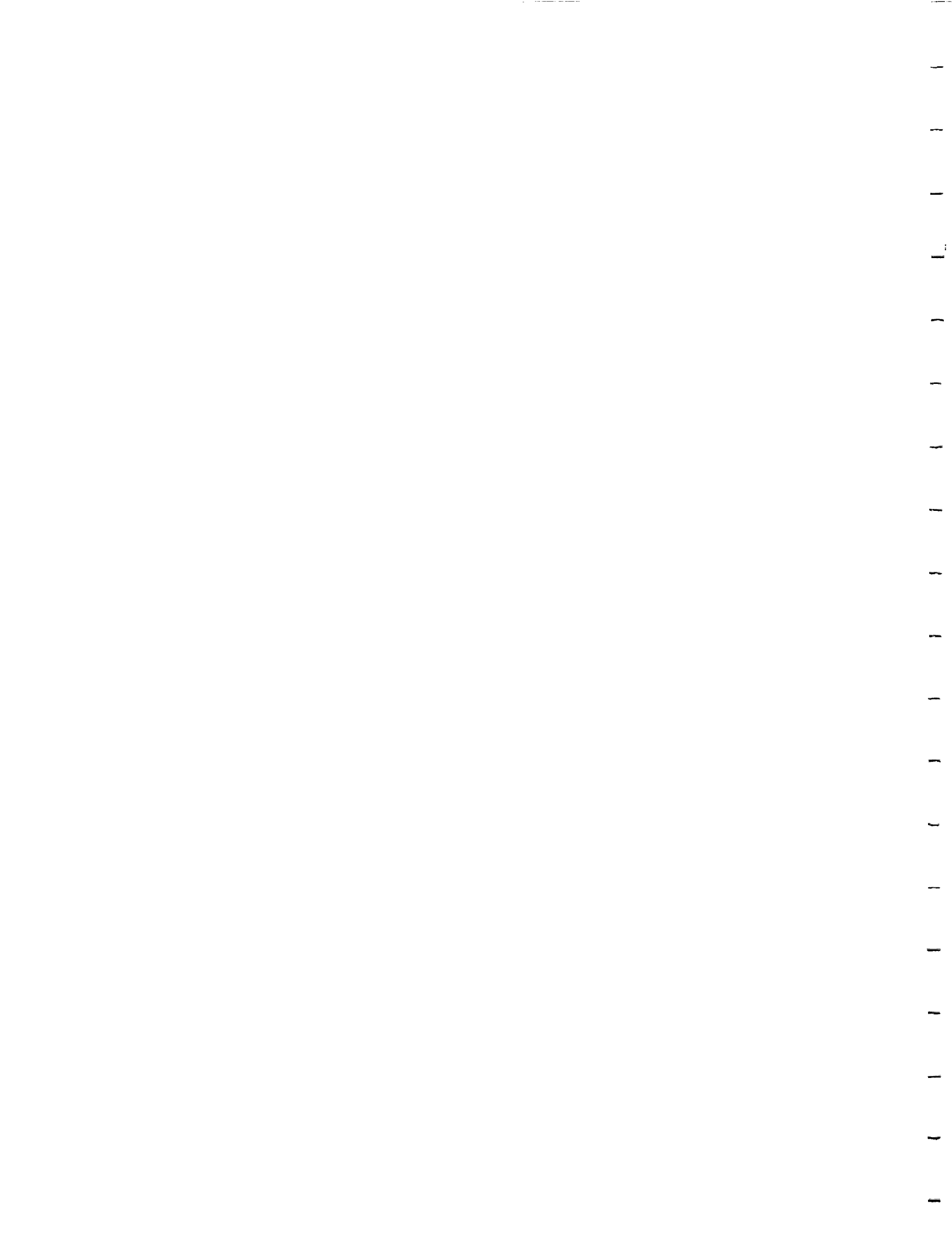
Acknowledgments

This work was supported under NASA grant NAG-5-898 and DOD University Research Instrumentation Program grant N00014-85-C-0039. Thanks are due to W. Rossow and E. Raschke for providing AVHRR GAC data.

References

- CAVALIERI, D. J., GLOERSEN, P., and CAMPBELL, W. J., 1984, Determination of sea ice parameters with Nimbus-7 SMMR. *Journal of Geophysical Research*, **88**, 5355-5369.
- CHOUDHURY, B. J., TUCKER, C. J., GOLUS, R. E., and NEWCOMB, W. W., 1987, Monitoring vegetation using Nimbus-7 scanning multichannel microwave radiometer's data *International Journal of Remote Sensing*, **8**, 533-538.
- D'ENTREMONT, R. P., and THOMASON, L. W., 1987, Interpreting meteorological satellite images using a color-composite technique. *Bulletin of the American Meteorological Society*, **68**, 762-768.
- GLOERSEN, P., and BARATH, F. T., 1977, A scanning multichannel microwave radiometer for Nimbus-G and Seasat-A. *I.E.E.E. Journal of Oceanic Engineering*, **2**, 172-178.
- LAURITSON, L., NELSON, G. J., and PORTO, F. W., 1979, Data extraction and calibration of TIROS-N/NOAA radiometers NOAA Technical Memorandum TM NESS 107. Washington, D.C., U.S.A.
- NOAA, 1984, *NOAA Polar Orbiter Data Users Guide* (Washington, D.C.: U.S. Department of Commerce, National Oceanic and Atmospheric Administration, NESDIS).
- POLAR RESEARCH BOARD, 1984, *The Polar Regions and Climatic Change* (Washington, D.C.: National Research Council, National Academy Press).
- ROSSOW, W. G., MOSHER, F., KINSELLA, E., ARKING, A., DESBOIS, M., HARRISON, E., MINNIS, P., RUPRECHT, E., SEZE, G., SIMMER, C., and SMITH, E., 1985, ISCCP cloud algorithm intercomparison. *Journal of Climate and Applied Meteorology*, **24**, 877-903.
- SCHIFFER, R. A., and ROSSOW, W. B., 1985, ISCCP global radiance data set: A new resource for climate research. *Bulletin of the American Meteorological Society*, **66**, 1498-1505.
- SHINE, K. P., HENDERSON-SELLERS, A., and SLINGO, A., 1984, The influence of the spectral response of satellite sensors on estimates of broadband albedo. *Quarterly Journal of the Royal Meteorological Society*, **110**, 1170-1179.

ATTACHMENT 2
CLOUD CLASSIFICATION WITH FUZZY SETS



**Cloud Classification from Satellite Data
Using a Fuzzy Sets Algorithm: a Polar Example**

J.R. Key, J.A. Maslanik, and R.G. Barry

**Cooperative Institute for Research in Environmental Sciences
and Department of Geography
University of Colorado, Boulder
Boulder, Colorado
80309-0449**

Abstract. Where spatial boundaries between phenomena are diffuse, classification methods which construct mutually exclusive clusters seem inappropriate. The Fuzzy c-means (FCM) algorithm assigns each observation to all clusters, with membership values as a function of distance to the cluster center. The FCM algorithm is applied to AVHRR data for the purpose of classifying polar clouds and surfaces. Careful analysis of the fuzzy sets can provide information on which spectral channels are best suited to the classification of particular features, and can help determine likely areas of misclassification. General agreement in the resulting classes and cloud fraction was found between the FCM algorithm, a manual classification, and an unsupervised maximum likelihood classifier.

Cloud Classification from Satellite Data Using a Fuzzy Sets Algorithm: a Polar Example

1. Introduction

Cloud detection and classification from satellite remote sensing data has received considerable attention in view of the significance of cloud cover for global climate. Various techniques are reported in the literature based on threshold, bispectral, 2-d or 3-d histograms, and split-window methods. Smith (1981) and Crane and Barry (1984) summarize these procedures. From a classification standpoint, most current approaches seek to designate mutually exclusive classes with well defined boundaries; these are termed "hard" classifications. Clustering algorithms used in such classifications are commonly based on either the Euclidean distance measure (e.g., Parikh 1977; Desbois et al. 1982) or the maximum likelihood classifier (e.g., Bolle 1985; Pairman and Kittler 1986; Ebert 1987). Areas where cloud identification is uncertain are usually treated by forcing them into existing classes, or leaving them unclassified.

Our particular interest in cloud conditions in polar regions indicates that this approach is especially undesirable where the spectral characteristics of the clouds and the underlying surface frequently overlap. Where cloud categories are poorly defined and the spatial boundaries between them are diffuse, it seems appropriate to represent this uncertainty in the taxonomic strategy.

The purpose of this study is to examine the applicability of the fuzzy sets approach to the classification of clouds from satellite data. In contrast to hard classifiers, the fuzzy sets approach assigns each observation to every class, with the strength of the membership being a function of the its similarity to the class mean. Fuzzy clustering was introduced by Ruspini (1969) and was later developed into the fuzzy c-means algorithm by Dunn (1974) and generalized by Bezdek (1975). Previous applications of the procedure to climatic data are limited to McBratney and Moore (1985) where the fuzzy c-means algorithm was applied to temperature and precipitation data, and Leung (1987) who took a linguistic approach to describing the imprecision of regional boundaries. There has been an increasing use of fuzzy set theory and fuzzy algorithms with digital images (e.g., Huntsberger et al. 1985, Pal and King 1983), but these procedures have not yet found their way into satellite data processing applications. We do not intend to present new information on cloud characteristics, but rather to provide an alternative method of dealing with the poorly defined boundaries of clouds and surfaces in satellite data.

2. Data

The AVHRR (Advanced Very High Resolution Radiometer) on board the NOAA-7 polar orbiting satellite is a scanning radiometer that senses in the visible, reflected infrared, and thermal (emitted) infrared portions of the electromagnetic spectrum with a nadir resolution of 1.1 km (IFOV of 1.4 milliradians) at a satellite

altitude of 833 km. Global Area Coverage (GAC) data provide a reduced-resolution product created through on-board satellite processing. GAC pixel resolution is used, with each pixel representing a 3 x 5 km field of view. Of the five channels available (0.58-0.68 μm , 0.725-1.00, 3.55-3.93, 10.3-11.30, 11.5-12.50) channels 1, 3 and 5 are employed here.

First-order calibration of the AVHRR GAC data was performed following the methods described in the NOAA Polar Orbiter Users Guide (NOAA 1984) and Lauritsen, et al. (1970). Channel 1 was converted to albedo and corrected for solar zenith angle; channels 3 and 5 were converted to radiance in $\text{mW m}^{-2} \text{sr}^{-1} \text{cm}$.

3. Example of Polar Clouds and Surfaces

Determination of the amount of cloud cover is the principal objective of cloud classification for the study of ice-atmosphere interactions in the polar regions. Secondly, breakdown of the cloud cover into different types, e.g. stratus, cirrus, cumulus provides useful information on cloud radiative properties, availability of moisture, and source of the cloudiness. To determine the amount of cloud requires that the classifier discriminate between clouds and underlying surfaces of snow, ice, water, and land. Distinguishing between cloud type may require information on cloud height (estimated from cloud-top temperature) and cloud morphology (related to large-scale patterns or local texture).

The study area is shown in Figure 1 (channels 1, 3, and 5).

This is a 250x250 pixel or $(1250 \text{ km})^2$ area centered over Novaya Zemlya and the Kara and Barents Seas on July 1, 1984. Open water, snow-covered and snow-free land, sea ice (various concentrations), and high, middle, and low cloud over different surfaces are present in the image. For computational efficiency, means of 2x2 pixel cells were used in the classification process, reducing the number of pixels from 62,500 to 15,625. A manual interpretation of this area is given in Figure 2.

The problem of distinguishing discrete cloud and surface categories is illustrated by Figure 3, which shows scatter plots of visible vs. near-infrared and visible vs. thermal data for a $(1250 \text{ km})^2$ segment of the study area. Based on training area statistics, the spectral responses of four surface types (snow-free and snow-covered land, sea ice, and open water) and three general cloud categories (high, middle, and low) are identified in the plots by their mean plus and minus two standard deviations in each of the two channels. The principal sources of confusion are likely to occur between snow/ice and cloud due to their similar responses in AVHRR Channel 1 and, to a lesser extent, Channel 2. In the thermal channels, similarities exist between the physical temperatures of low or thin clouds, ocean, and melting sea ice. The data in Figure 1 present several examples of cloud of varying optical depth overlying different concentrations of sea ice. In addition, the surface conditions of the sea ice (as estimated by reflectance and passive microwave emissivity differences) are not constant throughout the image. It is clear that the spectral

properties of the clouds and ice are not likely to form compact and distinct clusters in multispectral space. Hard classifiers are required to force these indistinct areas into spectrally similar, but perhaps unsuitable, classes. Otherwise, large areas of the image will remain unclassified.

4. Classification using Fuzzy Sets

In the fuzzy sets approach, points do not belong to only one class but instead are given membership values for each of the classes being constructed. Membership values are between zero and one and all the membership values for a given point must sum to unity. Memberships close to one signify a high degree of similarity between the sample point and a cluster while memberships close to zero imply little similarity.

In this respect, memberships are similar to probabilities. However, no assumption of distribution type is made in fuzzy c-means (FCM) clustering, and calculations of memberships are not based on probability density functions. Therefore, this methodology bears little theoretical relationship to probability-based techniques such as maximum likelihood which assumes multivariate normal distributions, or discriminant analysis which is based on the general linear model.

The fuzzy c-means algorithm is neither a "lumper" (conjunctive or clustering procedure), which operates by combining small clusters into larger clusters, or a "splitter" (disjunctive or divisive classification procedure) which begins with all pixels

belonging to the same class then subdividing. Instead, in the FCM algorithm all pixels begin and end with memberships in each of the specified number of clusters; each iteration adjusts these memberships to minimize an error function.

A brief explanation of the FCM procedure is provided below; for a more complete description, see Bezdek (1981) and Kandel (1982). Following Bezdek et al. (1984) and McBratney and Moore (1985), the fuzzy c-partition space is

$$M = \{U: u_{ik} \in [0,1]; \sum_{k=1}^n u_{ik} > 0, i=1..c; \sum_{i=1}^c u_{ik} = 1, k=1..n\}$$

where U is a fuzzy c-partition of a sample of n observations and c clusters. Each element of U , u_{ik} , represents the membership of a particular observation x_k in the i th fuzzy group. Each x_k is a vector of length p where p is the number of features (e.g. spectral channels, texture measures, etc.). These membership coefficients are values between 0 and 1 and for each observation sum to one. Also, the sum of the membership values for each cluster is greater than zero, otherwise the group does not exist.

Optimal fuzzy c-partitions may be identified with the generalized least-squared errors functional

$$J_m(U,V) = \sum_{k=1}^n \sum_{i=1}^c (u_{ik})^m (d_{ik})^2$$

where U is the fuzzy c-partition of the data, x_k , which is a c by n matrix with elements u_{ik} ; V is a c by p matrix where each element v_{ik} represents the mean of the k th of p attributes in the i th of c

groups; n is the number of observations; m is a weighting component, $1 < m < \infty$, which controls the degree of fuzziness; d_{ik} is the distance between each observation x_k and a fuzzy centroid v_i , a measure of dissimilarity given as

$$(d_{ik})^2 = (x_k - v_i)^T A (x_k - v_i)$$

where A is the inner product norm metric, discussed below. An optimal fuzzy c-partition is obtained when J_m is minimized. This is achieved by the Fuzzy c-Means algorithm, which is given in the appendix.

4.1 FCM Parameters

A number of options are available in the FCM algorithm so that the results may be tailored to the problem at hand. These are the weighting exponent, initial matrix, A-norm, and computational considerations.

Weighting exponent. According to Bezdek et al. (1984), no computational or theoretical evidence distinguishes an optimal weighting exponent. The range of useful values seems to be $[1, 30]$ while for most data, $1.5 \leq m \leq 3.0$ gives good results. In choosing values for m , it is important to remember that as m approaches unity the partitions become increasingly hard and as m approaches infinity the optimal membership for each data point approaches $1/c$. Therefore increasing m tends to increase "fuzziness".

McBratney and Moore (1985), applied the fuzzy c-means method

to temperature and precipitation data from stations in Australia. They tested a range of values for m and found that $m=100$ yielded memberships almost constant at 0.5 for each of two classes indicating that clustering was so fuzzy that no clusters would be distinguished. They also attempted to identify optimal combinations of c , the number of classes, and m by plotting the change in the error functional, J_m , with m for each number of clusters, c . In general, J_m decreases with increasing c and m , but its rate of change with changing m is not constant. Their work showed that, at least empirically, m of approximately 2 is optimal, though for a large number of groups m should be less than for a smaller number of groups to obtain similar balance between structure and continuity.

Initial matrix. The initial U matrix also provides a number of options: a random start, a random nonfuzzy start, or an almost uniform start. Alternatively, the results from another clustering method can be used as the initial matrix. In the random start, each membership coefficient is given a random value between zero and one. The random nonfuzzy start assigns a membership coefficient of one to a randomly chosen class and zero to the remaining sets. An almost uniform start is obtained by setting each membership to $1/c$ plus or minus a small random component. The algorithm presented by Bezdek et al. (1984) employs a random start, while McBratney and Moore (1985) found that an almost uniform start yielded faster convergence and similar results from different runs.

Starting with results from another cluster procedure has not previously been tested; in our experiments the number of iterations needed for convergence was usually reduced by 10-20%.

It is suggested by Bezdek that the FCM be run for several different starting membership matrices since the iteration method used, like all descent methods, is susceptible to local stagnations. If different starting matrices result in different final memberships, further analysis should be made.

A-norm. A detailed discussion of the geometric and statistical implications of the choices of the A-norm is given in Bezdek (1981). Three of these norms, Euclidean, diagonal, and Mahalanobis, are of interest in FCM. When the Euclidean norm is used, J_m identifies hyperspherical clusters, but for any other norm, the clusters are essentially hyperellipsoidal. A Euclidean metric can be used for uncorrelated variables on the same scale, a diagonal metric for uncorrelated variables on different scales, and Mahalanobis' for correlated variables on the same or different scales.

Computational considerations. The fuzzy sets program was not originally designed for application to very large data sets such as satellite images. The number of computations necessary is a function of the number of data items (pixels), the number of features, and the number of clusters. The number of data items being processed at any one time can be reduced by using a random

sample of the entire image, hopefully obtaining a representative subset. Clustering local areas of the image with the ultimate goal of global description is another possibility.

No alternative method of calculating cluster centers or updating the membership matrix is evident. However, an alternative method of error calculation - which controls termination of the algorithm - is to compare elements of each cluster center matrix from two successive iterations rather than comparing successive membership matrices. The cluster center matrix is of dimensions c by c rather than n by c for the membership matrix. If n is much larger than c , the savings in CPU time are significant. Additionally, computer memory would be reduced by approximately 40%. If this method is chosen, however, data should be on the same scale - either originally or standardized to a zero mean and unit variance - so that cluster centers can be compared with the same error criteria. Of course, relaxing the convergence criterion (maximum allowable error; see Appendix, step 4) will reduce the number of iterations required. If the channels employed are statistically independent, then the number of computations may be further reduced by eliminating those involving the A-norm metric, which for uncorrelated variables on the same scale would be the identity matrix.

Without these modifications for image processing, computational resources are certainly not trivial, as the execution of the FCM algorithm on a 125×125 pixel area requires approximately one hour of CPU time on a DEC VAX 8550 and up to ten

hours on a DEC MicroVAX configured for "typical" user loads. Adjustment of system parameters such as working set size can significantly reduce disk paging, which will in turn reduce total CPU time. With adjustments for large images, computation time can be reduced by a factor of ten.

4.2 Validity functionals

It is possible to obtain data sets where the error functional is globally minimal but where the resulting classes are visually unappealing. To aid in the resolution of this problem, two validity functionals are used to evaluate the effect of varying the number of clusters: the partition coefficient, F , and the entropy, H :

$$F = \sum_{i=1}^c \sum_{k=1}^n (u_{ik})^2 / n$$

and

$$H = - \sum_{i=1}^c \sum_{k=1}^n (u_{ik} \log_{\alpha} u_{ik}) / n, \quad 0 < \alpha < \infty$$

F will take values between $1/c$ and one, while H has a range of zero to $\log_{\alpha} c$. When F is unity or H is zero, clustering is hard, while an F value of $1/c$ or an H value of $\log_{\alpha} c$ implies that memberships are approximately $1/c$. A plot of F or H by the number of groups may be examined for local maxima of F or minima of H , which will give some indication of optimal c .

5. Results

The FCM program was applied to the study area in Figure 1 as represented by AVHRR channels 1, 3, and 5. A variety of fuzziness index values were tested as well as a range in the number of clusters. The partition coefficient, F , and entropy, H , for each run is listed in Table 1. Run #5 represents an essentially hard classification ($m=1.25$) where F is large and H is small. Conversely, the fuzziness index of 2.6 in run #2 resulted in a small F and large H . Run #6 produced the least visually appealing and least realistic results of all runs. This is supported statistically by the minimal F and maximal H . Figure 4 illustrates the change in F and H for a varying number of clusters. For these tests, $m=2.0$. A local maximum for F and minimum for H occur at $c=6$, with $c=10$ also being acceptable.

A visual examination of the results from each of these tests revealed that the 10-cluster solution best identified the cloud and surface types present in the scene, therefore an interpretation of this solution is given. Figures 5a-5j (hereafter Sets A-J) illustrate each of the ten classes where grey level represents membership of each pixel in the class, lighter grey shades indicating larger membership values. The most distinct classifications are shown by the bright areas (high probabilities) assigned primarily to land in Set C, sea ice under clear skies (Set H), and open water (Set I). The varying gradation of cloud conditions are represented in several of the other sets. Sets E

and G describe high stratocumulus, Sets A, D, and J show high memberships for lower stratus. Thin stratus over ice is represented in Set F. Large memberships in Set B occur for thin cloud over water, but also for mixed pixels at land, cloud, and ice edges. Areas that are not distinctly classified in a single set appear as intermediate gray-tones in several of the sets in Fig. 6. In particular, the ice cap on Novaya Zemlya is confused with thin cloud over ice (Set F), and thicker, higher clouds in Sets A, D, E, G, and J. These are areas that - at least for this particular algorithm - require additional information to be distinguished from other classes.

The distribution of memberships between the fuzzy sets described above presents a convenient graphical tool for interpreting the physical properties of clouds and surfaces, and thus the potential sources of confusion in multispectral classifiers. For example, the similarity between clouds and the Novaya Zemlya ice cap in several of the fuzzy sets is apparently due to similar albedos and temperatures yielding similar responses in AVHRR channels 1 and 5. Interestingly, the ice cap has the largest membership in Set F, with memberships similar to the thin cloud over ice in the upper-left portion of the image. A physical interpretation of the memberships in Set F suggests that the combination of thin cloud with an underlying, high-albedo surface yields a combined spectral return with physical temperature and albedo similar to the Novaya Zemlya ice cap under clear skies.

If desired, a hard classification can be obtained from the

fuzzy sets results where, for each pixel, the largest membership value is replaced with a membership of one, while membership values for the other classes are set to zero. In this manner, the same basic classes will result, but the fuzziness is eliminated.

5.1 Statistical Properties

The previous discussion pointing out the ability of the fuzzy sets to combine multispectral information into individual probability sets is suggestive of artificial orthogonal features created through principal components analysis. The fuzzy sets are, however, simpler to interpret in physical terms since their development is not restricted by the objective of creating uncorrelated components and maximizing the amount of variance accounted for by each component. No attempt is made to include as much information as possible in the first few sets created. Unlike principal components, the information content of each successive fuzzy set does not necessarily decrease. In fact, Sets H and I represent two of the most spectrally-distinct classes in the AVHRR data.

These differences between the fuzzy sets classifier and principal components is demonstrated by examining the cross-correlations between the individual probability sets. The maximum correlation (37%) occurs between Set A and Set J. Sets H and I are not positively correlated with any of the other sets. Sets A and J both predominantly represent slightly different conditions of stratus cloud. The lack of a requirement that the

two sets be uncorrelated allows the gradation of cloud height and thickness to be clearly represented in these two sets. On the other hand, the ability of the fuzzy sets classifier to identify basically uncorrelated classes such as open water and sea ice is demonstrated in Sets H and I.

Application of principal components analysis with fuzzy sets as variables and individual pixels as observations allows us to identify similarities among the sets more quantitatively. Using unrotated components, eight components are required to account for 94% of the variance present in the sets, while the first five components describe 69% of the variance. The large number of components required to represent the information content of the fuzzy sets confirms that each set provides a considerable amount of unique information. Comparison of the factor loadings in each set suggests that Principal Component 1 discriminates between different conditions of stratus cloud and open water (high loadings for Sets A and J, and negative loading for Set I. A similar type of interpretation can be made for Component 2, which appears to represent high cloud, with the greatest positive loadings for Fuzzy Sets E and G). With the exception of Components 1 and 2, no loadings exceed 50%. The relationships between the fuzzy sets as variables is perhaps slightly masked by the potential confusion of unique and common variances inherent in principal components. However, the component-derived groupings agree well with the correlations in the cross-correlation matrix. As a final confirmation of the uniqueness of each fuzzy set, a Varimax

rotation was applied to the principal components. Results of the rotation approach the desired ideal of simple structure, with a loading of nearly 1.0 on one set per component, again suggesting that large correlations are not found between groups of fuzzy sets.

5.2 Supervised Approach

A supervised approach may be taken if class means are known. In this case, the algorithm may be modified to simply calculate the memberships for each pixel in each of the known classes. The memberships are still a function of the weighted distance to the class means, but the class means are no longer determined by the algorithm. These are instead supplied in a manner analagous to using training sites to provide spectral statistics for a supervised classification. This approach is very fast (30-40 times faster than unsupervised) as it requires only one pass through the data.

We have found that class means must be very carefully selected, and that some experimentation may be necessary to reach a realistic solution. For example, Run #7 in Table 1 was a supervised classification where a seven-cluster solution was specified and class means were provided for snow-covered and snow-free land, sea ice, open water, high cloud, middle cloud, and low cloud in AVHRR channels 1, 3, and 5. Snow-covered land did not uniquely define any fuzzy set, but was instead grouped with low cloud because of similar albedos and brightness temperatures. While this problem may be solved by adjusting the class means,

perhaps a better solution would be to add a weighting function to the algorithm so that features which better define a particular class will be more influential in the calculation of membership coefficients.

5.3 Maximum Likelihood Classification

To provide a source of comparison to the fuzzy sets approach, the data shown in Figure 1 were classified using an unsupervised maximum likelihood (ML) procedure. The results are shown in Figure 6. The unsupervised clustering approach (with all image pixels taking part in the definition of spectral signatures) yielded 21 clusters, with four clusters accounting for 67% of the area. None of the remaining 17 clusters represented more than one percent of the image. Sixteen percent of the scene remained unclassified, and an additional 12% of the image pixels fell in more than one cluster. Misclassifications are noted for indistinct classes, specifically low concentration ice (grouped with low clouds), optically thin clouds, and for boundary pixels between different classes.

The restrictive effects of the hard classifier vs. fuzzy sets are apparent in the large number of unclassified pixels. Most high and middle cloud layers were left unclassified, as was the ice cap on Novaya Zemlya. For indistinct classes common in polar cloud analyses, the fuzzy sets approach avoids errors of commission and omission that occur when such indistinct values are forced into the nearest class in spectral space.

6. Discussion

Sets A, B, D, E, F, G, and J of the fuzzy sets classification each represent a separate cloud class, although other surface/cloud mixtures sometimes had large membership values in these classes. A map of cloud classes constructed from the maximum membership value for each pixel is shown in Figure 7. These results generally agree with the manual classification in Figure 2 and the maximum likelihood classification shown in Figure 6. Discrepancies occur with middle and high clouds (unclassified in the ML method), and with cumulus which, in the ML procedure, is grouped with an optically thin stratus deck over sea ice.

While there were some obvious differences in number of cloud classes and the cloud types that each class represented in the three methods, the total cloud amount computed for each procedure was similar. For the manual and ML classifications, cloud fraction is simply the proportion of cloud pixels in the image. In the ML results, this was computed for only those areas labeled as cloud in Figure 6, and again with the unclassified areas included. For the fuzzy sets results, two methods of computing cloud fraction were examined. In both cases, the membership values of each pixel in each of the cloud classes were summed. This may be considered an estimate of a pixel's "cloudiness". Then, in the first case, for each threshold from 0.4 to 0.9 in increments of 0.1, a pixel was considered cloud-filled if its cloudiness exceeded the threshold. Cloud fraction was expressed as the proportion of

cloudy pixels in the image. In the second case, the pixels were considered partially cloud-filled, with cloud fraction being the sum of all cloudiness values that exceeded the threshold, as a proportion of the total number of pixels in the image. Cloud fractions computed for the manual classification, ML method, and the fuzzy sets are given in Table 2. Best agreement between the methods occurs when the threshold is high (0.7) if pixels are considered completely cloud-filled, or in the midrange (0.4-0.6) if pixels are treated as partially cloud-filled.

7. Conclusion

The fuzzy sets method of classification was successfully adapted to the analysis of multispectral satellite imagery. The ability of the fuzzy sets approach to address indistinct spectral classes by calculating class memberships as opposed to the "in-or-out" decision required of hard classifiers is particularly well suited to the range of albedos and physical temperatures encountered in the analysis of ice and cloud conditions in the polar regions.

Application of the fuzzy sets classifier to an AVHRR image containing sea ice and cloud of varying condition and opacity yielded ten membership sets containing contextually and statistically unique information. Interpretation of intensities in images of these sets demonstrates the ability of the fuzzy sets to describe well-defined classes (such as open water and land) as well as classes that fall in intermediate spectral space (e.g.,

ice cap, thin stratus over water, or sea ice of varying concentration). Identification of such fuzzy areas in taxonomic space provides information on where data in additional spectral regions are required for accurate classification. Future work will use the fuzzy sets approach as a tool to help "tune" hard classifiers such as unsupervised clustering and bispectral threshold methods for cloud and ice mapping in the polar regions.

Acknowledgements

This work was supported under NASA grant NAG-5-898 and a DOD University Research Instrumentation Program grant N00014-85-C-0039. Thanks are due to W. Rossow and E. Raschke for providing AVHRR GAC data.

Appendix

Following Bezdek et al. (1984), the Fuzzy c-Means (FCM) algorithm is:

- (1) Fix: c , $2 < c < n-1$
 m , $1 < m < \infty$; the larger the m , the fuzzier the solution; many practitioners use $m=2$.
 A , the inner product norm metric for R^p , where p is the number of attributes
 U^0 , the initial fuzzy c-partition
 ϵ , the value for the stopping criterion ($\epsilon=0.01$ gives reasonable convergence.)

Repeat until convergence (step 4):

- (2) Calculate the c fuzzy group centroids, v_i

$$v_i = \frac{\sum_{k=1}^n (u_{ik})^m x_k}{\sum_{k=1}^n (u_{ik})^m} \text{ for all } i$$

- (3) Update U^l using

$$u_{ik} = 1 / \left[\sum_{j=1}^c \frac{d_{ik}^{2/(m-1)}}{d_{jk}^{2/(m-1)}} \right]$$

which may be rewritten in the more computationally efficient form:

$$u_{ik} = [1/d_{ik}^2]^{1/(m-1)} \left[1 / \sum_{j=1}^c (1/d_{jk}^2)^{1/(m-1)} \right]$$

The measure of dissimilarity, d_{ik}^2 , is given as

$$(d_{ik})^2 = (x_k - v_i)^T A (x_k - v_i)$$

where A is the inner product norm metric.

- (4) Compare U^{l+1} to U^l . If the difference between all corresponding elements is less than or equal to ϵ , then stop. Otherwise, set $U^l = U^{l+1}$ and return to step (2).

References

- Bezdek, J.C., 1981, Pattern Recognition with Fuzzy Objective Function algorithms. (New York: Plenum Press)
- Bezdek, J.C., Ehrlick, R., and Full, W., 1984, FCM: the fuzzy c-means clustering algorithm. **Computers & Geosciences**, 10, 191-203.
- Bezdek, J.C., 1975, Mathematical models for systematics and taxonomy. In Proc. Eighth Int. Conf. on Numerical Taxonomy, G. Estabrook (ed.), Freeman, San Francisco, pp. 143-164.
- Bolle, H.J., 1985, Assessment of thin cirrus and low cloud over snow by means of the maximum likelihood method. **Advances in Space Research**, 5(6), 169-175.
- Crane, R.G. and Barry, R.G., 1984, The influence of clouds on climate with a focus on high latitude interactions. **Journal of Climatology**, 4, 71-93.
- Desbois, M., Seze, G., and Szejwach, G., 1982, Automatic classification of clouds on METEOSAT imagery: application to high level clouds. **Journal of Applied Meteorology**, 21, 401-412.
- Dunn, J.C., 1974, A fuzzy relative of the isodata process and its use in detecting compact, well-separated clusters. **Journal of Cybernetics**, 3, 22-57.
- Ebert, Elizabeth, 1987, A pattern recognition technique for distinguishing surface and cloud types in the polar regions. **Journal of Climate and Applied Meteorology**, 26, 1412-1427.
- Huntsberger, T.L., Jacobs, C.L., and Cannon, R.L., 1985, Iterative fuzzy image segmentation. **Pattern Recognition**, 18 (2), 131-138.
- Kandel, A., 1982, Fuzzy Techniques in Pattern Recognition. (New York: Wiley)
- Lauritson, L., Nelson, G.G., and Port, R.W., 1979, Data extraction and calibration of TIROS-N/NOAA A-G radiometer. **NOAA Tech. Memor., NESS 107**, Natl. Oceanic and Atmos. Admin., Boulder, Colorado.
- Leung, Yee, 1987, On the imprecision of boundaries. **Geographical Analysis**, 19 (2), 125-151.
- McBratney, A.B. and Moore, A.W., 1985, Application of fuzzy sets to climatic classification. **Agricultural and Forest**

Meteorology, 35, 165-185.

NOAA, 1984, NOAA polar orbiter data user's guide. U.S. Department of Commerce, National Oceanic and Atmospheric Administration, NESDIS, February, 1984.

Pairman, D. and Kittler, J., 1986, Clustering algorithms for use with images of clouds. **International Journal of Remote Sensing**, 7(7), 855-866.

Pal, S.K. and King, R.A., 1983, On edge detection of X-ray images using fuzzy sets. **IEEE Transactions, PAMI-5**, 69-77.

Parikh, J.A., 1977, A comparative study of cloud classification techniques. **Remote Sensing of Environment**, 6, 67-81.

Ruspini, E.H., 1969, A new approach to clustering. **Information Control**, 15, 22-32.

Smith, E.A., 1981, Review of cloud climatologies. In Clouds and Climate; Modeling and Satellite Observational Studies, NASA, Goddard Institute for Space Studies (New York), 113.

Table 1

Results of FCM tests for varying m and c.
Scaling norm is diagonal in all cases.

Run #	Number of Clusters	Fuzziness Index, m	Partition Coefficient ¹	Entropy ¹	Comments
1	8	2.00	0.46	1.23	
2	8	2.60	0.25	1.73	
3	7	2.30	0.37	1.40	
4	10	1.25	0.90	0.19	Hard
5	8	1.80	0.12	2.08	Poor
6	10	2.00	0.50	1.20	Study run
7	7	2.00	0.53	0.98	Supervised

¹. See text.

Table 2

Cloud fraction computed for three classification methods.

Manual Interp.	ML ¹	ML ²	Fuzzy Sets (Threshold:)					
			0.4	0.5	0.6	0.7	0.8	0.9
0.53	0.40	0.55	0.69	0.65	0.62	0.57	0.46	0.19 ³
			0.56	0.54	0.52	0.49	0.40	0.18 ⁴

1. Classes labeled as cloud only.
2. Including unclassified areas as cloud.
3. Pixels treated as completely cloud-filled.
4. Pixels partially cloud-filled.

- Figure 1. Study area centered on Novaya Zemlya (approximately 75°N, 60°E) and containing the Kara and Barents Seas. The area covers (1250 km)². AVHRR channels 1, 3, and 5.
- Figure 2. Manual interpretation of the area shown in Figure 1. Cloud classes: LCLI - low cloud over sea ice; LCLW - low cloud over water; MCL - middle cloud; HCL - high cloud, Cu - cumulus.
- Figure 3. Bispectral plots of AVHRR data for the arctic. Class means \pm two standard deviations are shown as rectangles.
a) visible vs. near-infrared; b) visible vs. thermal.
- Figure 4. Plot of the partition coefficient, F (solid line), and entropy, H (broken line), as a function of the number of classes. In all cases, $m=2.0$.
- Figure 5. Ten classes produced by the FCM algorithm from the study area data. See text for interpretation of classes.
- Figure 6. Study area as classified by a unsupervised maximum likelihood procedure. Cloud classes are as defined for Figure 2. Additional class codes: U - unclassified, M - mixed classes, low cloud is defined by two classes: LCL1 and LCL2.
- Figure 7. Fuzzy sets classification of the study area. The class to which a pixel belongs is the one with the largest membership value. Cloud classes: LCLI - low cloud over sea ice; LCLW - low cloud over water; MCL - middle cloud; HCL - high cloud, Cu - cumulus.

*** NOTE TO REVIEWERS ***

Due to the high cost of producing prints, only one set of Figures 1 and 5 has been sent to the editor. These have been photocopied to the best of our ability and included here, but some grey levels have been lost. We feel that these are adequate for conveying the point of "partial memberships" in each class, but we ask that you keep in mind the unavoidable reduction in the quality of these copies.

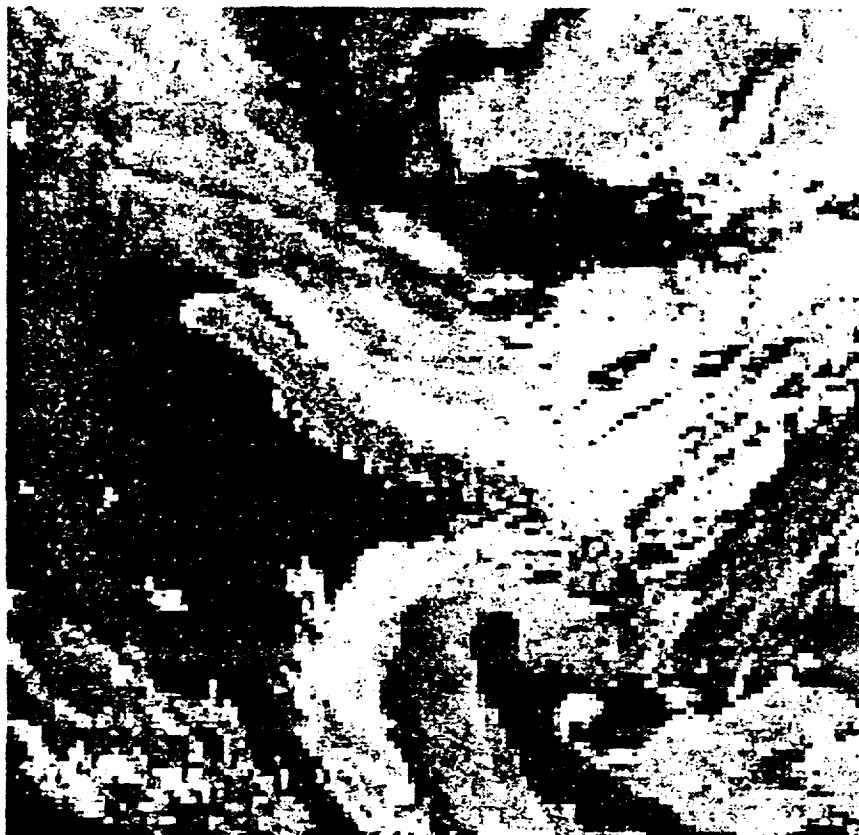


Fig. 1

ORIGINAL PAGE
BLACK AND WHITE PHOTOGRAPH

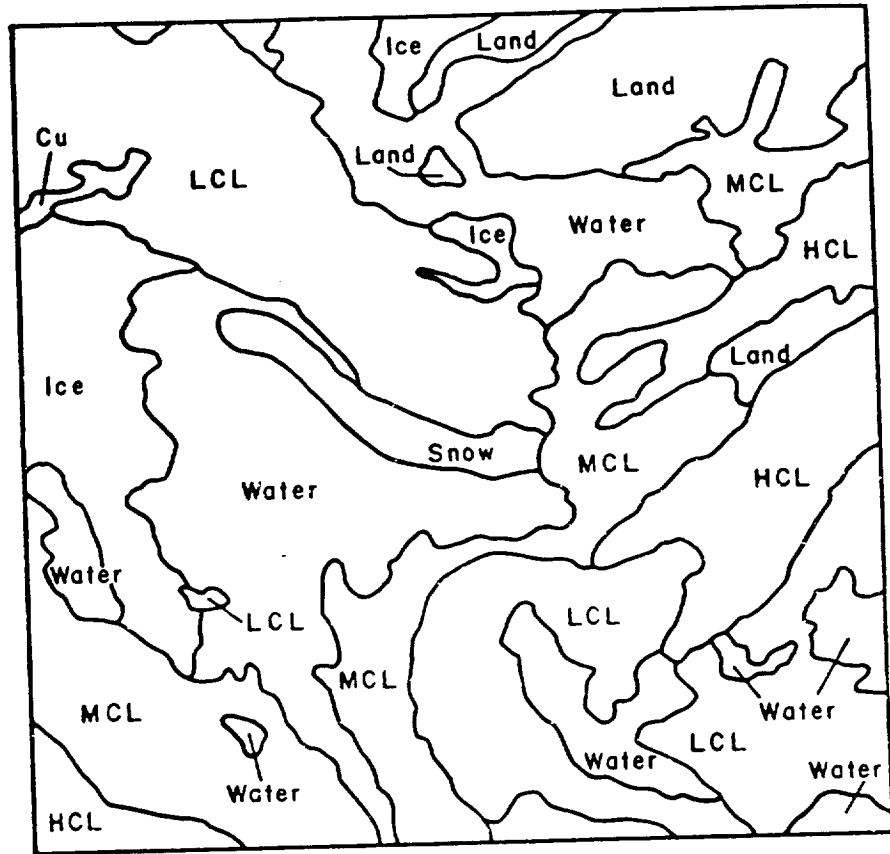


Fig. 2

AVHRR Channels 1 and 3



Fig. 3

AVHRR Channels 1 and 5

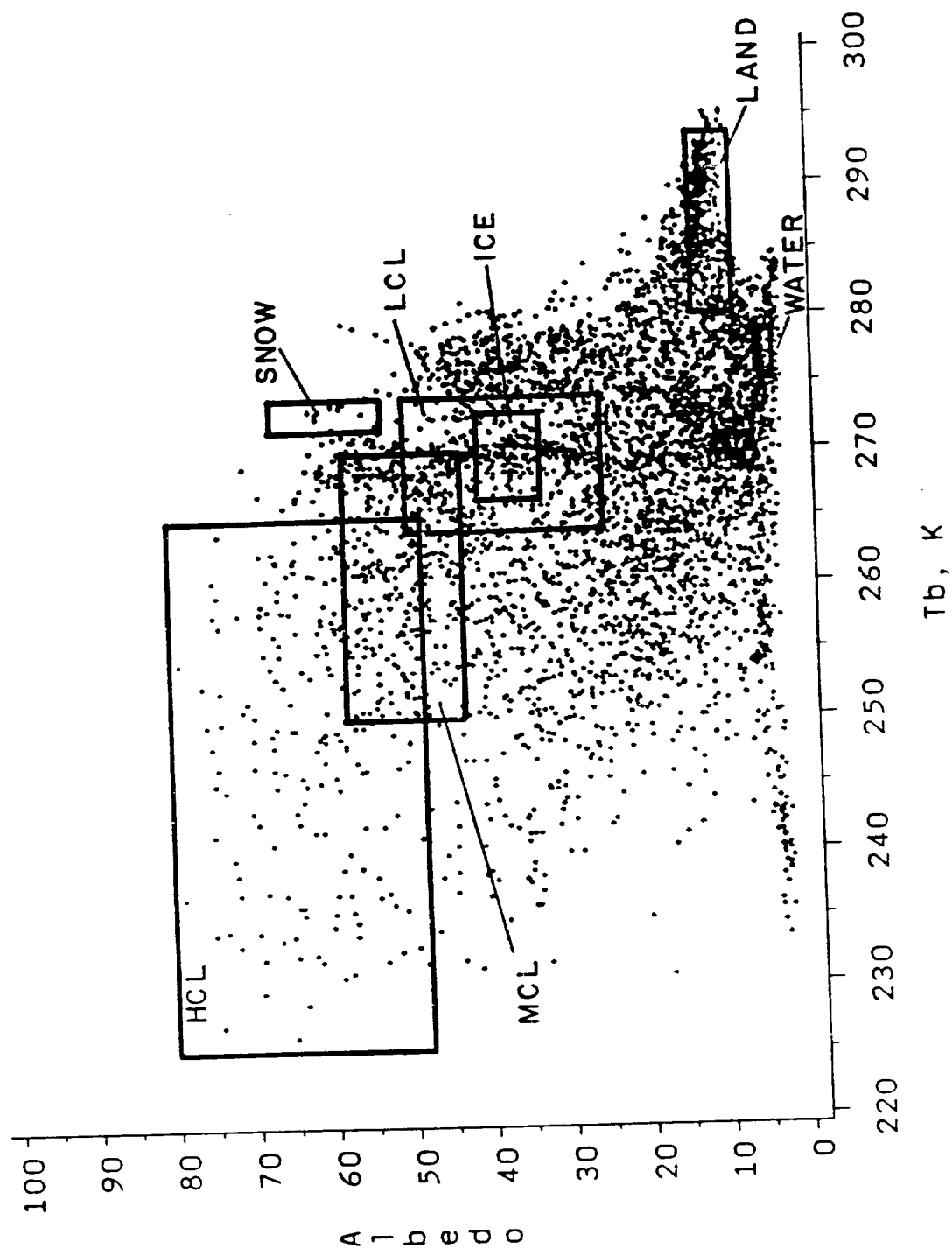


Fig. 3, cont.

PARTITION COEFFICIENT, F, AND ENTROPY, H BY # OF CLUSTERS

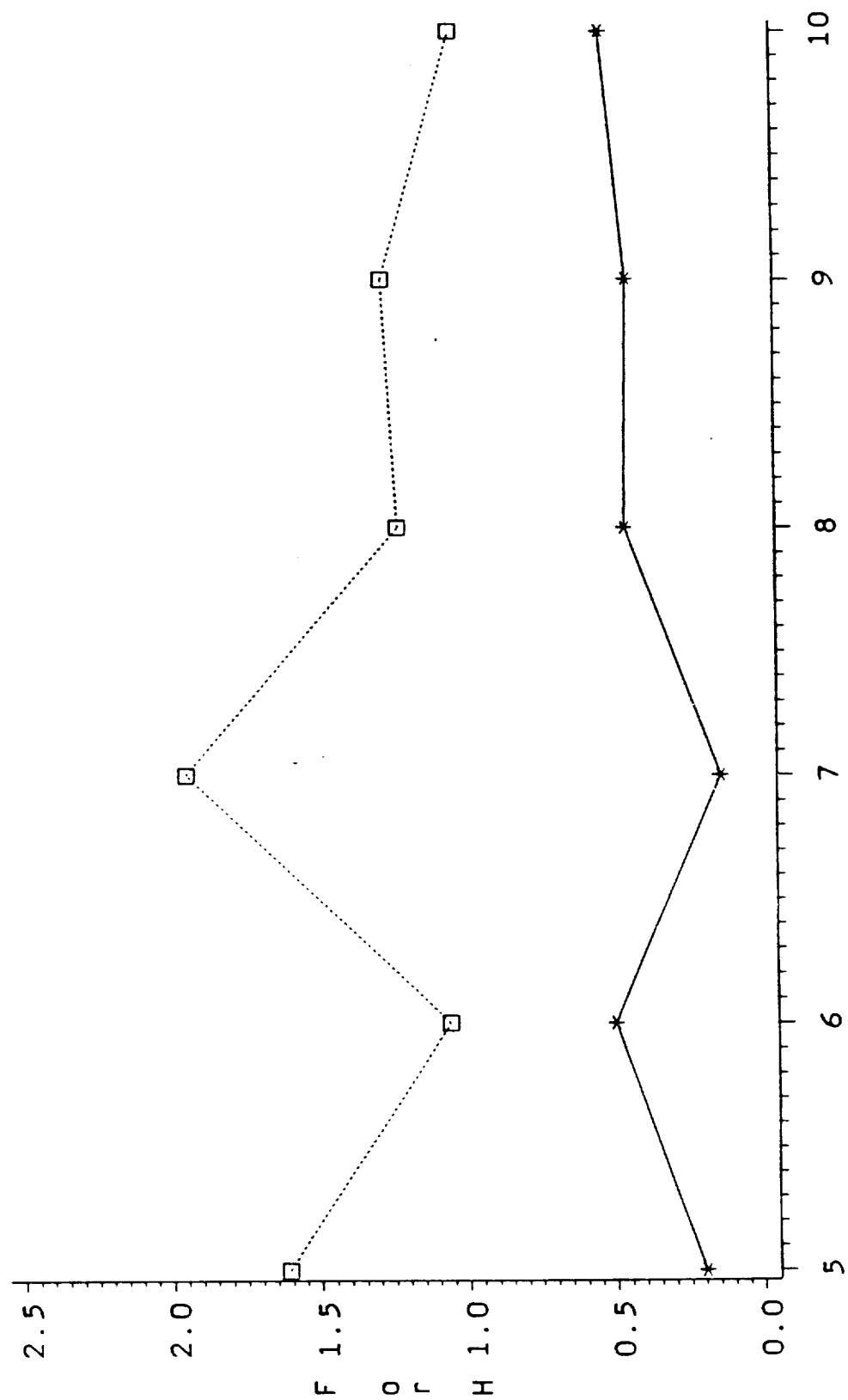
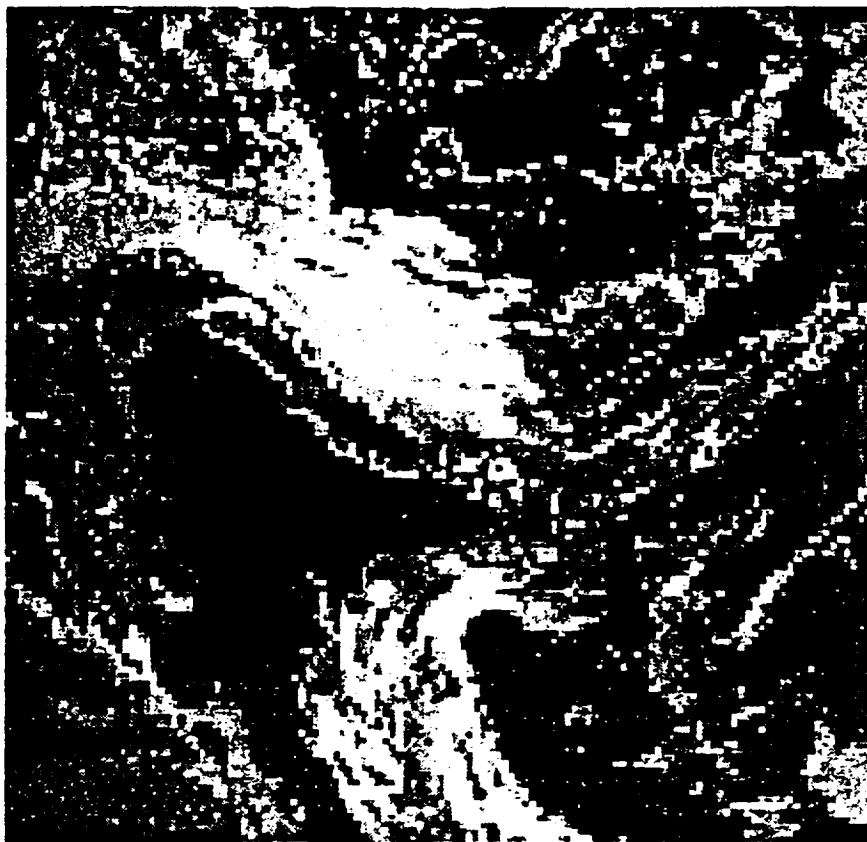
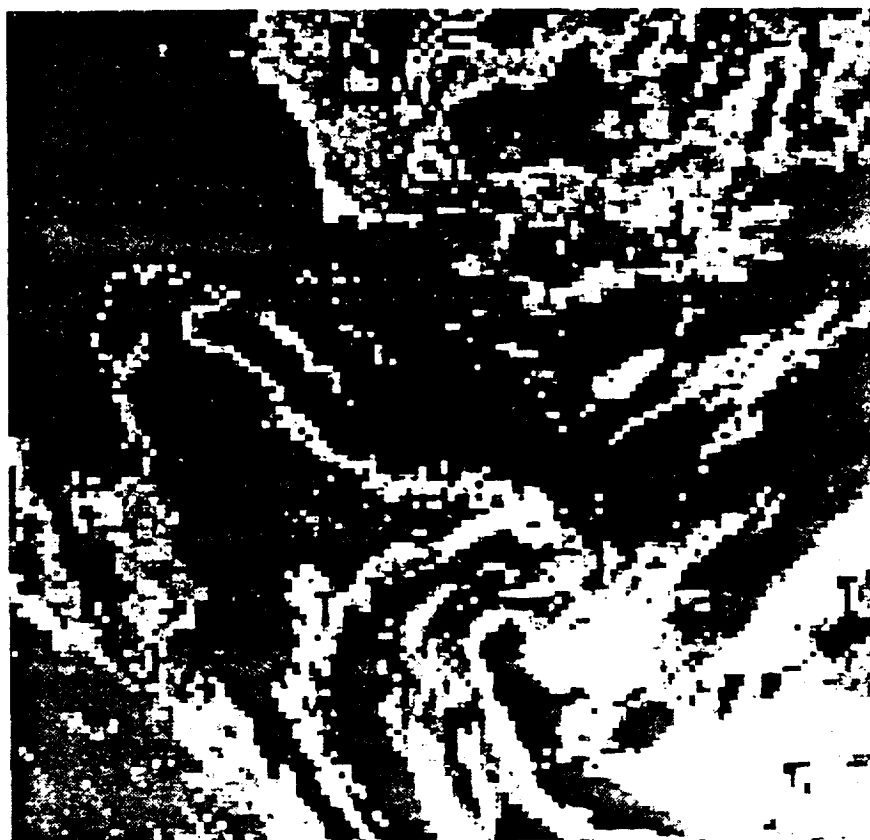
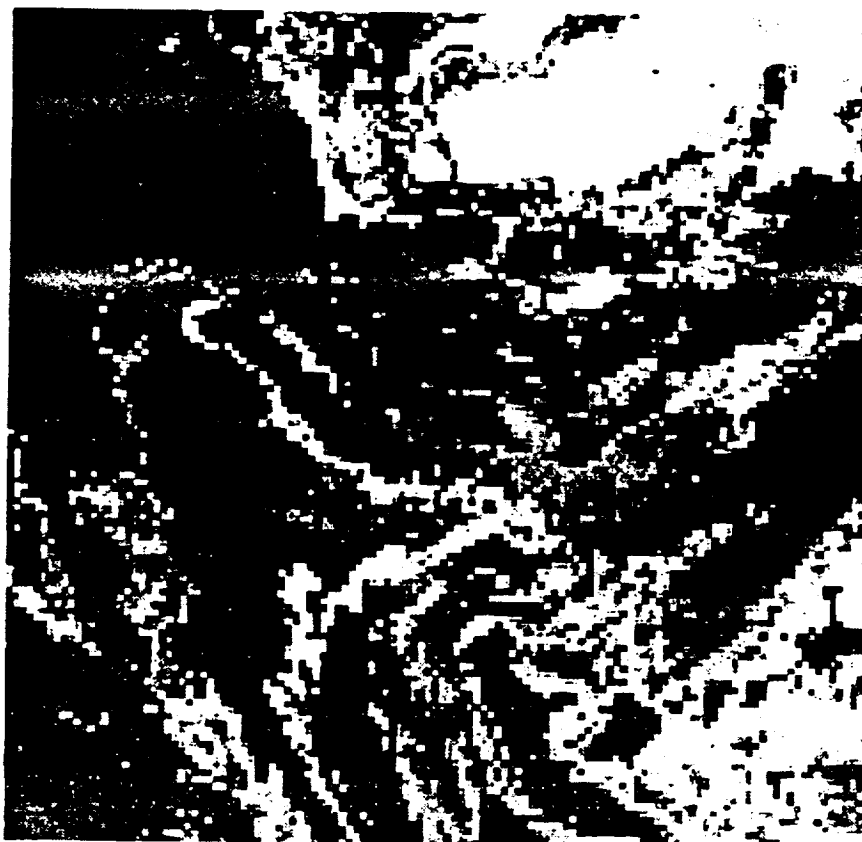


Fig. 4



ORIGINAL PAGE
BLACK AND WHITE PHOTOGRAPH

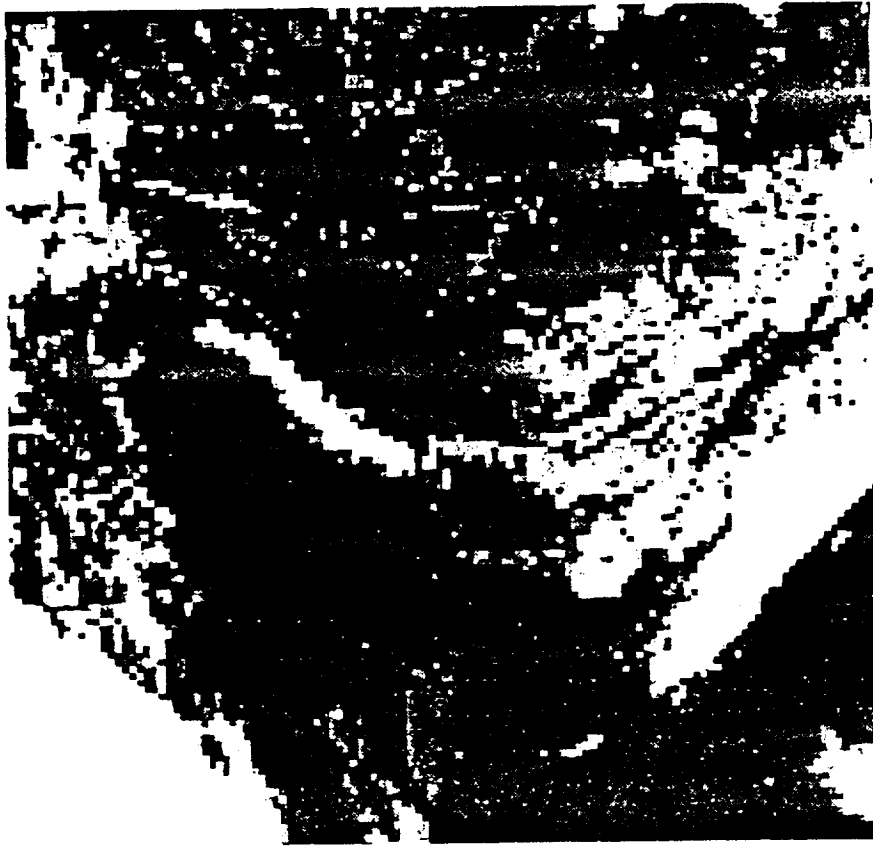




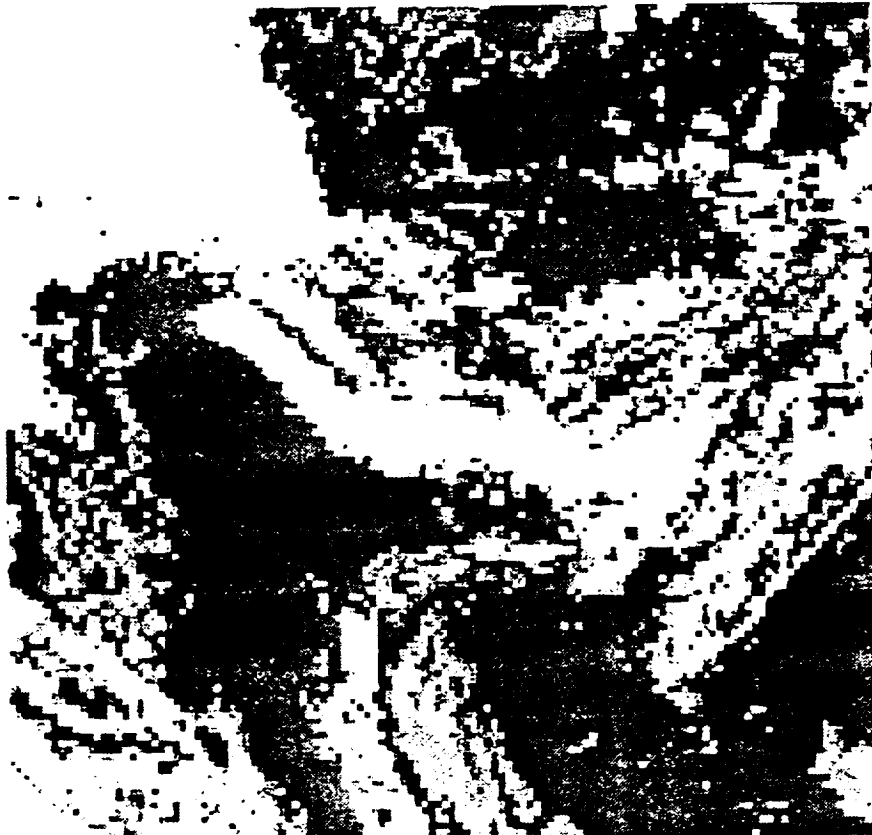
ORIGINAL PAGE
BLACK AND WHITE PHOTOGRAPH

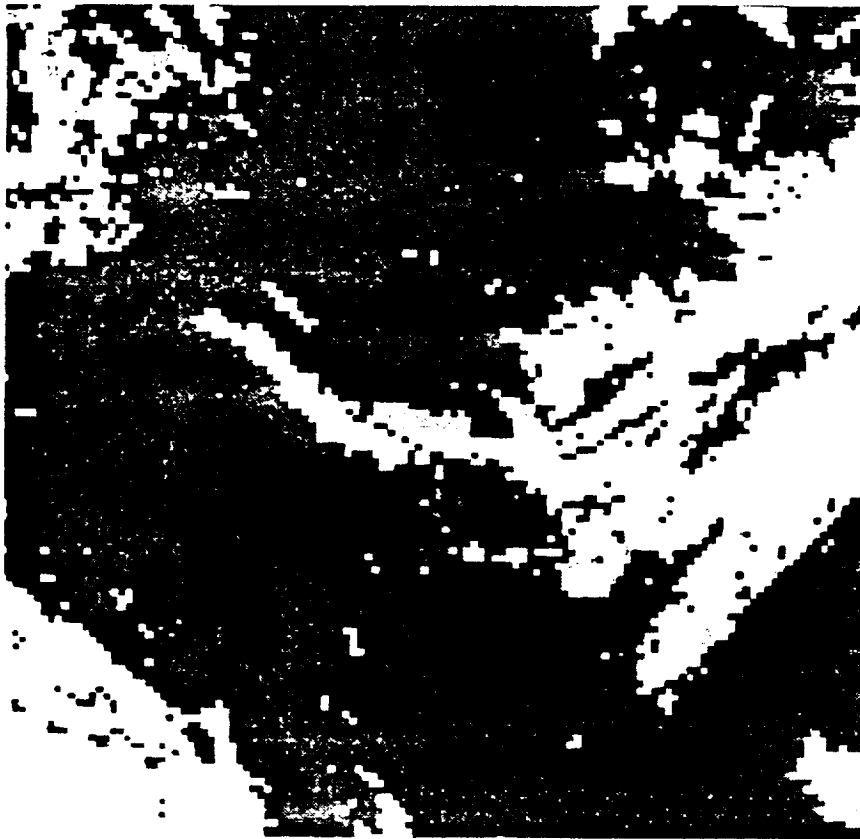


Fig 5, cont.



ORIGINAL PAGE
BLACK AND WHITE PHOTOGRAPH





ORIGINAL PAGE
BLACK AND WHITE PHOTOGRAPH

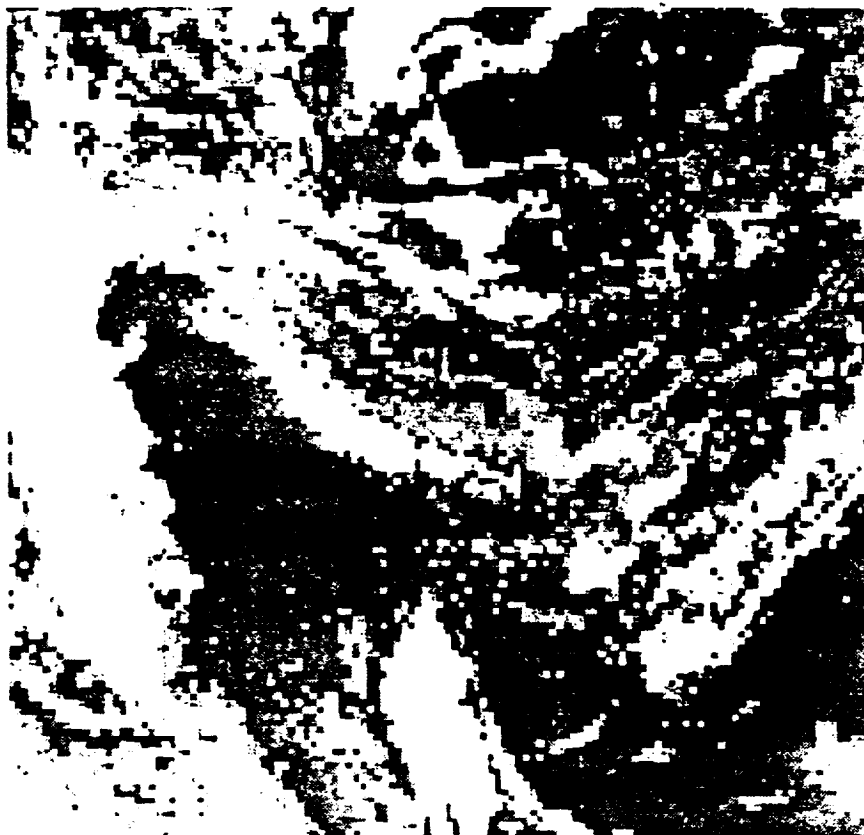
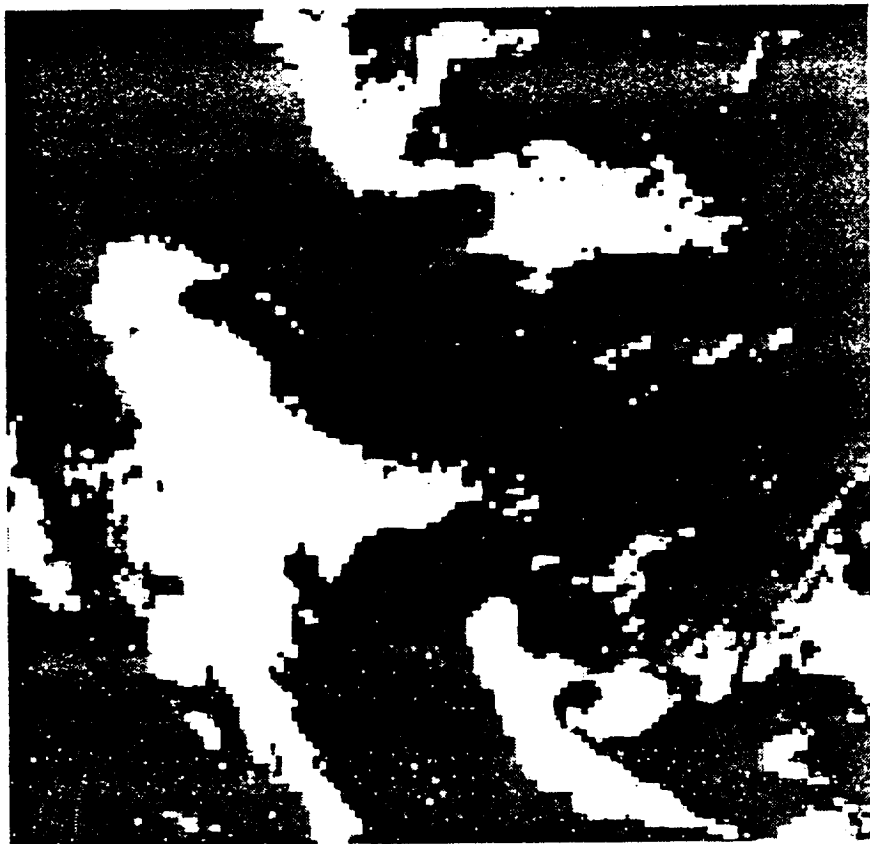


Fig. 5, cont.



ORIGINAL PAGE
BLACK AND WHITE PHOTOGRAPH

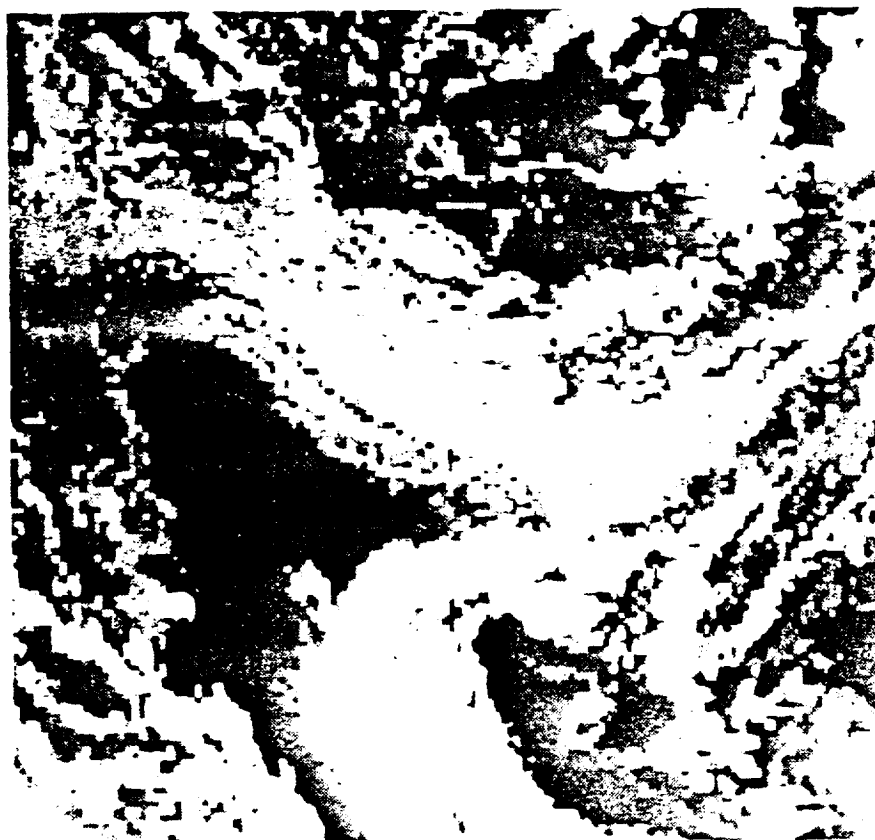


Fig. 5, cont.

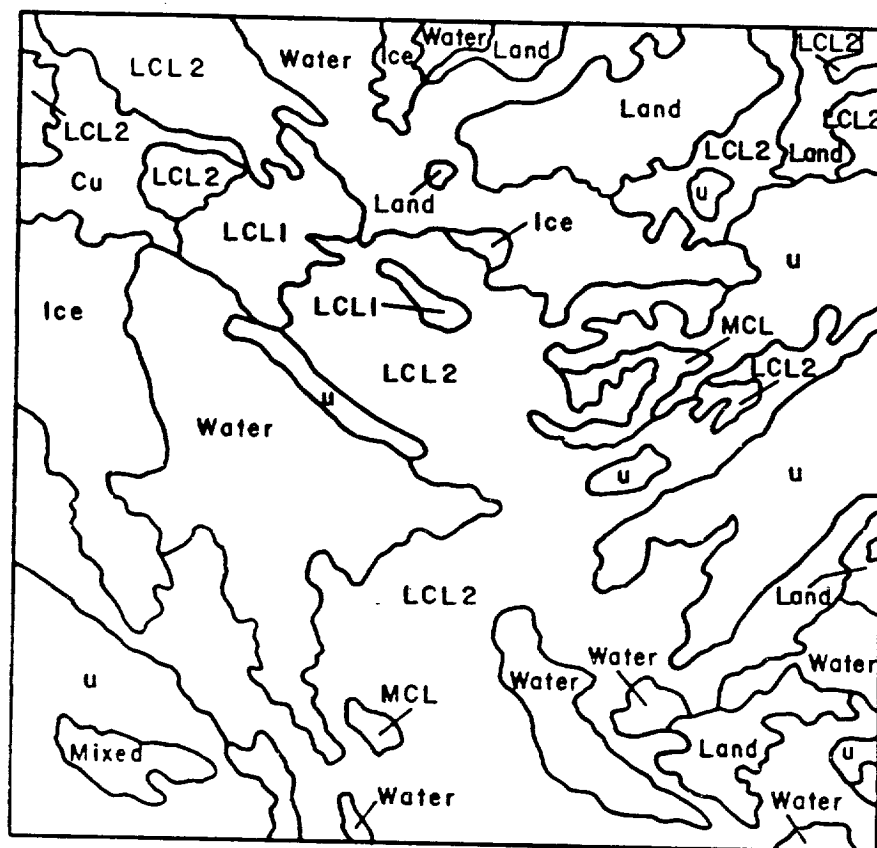


Fig. 6

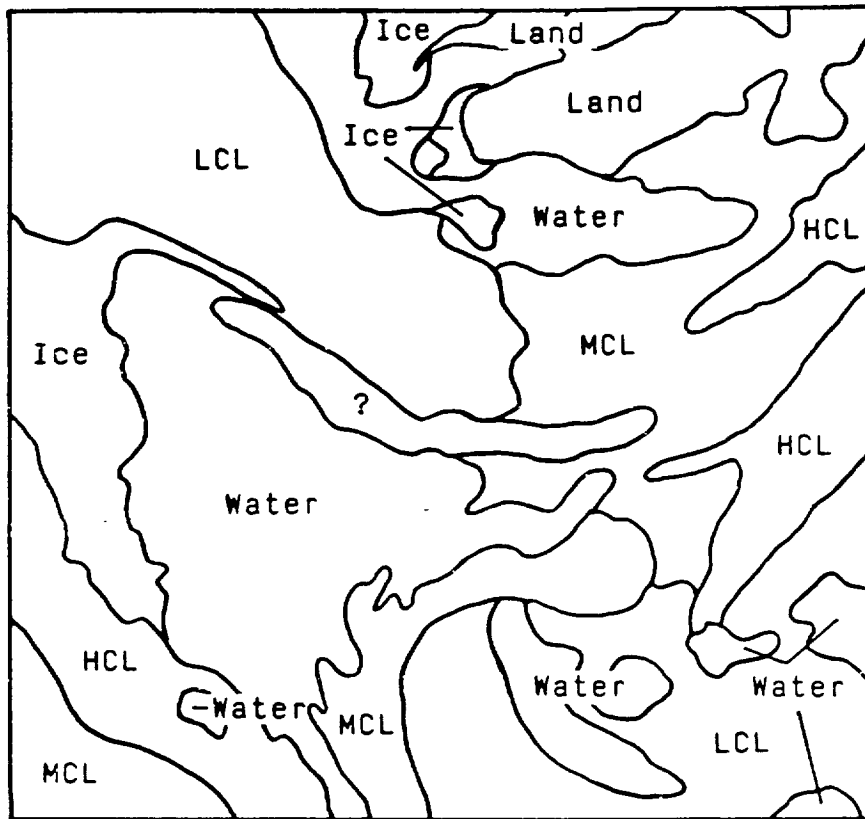
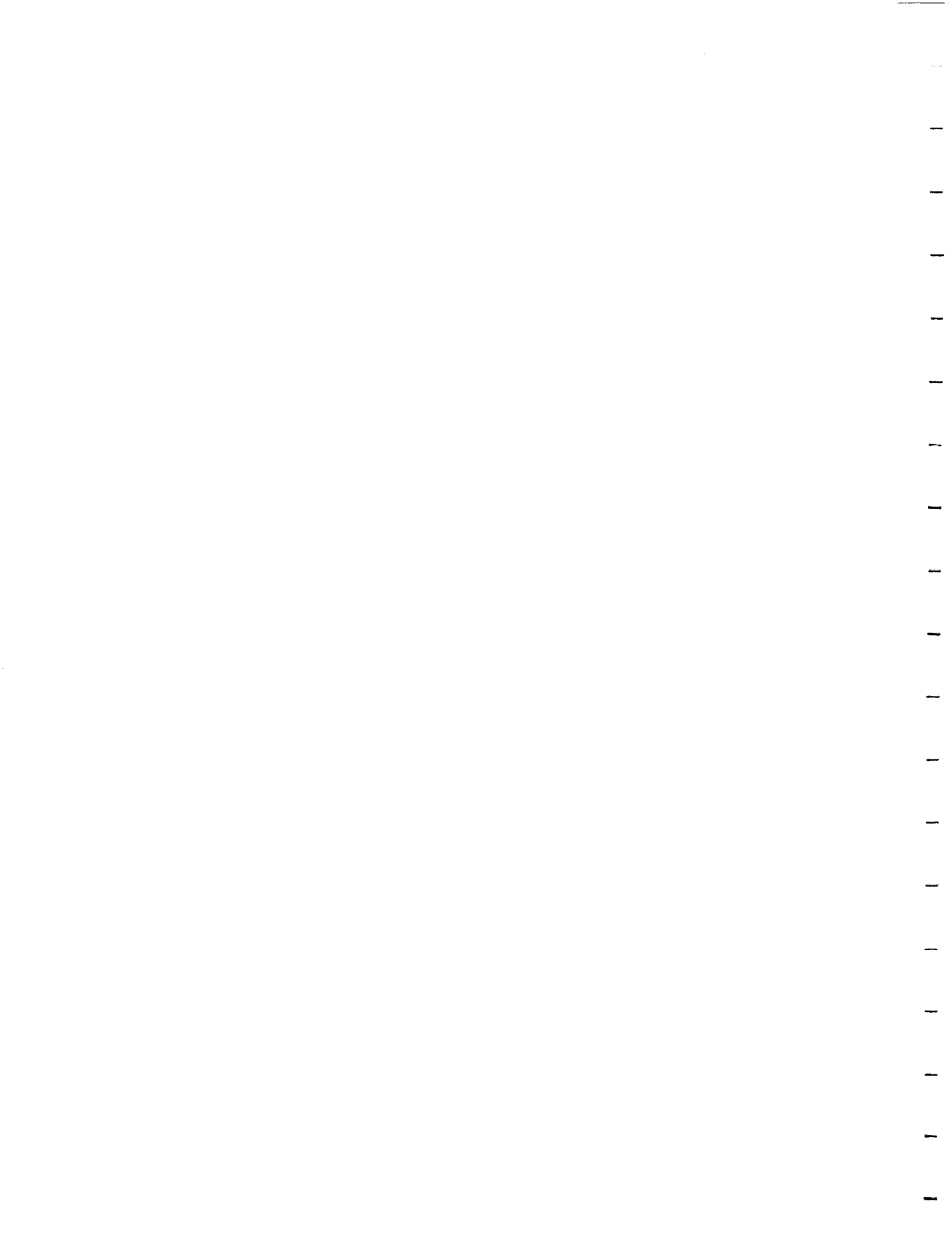


Fig. 7

ATTACHMENT 3
CLASSIFICATION WITH NEURAL NETWORKS



Classification of Merged AVHRR and SMMR

Arctic Data with Neural Networks

J. Key, J.A. Maslanik, A.J. Schweiger

**Cooperative Institute for Research in Environmental Sciences
University of Colorado
Boulder, CO 80309-0449**

Short title: Neural Networks Classification of AVHRR and SMMR Data

Subtitle: Using neural networks to classify Arctic clouds and surfaces in merged AVHRR and SMMR data offers some advantages over the traditional maximum likelihood method.

Photogrammetric Engineering and Remote Sensing

ABSTRACT

A forward-feed, back-propagation neural network is used to classify merged AVHRR and SMMR summer Arctic data. Four surface and eight cloud classes are identified. Partial memberships of each pixel to each class are examined for spectral ambiguities. Classification results are compared to manual interpretations and to those determined by a supervised maximum likelihood procedure. Results indicate that a neural network approach offers advantages in ease of use, interpretability, and utility for indistinct and time-variant spectral classes.

INTRODUCTION

The Arctic region provides a unique set of problems for image analysis algorithms. Current procedures for automated analyses of satellite radiance data have been developed for low and middle latitudes but their application to polar regions has been largely unexplored. Those that have been applied often fail in the polar regions because surface temperatures are commonly as low or lower than cloud-top temperatures, and because snow-covered surfaces exhibit albedos similar to those of clouds. Also, extremely low surface temperatures and solar illuminations cause satellite radiometers to operate near one limit of their performance range, and in winter no visible-wavelength data are available. Because of these problems, a complex analysis method is necessary (WMO, 1987). Classification of Arctic AVHRR data with clustering algorithms has been performed primarily by Ebert (1987, 1988), Key (1988), and Key et al. (1989).

In this paper, we investigate the ability of neural networks to extract four surface and eight cloud classes in the Arctic from a merged data set consisting of five Advanced Very High Resolution Radiometer (AVHRR) and two Scanning Multichannel Microwave Radiometer (SMMR) channels. Results are compared to manual interpretations and to

output from a supervised classification with a maximum likelihood class assignment scheme. Since cloud and sea ice mapping for climatological studies requires the processing of many images covering large areas (for example, 30 days worth of AVHRR images for the northern hemisphere), selection of training sites in a supervised scheme or the assignment of spectral clusters to physical classes in an unsupervised approach can involve an unacceptable amount of time and effort. Since a class such as low cloud over ice actually includes a range of cloud thicknesses overlying a range of ice concentrations, considerable spectral variability exists within the class as well as within individual pixels. Our primary goal in this work is to investigate the ability of a neural network classifier to deal with the considerable within-class variability encountered in our data based on a relatively small training set. The manual and supervised classifications are used to provide benchmarks for comparison of the neural network results, rather than as a test of the merits of these more traditional methods.

Motivated by the apparent limitations of multispectral feature extraction from imagery and the availability of expert system development tools, artificial intelligence (AI) techniques have come into increased use for the analysis of remotely sensed data (e.g., Nicolin and Gabler, 1987; Matsuyama, 1987; McKeown, 1987; Estes et al., 1986; Nandhakumar and Aggarwal, 1985; Campbell and Roelofs, 1984), and have also been employed in geographic information systems (GIS) applications (e.g., Userly and Altheide, 1988; Ripple and Ulshoefer, 1987; Robinson and Frank, 1987; Smith et al., 1987; Jackson and Mason, 1986; Smith, 1984). Due to the limited knowledge of the physical processes in the environment and the inherent noise in many geophysical data, environmental systems often cannot be accurately represented through numeric values describing their physical properties and interactions, but rather are subjected to categorization into broad classes. Most applications of expert systems have sought to apply qualitative knowledge to decision-making; expert

systems operate primarily on abstract symbolic structures. In remote sensing applications where pattern recognition, spatial and temporal context, and multivariate analysis are common requirements, coupled numeric/symbolic systems may be useful. This issue has recently been addressed by Kitzmiller and Kowalik (1987), Kowalik (1986), and Borchardt (1986). Traditional techniques may not be adequate to identify and make use of relationships across such a broad range of numeric and non-numeric variables.

The neural networks, or connectionist, approach was first introduced as a theoretical method of AI in the 1960s. However, limitations in simple systems were recognized by Minsky and Papert (1969) and the concept gave way to the symbol system approach for the next two decades. The idea has recently been revived due to advances in hardware technology allowing the simulation of neural networks and the development of nonlinear multi-layered architectures (Rumelhart et al., 1986). The technique has considerable potential for remote sensing, as suggested by applications to automated pattern recognition (e.g., Ritter et al., 1988). The relationship between symbolic AI and neural networks is addressed by Chandrasekaran et al. (1988).

DATA

The data sets used here provide a broad range of spectral information necessary to map clouds and surfaces in polar regions. These data are typical of the types of imagery used for mapping of global cloud, sea surface temperature, and other climatological variables. The Advanced Very High Resolution Radiometer (AVHRR) on board the NOAA-7 polar orbiting satellite measures radiance in five channels encompassing the visible, infrared, and thermal portions of the electromagnetic spectrum (1: 0.58-0.68 μ m, 2: 0.73-1.0 μ m, 3: 3.55-3.93 μ m, 4: 10.3-11.3 μ m, 5: 11.5-12.5 μ m) with a nadir resolution of 1.1 km. Global Area Coverage (GAC) imagery is a reduced-resolution product created through

on-board satellite processing, with each pixel representing a 3 x 5 km field of view (Schwalb, 1978). Channels 1 and 2 were converted to approximate spectral albedo; channels 3, 4, and 5 were converted to radiance in milliwatts/(m²-steradians-cm) then to brightness temperature (NOAA, 1984; Lauritsen et al., 1979). The typically low water vapor content in the polar atmosphere and the low physical temperatures reduce most atmospheric effects to a point where they may be neglected for the analyses performed here. Approximate corrections for solar zenith angle in channels 1 and 2 were accomplished through a division of the albedo by the cosine of the zenith angle.

The Nimbus-7 Scanning Multichannel Microwave Radiometer (SMMR) is a conically scanning radiometer that senses emitted microwave radiation in five channels: 6.6, 10.7, 18.0, 21.0, and 37.0 GHz, with two polarizations (horizontal and vertical) per channel. At these frequencies, passive microwave data is relatively unaffected by clouds and provides useful data year-round independent of solar illumination. The 18 and 37 GHz vertical polarization channels are used here primarily for surface parameterization, with fields of view of 55x41 km and 27x18 km, respectively.

In order to study both clouds and surfaces beneath clouds, it is worthwhile to combine the AVHRR and SMMR channels into a single image set. AVHRR and SMMR data were merged in digital form and mapped to a polar stereographic projection. This projection yields pixels true to scale at 70° latitude with a five kilometer pixel size. Five kilometer pixels were averaged over 2x2 cells yielding an effective pixel size of ten kilometers square. (Further constraints imposed by the image analysis system reduced this to 125x124 pixels.) SMMR data were converted to the five kilometer cells by simple duplication of pixels. Further details are given in Maslanik et al. (1989). In this form, color composites can be made consisting of combinations of microwave, visible, and thermal-wavelength channels to highlight different cloud and surface features in the data.

The study area (Figure 1) is centered on the Kara and Barents Sea extending north toward the pole and south toward Norway and the Siberian coast. Novaya Zemlya is near the center of the image. Shown are AVHRR channels 1, 3 and 4 for July 1, 1984. Both AVHRR and SMMR imagery were also acquired for July 4, 1984. While covering only a small portion of the Arctic Basin (1250x1250 km), it includes representative samples of all surface types found in the Arctic: snow-covered and snow-free land, sea ice of varying concentrations, and open water.

METHODOLOGY

Four surface classes are of interest in this study: snow-free land, snow-covered land/ice cap, open water, and sea ice (abbreviations used: LAND, SNOW, WATER, ICE). Three broad classes of cloud - low, middle, and high - are defined by temperature as measured in AVHRR channel 4 and are further categorized by the underlying surface type. Not all surface/cloud level combinations occur in the study image, and those that do not are excluded from the analysis. Eight cloud classes are examined: low cloud over land, water, and ice; middle cloud over water and ice; and high cloud over land, water, and ice (abbreviations used: LCLL, LCLW, LCLI, MCLW, MCLI, HCLL, HCLW, HCLI, respectively). The data are classified by two procedures: a neural network and a maximum likelihood classifier. The maximum likelihood procedure is supervised, initially using the same training areas as used to train the neural network.

The development of neural network architectures as a computational method builds on the fact that the brain is overall much more powerful in processing information than any serial computer. Neural networks (NN), connectionist systems, or parallel distributed processing systems (PDP) consist of networks of independent processors or units that are highly interconnected and process information through interaction between the individual

processing nodes. Interaction between processors is determined by the network architecture: the number of layers, number of units in each layer, strengths of the connections (weights) between the units, unit activation functions, learning rules, and data representation. The advantage of PDP in the example presented here is the capability of such networks to learn by example. Through the use of learning rules a neural network adjusts its connection weights to associate a set of input patterns with a set of output patterns and thereby "learns" the relationship between the input and output. In this study, multispectral data in training areas provide the input pattern; the desired cloud/surface class is the output pattern. Since processing in PDP systems is done through the interaction of many processing units, neural networks further display a feature known as "graceful degradation" where, given partially missing or noisy information, they are frequently capable of computing meaningful output. Of course, if classes are overlapping in feature space, and one or more of the features which best discriminate between classes are missing or otherwise corrupt, the network may produce an incorrect classification.

Forward-feed networks consists of a layer of input units, one or more layers of hidden units, and a layer of output units. The input units have direct connections to the units in the hidden layer which in turn are connected to the output layer. Information processing flows from the input layer through the hidden layer to the output layer and no feedback mechanism from the output to the input layer exists. There are also no direct connections between individual nodes within a layer. The relatively small number of connections, and therefore number of learnable connection weights, allows this type of network to train quickly while still being capable of solving complex problems through the construction of powerful generalizations.

A back-propagation network learns in the following way. An input and a training pattern - the "correct" output for a given input - are presented simultaneously to the

network. Through the connections, which are initially random, the network computes an output pattern, which is then compared to the training pattern. The error between the output pattern and the training pattern is used to adjust the weights between the output and hidden units to minimize the error between the training pattern and the output pattern. Since the output units are directly connected only to the hidden units, the training error is propagated backward through the network so that the weights between hidden and the input layer are also adjusted according to the learning rule (McClelland and Rumelhart, 1988). Training and input patterns are presented to the network many times while the network is adjusting its weights to minimize the error between all input and training patterns. The network will converge on a solution that maps the set of input vectors to the set of output vectors, if such a mapping function exists. During this training process the units in the hidden layer construct generalizations or internal representations of the input patterns.

The network presented in this paper uses a forward-feed architecture with a layer of 7 input units representing the AVHRR and SMMR channels, a layer of 10 hidden units, and a layer of 12 output units representing the surface/cloud classes. The network is trained on patterns (training areas) for each desired class. After training, the network is presented with the complete data set (image) and computes a membership value, represented by the activation of the output units.

Where spatial and spectral boundaries between phenomena are diffuse, hard classifiers which produce mutually exclusive classes seem particularly inappropriate. This issue is discussed further in Key et al. (1989) in relation to the fuzzy c-means algorithm. The neural networks approach addresses this problem of often indistinct spectral boundaries between classes by providing as output a numeric value as well as the class symbol for each pixel. This is a membership value for the pixel to each class, and is in the range [0,1], larger values implying greater strength of membership in a particular class. With the

activation function used in this study (sigmoid), these values are approximately linear throughout the range.

In this example, two sets of training areas (referred to as TA1 and TA2) were selected in the typical supervised manner, with each training area manually delineated in the digital imagery. The training sets were chosen so that the effects of different within- and between-class variability could be tested, with TA1 representing a relatively small sample designed to study the ability of the neural network to address within-class variability not contained in the training statistics (e.g., the variability expected due to changes in ocean and ice temperature, ice concentration, and cloud height and thickness over space and time). TA1 included 1% of the 15,500 pixels (125 lines x 124 pixels) in the test data set. Additional training areas were included in TA2 to expand the variance of the training statistics sufficiently so that a significant portion of the test images would be classified using the maximum likelihood classifier. TA2 included about 9% of available pixels. Class means by spectral channel were nearly the same in TA1 and TA2 but, with the exception of the LCLI class, standard deviations were twice as large on average in TA2 (mean standard deviation in DN of 1.9 for TA1 versus 3.8 for TA2). As noted earlier, selection of training areas this large is not practical for climate applications requiring analysis of many images over large areas (thus the impetus to test the neural network using TA1). However, TA2 was needed to address the trade-off between classification accuracy and human interaction using the supervised maximum likelihood approach for the types of data used here. The July 1 and July 4 images were manually interpreted using digital color composites of several AVHRR and SMMR channels. The manual interpretation thus acts as a hard classifier, with classes that consist of a "best-guess" estimate of class membership based on visual clues. Maximum likelihood (ML) classifications of the July 1 and July 4 images with seven data channels as input were carried out using TA1 and TA2 statistics. The ML

procedure was run on a DEC MicroVax computer and required approximately 1 CPU minute for the computation of training area statistics and 2.5 minutes for image classification.

The neural network was trained using the individual pixel values in TA1 as input patterns. The network learned these sets of spectral patterns in approximately 23 minutes on an IBM PC/AT (12 MHz) class machine. The trained network then classified the entire study area in approximately 4 minutes. To address indistinct spectral boundaries, pixels were assigned to the class with the highest membership value. Pixels with no membership value greater than 0.4 (arbitrary) were tagged as unclassified. In an attempt to similarly relax the restrictions of the maximum likelihood classifier, cut-off limits for pixel position within the n-dimensional Gaussian class-membership curve were varied to a maximum of 99%, and different apriori probabilities were tested.

RESULTS

Figure 1 illustrates many of the problems involved in mapping polar surfaces and clouds. With the exception of land/water boundaries, edges between classes are typically indistinct, as is the case at the sea ice margins where the transition from high concentration ice to open water is not distinct. For classes that include thin cloud, such as the regions of low cloud over ice and water, cloud opacity varies within the class. The sensors therefore record varying proportions of surface and cloud within a single class. Cloud height is also subjective; heights actually may fall anywhere within the low, medium, high designations.

A manual classification of the July 1 image with the classes described previously is shown in Figure 2, and will be used for comparison to the neural network and maximum likelihood results. Eighteen percent of the image was left unclassified where no dominant class could be determined. As noted above, within-class variance is large, particularly in

classes LCLI and LCLW. Coefficients of variation are greatest in the 18 GHz SMMR data and for the AVHRR visible-wavelength channels within these classes, suggesting some confusion between ice and open water.

Table 1 shows the total percentages of the July 1 and July 4 images that were actually classified using training areas TA1 and TA2, and the ML and NN classifiers. The neural network (NN) classification of the July 1 image is shown in Figure 3. Some important differences are apparent between the neural network output and the manual classification in the ICE and LCLI classes. The NN results underestimate the amount of low cloud over ice. The NN classification also puts a larger portion of the ice margin area into the WATER rather than ICE class. The contingency table (Table 2) comparing classifications of the July 1 image using NN and the manual interpretation confirm this, and also shows that NN tends to assign cloud/surface classes to surface classes, particularly in the case of ICE versus LCLI and WATER versus LCLW. Confusion also exists between cloud height classes. Of the pixels classified in both the NN and manual classifications (i.e., excluding unclassified pixels), overall agreement between classification schemes is 53%. The NN classification of the July 4 image shows similar patterns. As was the case for the July 1 data, nearly the entire image was classified. Differences between the NN results and manual classification for July 4 were greatest between cloud height classes and between low cloud over ice versus clear sky over ice.

Maximum-likelihood classified images are shown in Figure 4 for July 1 using TA2 statistics. Since the ML classifications using TA1 essentially included only those pixels within and adjacent to the TA1 training areas, these images are not illustrated. Comparing the manual interpretation in Figure 2 with the ML classification shows that the ML classification using the more comprehensive training areas of TA2 effectively captures the basic cloud and surface patterns. However, more than half of the manually-interpreted

MCLW class is left unclassified by ML. Remaining unclassified pixels are divided among cloud classes and ice/water classes. A contingency table (Table 3) of the manual classification versus the ML classification using the TA2 training areas illustrates the problem of distinguishing between cloud height classes and between intermediate mixes of cloud and surface classes. This supervised ML classification achieved a high agreement of 85%, representing the large training set in TA2. Extension of these TA2 signatures to the July 4 data using ML illustrates the reduction in applicability of training signatures over time compared to the NN classifications, as shown by a general decrease in the percentage of the image that is classified. Given the variability of ice conditions and cloud thicknesses within a single image, it is not surprising that day-to-day variability is enough to reduce the representativeness of the training areas in terms of class mean and covariance. With the exception of class LCLI, standard deviations of training areas in TA1 are considerably less than is the case for TA2 and the manually interpreted classes. TA1 signatures thus include only a small portion of the variance in the desired classes, as indicated by the low percentage of the image actually classified using TA1 statistics.

DISCUSSION

The pattern of weights in the network provides insight into the way decisions are made by the network. For our example, interpretation of these weights sheds light on which spectral channels are important for classifying particular cloud/surface classes. Similarly, the network weights indicate, for each output class, the degree of information redundancy among channels in the input data; channels that are only weakly weighted add little additional information to the classification process. Figure 5 shows an example of the connections between the input channels, hidden layer neurons, and the output classes in the trained network used here. Due to the complexity of the connections between units, only

the surface classes are shown in the figure. The identification of the exact role of hidden units is difficult, as they often represent generalizations of the input patterns. Strength of the connections shown varies from 0.6 to 0.9 (on a scale of -1.0 to +1.0). These connections are summarized in Tables 4 and 5. Table 4 shows which input data channel each hidden node is associated with in the trained network. Table 5 shows the association between hidden units and the output data classes. Following the connections through these two tables therefore indicates which input channels are linked to particular output classes. As shown in Figure 5 and Table 5, snow-free land has strong connections with hidden layer neurons 2, 3, and 6, all of which represent thermal AVHRR channels and the SMMR channels (Table 4). We may therefore conclude that land is best distinguished from the other channels by its physical temperature and its emissivity in the microwave portion of the spectrum. Snow/ice cap is identified by its albedo and temperature, with no significant information gained from the microwave signature. The identification and discrimination of ice from the other classes requires albedo, temperature, and microwave emissivity characteristics. The connections show that cloud identification is a function of height, with thermal characteristics being more important for middle- and high-level clouds. The identification of low cloud depends on the underlying surface, where temperature is an adequate discriminator if the cloud is over land, albedo and temperature are used if over water, and temperature and the longer-wave reflected solar component (AVHRR channel 3) are needed if over ice. The hidden layer neurons with connections to AVHRR channel 3 (numbers 7 and 9) are also connected to either channel 2 or channels 4 and 5, indicating that both the reflected solar and thermal components of channel 3 likely play a part in the classification. The connections demonstrate the usefulness of AVHRR channel 3 for discriminating between cloud and snow or ice. Finally, note that hidden layer neurons 1 and 5 do not "listen" to any inputs, and therefore do not add any information to the

network.

Although both the neural network and the ML classifier use the same training data, some fundamental differences exist in the way they are used. The neural network does not directly address the mean and covariance within a training area. Instead, each pixel within the training area is a separate pattern that directly influences the development of node weights. The multispectral characteristics of each pixel imprints itself to some degree on the network connections. During the development of unit weights as part of the network training phase, some aspects of training area means and covariances are included in the weight assignments. However, unlike the ML classifier, the neural network is not limited to assuming a statistical relationship between pixels within a class and is not restricted by assumptions of normality in the data. The fact that the multispectral data used here often violate these assumptions (Key, 1988) may contribute to the low percentage of the data classified using ML and the training statistics in TA1.

To test this hypothesis, a synthetic data set of AVHRR and SMMR data was developed that exhibited truly normal data distributions. Rectangular cloud and surface objects of varying sizes and locations were generated whose dimensions were randomly chosen within a restricted range. Object regions were then filled with normally distributed data for each channel based on pre-specified means and standard deviations (Gaussian random number generator) characteristic of the polar clouds and surfaces. With this data set there will be only one statistical class for each physical class (e.g., land, low cloud over water, etc.). For this reason, and because the data are normally distributed with a known variance, the probability of selecting a training area representative of the population is higher than with the actual data. Therefore, even small training areas should provide enough information about each class to allow a larger proportion of the area to be classified. This was in fact the case, where training areas extracted from less than 1% of

the synthetic image allowed approximately 70% of the image to be correctly classified by the ML procedure. This test suggests that deviations from a normal distribution likely contribute to the low percentages of classification using the ML classifier.

The ability of a neural network to compute similarity measures through a comparison of patterns contributes to its ability to classify large portions of data on two separate images. Thus, although a relatively small portion of the variability of clouds and surfaces were captured in the training areas (particularly TA1), the neural network was still able to reliably choose the most appropriate output class. This property provides a means to address the problem of signature extension over time and space, since a properly trained network can make class assignments - albeit with reduced confidence - in the face of atmospheric effects or slight changes in spectral properties without requiring apriori knowledge of within-class variance or probabilities of class membership. In fact, if one has a particular reason to use a statistical classifier, the strength-of-membership values calculated by a neural network could be fed back into the statistical classifier as apriori probabilities using, for example, the probability image feature in the ERDAS[™] MAXCLAS function.

The classification example presented has utilized numeric data - albedos and brightness temperatures - as input. Output is on the nominal level for both the neural network and the ML procedure, although the neural network also provides a type of membership value. In some cases, input such as category identifiers rather than measurements may be useful where pixels are assigned a class symbol and optionally an associated fuzziness value (e.g., the probability that the pixel belongs to the class). A second neural network was developed that uses both nominal and categorical input. For example, in the study area the locations of land and permanent ice cap are known, and the location and concentration of sea ice can be determined from the SMMR data. Consider also the case where only three broad categories of sea ice concentration are of interest: low

(15-40%), medium (41-70%), and high (71-100%). Other variables are also possible; for example, time of year, geographic location, spatial context, texture, stage of plant growth, and the a priori probability of occurrence of each surface or cloud type. For simplicity, however, the example is limited to symbols representing land/not land, ice cap/not ice cap, and low, medium, and high sea ice concentration variables.

This network was trained with input units corresponding to both spectral and categorical variables. Since some of the AVHRR and SMMR channels are highly correlated - as evidenced from principal components analysis and an examination of the previously described neural network, only AVHRR channels 1, 3, and 4, and SMMR channel 18 GHz vertical were used in the training. Categorical input variables represent land, ice cap, and sea ice concentration. Nine hidden layer units were specified with output classes as before. As expected, the resulting classification (not shown) is similar to that using only spectral information but the proportion of correctly identified surface pixels increased slightly, whereas the proportion of cloudy pixels remained essentially the same. In addition, the certainty with which surface pixels were classified as measured by the output membership values increased significantly; with some coastal pixels the increase was as much as 0.4.

CONCLUSIONS

Four surface and eight cloud categories in merged AVHRR and SMMR data for the Arctic summer were identified through a neural network approach and a traditional maximum likelihood procedure. Both the numeric and the numeric/symbolic neural networks extracted correct information from the multispectral images. The differences between the neural network and the supervised maximum likelihood classifications were primarily due to the greater flexibility of the neural network to classify indistinct classes, e.g., classes containing pixels with spectral values that differ significantly from those in the

training areas, while ignoring assumptions of statistical normality. The two classification approaches illustrate the tradeoffs between human interaction in the selection of training areas and classification accuracy and flexibility. Flexibility similar to that shown by the neural network might be achieved using a maximum likelihood routine by manipulating class membership probabilities and/or by adjusting probability thresholds to relax the membership requirements for individual classes. Such steps may require an apriori knowledge of probabilities or may increase classification error. In any case, such tuning was not effective in the example described here.

The neural network approach to classification is generally less rigid than the traditional maximum likelihood procedure in that 1) there are no assumptions of distributions of variables and relationships between them, 2) the network is easily trained to learn the relationships between input and output, and 3) the classification produces both a categorical value and a type of membership value for each pixel. It is recognized that there is some loss of information and interpretability with the departure from statistical theory. Additionally, computation time required for training the network is not trivial when compared to the training of the ML classifier (i.e., computation of mean vectors and the covariance matrix), although future hardware architectures should alleviate this problem. Of course, training time as a proportion of the total classification time decreases with the amount of data processed, so that if classes do not change and large images are being classified, overall processing time should be similar for both methods.

The ability to interpret weights within the trained network provides a potentially powerful tool for understanding the role of inputs and the geophysical processes they represent in the making of decisions. Through an examination of the connection strengths between input, hidden, and output units, it is possible to identify which inputs influence the classification most, and which are redundant. These relationships are not always clear, and

care must be taken in extending their interpretation to physical processes. It was also shown that ancillary information, even on a simplistic level, can improve classification accuracy and can be easily included in a network. Although the example provided indicated that maximum likelihood results could be made to agree more closely with the manual interpretation, this was achieved only after training areas were expanded to include 9% of the test image. Such a degree of training is impractical for remote sensing climate studies because of the volume of imagery that must be processed. We emphasize that the data and applications of interest for remote sensing of polar climate is not typical of applications such as land cover mapping, which may be limited to a single image covering relatively small areas with small within-class variance. This study does not show whether a neural network offers any advantages for the latter type of analyses. The merits and drawbacks of a neural network approach relative to others must therefore be considered based on the particular problem at hand.

ACKNOWLEDGEMENTS

This work was supported by NASA grant NAG-5-898 and the NASA Polar Oceans Branch. Thanks are due to W. Rossow and E. Raschke for providing AVHRR GAC data.

REFERENCES

- Andress, K. and A. Kak, 1988. Evidence accumulation and flow of control. *AI Magazine*, 9 (2), 75-94.
- Barr, A. and E.A. Feigenbaum, 1981, 1982. Handbook of Artificial Intelligence. 3 vols. Los Altos, CA: William Kaufmann, Inc.
- Borchardt, G.C., 1986. STAR: a computer language for hybrid AI applications. In Coupling Symbolic and Numerical Computing in Expert Systems. J.S. Kowalik (ed.), Amsterdam, The Netherlands: North-Holland.
- Campbell, W.J. and L.H. Roelofs, 1984. Artificial intelligence applications for the remote sensing and earth science community. Proceedings, Ninth Pecora Symposium on Spatial Information Technologies for Remote Sensing Today and Tomorrow, Sioux Falls, South Dakota.
- Chandrasekaran, B., A. Goel, and D. Allemang, 1988. Connectionism and information processing abstractions. *AI Magazine*, 9 (4), 24-34.
- Ebert, E., 1988. Classification and analysis of surface and clouds at high latitudes from AVHRR multispectral satellite data. Scientific Report #8, Dept. of Meteorology, Univ. of Wisconsin-Madison.
- Ebert, E., 1987. A pattern recognition technique for distinguishing surface and cloud types in the polar regions, *J. Clim. Appl. Meteor.*, 26, 1412-1427.
- Estes, J.E., C. Sailer, and L.R. Tinney, 1986. Applications of artificial intelligence techniques to remote sensing. *Professional Geographer*, 38 (2), 133-141.
- Holmes, Q.A., D.R. Nuesch, and R.A. Shuchman, 1984. Textural analysis and real-time classification of sea-ice types using digital SAR data. *IEEE Trans. Geosci. Rem. Sens.*, GE-22 (2), 113-120.
- Jackson, M.J. and D.C. Mason, 1986. The development of integrated geo-information

- systems. **Int. J. Rem. Sens.**, 7 (6), 723-740.
- Key, J.R., 1988. Cloud analysis in the Arctic from combined AVHRR and SMMR data. Ph.D. dissertation, Department of Geography, University of Colorado, Boulder, 180 pp.
- Key, J.R., J.A. Maslanik, and R.G. Barry, 1989. Cloud classification using a fuzzy sets algorithm: a polar example, **Int. J. Rem. Sens.** (in press).
- Kitzmiller, C.T. and J.S. Kowalik, 1987. Coupling symbolic and numeric computing in KB systems. **AI Magazine**, 8 (2), 85-90.
- Kowalik, J.S. (ed.), 1986. Coupling Symbolic and Numerical Computing in Expert Systems. Amsterdam, The Netherlands: North-Holland.
- Lauritsen, L., G.G. Nelson, and R.W. Port, 1979. Data extraction and calibration of TIROS-N/NOAA A-G radiometer, NOAA Tech. Memor., NESS 107, Natl. Oceanic and Atmos. Admin., Boulder.
- Maslanik, J.A., J.R. Key, and R.G. Barry, 1989. Merging AVHRR and SMMR data for remote sensing of ice and cloud in polar regions. **Int. J. Rem. Sens.** (in press).
- Matsuyama, T., 1987. Knowledge-based aerial image understanding systems and expert systems for image processing. **IEEE Trans. Geosci. Rem. Sens.**, GE-25 (3), 305-316.
- McClelland, J.L. and D.E. Rumelhart, 1988. Explorations in Parallel Distributed Processing. Cambridge, Mass.: MIT Press, 344 pp.
- McKeown, D.M. Jr., 1987. The role of artificial intelligence in the integration of remotely sensed data with geographic information systems. **IEEE Trans. Geosci. Rem. Sens.**, GE-25 (3), 330-348.
- Minsky, M. and S. Papert, 1969. Perceptrons. Cambridge, MA: MIT Press.
- Moravec, H., 1988. Sensor fusion in certainty grids for mobile robots. **AI Magazine**, 9

(2), 61-74.

Murthy, H. A. and S. Haykin, 1987. Bayesian classification of surface-based ice-radar images. **IEEE J. Ocean. Eng.**, OE-12 (3), 493-502.

Nandhakumar, N. and J.K. Aggarwal, 1985. The artificial intelligence approach to pattern recognition - a perspective and an overview. **Pattern Recognition**, 18 (6), 383-389.

Nicolin, B. and R. Gabler, 1987. A knowledge-based system for the analysis of aerial images. **IEEE Trans. Geosci. Rem. Sens.**, GE-25 (3), 317-328.

NOAA, 1984. NOAA polar orbiter data user's guide. U.S. Department of Commerce, National Oceanic and Atmospheric Administration, NESDIS, February.

Reddy, R., 1988. Foundations and grand challenges of artificial intelligence. **AI Magazine**, 9 (4), 9-21.

Ripple, W.J. and V.S. Ulshoefer, 1987. Expert systems and spatial data models for efficient geographic data handling. **Photogram. Eng. Rem. Sens.**, 53 (10), 1431-1433.

Ritter, N.D., T.L. Logan, and N.A. Bryant, 1988. Integration of neural network technologies with geographic information systems. GIS Symposium: Integrating Technology and Geoscience Applications, September 1988, Denver, Colorado, 102-103.

Robinson, V.B. and A.U. Frank, 1987. Expert systems for geographic information systems. **Photogram. Eng. Rem. Sens.**, 53 (10), 1435-1441.

Rumelhart, D.E., J.L. McClelland, and the PDP Research Group, 1986. Parallel Distributed Processing. Cambridge, MA: MIT Press, 547 pp.

Schwalb, A., 1984. The TIROS-N/NOAA A-G satellite series, NOAA Tech. Mem., NESS 25.

Smith, T.R., 1984. Artificial intelligence and its applicability to geographical problem solving. **Professional Geographer**, 36 (2), 147-158.

- Smith, T., D. Peuquet, S. Menon, and P. Agarwal, 1987. KBGIS II: a knowledge-based geographical information system. *Int. J. Geog. Sys.*, 1 (2), 149-172.
- Usery, E.L. and P. Altheide, 1988. Knowledge-based GIS techniques applied to geological engineering. *Photogram. Eng. Rem. Sens.*, 54 (11), 1623-1628.
- WMO, 1987. Report of the ISCCP workshop on cloud algorithms in the polar regions, World Climate Research Programme, WCP-131, WMO/TD-No. 170, Tokyo, Japan, 19-21 August 1986.

FIGURES

Figure 1: The study area on July 1, 1984 showing Novaya Zemlya (at #2) in the center (75°N, 60°E), and the Kara (at #4 and #7) and Barents Seas (at #3). Sea ice covers most of the Kara Sea as well as the area north (toward lower left corner of image) and east (left) of Novaya Zemlya. Total area covered is approximately (1250 km)². Shown are AVHRR channels 1, 3 and 4. Examples of each target surface/cloud class are shown numbered as (1) LAND: snow-free land; (2) SNOW: snow-covered land/ice cap; (3) WATER: open water; (4) ICE: sea ice; (5) LCLL, (6) LCLW, (7) LCLI: low cloud over land, water, and ice, respectively; (8) MCLW, (9) MCLI: middle cloud over water, ice; (10) HCLL (not shown), (11) HCLW, (12) HCLI: high cloud over land, water, ice. These classes were identified through a manual interpretation of AVHRR and SMMR data (see Figure 2).

Figure 2: Manual classification of the data shown in Figure 1. Classes are the same as in Figure 1 with the addition of U: unclassified.

Figure 3: Neural network classification of the study area. Classes are the same as in Figure 2. A pixel's class is the one in which it exhibited the largest membership value. A pixel is left unclassified if none of its membership values exceeds 0.4.

Figure 4: Supervised maximum likelihood classification of the study area. Classes are the same as in Figure 2.

Figure 5: Connections between the input channels, hidden layer neurons, and the output classes in the trained network. Output neurons represent the surface classes only. Strength of the connections shown varies from 0.6 to 0.9 (on a scale of -1.0 to +1.0). See also Tables 4 and 5.

Table 1

Percent of images classified by method and training set.

Method	Training Set	Image	% Classified
--------	--------------	-------	--------------

ML	TA1	JULY 1	2%
----	-----	--------	----

ML	TA1	JULY 4	3%
----	-----	--------	----

ML	TA2	JULY 1	70%
----	-----	--------	-----

ML	TA2	JULY 4	53%
----	-----	--------	-----

NN	TA1	JULY 1	96%
----	-----	--------	-----

NN	TA1	JULY 4	93%
----	-----	--------	-----

Table 3

Contingency table showing the percentage of pixels in the image classified in each of the twelve classes by the manual interpretation (horizontal) and the supervised maximum likelihood procedure (vertical) using training set TA2. Percentage = number of pixels in class / total number of classified pixels [9,374]. Total agreement (sum along the diagonal) = 84.8%, based on 9% of the image used in training areas.

ML CLASS.	MANUAL CLASSIFICATION											
	LAND	SNOW	WATER	ICE	LCLL	LCLW	LCLI	MCLW	MCLI	HCLL	HCLW	HCLI
LAND	4.46	0.00	0.00	0.00	0.00	0.00	0.00	0.00	0.00	0.00	0.00	0.00
SNOW	0.00	1.37	0.00	0.00	0.00	0.00	0.02	0.00	0.00	0.00	0.00	0.00
WATER	0.00	0.00	13.64	0.05	0.00	1.46	0.00	0.08	0.00	0.00	0.00	0.00
ICE	0.00	0.00	0.00	7.56	0.00	0.00	0.23	0.00	0.02	0.00	0.00	0.00
LCLL	0.05	0.00	0.00	0.00	0.00	0.00	0.00	0.00	0.00	0.00	0.00	0.00
LCLW	0.00	0.00	0.41	0.00	0.00	10.60	0.00	2.89	0.00	0.00	0.02	0.00
LCLI	0.02	0.12	0.00	1.09	0.00	0.17	29.38	0.07	0.10	0.12	0.00	0.00
MCLW	0.00	0.00	0.08	0.00	0.00	3.92	0.00	4.35	0.00	0.00	0.02	0.00
MCLI	0.00	0.00	0.00	0.00	0.00	0.02	0.33	0.36	5.79	0.45	0.07	0.05
HCLL	0.00	0.00	0.00	0.00	0.00	0.00	0.13	0.00	0.05	1.67	0.00	0.00
HCLW	0.00	0.00	0.03	0.00	0.00	0.64	0.00	1.54	0.00	0.00	3.29	0.00
HCLI	0.00	0.00	0.02	0.00	0.00	0.00	0.05	0.00	0.81	0.00	0.02	2.71
TOTAL %	4.5%	1.5	14.2	8.7	0.0	16.8	30.1	9.3	6.8	2.2	3.4	2.8
AGREEMENT	98.5%	91.9	96.1	86.9	0.0	63.1	97.6	48.8	85.5	74.6	96.2	98.2
(ML/TOTAL)												

ORIGINAL PAGE IS
OF POOR QUALITY

Table 4

Connections between the input channels and the hidden layer in the trained neural network.

Hidden Layer	Input Channel Connections
(Neuron number)	(AVHRR: 1,2,3,4,5; SMMR: 18,37)

0	1, 2, 4, 5
1	NONE
2	5, 18, 37
3	4, 5, 18
4	2, 18
5	NONE
6	4, 5, 18, 37
7	2, 3
8	1, 18
9	2, 3, 4, 5

Table 5

Connections between the output class and
the hidden layer in the trained neural network.

Output Layer (Class)	Hidden Layer (Neuron number)
LAND	2, 3, 6
SNOW	0
WATER	1, 3, 5, 6, 7, 8, 9
ICE	1, 3, 5, 8
LCLL	6
LCLW	0, 9
LCLI	9
MCLW	1, 4, 5, 7, 9
MCLI	0, 4, 5, 9
HCLL	2, 4, 7
HCLW	1, 4, 5, 7, 8
HCLI	0, 3, 4, 8

ORIGINAL PAGE
BLACK AND WHITE PHOTOGRAPH

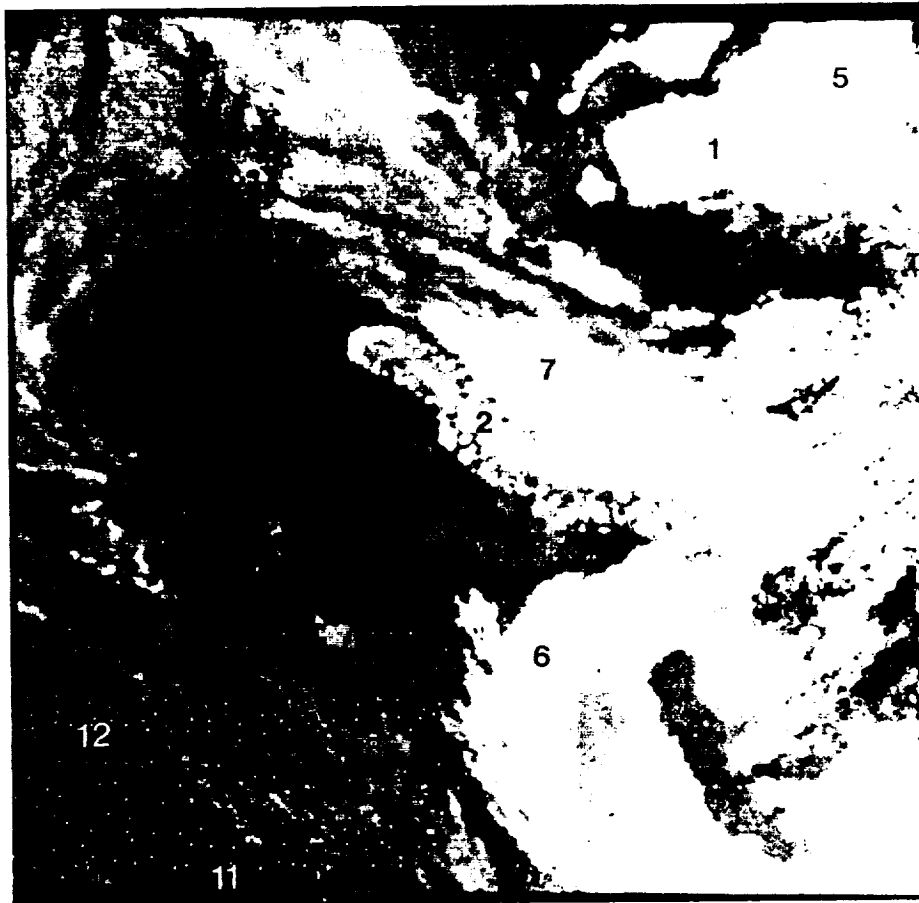


Fig 1

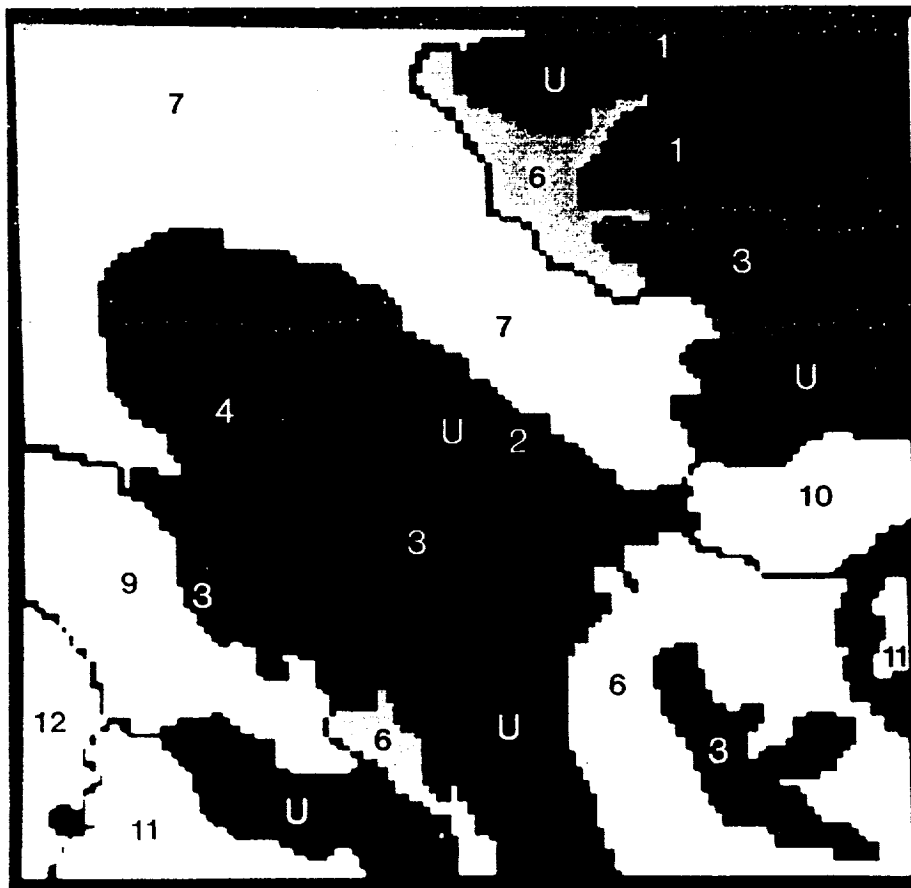


Fig 2

ORIGINAL PAGE
BLACK AND WHITE PHOTOGRAPH

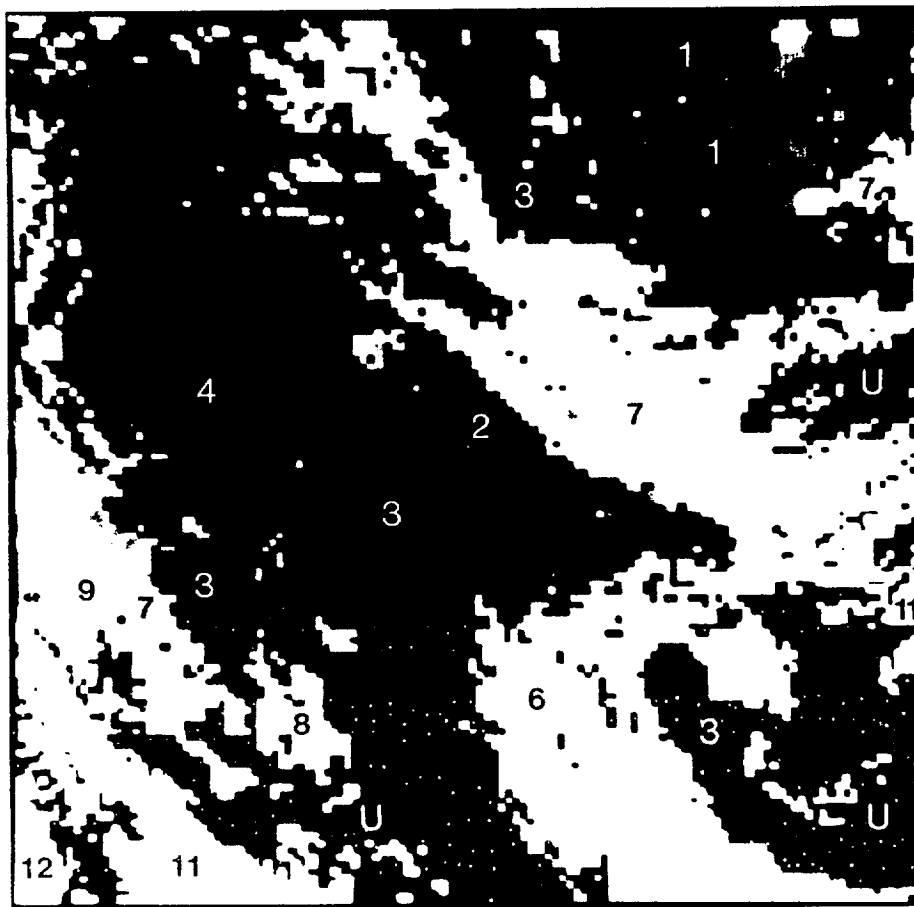


Fig 3

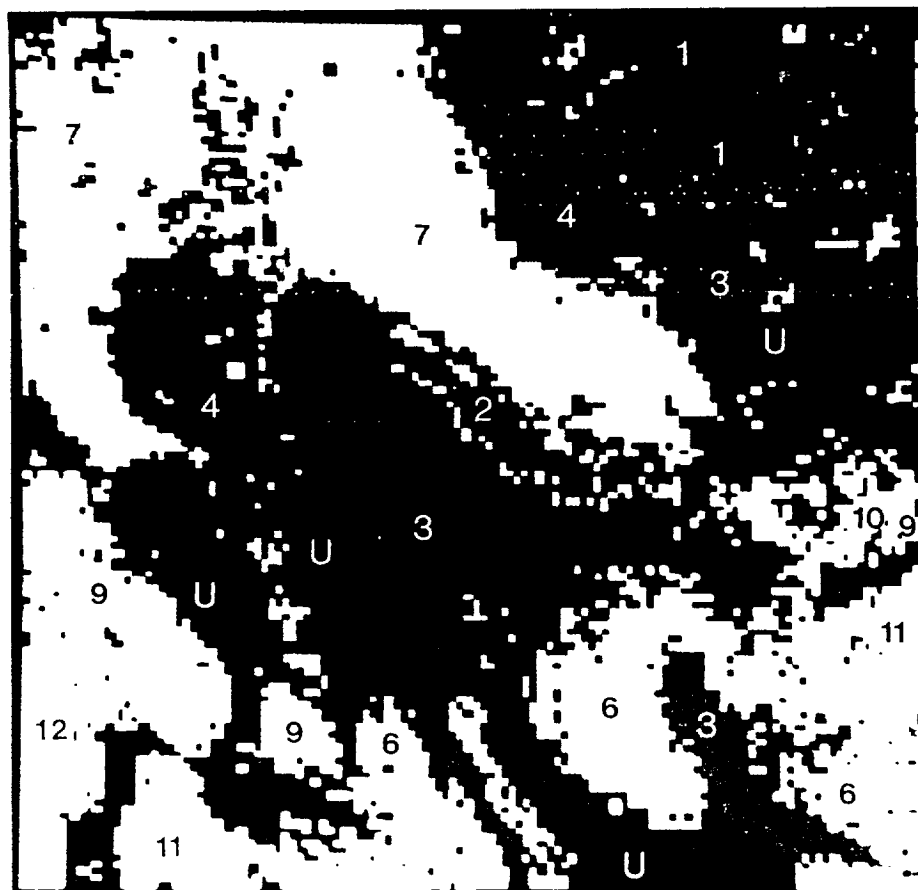


Fig 4

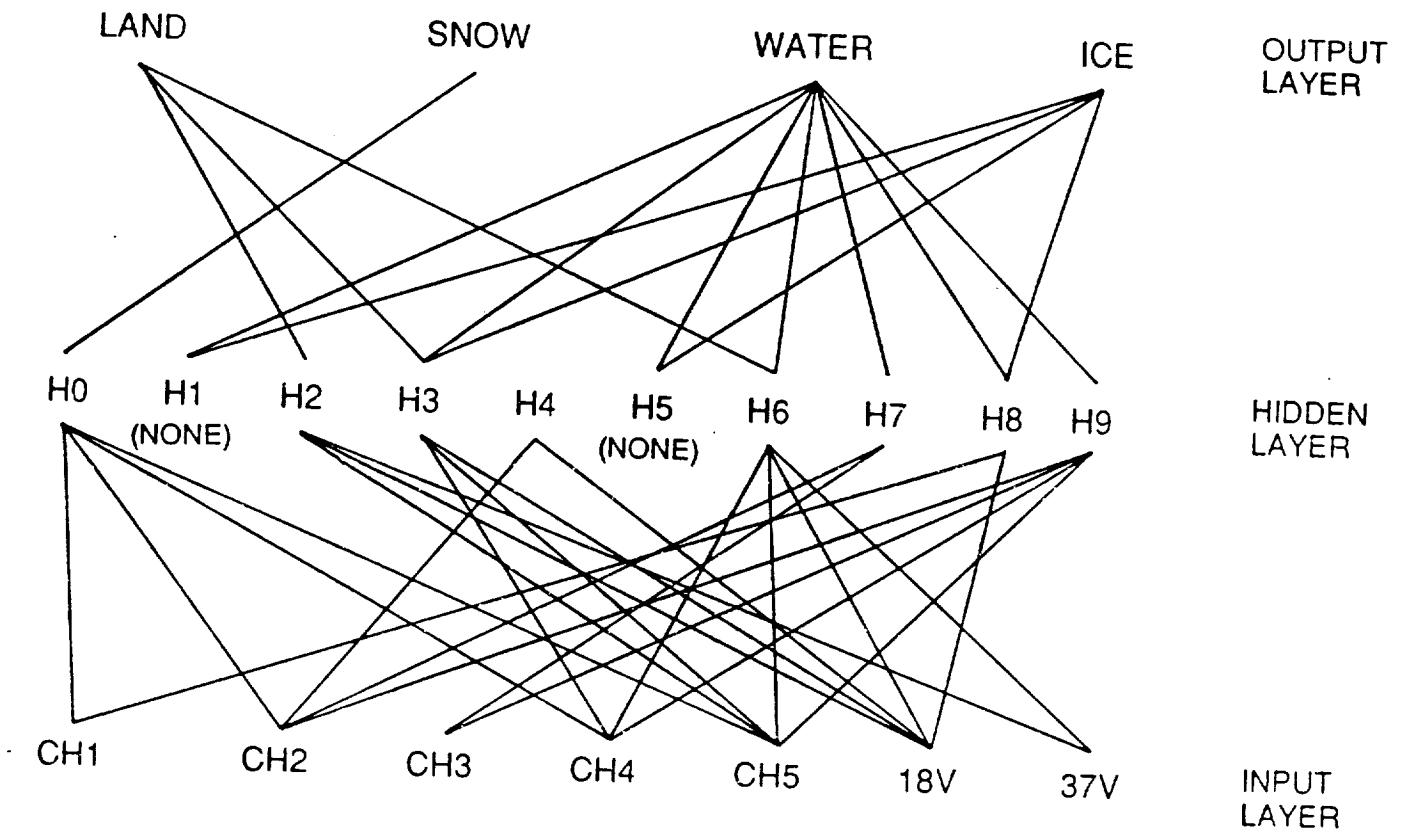


Fig. 5

ATTACHMENT 4
CLOUD COVER ANALYSIS: DETECTION

Cloud Cover Analysis with Arctic AVHRR Data, Part I: Cloud Detection

J. Key and R.G. Barry

Cooperative Institute for Research in Environmental

Sciences and Department of Geography

University of Colorado

Boulder, Colorado 80309-0449

Short title: Arctic Cloud Cover Analysis: Cloud Detection

Journal of Geophysical Research (Atmospheres)

ABSTRACT

Automated analyses of satellite radiance data have concentrated heavily on low and middle latitude situations. Some of the design objectives for the International Satellite Cloud Climatology Project (ISCCP) cloud detection procedure such as space and time contrasts are used in a basic algorithm from which a polar cloud detection algorithm is developed. This algorithm is applied to Arctic data for January and July conditions. Both Advanced Very High Resolution Radiometer (AVHRR) and Scanning Multichannel Microwave Radiometer (SMMR) data are utilized. Synthetic AVHRR and SMMR data for a seven-day analysis period are also generated to provide a data set with known characteristics on which to test and validate algorithms. Modifications to the basic algorithm for polar conditions include the use of SMMR and SMMR-derived data sets for the estimation of surface parameters, elimination of the spatial test for the warmest pixel, the use of AVHRR channels 1 ($0.7\mu\text{m}$), 3 ($3.7\mu\text{m}$), and 4 ($11\mu\text{m}$) in the temporal tests and the final multispectral thresholding, and the use of surface class characteristic values when clear sky values cannot be obtained. Additionally, the difference between channels 3 and 4 is included in the temporal test for the detection of optically thin cloud. Greatest improvement in computed cloud fraction is realized over snow and ice surfaces; over open water or snow-free land, all versions perform similarly. Since the inclusion of SMMR for surface analysis and additional spectral channels increases the computational burden, its use may be justified only over snow and ice-covered regions.

1. INTRODUCTION

The important role that polar processes play in the dynamics of global climate is widely recognized [Polar Research Group, 1984]. The variation of cloud amounts over polar ice sheets, sea ice, and ocean surfaces can have important effects on planetary albedo gradients and on surface energy exchanges [Barry et al., 1984; Shine and Crane, 1985].

Cloud cover exerts a major influence over the amount of solar and longwave radiation reaching the surface, and is linked to the sea ice through a series of radiative, dynamical, thermodynamic and hydrological feedback processes [Saltzman and Moritz, 1980]. Extent and thickness of sea ice influences oceanic heat loss and surface albedo which thereby influences global climate via the ice-albedo feedback [Budyko, 1969]. In turn, sea ice extent is controlled at least in part by radiative input from above.

Previous research in global cloud analysis has made clear the need for cloud retrieval procedures specific to particular climate regimes [e.g., Rossow, 1989; Rossow et al., 1989a,b]. Current procedures for automated analyses of satellite radiance data have been developed for low and middle latitudes but their application to polar regions has been largely unexplored. Those that have been applied to polar data often fail in the polar regions for a number of reasons including: snow-covered surfaces are often as reflective as the clouds, the thermal structure of the troposphere is characterized by frequent isothermal and inversion layers; the polar darkness during winter makes data collected in the visible portion of the spectrum largely unusable; satellite radiometers operate near one limit of their performance range due to extremely low surface temperatures and solar illuminations; there is a maximum concentration of aerosols in spring when the solar zenith angle is large increasing scattering of visible energy; and rapid small-scale variations - which in lower latitudes signify changes in cloud cover - occur on the surface as a result of changes in snow and ice distributions so that clear scenes are much more variable here than in lower latitude regions.

Generally not all of these difficulties are encountered at any one location. However, because they can result in rapid small-scale variation from one location and time to another, a complex analysis method that can recognize and cope with these situations is necessary [WMO, 1987]. The purpose of this paper is to present a cloud detection algorithm specifically for Arctic AVHRR data, based on ideas of the International Satellite Cloud

Climatology Project (ISCCP) algorithm [Rossow et al., 1985]. The procedure used as a starting point in this paper is a test version that shares some of the important features of the final ISCCP version [Rossow et al., 1988], such as space and time contrast, but also has some significant differences. Both summer and winter data are examined, although emphasis is placed on the summer analyses. Additionally, emphasis is placed on Arctic analyses, although many of the ideas also apply to Antarctic data.

2. BACKGROUND

Techniques for cloud detection from satellite data have been developed for use with visible, near-infrared, and thermal data, and have been based on threshold methods, radiative transfer models, and statistical classification schemes. A brief summary of some of the important methods is given here; an historical listing of cloud algorithms is given in Rossow et al. [1989b].

Cloud analysis methods which have included models of the physical properties involved in cloud formation have been developed by Shenk and Curran [1973], Shenk et al. [1976], Susskind et al. [1987], and d'Entremont [1986]. Bispectral threshold methods have been developed by Inoue [1987a], Minnis and Harrison [1984], Minnis et al. [1987], and applied to polar data by Inoue [1987b]. The effect of inaccurate snow cover information on retrieved cloud amount in the USAF nephanalysis system was examined by McGuffie and Robinson [1988].

To aid in the determination of clear sky radiances, the spatial aspects of cloud decks and ocean surfaces were examined by Coakley and Bretherton [1982], who developed the spatial coherence method. This was extended to two-layer systems by Coakley [1983] and Coakley and Baldwin [1984]. The spatial coherence method has also been applied by Crane and Anderson [1984] and Ebert [1989] for the analysis of polar clouds from AVHRR data. A variety of histogram and coherence threshold methods were tested by Saunders [1986].

Raschke [1987] developed decision trees for polar cloud detection with AVHRR data.

Statistical classification procedures, most commonly maximum likelihood and Euclidean distance methods, have been applied to cloud analysis by Desbois et al. [1982], Desbois and Seze [1984], Bunting and Fournier [1980], Bolle [1985], Harris and Barrett [1978], Pairman and Kittler [1986], Ebert [1987], Condal and Le [1984], Parikh [1977], Garand [1988], Welch et al. [1988], and Key et al. [1989a,b]. A further review of cloud detection procedures is given in Rossow [1989]. Global scale application of one cloud detection scheme for the determination of surface and cloud parameters detailed in Rossow et al. [1989a,b].

The International Satellite Cloud Climatology Project (ISCCP) to map clouds with satellite data began in July 1983. Its goal is to provide a uniform global climatology of satellite-measured radiances and from these to derive an experimental climatology of cloud radiative properties. As a basis for developing the ISCCP algorithm, Rossow et al. [1985] compared six cloud algorithms. However, the algorithms were not compared in the polar regions, and a separate study was organized to focus specifically on polar cloudiness [WMO, 1987]. The current ISCCP algorithm is composed of a series of steps, each of which is designed to detect some of the clouds present in the scene. The general idea in cloud detection is to first isolate the less variable clear scene radiances in the data and then identify the clouds by their alteration of these radiances (compare to Rossow et al. [1989a]). Spatial and temporal variation are used in the detection of clear pixels; clear sky composite maps (over five day periods) are then constructed. Finally, each pixel is compared to the clear sky radiances to determine if cloud is present. It has been recognized that reliable detection of cloudiness in the polar regions with the current ISCCP algorithm is particularly difficult, and it has been recommended that the study of clouds over polar regions be continued [WMO, 1988].

3. DATA

Satellite data for the polar regions are collected by the Tiros-N (NOAA 6 et seq), Nimbus, and Defense Meteorological Satellite Program (DMSP) satellites. Visible and thermal data from the NOAA-7 satellite are the primary data source for this study. Passive microwave data from the Nimbus-7 platform is used to aid in surface parameterization. DMSP visible and thermal imagery are used for validation.

The Advanced Very High Resolution Radiometer (AVHRR) on board the NOAA-7 polar orbiting satellite is a scanning radiometer that senses in the visible, reflected infrared, and thermal (emitted) infrared portions of the electromagnetic spectrum (1: 0.58-0.68 μ m, 2: 0.73-1.0 μ m, 3: 3.55-3.93 μ m, 4: 10.3-11.3 μ m, 5: 11.5-12.5 μ m) with a nadir resolution of 1.1 km. Global Area Coverage (GAC) imagery is a reduced-resolution (3x5 km) product created through on-board satellite processing. Construction of GAC data is described elsewhere [e.g., Schwalb, 1978].

First-order calibration of the AVHRR GAC data was performed following the methods described in the NOAA Polar Orbiter Users Guide [NOAA, 1984] and Lauritsen et al. [1970]. Brown et al. [1985] provide additional information on calibration. Channels 1 and 2 were converted to approximate spectral albedo in percent. Channels 3, 4, and 5 were converted to radiance in milliwatts/(m²-steradians-cm) then to brightness temperature in Kelvins [NOAA, 1984]. AVHRR channel 3, at 3.7 μ m, records both reflected and emitted energy. For some analyses, a separation of these two components may be useful [Raschke, 1987; Allen et al., 1988]. The channel 3 albedo was approximated by subtracting the thermal radiance that would be emitted in this channel from a blackbody radiating at the brightness temperature measured in channel 4. Emissivities in both channels are assumed equal since no a priori information exists about the cloud and surface types contained in the data.

The typically low water vapor content in the polar atmosphere and the low physical

temperatures reduce most atmospheric effects to a point where they may be neglected for the analyses performed here. Approximate corrections for solar zenith angle in channels 1 and 2 were accomplished through a division of the albedo by the cosine of the zenith angle. Bidirectional reflectance and emittance may also affect the spectral characteristics of surfaces and clouds but have been studied extensively only for snow [e.g., Dozier and Warren, 1982; Robock and Kaiser, 1985; Steffen, 1987]. In the visible channels, bidirectional reflectance may be useful in distinguishing haze from cirrus [Gerstl and Simmer, 1985]. Again, correcting for this effect would require a priori knowledge of surface and cloud types in the data, therefore, no corrections for these effects are made.

The Nimbus-7 Scanning Multichannel Microwave Radiometer (SMMR) is a conically scanning radiometer that senses emitted microwave radiation both vertically and horizontally polarized in five channels: 6.6, 10.7, 18.0, 21.0, and 37.0 GHz. Instantaneous field of view of the sensor varies with channel, ranging from 148x95 km for the 6.6 GHz channel to 55x41 km and 27x18 km for the 18 and 37 GHz channels, respectively. The 18 and 37 GHz channels are employed here. No distinction is made between day, night, and twilight orbits; data from overlapping orbits are averaged to yield a daily value. Sea ice concentration was calculated from SMMR data using the operational NASA Team algorithm [Cavalieri et al., 1984]. The 18 and 37 GHz polarization and gradient ratios are used to calculate ice type (i.e. first-year or multiyear) and concentration. A simple gradient ratio threshold is included to reduce the effects of ocean surface spray and foam on ice parameterization [Gloersen and Cavalieri, 1986].

AVHRR and SMMR data are merged in digital form to a polar stereographic grid. This projection yields equal-area pixels true at 70° latitude with a five kilometer pixel size, a slight degradation of the GAC resolution. The SMMR data were converted to the five kilometer cells by simple duplication of pixels. Further details are given in Maslanik et al. [1988].

Three areas of the Arctic are examined (Figure 1). One area is centered on the Kara and Barents Sea extending north to the pole and south to Norway and the Siberian coast. The second area covers most of the Canadian Archipelago and Greenland, and extends north to the pole. The third area extends from the coast of Norway to Ellesmere Island. A seven-day summer series (July 1-7, 1984) of areas 1 and 2, and a winter series (January 6-12, 1984) of area 3 were examined. These data are part of an ISCCP test data set. While covering only one-third of the Arctic Basin, they include representative samples of all surface types found in the Arctic: snow-covered and snow-free land, sea ice of varying concentrations, open water, and permanent ice cap. In fact, these areas during the July period present particularly difficult conditions for cloud algorithms to work with; sea ice is moving, snow is melting and ponds form, and the extensive coastlines exhibit mixed temperature regimes. In the study areas reflectances were found to vary significantly over one week intervals and north-south temperature gradients were observed. A portion of each study area is shown in Figure 2 where AVHRR channel 1 (visible) data on July 3, 1984 are shown for study areas 1 and 2; study area 3 on January 8, 1984 is displayed in AVHRR channel 4 (thermal).

These conditions are usual for summer in the Arctic, as are the pressure patterns which occurred. Surface pressure maps constructed from Arctic Ocean buoy data taken from Colony and Munoz [1986] provide an overall synoptic picture of daily weather which resembles the mean monthly pattern [Serreze and Barry, 1988; Gorshkov, 1983]. Conditions during the January study period are also similar to the monthly mean pattern. Although correlations have been observed between synoptic pressure systems, cloud amount, and cloud type [Barry et al., 1987], detailed cloud climatologies for the Arctic are not available and it is therefore more difficult to make such a statement concerning cloud cover.

Visible (0.4-1.1 μ m) and thermal (10.5-12.5 μ m) imagery from the DMSP - a near-polar orbiter with a resolution of 2.7 km for orbital swath format images - was used for

manual comparisons of cloud type and amount and surface conditions in cloud-free areas. Other ancillary data include surface temperatures from the European Centre for Medium Range Forecasting (ECMWF), and sea ice albedo from Scharfen et al. [1987] which are derived from a combination of DMSP imagery and the NOAA/Navy ice charts.

3.1 Synthetic Data Sets

In order to test the sensitivity of the various cloud algorithms, a control data set with known characteristics was needed. A synthetic data set was developed which consists of seven days of AVHRR data (channels 1, 3, 4), three days of SMMR brightness temperature data (every other day; 18 and 37 GHz vertical polarization), SMMR-derived sea ice concentrations, and a land mask. The procedure followed is to first generate the surface and cloud type maps for each day of the seven day period. Surface types are snow-covered and snow-free land, open water, and sea ice. Cloud layers are classified as low, middle, and high, where levels are defined by AVHRR channel 4 temperatures (T) as follows: low cloud $T > 265$ K, middle cloud $245 \leq T \leq 265$ K, and high cloud $T < 245$ K. The minimum and maximum allowable sizes of surface 'objects' (i.e., a single surface type surrounded by other surface types) for the first day, and cloud objects for each day are specified. An object is generated whose dimensions are randomly chosen within the restricted range, and the class of the object is randomly assigned (uniform random number generator).

Regions are then filled with data for each AVHRR and SMMR channel and for sea ice concentration using empirically-derived statistics. Data were based on class characteristic means and standard deviations computed from training areas. Values for each pixel in each channel were produced using a Gaussian random number generator [Ebert, 1988; Garand, 1988]. Each artificially-generated element of class j is a vector, v_j , of d features:

$$v_j = \mu_j + \Omega A_j$$

where μ_j is the class mean vector of length d , Ω is a vector of random deviations for each

feature selected from the multivariate Gaussian distribution of deviations, A_j is the lower triangular matrix decomposed from the $d \times d$ class covariance matrix, Σ_j (which is symmetric and positive definite), such that

$$A_j A_j^T = \Sigma_j$$

The values from the Gaussian random number generator have a zero mean and unit variance and are constrained to be in the range of -3 to +3 which include approximately 99% of the data in a normally distributed population.

In the synthetic images, the surface map for the first day and cloud maps for all days are created with this procedure. The surface maps for the third and fifth days, however, are modified versions of the first day. Snow and ice pixels are allowed to melt into land and water, respectively; ice pixels may advance into open water areas and snow may fall on land. The evolution is designed such that approximately 68% of the decisions resulted in an unchanged local area and 32% resulted in either an advance or a retreat.

4. SPECTRAL FEATURES AND CLASSES

Spectral features examined for each pixel are channels 1, 2, and 3 albedos, channels 3, 4, and 5 brightness temperatures, ratios of channels 2 and 1, and the differences between channels 3 and 4 and 4 and 5. The ratio of channel 2 to channel 1 or the difference between channels 2 and 1 enhances vegetation signals as well as snow and sea ice underneath clouds. The reflectance of cirrus clouds is greater than that of snow in the near-IR (channel 2) due to differences in particle effective mean radius, the albedo being higher for smaller grains [Wiscombe and Warren, 1980]. Channel 2 wavelengths are less affected by aerosols than are channel 1 responses; snow-free land surfaces have a higher albedo in channel 2 [Saunders, 1986]. Because snow- and ice-covered surface albedos decrease with increasing wavelength while cloud albedos decrease only slightly over the same range, channels 1 and 2 of the AVHRR are potentially useful for this discrimination.

Since cirrus clouds have higher transmissivities at channel 3 wavelengths than for channels 4 and 5 [Hunt, 1972], corresponding brightness temperatures are higher due to the greater contribution of radiation to the total upwelling radiance by warmer surfaces beneath the cirrus. Therefore, channel 3 temperatures will generally be higher than those of the other thermal channels, day or night. This is particularly true for optically thin clouds, and has been modeled by Olesen and Grassl [1985]. However, the effect is diminished or even reversed when $3.7\mu\text{m}$ emissivities are low, as they are for low water clouds and fog. During the day, the contribution of reflected energy to channel 3 is very low for clear sky pixels. The albedo of low and middle cloud in this band is much higher, due to a particle size effect. Therefore, channel 3 values will be similar to those measured in channel 4 for clear sky areas. Channel 5 is similar to channel 4, except that channel 5 radiation is more sensitive to water vapor. Therefore, in clear, cold atmospheres brightness temperatures measured by the two channels are similar, but channel 5 temperatures may be as much as three percent lower in moist atmospheres [d'Entremont and Thomason, 1987]. The brightness temperature difference between channels 4 and 5 is close to zero for stratocumulus but large for cirrus due to differences in emissivities.

Four surface and three cloud classes are analyzed. Surface types are snow-free land, snow-covered land/ice cap, open water, and sea ice. All pixels with ice concentration of at least 15% are classified as sea ice. While cloud detection results may be improved with more than one ice class on a local scale, the use of a single ice class did not produce significantly different results over the entire data set. Cloud classes are defined by brightness temperature in AVHRR channel 4, assumed to represent temperatures at the top of optically thick cloud layers, and encompass the same three temperature ranges as in the synthetic data (low, middle, high).

5. BASIC ALGORITHM

The basic cloud detection algorithm upon which the final polar procedure will be built is based on ideas presented by Rossow et al. [1985] as design criteria for the ISCCP algorithm. In particular, space and time contrast tests are two of the major steps used in both early and current ISCCP algorithms, and are employed here. Spatial and temporal variation are used in the detection of clear pixels; clear sky composite maps are then constructed. Finally, each pixel is compared to these clear sky radiances to determine if cloud is present. The algorithm assumptions are that cloud scene radiances are more variable in time and space than clear scene radiances and cloudy scenes are associated with larger visible channel and smaller infrared radiances than clear scenes. This algorithm version was tested by ISCCP but is not the final version. The major steps used here are summarized in Figure 3(a) and are:

Spatial and temporal variation. The image is divided into cloudy and "undecided" categories based on cold and warm pixels. If a pixel is much colder (defined later) than the warmest pixel in a small region ($(100 \text{ km})^2$ over land and $(300 \text{ km})^2$ over ocean), it is labeled "cloud". Otherwise, it is labeled "undecided". High and middle level clouds are identified. Only thermal data are used in this step.

Pixels are then compared to the day before and the day after for changes in temperature. If the middle day is much colder than either day, it is labeled "cloud". If the variation is small, it is labeled "clear". Those pixels exhibiting intermediate variability are labeled "undecided". Again, only thermal data are used in this step. High and middle clouds are most easily recognized. The class of a pixel based on these two steps is given in Table 1.

Compositing. The mean and extremum radiances for the clear pixels are calculated over 5 and 30 day periods. Statistics are calculated for a 3x3 compositing cell centered on the pixel of interest over the time period; i.e., 45 pixels are used for the 5 day period. The

number and mean of clear pixels only is recorded as well as the maximum temperature and minimum albedo of all pixels, regardless of previous labeling.

The clear sky radiances for each pixel are then determined. If, as determined by the statistical tests below, the compositing cell associated with a pixel is not variable, the clear sky value is the mean value over the period, otherwise the extremum (minimum visible and maximum thermal) values are used. The purpose of this and the previous step are to find the most accurate values of clear sky conditions, therefore the tests are very strict and will probably result in an overestimate of cloud amount.

Final threshold. The data are compared to the clear sky values modified by a threshold amount. Those that differ in either the thermal or visible channels by more than the threshold amount are labeled as cloud. This test is less strict than the previous one since the purpose is to detect cloudy conditions rather than clear.

6. MODIFICATIONS

This basic algorithm has been adjusted in order to deal with the problems cited in Section 1. Major modifications suggested include the use of snow and ice data sets for the estimation of surface parameters, elimination of the spatial test for the warmest pixel in a subregion, the use of AVHRR channels 1 ($0.7\mu\text{m}$), 3 ($3.7\mu\text{m}$), and 4 ($11\mu\text{m}$) in the temporal tests, statistical tests for compositing, and the final multispectral thresholding, and the use of surface class characteristic values when clear sky values cannot be obtained. Additionally, the difference between channels 3 and 4 is included in temporal tests for the detection of optically thin low cloud and cirrus. The steps of the modified algorithm are shown in Figure 3(b). Some of these modifications require further explanation.

6.1 Surface Types

Surface types are determined with a land/ice cap mask, SMMR data, and SMMR-

derived sea ice concentration. If the pixel is land, then a SMMR test is applied to determine if the land is snow-free or snow-covered. Snow-covered land exhibits a higher 18 GHz brightness temperature than that of the 37 GHz channel, and the vertical polarization is less variable than the horizontal for land (unless wet). This relationship may not hold over an ice cap, so a mask for permanent ice cap (e.g., Greenland and Novaya Zemlya) is included, and ice cap is then treated as snow. Problems with this method occur in coastal areas where this relationship may be observed even without the presence of snow. Therefore a coastal zone is defined to be approximately 20 km from the edge of the coast both inland and seaward. Finally, if the pixel is not land and if the sea ice concentration is less than 15%, the pixel is labeled water, otherwise it is sea ice.

The basic algorithm assumes a constant surface type over the five-day period. However, snow melt, snowfall, and ice advection cause changes in albedo, emissivity, and temperatures which create difficulties in cloud detection and alter clear sky composite values. Therefore, pixels in which the surface changes during the period are flagged, and receive more than one clear sky value in the compositing step. Since a 30 day sequence of data was not available, these values are likely to be derived from a small sample of clear pixels, and therefore may not be reliable.

6.2 Spatial and Temporal Variation Tests

One of the basic assumptions of the algorithm - that the surface is warmer than the cloud - is often violated in summer polar data and is commonly incorrect during the winter. It is not uncommon in summer for low cloud to be at the same or higher temperature than the underlying snow or ice surface. In winter it is not uncommon for all cloud but cirrus to be warmer than the surface. While use of a spatial test may be possible, it would require knowledge of the temperature profile. This is assumed not to be the case and, for this reason, the spatial variation test for the warmest pixel in a subregion was eliminated

entirely.

In the temporal variation test of the initial classification, where pixel temperatures are compared to the day before and after, if a pixel is much colder than either day (by the amount in Table 2, "Cloud") then that pixel is labeled cloud. If the albedo and temperatures are the same as either day (Table 2, "Clear") in channels 1, 3, and 4 then the pixel is labeled clear. Otherwise, it is labeled undecided. Obvious problems occur when warm, low clouds move into or out of a region where the surface temperature is within the "clear" range of the cloud. These cloudy pixels will consequently be labeled clear in this step, and will ultimately be labeled clear and used in the compositing step to determine clear sky radiances. Since thermal-only tests fail to label these pixels correctly, channels 1 and 3 data were also used in the temporal variation test. Values in Table 2 were derived experimentally except for channel 4 land and ocean temperatures which are taken from ISCCP specifications.

To reduce the computational burden, a test for a large difference between channels 3 and 4 is done. If the difference is greater than 3.5 K [Saunders, 1986; Olesen and Grassl, 1985], the pixel is labeled cloud and is not compared to the day before and after. Spatial/temporal tests which included the entire seven-day period were also tested. However, problems with the warmest pixel being low cloud were too frequent to justify their use.

6.3 Compositing

To determine clear sky composite values, distributions of those pixels initially labeled clear are tested for cloud contamination. The idea is that if a large enough sample of clear values for a given location is available, an average of this sample will provide a better clear sky composite value than the extrema radiances. Conversely, if only a few clear values were obtained in the initial classification, the extrema provide the most reliable

estimate upon which to base the final cloud detection. "Populations" against which to test compositing cell statistics are based on class characteristic means and standard deviations for each surface type are computed and updated with each region analyzed. These values are initially set to those determined for the previous 5-day period, or from training area statistics based on manual interpretations if no previous data are available. (Class characteristic values for polar surfaces and clouds in AVHRR data are also given in Ebert [1988, 1989].) Those clear sky composite mean values which pass the statistical tests are incorporated into the new class characteristic values.

The statistical tests are designed to determine the likelihood that the clear pixels in each compositing cell are in fact all clear. This is done by examining the mean, standard deviation and extremum of the distributions of radiances in each cell. The procedure followed here first checks the number of clear pixels in the compositing cell (maximum 45). The cutoff value for too few pixels is a sample size such that the population mean could be predicted from the sample mean to within one population standard deviation (arbitrary) at a specified confidence level; e.g., at a level of confidence of 0.99, this criterion requires that sample statistics and further tests be based on at least seven clear pixels. If the number of clear pixels is less than seven, then the maximum thermal and minimum visible values are used in the clear sky composite, assuming that the probability of them coming from the appropriate population (t-test) is greater than the specified level of significance.

If, on the other hand, the number of clear pixels is sufficient, the probability that the minimum thermal and maximum visible values come from the population is also tested. If the probability of obtaining either a smaller thermal or larger visible value is less than the significance level, cloud contamination is assumed and the opposite extrema are used as the clear sky composite values. Otherwise, a t-test is performed on the means of the composite cell and the class characteristic values where the null hypothesis is that the means of the respective populations are equal. If the null hypothesis in both tests is not rejected,

then the mean values are used as the clear sky composite. Otherwise, extrema are used.

The assumption of Gaussian distributions that these tests carry may be violated if data are examined over large spatial and temporal scales. In such cases, an informational class such as land albedo may comprise more than one statistical class. It is therefore important that class characteristic values be computed for relatively small geographic areas and time scales. In this study, radiance means and variances are derived from $(250 \text{ km})^2$ areas over five-day periods.

If the statistical tests during compositing fail, the clear sky value for a given location is assigned a value based on its spatial neighbors or class characteristic value. The neighborhood of pixels with the same surface type is searched and the first clear value found of the same surface type is used. The maximum search radius is determined by an autocorrelation function derived for each surface type in this data set (up to a radius of 12 pixels or 60 km). If no value is found within this radius, the clear sky value assigned is based on the class characteristic values.

6.4 Final Thresholds

The final thresholding step utilizes AVHRR channels 1, 3, and 4. Channel 3 is used only if the surface is sea ice or snow/ice cap, and is intended to detect low cloud. Middle and high clouds will normally be detected over any surface with thermal data alone. Thresholds for this step were derived empirically and are given in Table 3. They are relatively large so that the algorithm yields a conservative estimate of cloud fraction, in part adjusting for partially covered pixels. Some methods of cloud cover analysis have attempted to set thresholds which account for this condition [e.g., Coakley and Bretherton, 1982; Arking and Childs, 1985; Coakley, 1987]. However, radiances similar to those for partially covered pixels can also be produced by optically thin clouds, and there is currently no reliable method of distinguishing between these two effects [Rossow et al., 1985].

Therefore, the degree to which pixel values differ from the clear sky values in each channel is retained by the algorithm and can be used as an indication of the reliability of computed cloud fraction. This procedure follows the one currently employed in the ISCCP algorithm [Rossow et al., 1988].

For analyses presented here, a pixel is labeled cloud if it varies from the clear sky value by more than the threshold in any channel. The importance of this disjunction is illustrated in Figure 4 where the differences between cloudy pixel radiances and the radiance of the underlying surface - taken to be the clear sky composite value - are plotted for each channel. The data are based on summer samples taken imagery containing a variety of surface types and cloud distributions. Zero differences are found along the line in each plot. Of particular interest are the points near this line, representing optically thin clouds over ice or snow in channel 1, and low (possibly inversion) clouds in the channel 4 plot. With both a reflected and thermal component in channel 3, there are many possible combinations of surface and cloud top temperatures and reflectivities which would give rise to similar cloud and surface radiances in the middle plot. Over snow and ice, the most common are: optically thick low and middle cloud with reflectivity and temperature similar to the surface, thick cloud with higher reflectivity but lower brightness temperature, or thin low and middle cloud.

6.5 Winter Analysis

Surface temperatures over land in January 1984 were typically 225-235 K, ocean (open and thin ice) in the southern portion of the study area was 260-275 K, sea ice was 231-235 K, and clouds ranged from 215 to 258 K. In the final threshold step, the assumption that clouds are colder than the surface was eliminated and the test was modified so that a difference from the clear sky composite value in either direction signals a cloudy pixel. Additionally, temperatures within the broadly-defined surface classes vary

considerably across the image, in particular for Greenland snow/ice cap due to elevation change and open water from the Norwegian Sea north to Svalbard. Class characteristic values are no longer reliable, so statistical tests are based only on the range of the extremum.

7. TESTING AND ALGORITHM COMPARISON

Three algorithm versions are compared. The original algorithm (herein "Basic-VT") developed for low latitude summer conditions recognizes only two surface types: land and water. No SMMR or sea ice concentration data are employed. Spatial/temporal tests in the initial classification step are thermal only (AVHRR channel 4), and a visible/thermal bispectral threshold test (channels 1 and 4) is used in the final classification. This version with a thermal-only threshold test was also used to simulate winter applications ("Basic-T"). The algorithm with modifications described in the previous section is the third version tested ("Modified").

Four regions from the AVHRR imagery and four regions from the synthetic data sets, all summertime, are used as test data. Each region is 50x50 pixels or $(250\text{km})^2$ and differs in surface and cloud types and proportions. The synthetic data set image contains surface areas with 250 to 500 km as the minimum dimension ("objects" are rectangular). Cloud sizes and distributions changed from day to day, with the minimum dimension ranging from 20 to 300 km. Surface proportions changed in both data sets by up to 20%. These changes are due to sea ice movement and melting. The surface/cloud types and proportions are given in Table 4.

Cloud fractions computed by each algorithm for each region and day are given in Tables 5 and 6. Also given in the table are the number of clear pixels used in the compositing step for each region and version. The actual cloud amount is shown for synthetic data sets, determined by counting the number of pixels in the region assigned to a

cloud class. A manual interpretation was done utilizing all AVHRR, SMMR, and SMMR-derived data sets. Due to the subjective nature this procedure, however, measured cloud fraction should be used only as a "standard" by which to judge algorithm performance and should not be treated as an absolute.

All versions of the algorithm perform best over land and water. Snow and ice remain the problem areas although the modified versions performed best under these conditions. When cloud amounts are high (more than 80%), all versions compute cloud fraction to within approximately 5% of each other. When cloud amounts are low, the modified version is more accurate, although cloud fraction was often too high. In the actual data, this is at least in part due to possible discrepancies in the manual interpretation, as described above. In the synthetic data, this is probably due to the fact that clear sky areas are filled with values in the range of the mean plus or minus three standard deviations (following a Gaussian probability function), so that extreme values may be beyond threshold cutoffs and will consequently be labeled as cloud. Final thresholds are generally between two and three times the standard deviations used in the generation of synthetic images.

The basic algorithm versions often overestimate cloud amount. This is common over ice where, in the bispectral threshold test, the threshold for water is used. This albedo threshold is too small to account for variation in sea ice albedos, and consequently many clear pixels were mistaken as cloud. A related situation is that the basic version often makes an accurate assessment of cloud fraction, but for the wrong reason. For example, one sea ice region had over 70% of the cloud cover as very thin cloud, possibly haze. Channels 1 and 4 alone did not detect this condition, yet the threshold-determined cloud amount for Basic-VT is similar to the amount determined manually. Here again, albedo contributions from the thin cloud are insignificant, so that the algorithm is labeling cloud by the threshold step what it sees in channel 1 as sea ice. The snow and ice data sets used in the modified versions solve these problems by providing appropriate thresholds.

Root mean square and mean absolute difference errors given in Table 7 illustrate that the modified version was most accurate in computing cloud fraction for both data sets. The thermal-only version performed reasonably well with the synthetic data set, at least in part for reasons explained above.

8. APPLICATION

The modified version of the algorithm was next applied to the Arctic study areas. Surface albedos determined over the five-day compositing period for the two summer study areas, which overlap the winter area, are shown in Figure 5. Values are averages over each quarter of the 250x250 km analysis regions. Sea ice albedo from Scharfen et al. [1987] is shown in Figure 6 and is in general agreement with Figure 5 for sea ice. A direct comparison is complicated by the difference in resolution, the data in Figure 6 being much coarser and for sea ice only, and because those data are integrated over a broader spectral band. They are therefore expected to be somewhat lower than the albedo measured by AVHRR channel 1, depending on the amount of snow cover present. Composited surface temperatures are shown in Figure 7 for AVHRR channel 4. Since surface emissivities in channel 4 (11 μ m) are near unity, the temperatures presented may be considered as estimates of physical temperatures. These are similar to the ECMWF data presented in Figure 8. Differences are due to the averaging over quarter regions, and to the adjustment of temperatures over Greenland to sea level in the ECMWF data. Winter composite temperatures show greater departures from the meteorological data than the summer values, probably due to invalid lapse rate assumptions in the construction of the ECMWF data.

Cloud fraction for the third day of the analysis period for each study area is shown in Figure 5 and compares favorably with a manual interpretation of the DMSP imagery (not shown) and the images presented in Figure 2. The largest differences occur over sea ice where low cloud cannot be distinguished in the DMSP visible and thermal channels alone.

In these cases the DMSP-estimated cloud fraction is too small, as cloud is mistaken as sea ice. Similarities can also be seen between the computed cloud amount and the mean for July given in Gorshkov [1983], where the cloud amount increases to 0.9 toward the pole. Near Novaya Zemlya and also across the Canadian Archipelago cloud amounts of 0.7-0.8 in the July mean are typical. For the winter period, no visible data are available, so that accuracy assessment through a comparison with manual interpretations is more difficult. However, an examination of surface temperatures did not appear contaminated, so that cloud fraction computed by the threshold step should be reliable.

9. DISCUSSION

The initial classification step is the most difficult part of the algorithm to refine due to its sensitivity to changes in thresholds. Error will propagate from this point, so it is important that all pixels labeled clear in this step actually are clear, but it is also important to obtain as many clear pixels as possible. The spatial test is inappropriate for winter data in polar regions where strong surface temperature inversions are the norm, and is of questionable utility even in the summer when isothermal and inversion conditions are also common. The inclusion of AVHRR channel 3 aids in the discrimination of ice/snow and cloud, and the channel 3-4 difference detects optically thin cloud and fog.

Snow and ice information provided by the SMMR and SMMR-derived data sets was another important addition to the basic algorithm. No other use of SMMR data in conjunction with AVHRR data for polar cloud and surface analysis has been reported in the literature. The merged data sets capitalize on the unique capabilities of AVHRR and passive microwave data by reducing the inherent limitations of each sensor, and provide a means to improve automated cloud mapping in polar regions. Similar analyses will become possible with the suite of remote sensing data due to be collected from the Earth Observing System (EOS) in the 1990s. Unfortunately, extracting, calibrating, and registering three or

more AVHRR channels for seven days, two SMMR channels for each of three days, calculating sea ice concentration for three days, and developing a land/ice cap mask is not a trivial undertaking, so that this procedure is cost-effective only in areas where the more basic methods fail; e.g., over snow and ice.

The cloud detection algorithm presented here used as its starting point ideas that were presented in Rossow et al. [1985] as design criteria for an emerging ISCCP algorithm. From that point, this algorithm and that of the ISCCP developed for the most part independently. The ISCCP algorithm is currently being applied operationally on a global scale, and data for selected time periods are available for distribution. It is of interest to point out a few similarities and differences between the two algorithms. The basic steps of space/time tests, clear sky radiance composites, and bispectral thresholds have been retained in current ISCCP algorithms, although some threshold and test values have changed. These are also used here, with these exceptions: the spatial tests are eliminated (Section 6.2), the temporal tests are skipped if the pixel is first determined to be thin cloud, and winter thresholds and surface/cloud temperature relationships are treated separately. The importance of surface identification has resulted in the use of SMMR data here (25 km resolution), and the use of NOAA snow cover, USA Navy/NOAA sea ice data sets (1° lat-long grid) and land topography data in the ISCCP procedure. Statistical tests for the determination of cloud contamination here are based on probabilities of sample statistics coming from a population defined by previous analyses. In the ISCCP algorithm, average and extremum from radiance distributions are compared over short-term and long-term time periods. The difference between these methods is difficult to access because the initial classifications would produce different radiance distributions. There are other differences between the two algorithms; Rossow et al. [1988] provides greater detail on the ISCCP algorithm. However, the use of correlative data for surface identification and the use of temporal tests have been deemed crucial to both, and should be considered important components of a cloud

detection algorithm.

10. CONCLUSIONS

A cloud detection algorithm for use with Arctic AVHRR and SMMR data has been presented. Some of the design objectives for the International Satellite Cloud Climatology Project (ISCCP) cloud detection procedure such as space and time contrasts comprise basic thermal-only and visible/thermal algorithm versions, which are then modified for polar applications. All versions of the algorithm perform best over snow-free land and open water, so that improvement in computed cloud fraction using the modified algorithm will be greater over snow, ice cap, and sea ice and less over open water and snow-free land. In test cases, cloud fraction computed with the modified algorithm was found to be at least 5% more accurate when compared to manual interpretations.

For the data sets employed, the best method of cloud detection with Arctic AVHRR data includes first an accurate identification of surface types and changes. This allows thresholds to be set appropriately, and here is accomplished with SMMR passive microwave data. Next the temporal variability of pixel radiances is examined, using channels 1, 4, and the reflected component of channel 3 during summer and the difference between channels 3 and 4 in conjunction with channels 4 or 5 for winter analyses. Differences between thermal channels aid in the detection of thin cloud. Compositing over a 5-day period provides the clear sky information for the final multispectral thresholding of the daily data. The lack of 'ground truth' makes testing and validation difficult, a problem which can be alleviated to some extent with the use of synthetic data sets.

Acknowledgements. This work was supported under NASA grant NAG-5-898 and a DOD University Research Instrumentation Program grant N00014-85-C-0039. Thanks are due to W. Rossow and E. Raschke for providing AVHRR GAC data. We further thank the

reviewers for their suggestions and W. Rossow for his ideas on algorithm design and for valuable comments on an earlier version of this paper.

References

- Allen, R.C., P.A. Durkee, and C.H. Walsh, Snow and low cloud discrimination from multi-spectral satellite measurements, Third Conf. on Sat. Met. and Oceanog., American Meteorological Society, 383-387, 1988.
- Arking, A. and J.D. Childs, Retrieval of cloud cover parameters from multispectral satellite measurements, *J. Clim. Appl. Meteor.*, 24, 322-333, 1985.
- Barry, R.G., R.G. Crane, A. Schweiger, and J. Newell, Arctic cloudiness in spring from satellite imagery, *J. Climatol.*, 7, 423-451, 1987.
- Barry, R.G. A. Henderson-Sellers, and K.P. Shine, Climate sensitivity and the marginal cryosphere, in Climate Processes and Climate Sensitivity, J. Hansen and T. Takahashi (eds.), Geophys. Monog. 29, Amer. Geophys. Union, Washington, DC, pp. 221-337, 1984.
- Bolle, H.J., Assessment of thin cirrus and low cloud over snow by means of the maximum likelihood method. *Adv. Space Res.*, 5 (6), 169-175, 1985.
- Brown, O., J. Brown, and R. Evans, Calibration of Advanced Very High Resolution Radiometer infrared observations, *J. Geophys. Res.*, 90 (C6), 11667-11677, 1985.
- Budyko, M.I., The effect of solar radiation variations on the climate of the Earth, *Tellus*, 21, 611-619, 1969.
- Bunting, J.T. and R.F. Fournier, Tests of spectral cloud classification using DMSP fine mode satellite data, Air Force Geophysics Laboratory, AFGL-TR-80-0181, Environmental Research Papers No. 704, 42 pp., 1980.
- Cavalieri, D.J., Gloersen, P., and Campbell, W.J., Determination of sea ice parameters with Nimbus-7 SMMR, *J. Geophys. Res.*, 88, 5355-5369, 1984.
- Coakley, J.A., Jr., Properties of multi-layered cloud systems from satellite imagery, *J. Geophys. Res.*, 88, 818-828, 1983.
- Coakley, J.A., Jr., A dynamic threshold method for obtaining cloud cover from satellite

- imagery data, *J. Geophys. Res.*, 92 (D4), 3985-3990, 1987.
- Coakley, J.A., Jr. and D.G. Baldwin, Towards the objective analysis of clouds from satellite imagery data, *J. Clim. Appl. Meteor.*, 23, 1065-1099, 1984.
- Coakley, J.A., and F.P. Bretherton, Cloud cover from high-resolution scanner data: detecting and allowing for partially filled fields of view, *J. Geophys. Res.*, 87 (C7), 4917-4932, 1982.
- Colony, R. and E.A. Munoz, Arctic Ocean buoy program, data report, 1 January 1984 - 31 December 1985, Polar Science Center, University of Washington, 227 pp., 1986.
- Condal, A.R. and H.V. Le, Automated computer monitoring sea-ice temperature by use of NOAA satellite data, 8th Canadian Symposium on Remote Sensing, 136-150, 1984.
- Crane, R.G. and M.R. Anderson, Satellite discrimination of snow/cloud surfaces. *Int. J. Rem. Sens.*, 5, 213-223, 1984.
- Crane, R.G. and R.G. Barry, The influence of clouds on climate with a focus on high latitude interactions, *J. Climatol.*, 4, 71-93, 1984.
- d'Entremont, R.P., Low- and mid-level cloud analysis using nighttime multispectral imagery, *J. Clim. Appl. Meteor.*, 25, 1853-1869, 1986.
- D'Entremont, R.P. and L.W. Thomason, Interpreting meteorological satellite images using a color-composite technique. *Bull. Amer. Meteor. Soc.*, 68 (7), 762-768, 1987.
- Desbois, M. and G. Seze, Use of space and time sampling to produce representative satellite cloud classifications, *Annals Geophys.*, 2 (5), 599-606, 1984.
- Desbois, M., G. Seze, and G. Szejwach, Automatic classification of clouds on METEOSAT imagery: application to high level clouds, *J. Appl. Meteor.*, 21, 401-412, 1982.
- Dozier, J. and S.G. Warren, Effect of viewing angle on the infrared brightness temperature of snow, *Water Resources Res.*, 18(5), 1424-1434, 1982.
- Ebert, E., A pattern recognition technique for distinguishing surface and cloud types in the polar regions, *J. Clim. Appl. Meteor.*, 26, 1412-1427, 1987.

- Ebert, E., Analysis of polar clouds from satellite imagery using pattern recognition and a statistical cloud analysis scheme, *J. Appl. Meteor.*, 1989 (in press).
- Garand, L., Automated recognition of oceanic cloud patterns. Part I: methodology and application to cloud climatology, *J. Climate*, 1, 20-39, 1988.
- Gerstl, S.A.W. and C. Simmer, Radiation physics and modelling for off-nadir satellite sensing of non-Lambertian surfaces. LA-UR-85-4204, Los Alamos National Laboratory, 1985.
- Gloersen, P. and Cavalieri, D.J., Reduction of weather effects in the calculation of sea ice concentration from microwave radiances, *J. Geophys. Res.*, 91 (C3), 3913-3919, 1986.
- Gorshkov, S.G. (editor), World Ocean Atlas, Vol. 3, Arctic Ocean, Oxford: Pergamon Press, 1983.
- Grenfell, T.C. and G.A. Maykut, The optical properties of ice and snow in the Arctic basin, *J. Glaciol.*, 18, 445, 1977.
- Harris, R., and E.C. Barrett, Toward an objective neph- analysis, *J. Appl. Meteor.*, 17, 1258-1266, 1978.
- Hunt, G.E., Radiative properties of terrestrial clouds at visible and infra-red thermal window wavelengths, *Quart. J. Roy. Meteor. Soc.*, 99, 346-359, 1972.
- Inoue, Toshiro, A cloud type classification with NOAA 7 split-window measurements, *J. Geophys. Res.*, 92 (D4), 3991-4000, 1987a.
- Inoue, T., The clouds and NOAA-7 AVHRR split window, in WMO, 1987. Report of the ISCCP workshop on cloud algorithms in the polar regions, National Institute for Polar Research, WCP-131, WMO/TD-No. 170, Tokyo, Japan, 19-21 August 1986, 1987b.
- Key, J.R., J.A. Maslanik, and R.G. Barry, Cloud classification using a fuzzy sets algorithm: a polar example, *Int. J. Rem. Sens.*, 1989a (in press).

- Key, J., J.A. Maslanik, and A.J. Schweiger, Classification of merged AVHRR and SMMR data with neural networks, *Photogram. Eng. Rem. Sensing*, 1989b (in press).
- Lauritson, L., G.G. Nelson, and R.W. Port, Data extraction and calibration of TIROS-N/NOAA A-G radiometer, NOAA Tech. Memor., NESS 107, Natl. Oceanic and Atmos. Admin., Boulder, 1979.
- Maslanik, J.A., Key, J.R., and Barry, R.G. Merging AVHRR and SMMR data for remote sensing of ice and cloud in the polar region. *Int. J. Rem. Sens.*, 1989 (in press).
- McGuffie, K. and D.A. Robinson, Examination of USAF Nephanalysis performance in the marginal cryosphere region. *J. Climate*, 1 (11), 1124-1137, 1988.
- Minnis, P., E.F. Harrison, and G.G. Gibson, Cloud cover over the equatorial Eastern Pacific derived from July 1983 International Satellite Cloud Climatology Project data using a hybrid bispectral threshold method, *J. Geophys. Res.*, 92 (D4), 4051-4073, 1987.
- Minnis, P. and E.F. Harrison, Diurnal variability of regional cloud and clear sky radiative parameters derived from GOES data. Part I: analysis method, *J. Clim. Appl. Meteor.*, 23, 993-1011, 1984.
- NOAA, NOAA polar orbiter data user's guide. U.S. Department of Commerce, National Oceanic and Atmospheric Administration, NESDIS, February, 1984.
- Olesen, F. and H. Grassl, Cloud detection and classification over oceans at night with NOAA-7, *Int. J. Rem. Sens.*, 6 (8), 1435-1444, 1985.
- Pairman, D. and J. Kittler, Clustering algorithms for use with images of clouds, *Int. J. Rem. Sens.*, 7 (7), 855-866, 1986.
- Parikh, J.A., A comparative study of cloud classification techniques, *Rem. Sens. Environ.*, 6, 67-81, 1977.
- Polar Research Board, The Polar Regions and Climatic Change. National Research Council, National Academy Press, Washington, D.C., 59 pp., 1984.
- Raschke, E., Cloud analysis of AVHRR data measured over polar regions, in WMO, 1987.

- Report of the ISCCP workshop on cloud algorithms in the polar regions, National Institute for Polar Research, WCP-131, WMO/TD-No. 170, Tokyo, Japan, 19-21 August 1986, 1987.
- Robock, A. and D. Kaiser, Satellite-observed reflectance of snow and clouds, *Mon. Wea. Rev.*, 113(11), 2023-2029, 1985.
- Rossow, W.B., Measuring cloud properties from space: a review, *J. Climate*, 2, 201-213, 1989.
- Rossow, W.B., F. Mosher, E. Kinsella, A. Arking, M. Desbois, E. Harrison, P. Minnis, E. Ruprecht, G. Seze, C. Simmer, and E. Smith, ISCCP cloud algorithm intercomparison, *J. Clim. Appl. Meteor.*, 24, 877-903, 1985.
- Rossow, W.B., L.C. Garder, P-J Lu, and A. Walker, The International Satellite Cloud Climatology Project documentation of cloud data, WMO TD266, December 1988.
- Rossow, W.B., C.L. Brest, and L.C. Garder, Global, seasonal surface variations from satellite radiance measurements, *J. Climate*, 2, 214-247, 1989a.
- Rossow, W.B., L.C. Garder, and A.A. Lacis, Global, seasonal cloud variations from satellite radiance measurements. Part I: sensitivity of analysis, *J. Climate*, 2, 419-458, 1989b.
- Saltzman, B. and R.E. Moritz, A time-dependent climatic feedback system involving sea-ice extent, ocean temperature, and CO₂, *Tellus*, 32, 93-118, 1980.
- Saunders, R.W., An automated scheme for the removal of cloud contamination from AVHRR radiances over western Europe. *Int. J. Rem. Sens.*, 7 (7), 867-886, 1986.
- Saunders, R.W. and K.T. Kriebel, An improved method for detecting clear sky and cloudy radiances from AVHRR data, *Int. J. Rem. Sens.*, 9, 123-150, 1987.
- Scharfen, G., R.G. Barry, D.A. Robinson, G. Kukla, and M.C. Serreze, Large-scale patterns of snow melt on arctic sea ice mapped from meteorological satellite imagery, *Annals Glaciol.*, 9, 1-6, 1987.

- Schwalb, A., The TIROS-N/NOAA A-G satellite series, NOAA Tech. Mem., NESS 95, 1978.
- Serreze, M.S. and R.G. Barry, Synoptic activity in the Arctic Basin, 1979-85, *J. Climate*, 1, 1276-1295, 1988.
- Shenk, W.E., R.J. Holub, and R.A. Neff, A multispectral cloud type identification method developed for tropical ocean areas with Nimbus-3 MIRR measurements, *Mon. Wea. Rev.*, 104, 284, 1976.
- Shenk, W.E. and R.J. Curran, A multi-spectral method of estimating cirrus cloud top heights, *J. Appl. Meteor.*, 12, 1213, 1973.
- Shine, K.P. and R.G. Crane, The sensitivity of a one dimensional thermodynamic sea ice model to changes of cloudiness, *J. Geophys. Res.*, 89 (C6), 10, 615-622, 1984.
- Steffen, K., Bidirectional reflectance of snow at 500-600 nm, **Large Scale Effects of Seasonal Snow Cover** (Proceedings of the Vancouver Symposium, August 1987). IAHS Publ. no. 166, 415-425, 1987.
- Susskind, J., D. Reuter, and M.T. Chahine, Cloud fields retrieved from analysis of HIRS2/MSU sounding data, *J. Geophys. Res.*, 92 (D4), 4035-4050, 1987.
- Taylor, R.V. and L.L. Stowe, Reflectance characteristics of uniform earth and cloud surfaces derived from Nimbus-7 ERB, *J. Geophys. Res.*, 89 (D4), 4978-4996, 1984.
- Welch, R.M., S.K. Sengupta, and D.W. Chen, Cloud field classification based upon high spatial resolution textural features 1. gray level co-occurrence matrix approach, *J. Geophys. Res.*, 93 (D10), 12663-12681, 1988.
- WMO, Report of the ISCCP workshop on cloud algorithms in the polar regions, World Climate Research Programme, WCP-131, WMO/TD-No. 170, Tokyo, Japan, 19-21 August 1986, 1987.
- WMO, Report of the third session of the working group on sea ice and climate, WCRP-18, WMO/TD-No. 272, Oslo, Norway, 31 May - 3 June, 1988.

Figures

Figure 1. The three study areas within the Arctic, one centered on the Kara and Barents Sea and the other two covering much of the Canadian Archipelago and northern Greenland.

Figure 2. AVHRR channel 1 (visible) images showing a portion of each summer study area (July 3, 1984; top and middle) and an AVHRR channel 4 (thermal) image of the winter study area (January 8, 1984; bottom). In study area 1 (top), Novaya Zemlya is top center though largely obscured by cloud, Spitsbergen is lower left, and the North Pole is just off the lower left of the image. Sea ice occupies the left third of the image. Study area 2 (middle) is centered on Baffin Bay. Sea ice can be seen extending southward to the coast of Greenland. Study area 3 (bottom) is centered on northern Greenland. In this thermal image, lower temperatures are represented by darker grey shades, for example, low surface temperatures over central Greenland and portions of the Canadian Archipelago. See also Figure 1.

Figure 3. Flow chart of a) the basic cloud detection algorithm and b) the algorithm modified for use in polar regions. Input are shown on the left; additional details are given on the right.

Figure 4. Five-day clear sky composite values from the modified algorithm for a sample of pixel locations plotted against AVHRR measured values for the same locations under cloudy conditions. Channels 1 (top), 3 (middle), and 4 (bottom) are shown. The line in each plot represents equal clear sky composite and measured values.

Figure 5. Surface albedos (AVHRR channel 1) in study areas 1 and 2 for the compositing period July 2-6, 1984, in tenths.

Figure 6. Sea ice albedoes for the period July 3-5, 1984, in tenths. After Scharfen et al. (1987).

Figure 7. Surface temperatures (AVHRR channel 4) for the compositing periods, July 2-6, 1984 (top and middle) and January 7-11, 1984 (bottom), degrees Kelvin, for all three study areas.

Figure 8. Surface temperatures in Kelvins from the European Centre for Medium Range Forecasting (ECMWF); July 4, 1984 and January 9, 1984.

Figure 9. Cloud fraction for each study area on July 3, 1984 and January 8, 1984, in tenths.

Table 1

Truth table for the initial classification of a pixel based on the results of the spatial and temporal variation tests.

Spatial Variation	Temporal Variation		
	Cloud	Undecided	Clear
Cloud	Cloud	Cloud	Mixed
Undecided	Cloud	Undecided	Clear

Table 2

Temporal thresholds by surface type. A pixel is compared to the same location on the day before and the day after. Channel 1 values are percent albedo; channels 3 and 4 are Kelvins.

	LAND	OCEAN	ICE	SNOW

CLOUD if greater				
Channel 4	8.0	3.5	5.0	7.0
CLEAR if within				
Channel 1	4.4	1.4	8.8	3.8
Channel 3	4.0	3.5	3.5	3.5
Channel 4	2.5	1.1	2.0	2.0

Table 3

Final Thresholds for the three AVHRR channels. Channel 1 values are percent albedo; channels 3 and 4 are Kelvins.

Channel	LAND	OCEAN	ICE	SNOW
1	6.0	3.5	6.0	4.0
3	6.0	6.0	5.0	5.0
4	8.0	3.0	4.0	4.0

Table 5

"Actual" cloud fraction for synthetic data and cloud fraction computed by the three versions of the cloud detection algorithm. Values are for each of the middle five days of an analysis period. The number of clear pixels in the compositing step is also shown.

Region:		Algorithm Version			
day		Actual	Basic-VT	Basic-T	Modified
1:	2	71	76	76	78
	3	73	80	80	75
	4	99	100	98	100
	5	87	90	90	90
	6	99	100	98	100
# clear:		--	643	643	125
2:	2	87	93	92	94
	3	80	97	97	82
	4	58	83	80	77
	5	95	100	100	95
	6	99	100	98	100
# clear:		--	219	219	71
3:	2	33	82	78	83
	3	68	94	91	94
	4	100	100	94	100
	5	100	100	100	100
	6	61	96	90	97
# clear:		--	415	415	425
4:	2	52	90	76	58
	3	99	99	98	99
	4	40	79	66	54
	5	81	98	95	81
	6	83	96	88	92
# clear:		--	420	420	32

Table 6

Cloud fraction for actual (AVHRR) data as computed by manual interpretation and three versions of the ISCCP algorithm.

Region:		Algorithm Version			
day		Manual	Basic-VT	Basic-T	Modified

1:	2	3	56	2	1
	3	90	99	78	79
	4	21	70	12	10
	5	46	90	65	55
	6	95	99	89	85
# clear:	--		2404	2404	2264
2:	2	99	99	99	100
	3	96	97	81	98
	4	98	94	75	96
	5	99	100	99	100
	6	98	92	73	98
# clear:	--		159	159	9
3:	2	80	83	75	85
	3	60	62	55	61
	4	80	83	73	80
	5	23	31	18	29
	6	75	77	72	77
# clear:	--		1509	1509	972
4:	2	97	100	99	100
	3	97	99	63	98
	4	81	95	46	85
	5	60	76	51	75
	6	90	95	80	92
# clear:	--		1031	1031	362

Table 7

Root mean square error in cloud fraction computed by each algorithm version for the manually interpreted amount in the AVHRR data and the "actual" amount in the synthetic data (Tables 5 and 6). Mean absolute difference is also given (in parentheses).

Data Set	Algorithm Version		
	Basic-VT	Basic-T	Modified
AVHRR	19.8 (11.5)	15.3 (11.3)	6.2 (4.4)
Synthetic	21.0 (14.4)	17.0 (12.0)	16.3 (9.2)

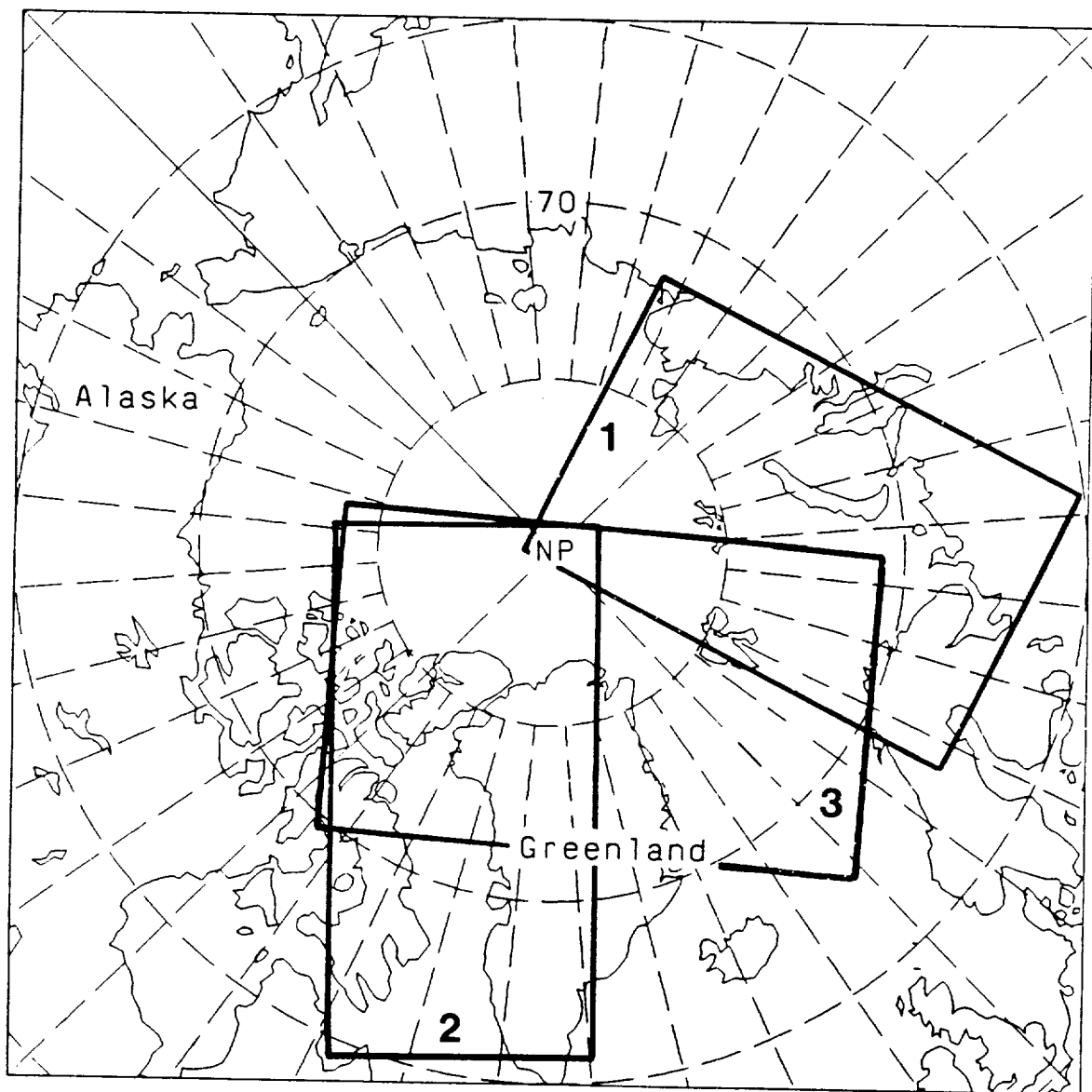
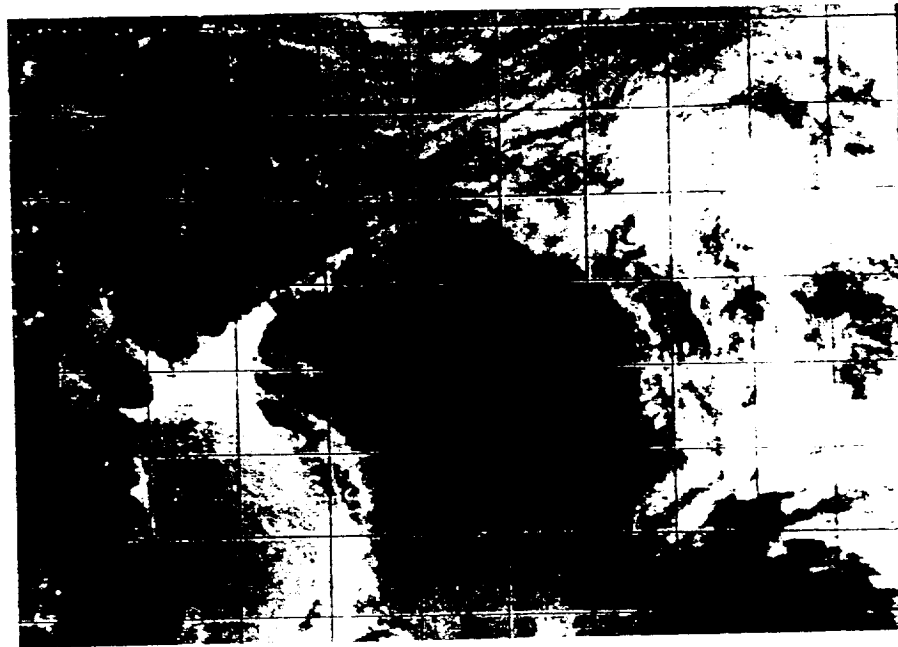
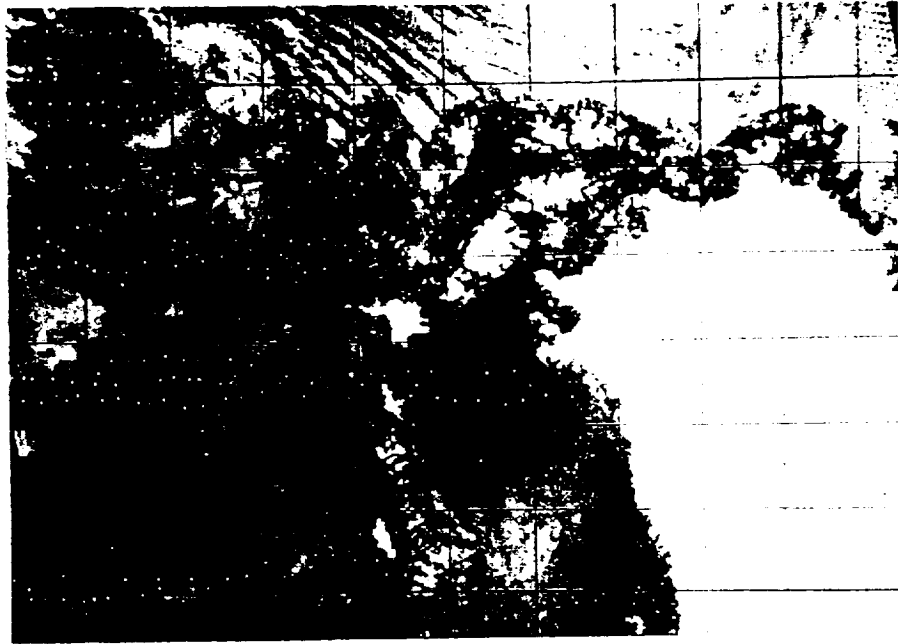
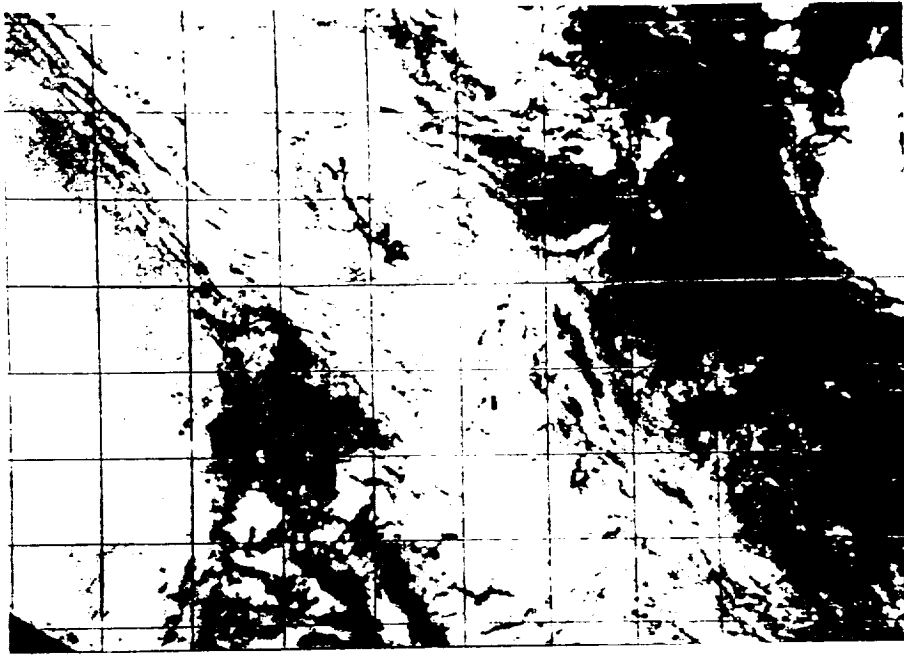


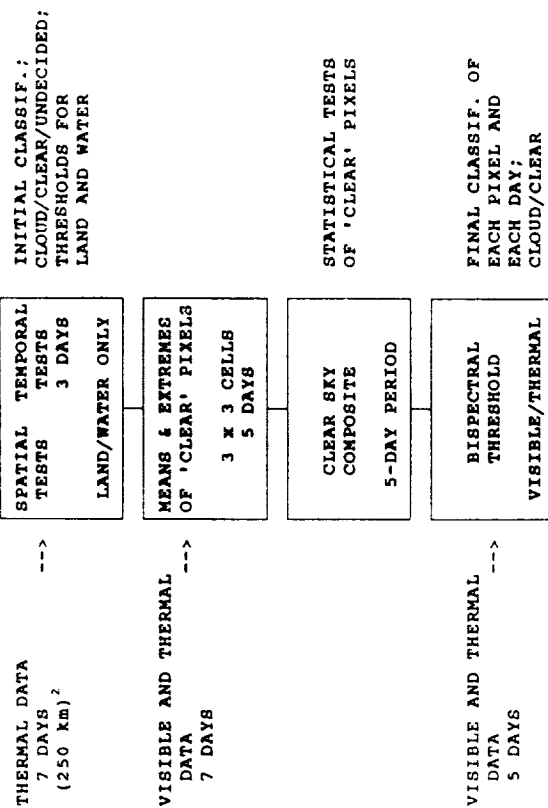
Fig. 1

ORIGINAL PAGE
BLACK AND WHITE PHOTOGRAPH



a)

BASIC CLOUD DETECTION ALGORITHM



b)

MODIFIED POLAR CLOUD DETECTION ALGORITHM

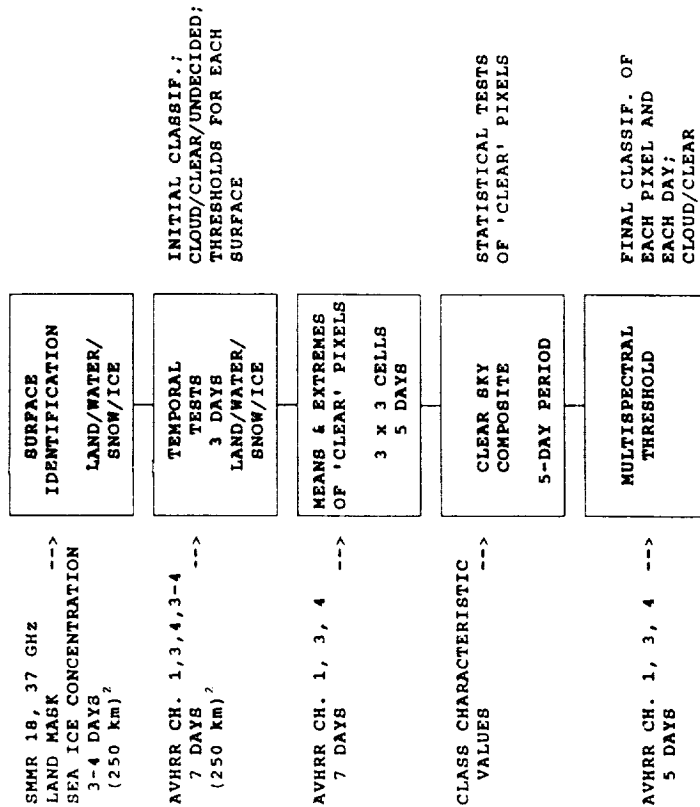
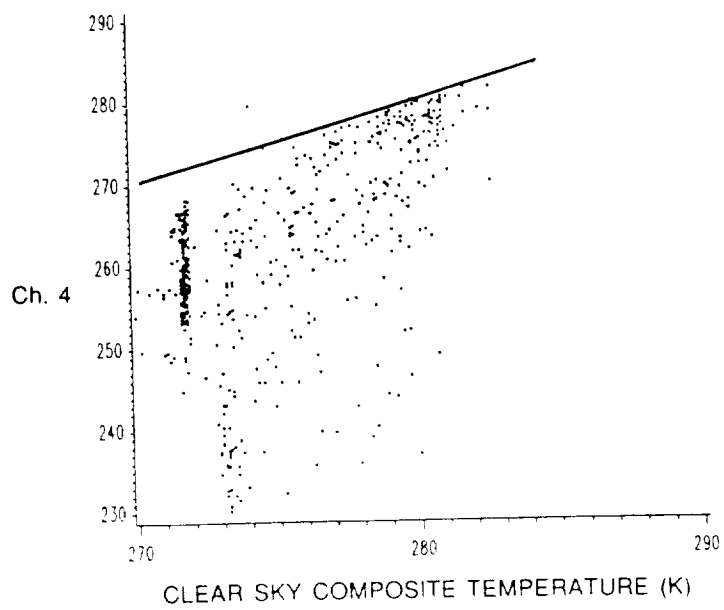
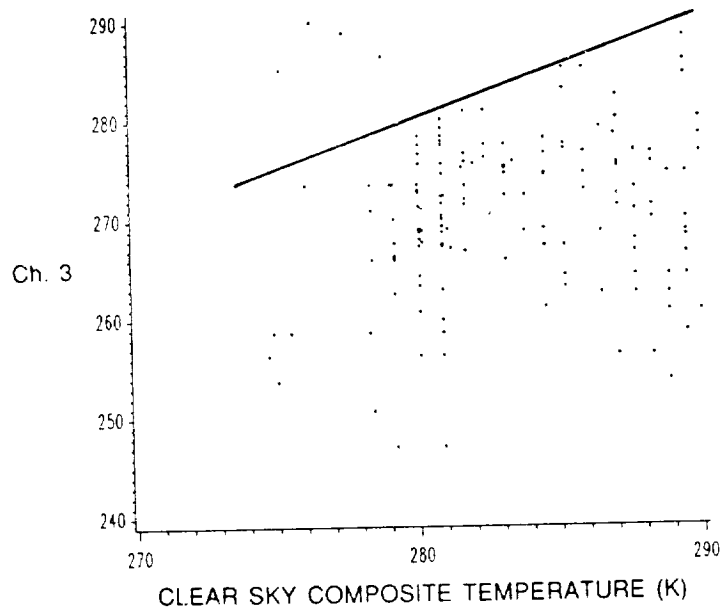
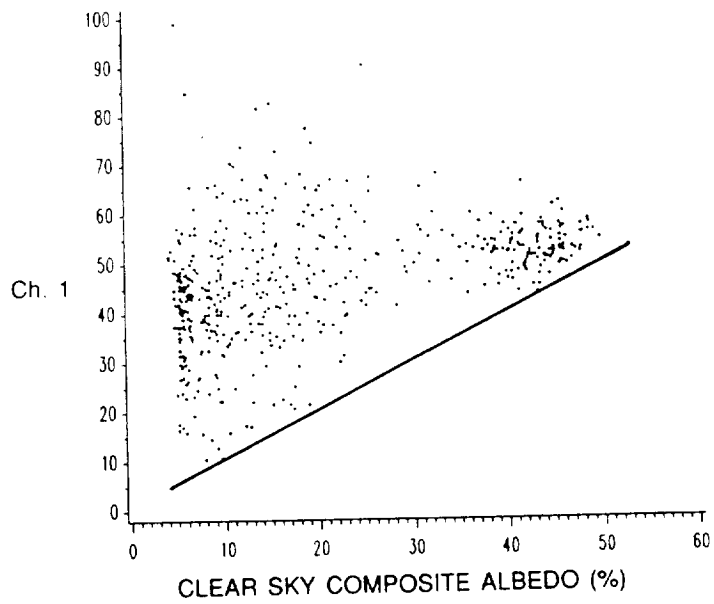
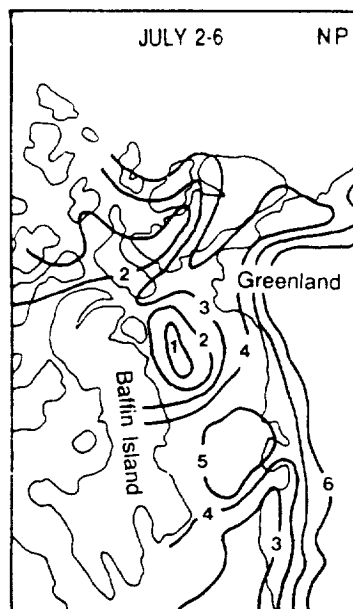
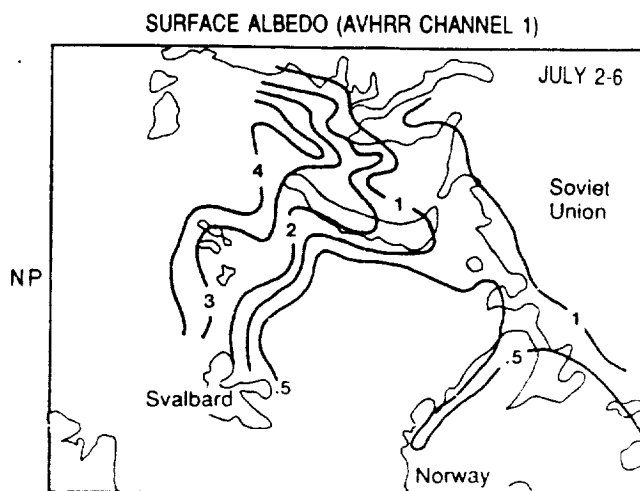
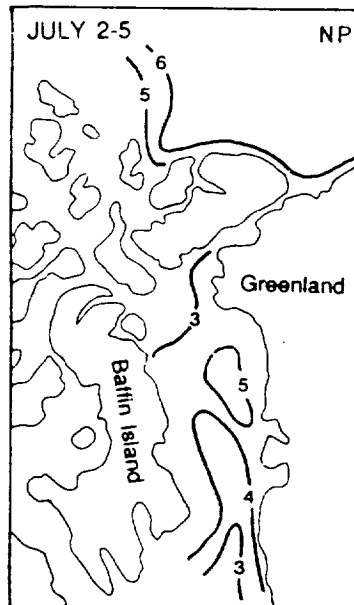
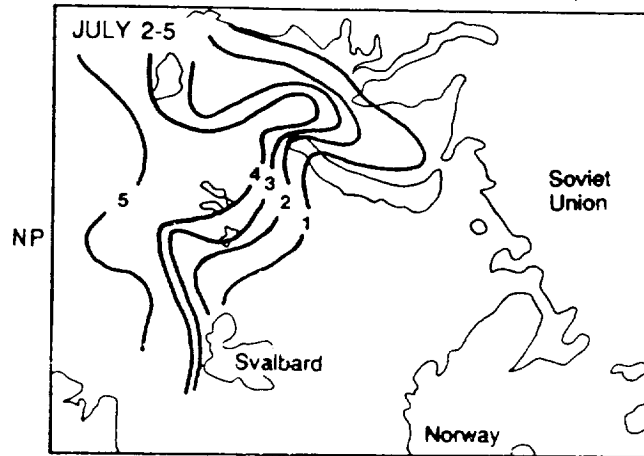


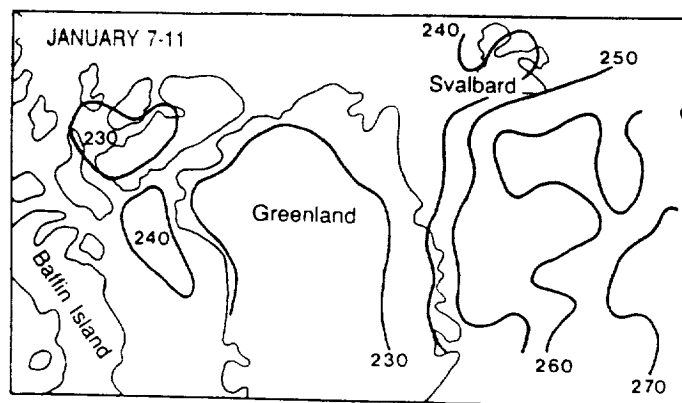
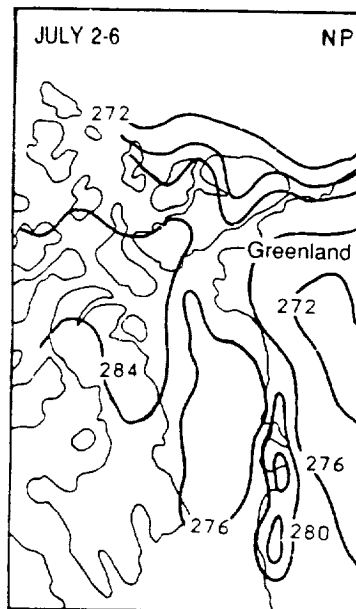
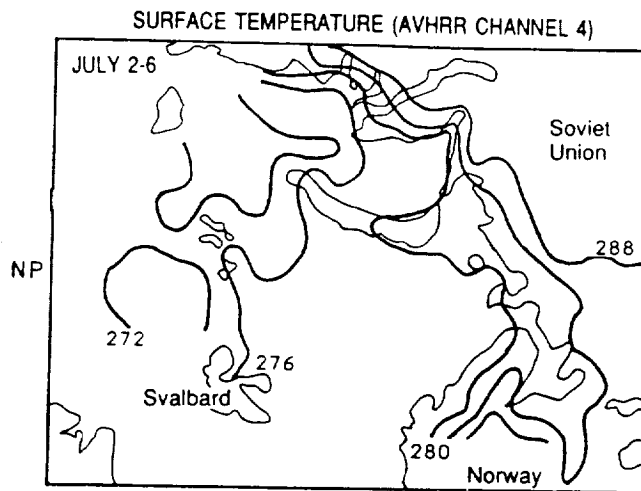
Fig 3



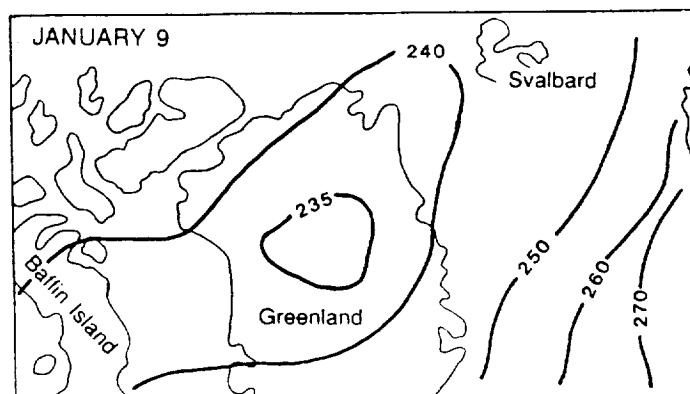
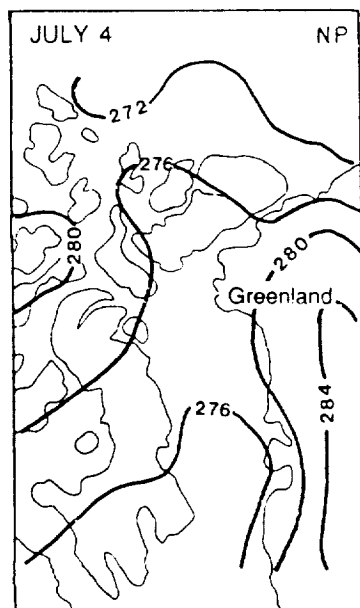
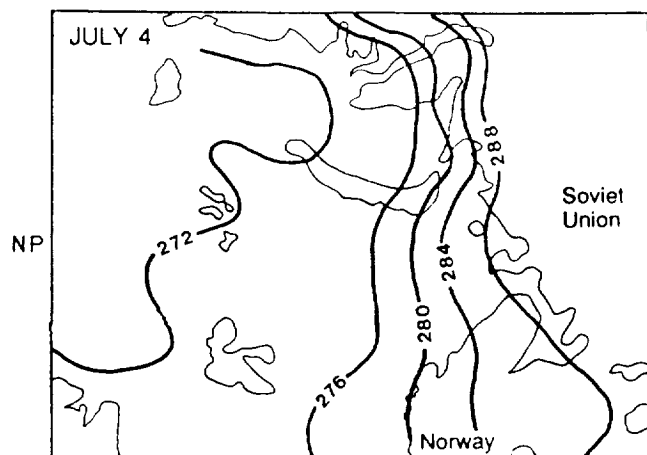


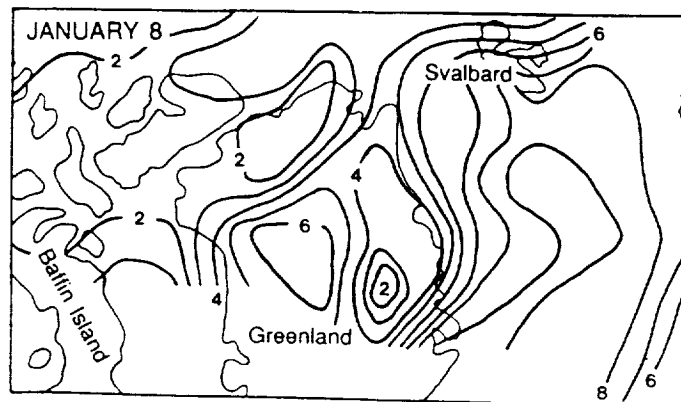
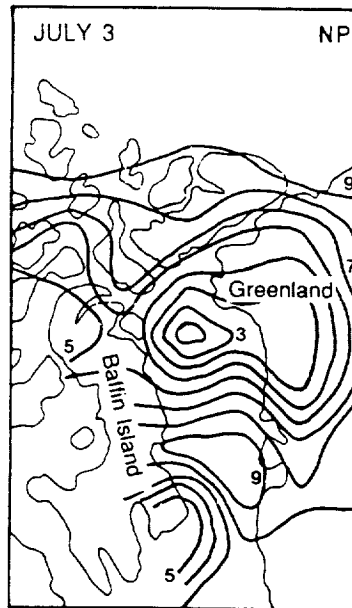
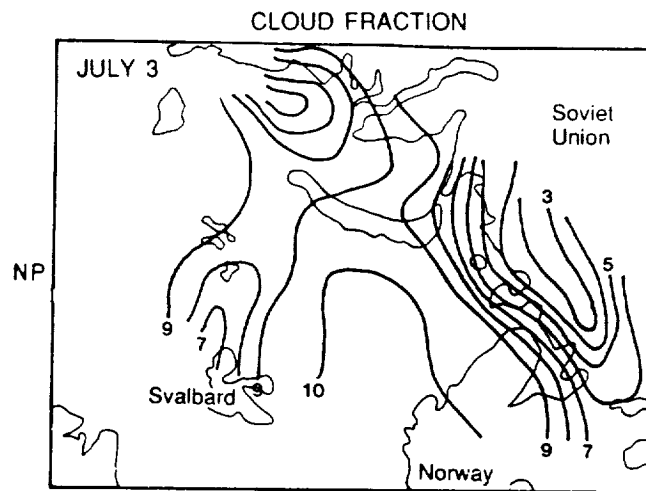
SEA ICE ALBEDO (DMSP,NOAA/NAVY)



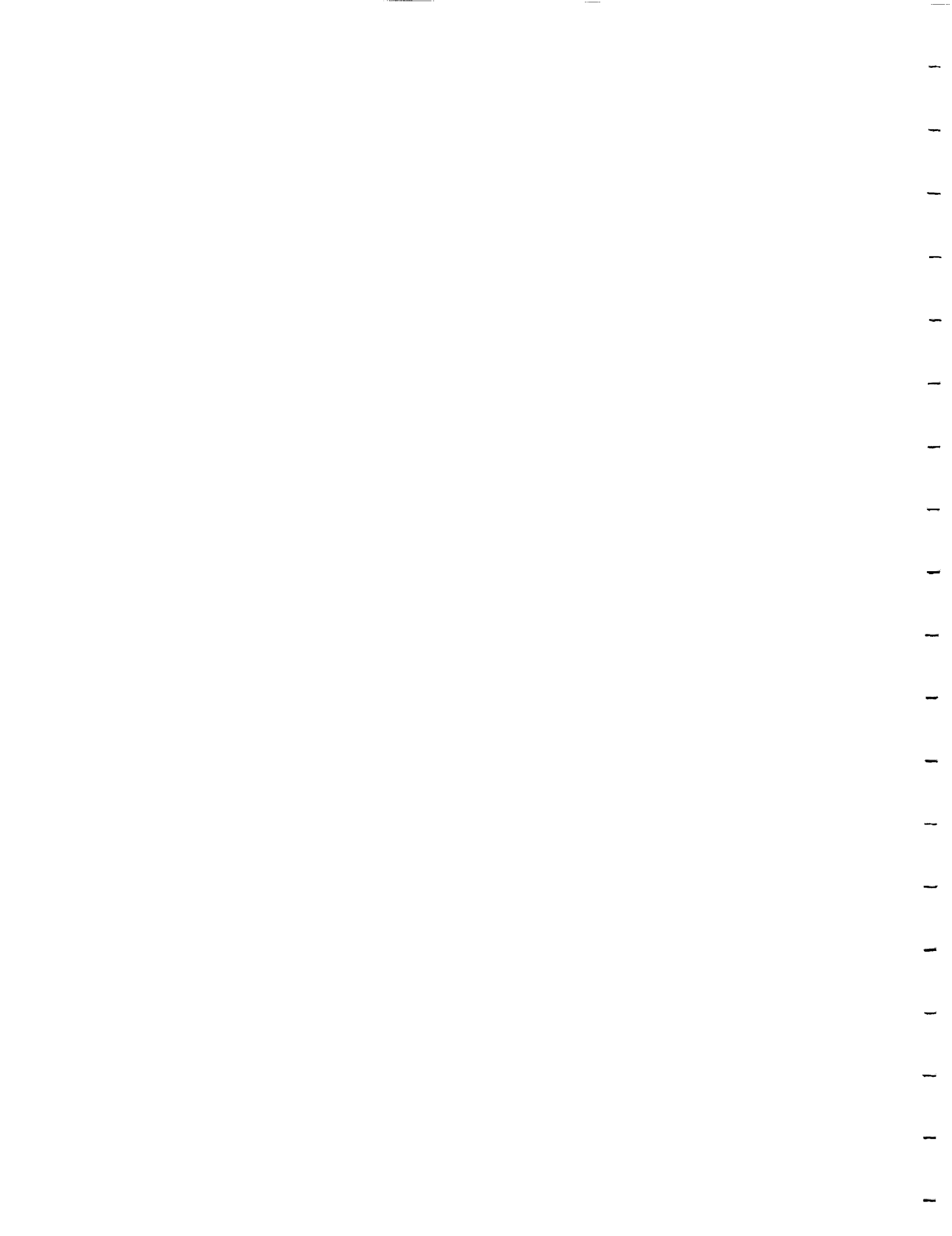


ECMWF 1000 MB TEMPERATURE





ATTACHMENT 5
ADAPTATION OF THE ISCCP CLOUD DETECTION ALGORITHM



ADAPTATION OF THE ISCCP CLOUD DETECTION ALGORITHM
TO COMBINED AVHRR AND SMMR ARCTIC DATA

J. Key and R.G. Barry

Cooperative Institute for Research in Environmental Sciences
University of Colorado, Boulder
Boulder CO 80309-0449 USA

ABSTRACT

Cloud cover and surface temperatures in the polar regions are important indicators of global climate change, however, automated analyses of satellite radiance data have concentrated on low and middle latitude situations. The International Satellite Cloud Climatology Project (ISCCP) cloud detection algorithm is applied to Arctic data, and modifications are suggested. Both Advanced Very High Resolution Radiometer (AVHRR) and Scanning Multichannel Microwave Radiometer (SMMR) data are examined. Synthetic AVHRR and SMMR data are also generated. Modifications suggested include the use of snow and ice data sets for the estimation of surface parameters, additional AVHRR channels, and surface class characteristic values when clear sky values cannot be obtained. Greatest improvement in computed cloud fraction is realized over snow and ice surfaces; over other surfaces all versions perform similarly. Since the inclusion of SMMR for surface analysis increases the computational burden, its use may be justified only over snow and ice-covered regions.

Keywords: ISCCP, AVHRR, Arctic clouds.

INTRODUCTION

The important role that polar processes play in the dynamics of global climate is widely recognized (Polar Research Group, 1984). The variation of cloud amounts over polar ice sheets, sea ice, and ocean surfaces can have important effects on planetary albedo gradients and on surface energy exchanges (Barry et al., 1984). Cloud cover exerts a major influence over the amount of solar and longwave radiation reaching the surface, and is linked to the sea ice through a series of radiative, dynamical, thermodynamic and hydrological feedback processes (Saltzman and Moritz, 1980). Extent and thickness of sea ice influences oceanic heat loss and surface albedo which thereby influences global climate via the ice-albedo feedback (Budyko, 1969).

Current procedures for automated analyses of satellite radiance data have been developed for low and middle latitudes but their application to polar regions has been largely unexplored. These methods are reviewed in Key (1988), Rossow (1989), and Key et al. (1989). Those that have been applied to polar data often fail in the polar regions because snow-covered surfaces are often as reflective as the clouds and the thermal structure of the troposphere is characterized by frequent isothermal and inversion layers. Additionally, the polar darkness during winter makes that data collected in the

visible portion of the spectrum largely unusable. A complex analysis method that can recognize and cope with these situations is therefore necessary (WMO, 1987).

The purpose of this study is to implement, test, and modify the basic International Satellite Cloud Climatology Project (ISCCP) algorithm for use with polar data. The International Satellite Cloud Climatology Project (ISCCP) to map clouds with satellite data began in July 1983. Its goal is to provide a uniform global climatology of satellite-measured radiances and from these to derive an experimental climatology of cloud radiative properties. As a basis for developing the ISCCP algorithm, Rossow et al. (1985) compared six cloud algorithms. The current state of the project is such that there is no single version of the algorithm which can be applied to all areas of the globe. The algorithm is currently operational globally, but performs rather poorly at high latitudes (Rossow, 1987), where it was found that the method in general detected too much cloudiness, in part because it does not distinguish between open water/sea ice and snow-covered/snow-free land, and because thresholds were not "tuned" for the small temperature differences and generally low IR radiances common in the polar regions.

DATA

The Advanced Very High Resolution Radiometer (AVHRR) on board the NOAA-7 polar orbiting satellite measures radiance in five channels encompassing the visible, infrared, and thermal portions of the electromagnetic spectrum (1: 0.58-0.68 μ m, 2: 0.73-1.0 μ m, 3: 3.55-3.93 μ m, 4: 10.3-11.3 μ m, 5: 11.5-12.5 μ m) with a nadir resolution of 1.1 km. Global Area Coverage (GAC) imagery is a reduced-resolution product created through on-board satellite processing, with each pixel representing a 3 x 5 km field of view. Channels 1 and 2 were converted to approximate spectral albedo and corrected for solar zenith angle; channels 3, 4, and 5 were converted to brightness temperature (NOAA, 1984). The typically low water vapor content in the polar atmosphere and the low physical temperatures reduce most atmospheric effects to a point where they may be neglected for these analyses.

The Nimbus-7 Scanning Multichannel Microwave Radiometer (SMMR) senses emitted microwave radiation in five channels: 6.6, 10.7, 18.0, 21.0, and 37.0 GHz, with two polarizations (horizontal and vertical) per channel. At these frequencies, passive microwave data is relatively unaffected by clouds and provides useful data year-round independent of solar illumination. The 18 and 37 GHz vertical polarization channels are employed here for surface parameterization, with

fields of view of 55x41 km and 27x18 km, respectively.

In order to study both clouds and surfaces beneath clouds, it is worthwhile to combine the AVHRR and SMMR data into a single image set. These are merged in digital form and mapped to a polar stereographic projection. This projection yields equal-area pixels true at 70° latitude with a five kilometer pixel size. SMMR data were converted to the five kilometer cells by duplication of pixels. Further details are given in Maslanik et al. (1988).

Three areas of the Arctic are examined (Figure 1); a seven-day summer series (July 1-7, 1984) of areas 1 and 2, and a winter series (January 6-12, 1984) of area 3. These data are part of an ISCCP test data set and include representative samples of all surface types found in the Arctic: snow-covered and snow-free land, sea ice of varying concentrations, open water, and permanent ice cap.

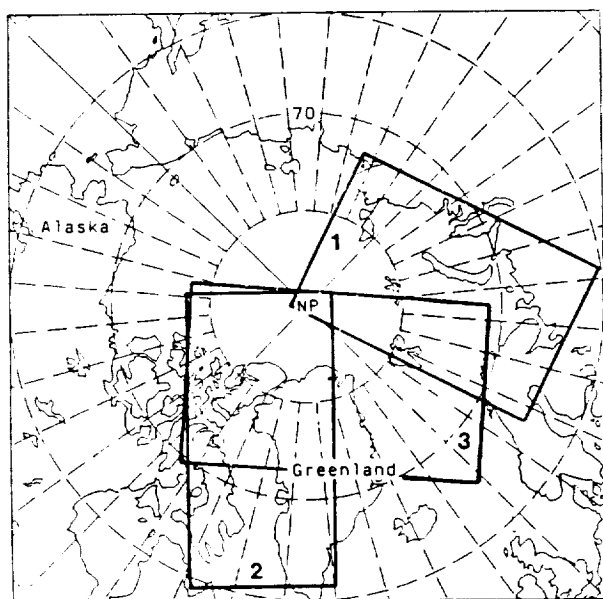


Figure 1. The three study areas within the Arctic, one centered on the Kara and Barents Sea and the other two covering much of the Canadian Archipelago and northern Greenland.

Ancillary data include surface temperatures from the European Centre for Medium Range Forecasting (ECMWF) and sea ice albedo derived from a combination of DMSP imagery and the NOAA/Navy ice charts.

Spectral features examined are AVHRR channels 1, 2, and 3 albedos, channels 3, 4, and 5 brightness temperatures, and the differences between channels 3 and 4 and 4 and 5. Four surface and three cloud classes are analyzed. Surface types are snow-free land, snow-covered land, open water, and medium to high concentration sea ice. Cloud classes are low, middle, and high as defined by brightness temperature in AVHRR channel 4, assumed to represent temperatures at the top of optically thick cloud layers.

In order to test the sensitivity of the various cloud algorithms, a control data set with known characteristics was needed. A synthetic data set was developed which consists of seven days of AVHRR and SMMR data, SMMR-derived sea ice concentrations, and a land mask. The surface and cloud type maps for each day of the seven day period are first generated, where the minimum and maximum allowable sizes of surface and cloud "objects" are specified. Object

dimensions are randomly chosen within the restricted range, and the class of the object is randomly assigned. Regions are then filled with normally-distributed data for each AVHRR and SMMR channel and for sea ice concentration using empirically-derived statistics.

THE ISCCP ALGORITHM

The ISCCP cloud algorithm has three major components: cloud detection, radiative analysis, and statistical analysis (Rossow et al., 1985). Of concern here is the cloud detection step. The algorithm assumptions are that cloud scene radiances are more variable in time and space than clear scene radiances and cloudy scenes are associated with larger visible channel and smaller infrared radiances than clear scenes. The major steps of the basic algorithm are summarized in Figure 2a and include a spatial variation test for the warmest pixel in a subregion (assumed clear), a temporal variation test, five-day clear sky compositing (requiring seven days of data), and a final bispectral threshold test of each pixel on each day based on clear sky composite values. Although this algorithm is undergoing constant change, the basic steps described here remain valid.

The algorithm has been adjusted here in order to deal with the problems cited earlier. Major modifications suggested include the use of snow and ice data sets for the estimation of surface parameters, elimination of the spatial test for the warmest pixel, the use of AVHRR channels 1 (0.7 μ m), 3 (3.7 μ m), and 4 (11 μ m) in the temporal tests, statistical tests for compositing, and the final multispectral thresholding, and the use of surface class characteristic values when clear sky values cannot be obtained. Additionally, the difference between channels 3 and 4 is included in temporal tests for the detection of optically thin low cloud and cirrus. The major steps of the modified algorithm are shown in Figure 2b.

TESTING AND ALGORITHM COMPARISON

Three versions of the ISCCP algorithm are compared. The original algorithm developed for low latitude summer conditions recognizes only two surface types: land and water. No SMMR or sea ice concentration data are employed. Spatial/temporal tests in the initial classification step are thermal only (AVHRR channel 4), and a bispectral threshold test (channels 1 and 4) is used as the final classification. This version with a thermal-only threshold test was also used to simulate winter applications. The algorithm with modifications described in the previous section is the third version tested. Four regions from the AVHRR imagery and four regions from the synthetic data sets are used as test data. Each region is 50x50 pixels or (250km)² and differs in surface and cloud types and proportions. Surface proportions changed in both data sets over the analysis period by up to 20%. These changes are due to sea ice movement and melting.

All versions of the algorithm perform best over land and open water. Snow and ice remain the problem areas although the modified versions performed best under these conditions. When cloud amounts are high (more than 80%), all versions compute cloud fraction to within approximately 5%. When cloud amounts are low, the modified version is more accurate, although cloud fraction often appeared to be too high. In the actual data, this is at least in part due to errors in the manual interpretation. In the synthetic data, this is probably due to the fact that clear sky areas are filled with values in the range of the mean plus or minus three standard deviations (following a Gaussian probability function), so that extreme values may be beyond threshold cutoffs and will consequently be labeled as cloud.

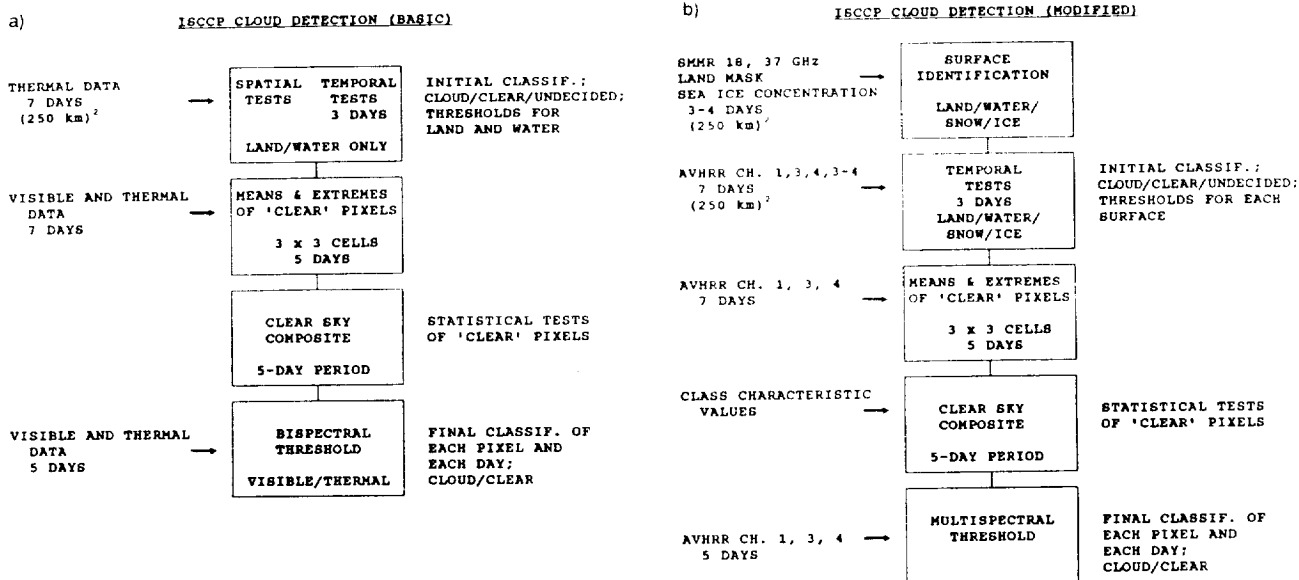


Figure 2. Flow chart of (a) the basic ISCCP cloud detection algorithm and (b) the algorithm modified for use with Arctic data. Input are shown on the left; additional details are given on the right.

The basic versions of the algorithm often overestimate cloud amount by up to 20%. This is common over ice where, in the bispectral threshold test, the threshold for water is used. This albedo threshold is too small to account for variation in sea ice albedos, and consequently many clear pixels were mistaken as cloud. Similar observations were made by Rossow (1987). A related situation is that the basic version often makes an accurate assessment of cloud fraction, but for the wrong reason. For example, one sea ice region was covered by a very thin cloud layer. Channels 1 and 4 alone did not detect this condition, yet the cloud amount determined by the original algorithm version is similar to the manually-interpreted amount. It appears that the algorithm is labeling cloud what it sees in channel 1 as sea ice. The snow and ice data sets used in the modified versions solve these problems by providing appropriate thresholds.

Root mean square (RMS) errors illustrate that the modified version was most accurate in computing cloud fraction for both data sets. The thermal-only version performed reasonably well with the synthetic data set, at least in part for reasons explained above.

APPLICATION

The modified version of the algorithm is next applied to the Arctic study areas. Surface albedos determined over the five-day compositing period for the two summer study areas, which overlap the winter area, are shown in Figure 3. Values are averages over each quarter region. Sea ice albedo derived from DMSP imagery and NOAA/NAVY ice charts is in general agreement for sea ice. Composited surface temperatures are shown in Figure 4 for AVHRR channel 4. Since surface emissivities in channel 4 (11 μ m) are near unity, the temperatures presented are considered to be close estimates of physical temperatures. These are in close agreement with the ECMWF data.

Cloud fraction for the middle five days of the period was also computed with the modified ISCCP algorithm (not shown), and is similar to the mean cloud amount for each month. Cloud amount tends to be lowest over northern

Greenland and the Canadian Archipelago, and highest over the Greenland Sea.

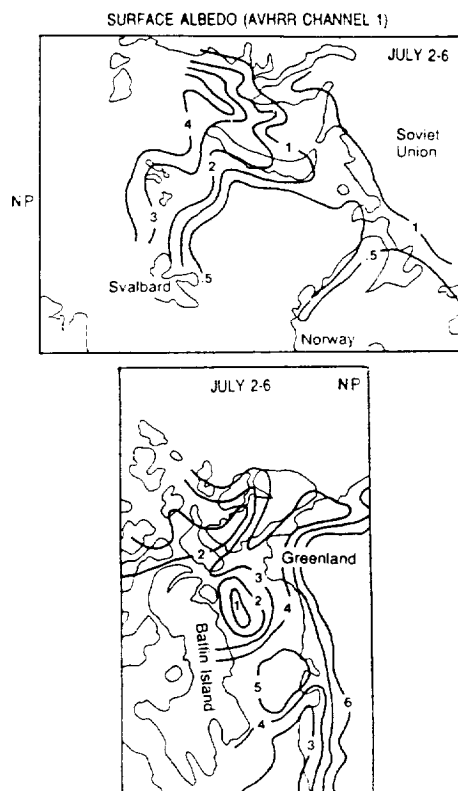


Figure 3. Surface albedos (AVHRR channel 1) in study areas 1 and 2 for the compositing period July 2-6, 1984, in tenths.

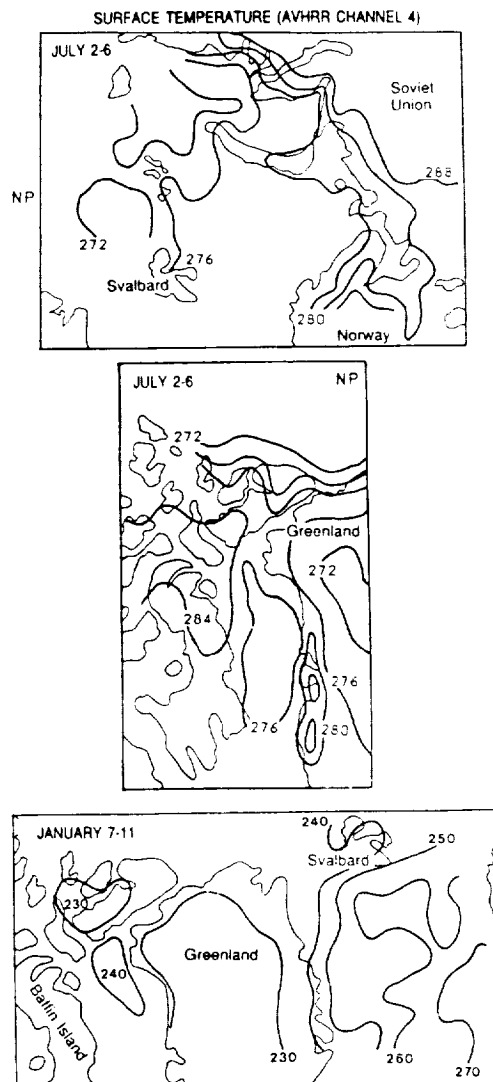


Figure 4. Surface temperatures (AVHRR channel 4) for the compositing periods, July 2-6, 1984 (top and middle) and January 7-11, 1984 (bottom), Kelvins, for all three study areas.

CONCLUSIONS

The cloud detection step of the International Satellite Cloud Climatology Project algorithm has been adapted for use with Arctic AVHRR and SMMR data. Based on test data for summer conditions in the Arctic, the modified algorithm is expected to yield an average improvement of 5-10% in computed cloud amount over the original version, depending on surface type and cloud proportions. All versions of the algorithm perform best over snow-free land and open water, so that improvement will be greater than this figure over snow, ice cap, and sea ice, but less over open water and snow-free land. Synthetic data sets have proven useful in testing and validation.

The best method of cloud detection with Arctic AVHRR data includes first an accurate identification of surface types and changes. This allows thresholds to be set appropriately. Passive microwave data is useful in this step.

Next the temporal variability of pixel radiances must be examined, using AVHRR channels 1, 4, and the reflected component of channel 3 during summer and the difference between channels 3 and 4 in conjunction with channels 4 or 5 for winter analyses. Temporal changes are most important in winter when surfaces may be colder than cloud layers and spectral information alone is inadequate. Compositing over a 5-day period, using 30-day values where necessary, provides the clear sky information for the multispectral thresholding of the daily data. This method provides a basis for future cloud detection algorithms for the polar regions.

ACKNOWLEDGEMENTS. This work was supported under NASA grant NAG-5-898. Thanks are due to W. Rossow and E. Raschke for providing AVHRR GAC data.

REFERENCES

1. Barry, R.G. A. Henderson-Sellers, and K.P. Shine, "Climate sensitivity and the marginal cryosphere", in *Climate Processes and Climate Sensitivity*, J. Hansen and T. Takahashi (eds.), Geophys. Monog. 29, Amer. Geophys. Union, Washington, DC, pp221-337, 1984.
2. Budyko, M.I., "The effect of solar radiation variations on the climate of the Earth", *Tellus*, Vol. 21, pp611-619, 1969.
3. Key, J.R., "Cloud analysis in the Arctic from combined AVHRR and SMMR data", Ph.D. dissertation, Department of Geography, University of Colorado, Boulder, 180 pp., 1988.
4. Key, J.R., J.A. Maslanik, and R.G. Barry, "Cloud classification using a fuzzy sets algorithm: a polar example", *Int. J. Rem. Sens.*, 1989 (in press).
5. Maslanik, J.A., Key, J.R., and Barry, R.G., "Merging AVHRR and SMMR data for remote sensing of ice and cloud in the polar region", *Int. J. Rem. Sens.*, 1989 (in press).
6. NOAA, *NOAA polar orbiter data user's guide*, U.S. Department of Commerce, National Oceanic and Atmospheric Administration, NESDIS, February, 1984.
7. Polar Research Board, *The Polar Regions and Climatic Change*, National Research Council, National Academy Press, Washington, D.C., 59 pp., 1984.
8. Rossow, W.B., "Application of ISCCP cloud algorithm to satellite observations of the polar regions", in WMO, 1987. Report of the ISCCP workshop on cloud algorithms in the polar regions, National Institute for Polar Research, WCP-131, WMO/TD-No. 170, Tokyo, Japan, 19-21 August 1986, 1987.
9. Rossow, W.B., "Measuring cloud properties from space: a review", *J. Climate*, Vol. 2, pp201-213, 1989.
10. Rossow, W.B., F. Moshier, E. Kinsella, A. Arking, M. Desbois, E. Harrison, P. Minnis, E. Ruprecht, G. Seze, C. Sinner, and E. Smith, "ISCCP cloud algorithm intercomparison", *J. Clim. Appl. Meteor.*, Vol. 24, pp877-903, 1985.
11. Saltzman, B. and R.E. Moritz, "A time-dependent climatic feedback system involving sea-ice extent, ocean temperature, and CO₂", *Tellus*, Vol. 32, pp93-118, 1980.
12. WMO, "Report of the ISCCP workshop on cloud algorithms in the polar regions", World Climate Research Programme, WCP-131, WMO/TD-No. 170, Tokyo, Japan, 19-21 August 1986, 1987.

ATTACHMENT 6

CLOUD CLASSIFICATION WITH SPECTRAL AND TEXTURAL MEASURES



**Cloud Cover Analysis with Arctic AVHRR Data, Part II:
Classification with Spectral and Textural Measures**

J. Key

Cooperative Institute for Research in Environmental Sciences

University of Colorado

Boulder, Colorado 80309-0449

Short title: Arctic Cloud Cover Analysis: Classification

Journal of Geophysical Research (Atmospheres)

[illegible]

Abstract

The variation in cloud amount over polar ice sheets, sea ice, and ocean surfaces can have important effects on planetary albedo gradients and on surface energy exchanges, so that monitoring of polar cloud cover is crucial to studies of climate change. The spectral and textural characteristics of polar clouds and surfaces for a seven-day summer series of Advanced Very High Resolution Radiometer (AVHRR) data in two Arctic locations are examined, and the results used in the development of a cloud classification procedure for polar satellite data. Since spatial coherence and texture sensitivity tests indicate that a joint spectral-textural analysis based on the same cell size is inappropriate, cloud detection with AVHRR data and surface identification with passive microwave data are first done on the pixel level as detailed in Part I [Key and Barry, 1989]. Next, cloud patterns within $(250 \text{ km})^2$ regions are described, then the spectral and local textural characteristics of cloud patterns in the image are determined and each cloud pixel is classified by statistical methods. Results indicate that both spectral and textural features can be utilized in the classification of cloudy pixels, although spectral features are most useful for the discrimination between cloud classes. This methodology provides a basis for future "objective" automated mapping of cloud types and amount over snow and ice covered surfaces.

1. INTRODUCTION

High latitude response to changes in cloud cover is a key area of uncertainty in evaluating changes in the global climate system. To better understand climatic forcing, statistical frameworks for describing the morphology of cloud fields as well as the radiative, dynamical, and microphysical processes determining this morphology are needed [CGC, 1988, pg. 117]. Major uncertainties exist in current cloud climatologies for polar regions as a result of the problem of discriminating clouds over snow and ice using satellite visible or

infrared data.

This issue has been addressed in Part I of this research [Key and Barry, 1989], where an algorithm was presented that performs pixel-scale analysis of surface and cloud radiances utilizing visible, thermal, and passive microwave data over a seven-day period. The purpose of this paper is to examine the spectral and textural characteristics of summertime polar clouds and surfaces in Advanced Very High Resolution Radiometer (AVHRR) data; the issue of the appropriate scale of measurement for texture measures will be addressed and an optimal set of features is determined. This information is then used in the development of a procedure that classifies cloudy pixels - identified as such by the algorithm described in Part I - into recognizable cloud patterns. The methodology employed differs from other studies in that only the cloudy pixels are classified, in contrast to the method of gridding an image and classifying the grid cells, which themselves may contain mixtures of surface and cloud types. As detailed in a later section, some of the problems that have been recognized with traditional spectral/textural classifiers have been alleviated, but others have been created.

Cloud detection methods for use with satellite data that examine only spectral characteristics of pixels include single- and multi-channel threshold methods, radiative transfer models, histogram techniques, and statistical clustering procedures. These are reviewed in Part I [Key and Barry, 1989]. Some studies have included an analysis of texture in cloud classification schemes, generally in a clustering framework [e.g., Welch et al., 1988, 1989a,b; Garand, 1988; Ebert, 1987, 1988; Parikh, 1977]. Contextual analyses of frontal patterns and cloud shadows are given in Gurney and Townshend [1983], Wang et al [1983], Swain et al. [1981], and the spatial classifier of Kettig and Landgrebe [1976].

Global cloud climatologies are reviewed by Hughes [1984]. Vowinckel [1962], Huschke [1969], and Gorshkov [1983] provide perhaps the most comprehensive cloud climatologies for the Arctic, but are derived primarily from surface observations. They

show general agreement in the seasonal cycle of total cloud amount, but differ in the geographical distribution of cloud cover, particularly in the case of low cloud in winter. Spring and summer cloud amounts and patterns in the Arctic have been recently examined by Kukla [1984], Robinson et al. [1986], Barry et al. [1987], and McGuffie et al. [1988]. McGuffie et al. [1988] compared three cloud analysis methods (two manual and one automated) based on Defense Meteorological Satellite Program (DMSP) images. While cloud detection schemes exist for many data types and geographic locations, the inherently subjective nature of defining cloud types and the algorithmic difficulty of incorporating texture into the analyses are two inhibitory factors in the development of the automated cloud typing methods needed for large scale cloud climatologies.

2. DATA SET

All five AVHRR channels (1: 0.58-0.68 μ m, 2: 0.73-1.0 μ m, 3: 3.55-3.93 μ m, 4: 10.3-11.3 μ m, 5: 11.5-12.5 μ m) are initially employed. Data from the Nimbus-7 Scanning Multichannel Microwave Radiometer (SMMR) in channels 18 and 37 GHz vertical polarization, as well as SMMR-derived sea ice concentration, are used for surface parameterization in the cloud detection step described in Part I [Key and Barry, 1989], but are not used directly in the analysis of cloud patterns. SMMR, SMMR-derived sea ice concentration, and AVHRR data were co-registered to a polar stereographic projection and used simultaneously. The effective pixel size of the AVHRR data is reduced to 5x5 km [Maslanik et al., 1989].

Two areas of the Arctic are examined (Figure 1). One area is centered on the Kara and Barents Sea extending north to the pole and south to Norway and the Siberian coast. The second area covers most of the Canadian Archipelago and Greenland, also extending to the pole. A seven-day summer series (July 1-7, 1984) of these two areas is used in the analysis of cloud patterns. These areas include representative samples of all surface types

found in the Arctic: snow-covered and snow-free land, sea ice of varying concentrations, open water, and permanent ice cap. The observed conditions are usual for summer in the Arctic, as are the pressure patterns which occurred. Synoptic pressure patterns observed in Arctic Ocean buoy data [Colony and Munoz, 1986] during the study period are similar to the mean pattern for the month [Serreze and Barry, 1988; Gorshkov, 1983]. Although correlations have been observed between synoptic pressure systems, cloud amount, and cloud type [Barry et al., 1987], detailed cloud climatologies for the Arctic are not available and it is therefore more difficult to make such a statement concerning cloud cover.

Area 1 on July 1 exhibits the greatest mixture of cloud patterns and clear sky conditions of all the imagery, and will be used to illustrate the methodology and classification results throughout the remainder of the paper. However, spectral and textural characteristics as well as cloud pattern training areas were extracted from the complete set of imagery, and results are expected to be similar for other days. Figure 2 shows the study area in AVHRR channel 1 (visible). Novaya Zemlya is at upper center with sea ice above and to the left. Sea ice also occupies the lower left portion of the image. Grid lines delineate 50x50 pixel or $(250 \text{ km})^2$ regions. Figure 3 is an image of the cloud-only portion of Figure 2, shown in AVHRR channel 1 (visible) with grid lines delineating cells of 16x16 pixels (Section 3.3). This image was classified using the algorithm described in Part I [Key and Barry, 1989], and briefly described in Section 4 below. Low thin cloud over sea ice in the Kara Sea, which is not apparent in Figure 2, is identified with AVHRR channel 3 and the temporal tests of the algorithm. Figure 4 is an image of SMMR-derived surface types showing land, sea ice, ice cap, open water, and a narrow coastal zone. Inaccuracies in the identification of cloudy pixels result from incorrect surface identification due to weather effects in the passive microwave, resolution differences between the SMMR and the AVHRR, and coastal effects.

3. FEATURES

3.1 Spectral Features

Five surface and three broad cloud classes are analyzed for their spectral characteristics. Surface types are snow-free land, snow-covered land, open water, medium to high concentration sea ice, and low concentration sea ice. Cloud classes are defined by channel 4 brightness temperature (T) assumed to represent temperatures at the top of optically thick cloud layers, and encompass the categories: low $T > 265$ K, middle $245 \leq T \leq 265$ K, and high $T < 245$ K. Spectral and textural features were calculated only for "pure" classes, i.e., groups of contiguous pixels, or cells, that contain one and only one the class as determined through a manual interpretation. Training areas were defined manually.

Spectral features examined for each pixel are channels 1, 2, and 3 reflectance, channels 3, 4, and 5 brightness temperatures, ratios of channels 2 and 1, 3 (reflectance) and 1, and channel 4 minus 5 (brightness temperature difference). The ratio of channel 2 to channel 1 in AVHRR data or the difference between channels 2 and 1 enhances vegetation signals, arctic haze, and snow and sea ice underneath clouds. Channel 3 is important for the discrimination of low cloud over snow and ice surfaces. The difference between channels 3 and 4 aids in the detection of optically thin cloud and fog, while the difference between channels 4 and 5 is useful for identifying cirrus [Olesen and Grassl, 1985; Saunders, 1986]. For each cell, the mean and standard deviation are examined. These are first order statistics that describe the distribution of pixel values within a cell.

3.2 Textural Features

Second order statistics summarize the probability of the intensity values of a pair of pixels. These relative frequencies are computed for each pair of pixels in a given positional relationship and are summarized in a grey level co-occurrence matrix (GLCM). Positional relationships refer to separation distance, d , and direction, θ . Haralick et al. [1973] first

used co-occurrence matrices to classify terrains in aerial photographs with a very small matrix. Welch et al. [1988] and Kuo et al. [1988] computed a number of measures from the GLCM for cloud analysis. Higher order textural statistics may also be calculated, although they generally involve more computation and do not necessarily yield better results. Julesz [1975] has argued that two textures with identical second-order statistics are not discriminable. It is possible, therefore, that first and second-order statistics are all that are needed to discriminate texture.

Weszka et al. [1976] modified this method to operate on grey level difference (GLD) histograms rather than grey level pairs. The data are first quantized to 64 grey levels, and the grey level difference, g , is computed for each pair of pixels in the cell over each of four angles: up-down (0°), left-right (90°), upper left-lower right (135°), upper right-lower left (45°). Texture may contain a directional component so that the histogram must be specified as a function of angle as well as distance. A histogram of gray level differences is then constructed for each distance and angle, and used to compute various texture measures. The histograms will be spread over a larger range of g as graininess or streakiness increase. The grey level difference texture measures calculated from the histograms are the mean, contrast, angular second moment, and entropy for the cell. The mean, maximum, and range of these quantities over the four angles are used in subsequent analyses. Both GLD and GLCM texture measures were initially computed for the AVHRR data sets. However, due to the similarity of these measures, only the GLD measures were retained because they are computationally simpler.

The variability of grey level differences is summarized by the contrast. Large values correspond to structured clouds such as cumulus with shadows. The angular second moment measures the homogeneity of gray level differences with distance and direction. Angular second moment will be high for decks of stratus and for bands of clouds oriented in the direction of θ . Entropy describes the degree to which distinct scales of organization

are unrecognizable. It is maximum when all radiance differences have an equal probability of occurring (i.e. the histogram is uniform) and low when texture is smooth. See the appendix for more detail and definitions of the texture measures.

If texture is coarse and d is small compared to the texture element size, the pairs of points at separation d will usually have similar gray levels and the histogram will have high frequencies around $g=0$. Conversely, with fine texture and d comparable to element size, the gray level differences will often be large with a large spread in the frequencies of g . If texture is directional and d is in the proper range, the degree of spread in the histogram should vary with direction. Separation distances of 1, 2, 4, and 8 have been examined elsewhere [e.g., Weska et al., 1976 and Parikh, 1977] with distances of 1 or 2 being the preferred. Welch et al. [1988] found that optimal separation distance depends on cloud type. However, the effect of pixel resolution on textural features is unclear. Since a small cell size is used here (discussed below), and because separation distances of 1 and 2 function similarly in this data set, $d=1$ is used.

Other texture measures are also examined. The area averaged Roberts gradient is maximum in regions of sharp brightness contrast and is therefore a measure of edge strength [e.g., Gonzalez and Wintz, 1977]. It is defined over any separation distance but does not have directional sensitivity. Hobson [1972] and Harris and Barrett [1978] utilize a measure called vector strength. If the pixels within a cell are connected into a set of adjacent triangular planes, then texture can be measured through the dispersion in three-dimensional space of normal vectors to these planes. Vector strength is a summary of the distribution of normal vectors and is high for smooth surfaces and low for rough surfaces.

A two dimensional Fourier transform [e.g., Bunting and Fournier, 1980] is also applied to each cell as a means of defining the texture of cyclical cloud patterns. Three measures are used: the streakiness factor, cell intensity, and the maximum ring density wavelength. The streakiness factor is a directional measure which takes on values between

0 and 1, values near 1 being highly directional [Garand, 1988]. Cell intensity is the proportion of power in the spectrum associated with wavelengths between 20 and 40 km, the typical size of convective cells [Agee and Dowell, 1976]. The maximum ring density wavelength is the wavelength of the center of the annular ring in the power spectrum with the maximum density, where the spectrum is divided into four rings. The spectral and textural features are summarized in Table 1 where abbreviations used in the remainder of the text are also given.

These texture measures are calculated for the five surface classes defined previously, and for twelve cloud classes which include some of the basic cloud groups and mixtures of these as observed in the data:

1. Low thin cloud over water (stratus);
2. Low thin cloud over ice (stratus);
3. Low thin cloud over land (stratus);
4. Low thick cloud, smooth texture (stratus);
5. Low thick cloud, bumps or broken (stratocumulus);
6. Middle cloud rolls (broken, linear altostratus usually over a stratiform layer);
7. Broken middle cloud, not linear;
8. Middle thick cloud, smooth (altostratus, possibly over stratus);
9. Middle/high bumps (cirrocumulus or altocumulus);
10. High thick cloud with some middle cloud (broken cirrostratus over altostratus);
11. High thick cloud, smooth (cirrus or cirrostratus);
12. Cumulus.

The surface was included in classes 1-3 only because the clouds are thin and differed primarily in albedo. Contributions from surfaces to cloud albedo or temperature in the other classes was not significant enough to justify defining additional classes. Class 7 is similar to class 6, but occurred at a higher altitude (lower temperature).

3.3 Cell Size

The issue of cell size is important in that too large a cell may blur the boundaries between classes, while too small a cell may not permit adequate description of the textural and spectral features which distinguish between the classes. In addition, the larger the number of pixels in each cell, the more reliable the statistical estimates will be. A number of cell sizes have been used in previous cloud classifications; e.g. Ebert [1987] clustered 32×32 (128 km)² AVHRR cells; Garand [1988] analyzed 64×64 (128 km)² GOES cells; Wu et al. [1985] examined 20×20 and 5×3 (20 km)² GOES-2, SMS-2, and GOES-4 cells in a study of rainfall; Weszka et al. [1976] used 64×64 LANDSAT-1 cells; Parikh [1977] computed texture from 64×64 (205x355 km) NOAA-1 data; Haralick and Shanmugam [1974] introduced many of the texture measures described with 64×64 (7.5 sq. mi) ERTS-1 data, Welch et al. [1988] used 512×512 (29 km)² Landsat cells. Cell sizes seem to be chosen somewhat arbitrarily, although cell size has been chosen as a power of two in those studies which employ the Fast Fourier Transform. The cell size used here was based on a number of measures, both quantitative and qualitative.

In an attempt to quantify the effect of cell size, the texture measures were calculated for the cloud and surface classes using cell sizes of 4 to 24 in increments of 2 with a separation distance of 1. Generally the texture values either remain essentially unchanged or decrease/increase linearly for cells of size 24 down to 16. Cell sizes of 10 or less often produce highly variable texture values. Values for cells of size 12 and 14 are similar to those with sizes 16 and larger, but are more variable. A paired t-test for the difference between cell sizes, with the null hypothesis that there is no difference between the means, indicates that there appears to be a difference between cells of sizes 8, 16, and larger (0.05 level of significance). In no cases can we conclude that there is a significant difference between texture measures extracted from cells of sizes 14 and 16, 16 and 18, and

14 and 18. Other pairs show results between these two extremes. These results are reasonable if we wish to maximize the number of texture elements within a cell. Usually, these basic texture elements exist on a smaller scale, for example open convective cells are 20-40 km and cloud rolls which have wavelengths of approximately 40 km. Additionally, Garand and Weinman [1986] found that cloud texture is best measured over mesoscale regions, on the order of 100-250 km square. The approximate lower limit in the above analyses is 16x16 pixels, or $(80 \text{ km})^2$ at the 5 km pixel mapping.

In addition to capturing the basic texture of a class, we are also interested in ensuring that as many cells as possible in an image represent only one class. The pixels within a cell containing a relatively uniform surface should exhibit a high degree of spatial coherence and therefore have a relatively low standard deviation when compared to a cell which contains a boundary between two classes that are widely separated in feature space. To further investigate the effects of different cell sizes, a single-channel synthetic image was created which consists of rectangular "objects" of varying sizes and locations. The minimum and maximum allowable sizes of objects are specified. An object is generated whose dimensions are randomly chosen within the restricted range, and the class of the object is randomly assigned (uniform random number generator). Regions are filled with data for that class with a Gaussian random number generator based on a specified mean and standard deviation. A grid of size 300 x 300 "pixels" was generated with subregions of sizes 5 to 40 pixels, representing objects of sizes 25-200 km. Each of these areas was then assigned a class number from 1 to 6. Means of cells of sizes 2, 6, 10, 14, 18, and 22 pixels square were then calculated and their relative frequency distributions were examined. These are shown in Figure 5 for cell sizes of 6 to 22. Classes in the synthetic data set with means of 10, 30, 50, 70, 90, and 110 (the standard deviation of each class is 1.5) are well represented by means of 6x6 cells, and poorly represented by 22x22 cells. Cells with means between the class means contain one or more boundaries. In all cases but the last,

each of the class means is apparent in the histogram, with mixing increasing with increasing cell size.

Cells representing single classes will exhibit a mean very near the class mean, and will have a small standard deviation. In determining which cell size is optimal, these cells are located in the histograms, and the change in their relative frequency with changing cell size is observed. We accept as "pure" cells which have standard deviations no greater than a small percentage of the range of the data, as defined by the spatial coherence method of Coakley and Bretherton [1982]. The relative frequency histogram of these cells is then determined (Figure 5, horizontal bars). The figure shows differences between the frequency of pure cells with means the same as the class means and the frequency of all cells with those means. This difference tends to increase with increasing cell size, and is attributable to cells which contain a mixture of classes and therefore have large standard deviations. This indicates that classifications which rely solely on cell means for discriminating between classes are likely to have a high error rate. Next, peaks in the histogram of pure cells are examined to determine the probability that the grouping would occur by chance; i.e., that the peak and surrounding intervals represents a uniform distribution. These probabilities are given by a multinomial distribution function. This test of separability shows that two classes are lost with cells of size 14, three are lost when cells of size 18 are used, and none are represented by cells of size 22.

Based on these tests, a cell size of 10 pixels square is the approximate upper limit of spatial coherence if an image is uniformly gridded. Conversely, a cell size of 16 seems to be the approximate lower limit for texture analysis. This discrepancy implies that a joint spectral-textural analysis based on the same cell size is inappropriate. For the following texture analyses of pure classes, a cell size of 16 is used. Of course, these tests apply to this data set only. See Welch et al. [1989b] for a discussion of resolution effects on texture measures.

3.4 Choice of Features

There will undoubtedly be a high degree of redundancy in the spectral and textural variables available for analysis. Benefits in terms of processing as well as interpretability are gained by reducing this set of features to a set which includes only those containing the greatest amount of discriminatory information for the classes of interest. To create this set for cloud/surface analysis using the AVHRR imagery, correlations between features over all classes were examined through principal components analysis (PCA), both unrotated and rotated (Varimax). It is also possible to examine correlations between pairs of variables in a correlation matrix, as has been done in Garand [1988] and Ebert [1987]. Since variables which have large loadings on the same component generally have large correlations between themselves, this method provides little additional information.

Principal components analysis was applied to both study areas, and the original nine spectral features were reduced to four components with eigenvalues greater than 1.0. Components with eigenvalues less than 1.0 account for less variance than the original variable and are not retained. It is also recognized that beyond the first few components, patterns may be essentially random. The representation of each component is listed in Table 2. The first component represents channel 3, the 3-4 difference, and the ratio of channel 3 to channel 1. Component II represents channels 4 and 5; channels 1 and 2 load highly on component III; component IV represents only the 4-5 difference. The 2/1 ratio loaded highly on component V, but its eigenvalue was only 0.5.

The discriminatory capability of features for all pairs of classes was also determined using a divergence parameter, Fisher distance, defined as

$$D_{ijk} = \frac{|\mu_{ij} - \mu_{ik}|}{\sigma_{ij} + \sigma_{ik}}$$

where μ_i is the mean for variable i on class j or k and σ_i is the corresponding standard deviation. The divergence parameter measures the ability of the feature to differentiate between classes and is computed for each variable and each pair of classes. The higher divergence values correspond to greater usefulness in distinguishing between classes, where $D_{ijk} > 1.0$ has discriminatory skill and $D_{ijk} < 0.5$ generally has poor separating power [Garand, 1988]. The number of times a variable ranked first, second, etc., in Fisher distance was tabulated in matrix form. Since PCA implies that of the nine original features only three or four are statistically independent, the top four ranked features for each class pair are most important. Channel 1 scores highest most often followed by channel 2 and channel 4. The ratio features 2/1 and 3/1 and channel 3 follow in rank.

The number of features can now be reduced even further based on the joint results of PCA and divergence calculations. Since channel 1 scored higher more often than channel 2 and since they are highly correlated, channel 2 was eliminated and channel 1 retained. Similarly, channel 4 was retained and channel 5 eliminated. The channel 3 features were similar in discriminatory capability so any could be retained. These two features are of particular interest in discriminating between water and ice clouds. The 4-5 difference did poorly in divergence ranking and would be of little value in this classification application.

The same PCA and divergence parameter methods were applied to the spectral and textural features calculated for the 16x16 pixel cells. PCA identified twelve components with eigenvalues greater than 1.0. Table 3 lists these components and which variables they represent. The first three components represent most of the variables, and provide an obvious division of the three channels. This indicates that texture measures within a channel vary together to a stronger degree than between channels. This result is important when considering the utility of spectral and textural variables in classification studies.

The results of the divergence parameter testing for the texture measures are given in

Table 4. RG, VECTOR, XASM, MENT, and SD ranked high in all three channels. XASM, XENT, and XMEAN indicate that directionality is an important component to the texture of some of the classes. With most pairs of classes, the spectral MEAN and SD features ranked higher than the GLD texture measures.

The angular second moment, vector strength, and entropy texture measures are most useful in surface/cloud discrimination. Specifically, snow/water/land and cloud texture differences were best described by angular second moment and entropy while ice and cloud differences appeared in the vector strength and entropy measures. Entropy was also important in discriminating between the cloud classes. Differences between ice concentrations appeared in the Roberts gradient, entropy, and vector strength. Overall, spectral features were most important for discriminating between surface types, this being in agreement with the findings of Ebert [1987]. Entropy and angular second moment were also chosen in the cloud texture analyses of Welch et al. [1988] and Ebert [1987, 1988].

When the divergence parameter ranking is considered for pairs of cloud classes only, the number of useful texture measures is reduced even further. Channel 3 texture measures did not rank as highly as channels 1 and 4 measures. In the latter two channels, the Roberts Gradient, vector strength, maximum angular second moment, mean entropy, and standard deviation ranked highly most often and are used in the final analysis of cloud patterns.

4. CLOUD PATTERNS

The cloud analysis methodology employed here includes cloud detection on the pixel scale, a description of cloud patterns on a regional scale, and a classification of cloudy pixels based on spectral and local textural characteristics. This procedure is summarized in Figure 6. The cloud detection procedure is described in Part I [Key and Barry, 1989], and is based on the major steps of an International Satellite Cloud Climatology Project (ISCCP)

test algorithm [Rossow et al., 1985]. In the current procedure, surface identification with SMMR and SMMR-derived data sets is the first step. The algorithm then proceeds through a series of steps, each of which is designed to detect some of the clouds present in the scene. Temporal variability at each pixel location is examined for an initial detection of cloudy conditions, and clear sky composite maps for a five-day period are produced. A multispectral threshold test of the original data with the clear sky composites yields a final cloud/no-cloud labeling of the original data.

The two methods of cloud pattern analysis are presented for different purposes: in one case (left side of Figure 6), simple measures are used to describe the characteristics of clouds which occur in regions with artificially defined boundaries. The size of the regions is consistent with that used by the ISCCP and some climate models. The second method is presented as an attempt to eliminate the problems inherent in analyses that impose artificial boundaries on cloud and surface patterns, that being the mixture of different classes within a single cell. It differs from other analyses that have incorporated texture analyses in that only the cloudy pixels are examined; surface pixels are identified in the cloud detection step. Additionally, texture values are assigned to each pixel rather than to a grid cell, and classification of pixels is performed. Other studies have utilized texture to identify both surface and cloud classes, and have employed statistical classifiers to distinguish between the two [e.g., Garand, 1988; Welch et al., 1988; Ebert, 1987]. In supervised classification procedures, training patterns have often been comprised of mixtures of cloud and surface types.

The bottom two boxes in Figure 6 identify future work in the automatic (i.e., computer) analysis of cloud patterns and their relationships with synoptic variables. As a part of this goal, the compilation of statistics for cloud fraction, temperature, and number of clouds per grid box is accomplished by the procedure shown in the left side of the figure. However, the comparison of recognizable cloud morphologies (identified through texture

analysis shown in the right side of the figure) to gridded synoptic data is the more complex goal and will be the focus of future research.

4.1 Description of Cloud Within Regions

Mesoscale analysis is performed within regions that are $(250 \text{ km})^2$, 50×50 pixels, or approximately 2.5° latitude by 2.5° longitude (Figure 2). Cloud properties are computed for the cloud-only portion of each region and include overall cloud fraction, cloud fraction at three levels, and connectivity measures. Low, middle, and high cloud amounts were estimated as the percentage of pixels of temperature, T , such that if

1. $T_s - 13 < T \leq T_s$ then low,
2. $T_s - 39 < T \leq T_s - 13$ then middle,
3. $T \leq T_s - 39$ then high,

where T_s is the surface temperature estimated by the clear sky composite value in AVHRR channel 4.

Cloud connectivity features [Garand, 1988] can be extracted from a binary image where each pixel is classed as either cloudy or clear. Cloud connectivity is smaller for highly disconnected elements such as cumulus and larger for uniform stratus decks. Cloud pixels connected only diagonally belong to a different entity, whereas cloud pixels connected above, below, left, or right belong to the same cloud entity. In this manner, the number of clouds and the number of background areas may be counted. If $h_c(i)$ and $h_b(j)$ are the number of pixels in the cloud entity, i , and the background entity, j , respectively, and if we rank the clouds and background areas from smallest to largest, the cloud connectivity, CC , is defined as

$$CC = h_c(k) / (mA_c), \quad A_c > 0$$

where A_c is cloud fraction, m is the number of pixels in the image and k is the cloud

number in the ranked list such that

$$\sum h_c(i) \geq mA_c / 2, \quad i=1,k$$

If $A_c = 0$, $CC = 1$. Background connectivity is similarly defined as

$$BC = h_b(k') / [m(1-A_c)], \quad A_c <> 1$$

where k' satisfies

$$\sum h_b(j) \geq m(1-A_c)/2, \quad j=1,k'$$

If $A_c = 1$, then $BC = 1$. Background connectivity is a good detector of holes and is low for open cells such as those associated with convective patterns.

The proportion of thin cloud within a region was estimated from the number of cloud pixels with a large difference between channels 3 and 4. Based on empirical studies with the summer data, and following Saunders [1986] and Olesen and Grassl [1985], if the difference between these two channels exceeds 3.5 K then the cloud is considered to be thin. This applies to cloud at any height.

Finally, the three power spectrum measures, streakiness factor, cell intensity, and maximum ring density wavelength, are useful in describing the structure of clouds. Although in the divergence parameter analysis they were less useful in discriminating between cloud classes than the grey level difference measures, they are nonetheless important descriptors and are easier to interpret. Additionally, the methods of feature selection were based on "pure" classes, not the mixtures that will often occur within the artificial boundaries imposed here.

Two of the parameters described above are shown in Figure 7 for the study area, where regional values of low cloud fraction and cloud connectivity are mapped.

4.2 Cloud Classification with Spectral and Textural Measures

The second method of examining cloud patterns is to classify each cloud pixel based on its spectral and local textural characteristics. AVHRR channels 1, 3, and 4 are used as the spectral features. Textural features include those given in Table 4 (underlined) and are determined for each pixel in the following manner. A 16x16 pixel cell is moved across the image shifting two pixels at a time. At each location, if the cell contains at least 80% cloud, each texture measure is computed. The value of texture for the cell is assigned to each pixel. With this method, each pixel may be assigned as many as $16^2/2=128$ values. The mean of these values is the value finally assigned to the pixel. While this method does not eliminate the problem of mixtures of classes within a cell, it does provide a value which is generally representative of the texture within the neighborhood, although when edges between cloud classes are present, the value will be skewed. Figure 8 is an image of the maximum angular second moment GLD measure in AVHRR channel 1 computed over the study area. Large values (lighter grey shades) indicate smooth cloud layers and correspond to both the low and middle level cloud decks seen in Figure 2. Similarly, the darker areas correspond to inhomogeneous grey level pairs, primarily the mixtures of clouds at all levels in cellular or linear patterns.

The maximum likelihood classifier (MLC) (cf., Ebert [1987], Garand [1988]) is employed; the potential problems and alternatives are discussed in the next section. The twelve cloud classes defined in Section 3.2 are used in the classification. A priori probability for each class is 1.0. The classification results are shown in Figure 9 with cloud classes as listed in Section 3.2. Only those cloud classes which occurred in the image and were identified by the MLC are shown. Comparison of the results to other classifications is complicated by the subjectivity inherent in defining cloud classes, which are based on those observed in the imagery chosen as a function of both their textural and spectral characteristics. Error analysis implies that there is a correct classification, which at

best is difficult to define. For this reason, the discussion is limited to a comparison of Figure 9 to the manual classification shown in Figure 10. Differences are given in Table 5, which is a contingency table showing the percent of pixels classified by each method into each of the classes. Overall classification agreement is 68.3% with 10.3% of the image left unclassified. The largest differences are due to (1) differences in the location of boundaries between cloud systems, (2) labeling of low thin cloud over ice as low thick cloud by the MLC (Kara Sea), (3) the MLC detecting a linear pattern in some middle cloud areas which appeared broken in the manual interpretation, and (4) some low thick cloud areas labeled as middle broken by the MLC. Additionally, the cumulus complex to the left of Novaya Zemlya (Figures 2, 10) was missed completely by the MLC apparently due to a combination of an insufficient number of training samples and the large number of non-cloud pixels within the complex which decreased the number of cells for which texture was computed. From these observations it can be seen that the classification results could be improved by redefinition of some classes and by choosing more appropriate training areas. However, given the complexity of the problem - how to define and classify cloud patterns - the areas in which this method performed poorly are perhaps more informative than tuning the classifier to achieve a high classification accuracy.

Comparisons of the MLC results to other methods are also problematic. The question of how this classification would compare to one utilizing only spectral features, for example, is inappropriate because in such a case the cloud classes would have to be defined without a textural component. In this case we examine the results of the principal components and divergence parameter analyses to obtain some indication of the importance of textural measures in distinguishing between classes. The question of how this classification compares to one that uses texture for fixed grid cells is similarly complicated by the fact that in the fixed grid method, some of the defined classes would include mixtures of cloud types.

4.2.1 *Alternate Methodologies*

Within this procedural framework of cloud pattern analysis starting from a map of cloudy pixels, a number of other methods of textural analysis and classification could be chosen. This is largely an image processing problem, and as such a detailed analysis of the differences of using, for example, one classifier over another, are beyond the scope of this paper. Still, it is useful to mention some of the alternatives which may effect the resulting classification.

A maximum likelihood procedure is employed for the classification although arguments could be made for using other procedures, for example, Euclidean distance [Ince, 1987] or fuzzy sets [Key et al., 1989] clustering algorithms. Since texture and spectral response are not always equally important in identifying the cloud types, a classifier which allows weighting the different sources of information for each class would be useful. Such a method is proposed by Benediktsson and Swain [1989].

Related to the choice of classification method, the question of the normality of distributions of features used in the MLC is an important one, and is addressed in detail by Ince [1987]. When training areas comprise data from a large geographic area and/or time period, a single informational class (e.g., land albedo) may consist of more than one statistical class. This is certainly the case in the data set employed here, as a chi-square goodness-of-fit test has shown for some of the spectral and textural features extracted over a number of images in different locations and time. However, this does not necessarily mean that the spectral or textural features themselves are not Gaussian in a single spatial and temporal location. In fact, it is likely that the normal distribution is the correct population distribution in such a restricted domain. This is the case in the study area of Figure 2, where chi-square tests show distributions to be approximately normal.

The objective of the moving texture grid cell is to assign the most appropriate

texture value to each pixel, one which best represents the texture of the cloud class to which the pixel belongs. Toward this end, other methods of extracting information from the distribution of texture values for a given pixel may be more appropriate than the mean, for example using the median or mode(s). In some cases these would provide more representative values in that boundaries between overlapping cloud layers would be less blurred, but the computational burden would increase. Ideally, texture would be computed only for homogeneous regions, which of course require texture to be defined. In some cases it may be appropriate to follow a region growing procedure based on temperature, for example, where cloud patterns are grown out of homogeneous pixels which are spatially connected (e.g., Kettig and Landgrebe [1976]). The texture of these regions would then be determined, and if more than one characteristic texture is found, the region could be split.

5. CONCLUSIONS

The cloud analysis methodology presented here provides an alternative to the traditional method of gridding an image, computing spectral and textural features for each cell, and then classifying the cells. Simulations indicate that in such methods, cells small enough to retain a high degree of spatial coherence may be too small to adequately measure texture in the AVHRR GAC data set. Our method includes cloud detection on the pixel scale, a description of cloud patterns on a regional scale, and a classification of cloud pixels based on spectral and local textural characteristics. The cloud detection step involves surface identification, tests of temporal variability at each pixel location, clear sky compositing over a five-day period, and a multispectral threshold test of the original data with the clear sky composites for a final cloud/no-cloud labeling.

From this point, two methods of cloud pattern analysis are presented. In one case, simple measures are used to describe cloud types which occur in $(250 \text{ km})^2$ regions with artificially defined boundaries. Such parameters as cloud fraction at three levels, cloud

connectivity, and Fourier measures of cloud cover structure within the regions are computed. These descriptors may be useful for applications which require gridded data; e.g., in climate models. The second method is presented as an attempt to eliminate the problems inherent in analyses which impose artificial boundaries on cloud and surface patterns, that being the mixture of different classes within a single cell. Each pixel receives as its texture value the mean value of all cloudy cells to which it belongs. Cloud pixels are then classified by their spectral and textural features following a maximum likelihood procedure.

This methodology differs from others which have incorporated cloud texture analyses in two important ways: only the cloudy pixels are examined (surface pixels are identified in the cloud detection step), and texture values are assigned to each pixel rather than to a grid cell. In this manner, training classes can be defined based on texture, and do not need to include mixtures of cloud and/or surface classes. However, the subjectivity inherent in defining cloud types makes an objective assessment of the accuracy of the results difficult. This problem is compounded in the test data, where cloud systems are complex. With classes defined in part by texture, comparisons to spectral-only classifications are not appropriate. The test case resulted in 68% of the cloud pixels being correctly classified when compared to a manual interpretation, although no redefinition of classes or training areas was done to increase this value.

Correlation between spectral and textural features and the discriminatory capability of each indicates that spectral features are most useful in discriminating between polar surface and cloud classes but that a few texture measures, such as angular second moment, vector strength, and entropy, as well as standard deviation, retrieve structural information of clouds.

The classification results indicate that, as expected, cloud fields are organized into recognizable mesoscale morphologies. An analysis of cloud morphology may in turn give some indication of the physical state of the atmosphere. A detailed examination of the

3

relationship between cloud patterns and synoptic variables requires greater spatial coverage than examined here, as well as a procedure to correlate the cloud patterns - derived with the procedure presented above - to other meteorological data sets. The development of such a procedure is the subject of future research.

APPENDIX

The concept of grey level difference is used to compute the grey-level texture statistics [Weszka et al., 1976]. The grey level difference, g , is computed for each pair of pixels in the cell. A histogram $h_{\theta,d}(g)$ of grey level differences is then constructed for each distance, d , and angle, θ , and used to compute various texture measures. Pixels to the right and left of the pixel being examined are at an angle of 0° , those above and below are at 90° , the upper right and lower left are at 45° , and the upper left and lower right are at 135° . Texture may contain a directional component so that the histogram must be specified as a function of angle as well as distance. Here, spectral values are quantized into 64 equal intervals, based on the expected range in each channel (e.g. for channel 4, the minimum is approximately 220 K, while the normal maximum is 295 K).

The texture measures calculated from the histograms, $h_{\theta,d}(g)$, are the mean, contrast, angular second moment, and entropy for the cell. These are defined as

$$\text{MEAN}(\theta,d) = \frac{1}{64} \sum_g g \frac{h_{\theta,d}(g)}{H_{\theta,d}}$$

$$\text{CON}(\theta,d) = \sum_g g^2 \frac{h_{\theta,d}(g)}{H_{\theta,d}}$$

$$\text{ASM}(\theta,d) = \sum_g \left\{ \frac{h_{\theta,d}(g)}{H_{\theta,d}} \right\}^2$$

$$\text{ENT}(\theta,d) = - \sum_g \frac{h_{\theta,d}(g)}{H_{\theta,d}} \ln \frac{h_{\theta,d}(g)}{H_{\theta,d}}$$

$$g=0,1,\dots,63$$

where $H_{\theta,d}$ is the total number of grey level differences calculated for distance d and angle

θ. The mean, maximum, and range of these quantities over the four angles are used in the classification.

The area averaged Roberts gradient [e.g. Gonzalez and Wintz, 1977] is defined as

$$RG = \frac{\sum_{m=1}^{M-d} \sum_{n=1}^{N-d} [|B(m,n) - B(m+d,n+d)| + |B(m+d,n) - B(m,n+d)|]}{(M-d)(N-d)}$$

where d is the separation distance across which RG is computed.

Vector strength considers the cell of pixels as a set of adjacent triangular planes rather than a set of density points, and texture is then measured through the dispersion in three-dimensional space of normals (vectors) to the cell planes. Triangular planes are constructed by connecting midpoints of a pixel and two of its neighbors. The value of each vertex of the triangle is the value of the corresponding pixel. An number of possibilities for triangle construction exist; here the right and below neighbors are used, as well as the above and left.

Let (l_i, m_i, n_i) be the direction cosines of the i th plane, which are calculated from the coordinates of the normal vector to the plane (x, y, z) by

$$\begin{aligned} \cos \alpha &= x/w \\ \cos \beta &= y/w \\ \cos \delta &= z/w \end{aligned}$$

where

$$w = \sqrt{x^2 + y^2 + z^2}$$

The plane normal is calculated as the cross product of two vectors that are known to be on the plane (translated to the origin), the most convenient being the two which form the right triangle of the plane.

The ratio of R to N where N is the number of plane normals and

$$R = \sqrt{(\sum l_i)^2 + (\sum m_i)^2 + (\sum n_i)^2}$$

is the vector strength and has a value near unity for a smooth surface (e.g., stratus deck) and near zero for an uneven surface (e.g., a cumulus cloud).

Two-dimensional Fourier analysis of spectral data may be used to obtain information on the extended structure of a cloud field, especially where that structure consists of a repeating pattern in either or both dimensions. The Fourier transform of the image $f(k,l)$ is

$$Q(u,v) = 1/KL \sum_{k=0}^{K-1} \sum_{l=0}^{L-1} f(k,l) \exp\{-2i\pi(ku/K + lv/L)\}$$

$$u = 0, 1, \dots, K-1, \quad v = 0, 1, \dots, L-1$$

where K and L are the dimensions of the cell over which the transform is computed. The power spectrum intensity, $PS(u,v)$, is defined as the sum of the squared values of the real and imaginary parts of the transform. Three features are used to summarize the power spectrum: the streakiness factor, cell intensity, and the maximum ring density wavelength. The streakiness factor, SF , detects directional patterns [Garand, 1988], is

$$SF = |\sum_u \sum_v uv PS(u,v)| / \{[\sum_u \sum_v u^2 PS(u,v)][\sum_u \sum_v v^2 PS(u,v)]\}^{1/2}$$

$$u = 0, 1, \dots, K-1, \quad v = 0, 1, \dots, K-1, \quad (u,v) \neq (0,0)$$

If the pattern has a north-south or east-west orientation, $SF=0$. To avoid this problem, SF is also evaluated with the axes rotated 45° , and the maximum SF is retained. The cell intensity, CI , is the proportion of power in the spectrum associated with wavelengths between 20 and 40 km and is defined as

$$CI = \sum_u \sum_v PS(\lambda) / \sum_u \sum_v PS(u,v)$$

$$u = 1, 2, \dots, K-1, v = 1, 2, \dots, K-1, 20 \leq \lambda \leq 40$$

$$\lambda = K\rho/(u^2+v^2)$$

where ρ is the spacing between observations (i.e., 5 km in the AVHRR/SMMR data set) and $PS(\lambda)$ refers to all spectral density estimates with wavelengths, λ , between 20 and 40 km. More cellular patterns have higher CI values. The maximum ring density wavelength, WAVE, is a scalar representation of the annular area of the spectrum with the maximum density. The density within a ring with radii r_1, r_2 , RDW, is given as

$$RDW(r_1, r_2) = \sum_u \sum_v PS(u,v)$$

$$r_1^2 \leq u^2+v^2 \leq r_2^2$$

The power spectrum is divided into four rings, each $K/4$ in u, v dimensions, and the wavelength of the center of the ring with the maximum density is retained.

Acknowledgements. This work was supported under NASA grant NAG-5-898. Thanks are due to W. Rossow and E. Raschke for providing AVHRR GAC data, and to R.G. Barry, J.A. Maslanik, and the reviewers for their comments on an earlier version of this paper.

References

- Agee, E.M., and K.E. Dowell, Observational studies of mesoscale cellular convection, *J. Appl. Meteor.*, 13, 46-53, 1974.
- Barry, R.G., R.G. Crane, A. Schweiger, and J. Newell, Arctic cloudiness in spring from satellite imagery, *J. Climatol.*, 7, 423-451, 1987.
- Benediktsson, J.A. and P.H. Swain, A method of statistical multisource classification with a mechanism to weight the influence of the data sources, IGARSS'89, 12th Can. Symp. Rem. Sens., 2, 417-420, 1989.
- Bunting, J.T. and R.F. Fournier, Tests of spectral cloud classification using DMSP fine mode satellite data, Environmental Research Papers, No. 704, AFGL-TR-80-0181, 42 pp., Air Force Geophys. Lab., 1980.
- CGC, Toward an Understanding of Global Change. Committee on Global Change, National Research Council. Washington, D.C.: National Academy Press, 1988.
- Coakley, J.A., and F.P. Bretherton, Cloud cover from high-resolution scanner data: detecting and allowing for partially filled fields of view, *J. Geophys. Res.*, 87 (C7), 4917-4932, 1982.
- Colony, R. and E.A. Munoz, Arctic Ocean buoy program, data report, 1 January 1984 - 31 December 1985, Polar Science Center, University of Washington, 227 pp., 1986.
- Ebert, Elizabeth E., Classification and analysis of surface and clouds at high latitudes from AVHRR multispectral satellite data, Scientific Report #8, Dept. of Meteorology, Univ. of Wisconsin-Madison, February 1988.
- Ebert, Elizabeth, A pattern recognition technique for distinguishing surface and cloud types in the polar regions, *J. Clim. Appl. Meteor.*, 26, 1412-1427, 1987.
- Garand, L., Automated recognition of oceanic cloud patterns. Part I: methodology and application to cloud climatology, *J. Climate*, 1, 20-39, 1988.
- Garand, L. and J.A. Weinman, A structural-stochastic model for the analysis and synthesis

- of cloud images, *J. Clim. Appl. Meteor.*, 25, 1052-1068, 1986.
- Gonzalez, R.C. and Wintz, P., Digital Image Processing. Reading, Mass.: Addison-Wesley, 431 pp., 1977.
- Gorshkov, S.G. (editor), World Ocean Atlas, Vol. 3, Arctic Ocean, Oxford: Pergamon Press, 1983.
- Gurney, C.M. and J.R. Townshend, The use of contextual information in the classification of remotely sensed data, *Photogram. Engin. Rem. Sens.*, 49(1), 55-64, 1983.
- Haralick, R.M., and K.S. Shanmugan, Combined spectral and spatial processing of Landsat data, *Rem. Sens. Environ.*, 3, 3-13, 1974.
- Haralick, R.M., K. Shanmugam, and I. Dinstein, Textual features for image classification, *IEEE Trans. Syst., Man, Cybern.*, SMC-3, 610-621, 1973.
- Harris, R., and E.C. Barrett, Toward an objective neph- analysis, *J. Appl. Meteor.*, 17, 1258-1266, 1978.
- Hobson, R.D., Surface roughness in topography: quantitative approach, in: Chorley, R.J. (ed.), Spatial Analysis in Geomorphology. New York: Harper & Row, 393 pp., 1972.
- Hughes, N.A., Global cloud climatologies: a historical review, *J. Clim. Appl. Meteor.*, 23, 724, 1984.
- Huschke, R.E., Arctic cloud statistics from 'air-calibrated' surface weather observations, RAND Corporation Memo RM-6173-PR, Santa Monica, California, p. 79, 1969.
- Ince, Fuat, Maximum likelihood classification, optimal or problematic? A comparison with the nearest neighbour classification, *Int. J. Rem. Sens.*, 8 (12), 1829-1838, 1987.
- Julesz, B., Experiments in the visual perception of texture, *Scientific American*, 232, 24-43, 1975.
- Kettig, R.L. and D.A. Landgrebe, Classification of multispectral image data by extraction and classification of homogeneous objects, *IEEE Trans. Geosci. Elect.*, GE-14 (1),

19-26, 1976.

Key, J. and R.G. Barry, Cloud analysis with Arctic AVHRR data, part 1: adaptation of the ISCCP cloud detection algorithm, *J. Geophys. Res.*, 1989 (in press).

Key, J.R., J.A. Maslanik, and R.G. Barry, Cloud classification using a fuzzy sets algorithm: a polar example, *Int. J. Rem. Sens.*, 1989 (in press).

Kukla, G.J., Variation of Arctic cloud cover during summer 1979, Part 1, Technical Report LDGO-84-2, Lamont-Doherty Geological Observatory of Columbia University, 1984.

Kuo, K.S., R.M. Welch, and S.K. Sangupta, Structural and textural characteristics of cirrus clouds observed using high spatial resolution LANDSAT imagery. *J. Appl. Meteor.*, 27 (11), 1242-1260, 1988.

Maslanik, J.A., Key, J.R., and Barry, R.G. Merging AVHRR and SMMR data for remote sensing of ice and cloud in the polar region. *Int. J. Rem. Sens.*, 1989 (in press).

McGuffie, K., R.G. Barry, A. Schweiger, D.A. Robinson, and J. Newell, Intercomparison of satellite-derived cloud analyses for the Arctic Ocean in spring and summer. *Int. J. Rem. Sens.*, 9 (3), 447-467, 1988.

Olesen, F. and H. Grassl, Cloud detection and classification over oceans at night with NOAA-7, *Int. J. Rem. Sens.*, 6 (8), 1435-1444, 1985.

Parikh, J.A., A comparative study of cloud classification techniques, *Rem. Sens. Environ.*, 6, 67-81, 1977.

Robinson, D.A., Kukla, G.J., and Serreze, M., Arctic summer cloudiness, Proceedings of the Sixth Conference on Atmospheric Radiation, Boston: American Meteorological Society, p. 176, 1986.

Rossow, W.B., F. Mosher, E. Kinsella, A. Arking, M. Desbois, E. Harrison, P. Minnis, E. Ruprecht, G. Seze, C. Simmer, and E. Smith, ISCCP cloud algorithm intercomparison, *J. Clim. Appl. Meteor.*, 24, 877-903, 1985.

Saunders, R.W., An automated scheme for the removal of cloud contamination from

- AVHRR radiances over western Europe. *Int. J. Rem. Sens.*, 7 (7), 867-886, 1986.
- Serreze, M.S. and R.G. Barry, Synoptic activity in the Arctic Basin, 1979-85, *J. Climate*, 1988 (in press).
- Swain, P.H., S.B. Vardeman, and J.C. Tilton, Contextual classification of multispectral image data, *Pattern Recognition*, 13, 429-441, 1981.
- Vowinckel, E., Cloud amount and type over the Arctic, Publications in Meteorology, No. 51, Montreal: Arctic Meteorology Research Group, McGill University, p. 27, 1962.
- Wang, S., D.B. Elliot, J.B. Campbell, R.W. Erich, and R.M. Haralick, Spatial reasoning in remotely sensed data, *IEEE Trans. Geosci. Rem. Sens.*, GE-21, 94-101, 1983.
- Welch, R.M., S.K. Sengupta, and D.W. Chen, Cloud field classification based upon high spatial resolution textural features 1. gray level co-occurrence matrix approach, *J. Geophys. Res.*, 93 (D10), 12663-12681, 1988.
- Welch, R.M., K.S. Kuo, and S.K. Sengupta: Cloud field classification based upon high spatial resolution textural. Part 3: discrimination of cloud and surface features in polar regions from digitized imagery, 1989a, in press.
- Welch, R.M., M.S. Navar, and S.K. Sengupta, Cloud field classification based upon high spatial resolution textural features. Part 4: the effect of spatial resolution, *J. Geophys. Res.*, 1989b, in press.
- Weszka, J.S., C.R. Dyer and A. Rosenfield, A comparative study of texture measures for terrain classification, *IEEE Trans. Syst. Man. Cybern.*, SMC-6, 269-285, 1976.
- Wu, R., J.A. Weinman, and R.T. Chin, Determination of rainfall rates from GOES satellite images by a pattern recognition technique. *J. Atmos. Ocean. Tech.*, 2, 314-330, 1985.

Figures

Figure 1. The two study areas within the Arctic, one centered on the Kara and Barents Seas and the other covering much of the Canadian Archipelago and northern Greenland.

Figure 2. Visible (AVHRR channel 1) image of a portion of study area 1 on July 1, 1984. Novaya Zemlya is at upper center. Grid lines delineate $(250 \text{ km})^2$ regions.

Figure 3. The cloud only portion of Figure 2, as determined following the methodology given in Part I, Key and Barry [1989]. AVHRR channel 1 (visible) data are shown. Grid lines delineate 16×16 pixel cells, the size used in subsequent texture analyses.

Figure 4. Surface types corresponding to the area shown in Figure 2, from SMMR and SMMR-derived data. Surface categories are land, snow/ice cap, sea ice (all concentrations), open water, and a narrow coastal zone.

Figure 5. Effect of cell size on the computation of the mean of all cells over an artificially-generated data set. Means of classes are 10, 30, 50, 70, 90, and 110. The plots show the relative frequency of cells with various means, indicating mixtures of classes. Horizontal bars show frequency of "pure" cells; i.e., cells containing only one class.

Figure 6. Flow chart of the cloud analysis procedure. Cloud detection is addressed in Part I, Key and Barry [1989]. The analysis of cloud patterns is done both for $(250 \text{ km})^2$ regions, and over the entire image utilizing spectral and local textural measures. In the latter case, pixels are classified with a maximum likelihood procedure.

Figure 7. Low cloud fraction and cloud connectivity determined for each $(250 \text{ km})^2$ region within the study area shown in Figure 2. Cloud connectivity (CC) is smaller for highly disconnected cloud elements and larger for connected elements. By definition, CC is set to 1 if overall cloud fraction within a region is 0.

Figure 8. Texture of the clouds within the study area as measured by the maximum angular second moment in AVHRR channel 1. The procedure of moving windows and averaging to obtain texture for each pixel was used. See text for details. Lighter grey shades represent uniform cloud decks.

Figure 9. Maximum likelihood classification of cloudy pixels based on their spectral and local textural values. Cloud classes - 1: low thin cloud over water; 2: low thin cloud over ice; 4: low thick cloud smooth; 6: middle cloud rolls; 7: broken middle cloud, not linear; 10: high/middle broken; 12: cumulus. Additionally, clear (bold lines) and unclassified (U) areas are shown.

Figure 10. Manual classification of the cloud patterns shown in Figure 3. Classes are the same as in Figure 9.

Table 1

Summary of AVHRR spectral and textural measures.

Feature	Abbreviation
<i>SINGLE PIXEL SPECTRAL MEASURES:</i>	
Channels 1, 2, 3 reflectance	CH01, CH02, CH03
Channels 3, 4, 5 brightness temperature	CHT3, CHT4, CHT5
Ratios: 2/1, 3/1	RA21, RA31
Brightness temperature difference: channels 4-5	DF45
<i>CELL SPECTRAL/TEXTURAL MEASURES (channels 1, 3, 4):</i>	
Spectral Mean	MEAN
Standard Deviation	SD
Grey Level Difference (mean, maximum, range over 4 directions):	
Mean	MMEAN, XMEAN, RMEAN
Contrast	MCON, XCON, RCON
Angular Second Moment	MASM, XASM, RASM
Entropy	MENT, XENT, RENT
Roberts Gradient	RG
Vector Strength	VECTOR
Fourier Measures	
Streakiness Factor	SF
Cell Intensity	CI
Maximum Ring Wavelength	WAVE

Table 2

The first four principal components of the nine spectral variables.
Underlined features are used in the final classification.

Component	Features	% Variance
1	Channel <u>3</u> , 3-4 difference, 3/1 ratio	27.0
2	Channels <u>4</u> and 5	25.5
3	Channels <u>1</u> and 2	25.1
4	4-5 difference	12.0
TOTAL		89.6

Table 3

First twelve principal components of the textural variables.
Subscripts refer to AVHRR channel numbers.

Component	Features	% Variance
1	Channel 4: all except those listed below	23.2
2	Channel 3: all except those listed below	19.4
3	Channel 1: all except those listed below	18.2
4	Channel 1: MEAN, VECTOR, MASM, XASM	7.0
5	Channel 3: RASM, RENT	
	Channel 4: RASM	4.9
6	Channel 1: RASM, RENT	3.9
7	MEAN ₃	2.4
8	CI ₁ , RCON _{1,3,4} *	2.2
9	SF ₃ , WAVE ₃ *	2.1
10	CI ₃	1.8
11	SF ₄ , WAVE ₁ , CI ₁ *	1.8
12	CI ₄ , WAVE ₄ , WAVE ₃ *	1.7
TOTAL		88.6

* Loading ≤ 0.4 ; no large loading on any component.

Table 4

Texture variables retained after divergence parameter analysis.
Underlined features ranked highly for cloud class pairs and are used
in the final analysis. Superscripts refer to principal components.

Channel	Texture Features
1	<u>RG</u> ³ , <u>VECTOR</u> ⁴ , MMEAN ³ , XMEAN ³ , MASM ⁴ , <u>XASM</u> ⁴ , <u>MENT</u> ³ , RENT ⁶ , XENT ³ , <u>SD</u> ³
3	RG ² , VECTOR ² , MMEAN ² , XMEAN ² , MASM ² , XASM ² , MENT ² , XENT ² , SD ²
4	<u>RG</u> ¹ , <u>VECTOR</u> ¹ , <u>XASM</u> ¹ , <u>MENT</u> ¹ , <u>SD</u> ¹

Table 5

Percent of the study area (Figure 2, including surface areas) predicted for each class by the maximum likelihood classification (horizontal) shown in Figure 9 and the manual interpretation (vertical) shown in Figure 10. See text for class number references. Cloud occupies 51.6% of the image. Also given is the percent correctly classified in each class. Total percent correctly classified: 68.3.

Manual Class	Maximum Likelihood Class						
	1	2	4	6	7	10	12
1	2.96	0.27	0.54	0.01	0.57	0.05	0.00
2	0.83	5.05	1.73	0.06	0.04	0.00	0.00
4	0.12	0.11	2.70	0.49	1.69	0.01	0.00
6	0.00	0.00	0.08	10.04	1.40	0.56	0.00
7	0.01	0.00	0.49	4.82	6.80	0.56	0.00
10	0.00	0.00	0.03	1.79	0.09	7.67	0.00
12	0.00	0.02	0.00	0.00	0.01	0.00	0.00
Total (MLC)	3.92	5.45	5.57	17.21	10.60	8.85	0.00
% Correct	75.5	92.7	48.5	58.3	64.2	86.7	0.0

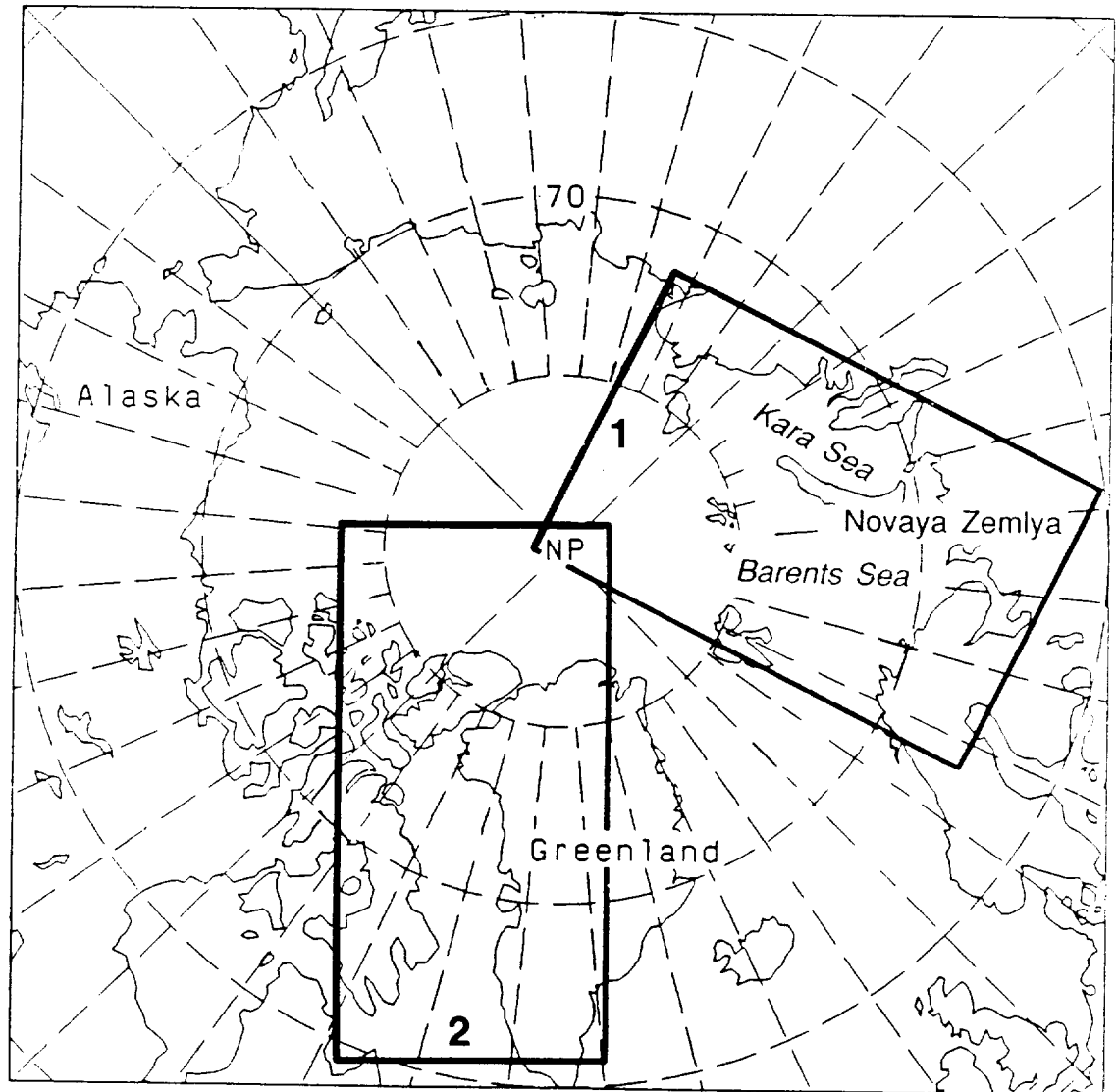


Fig 1

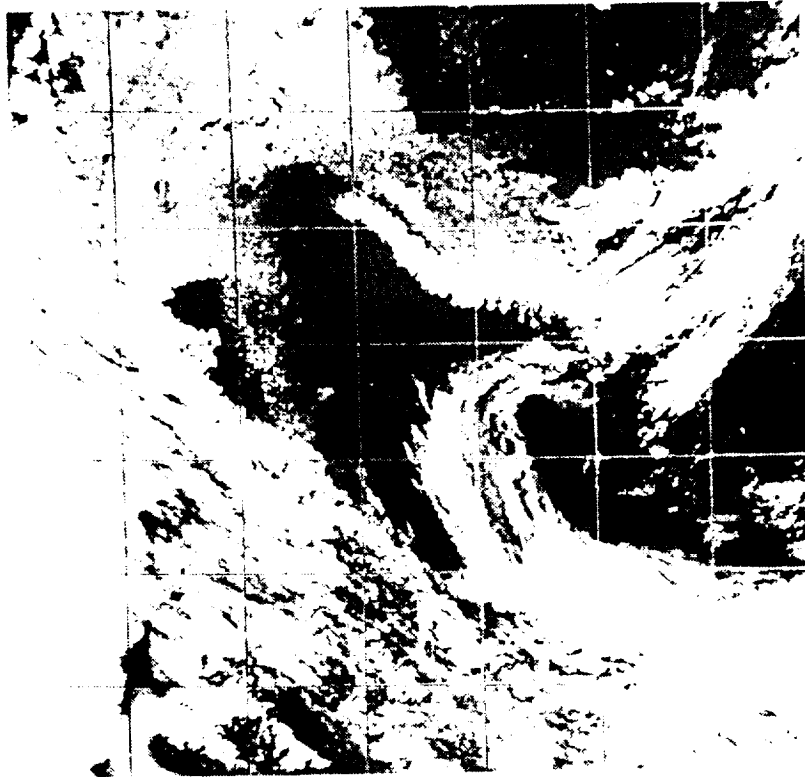


Fig 2

ORIGINAL PAGE
BLACK AND WHITE PHOTOGRAPH

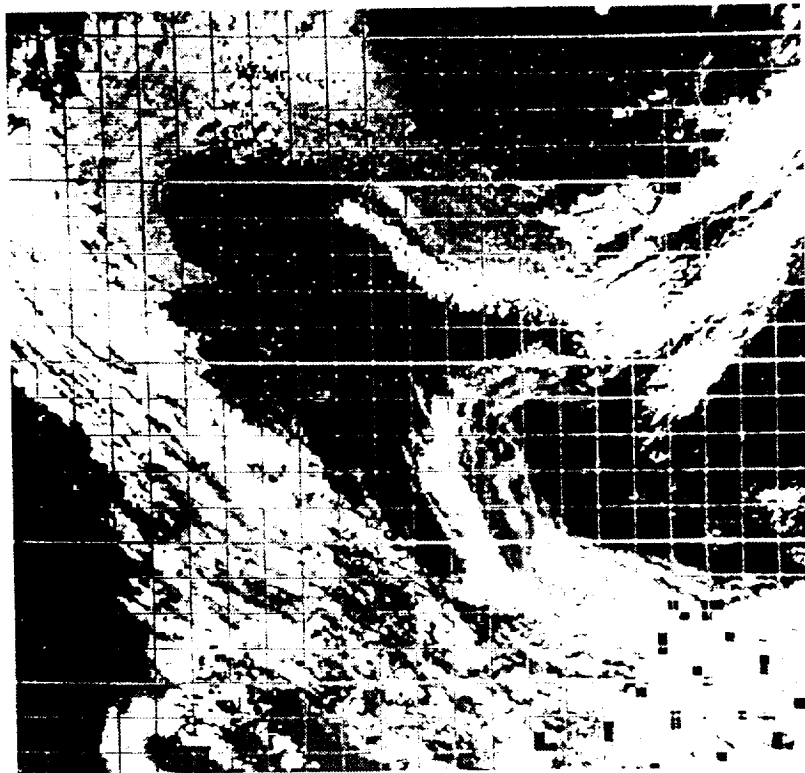


Fig 3

ORIGINAL PAGE
BLACK AND WHITE PHOTOGRAPH

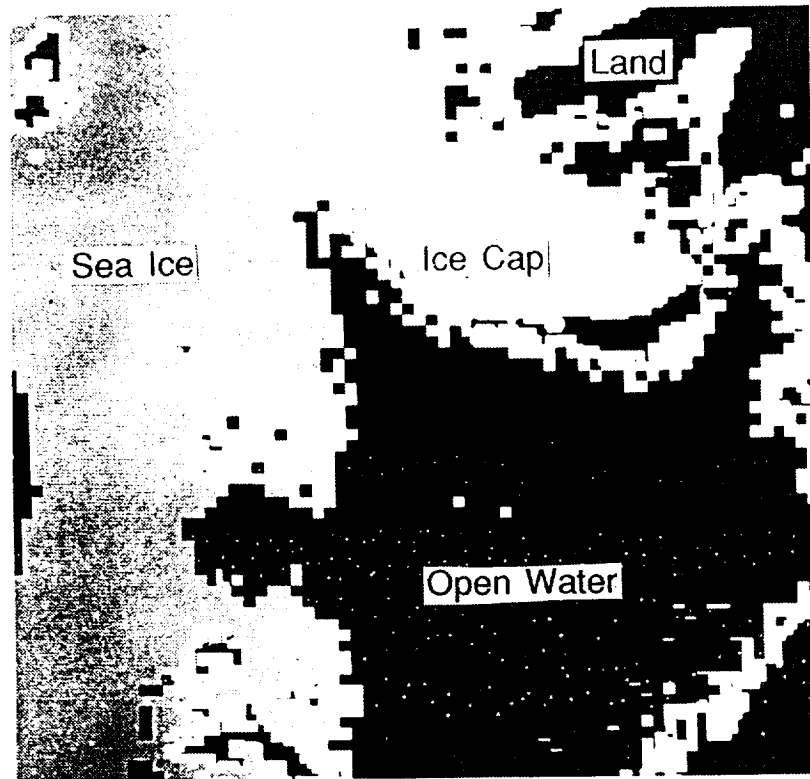


Fig 4

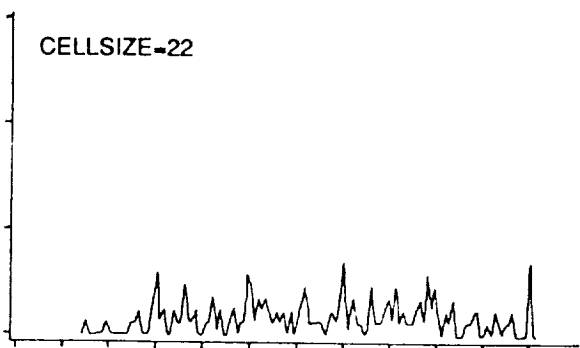
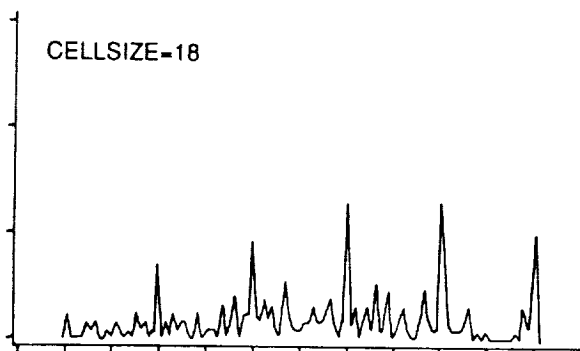
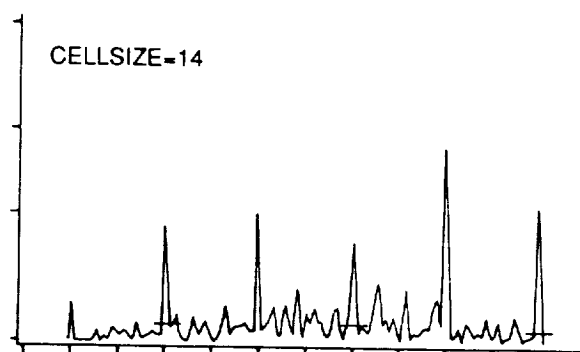
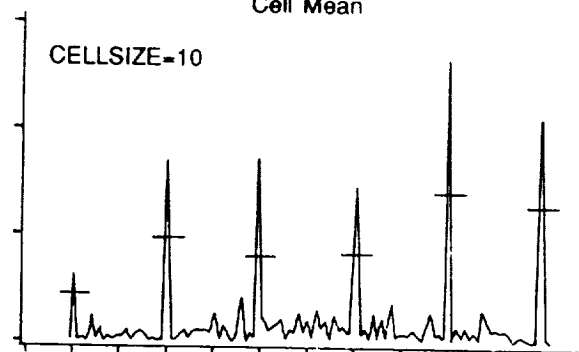
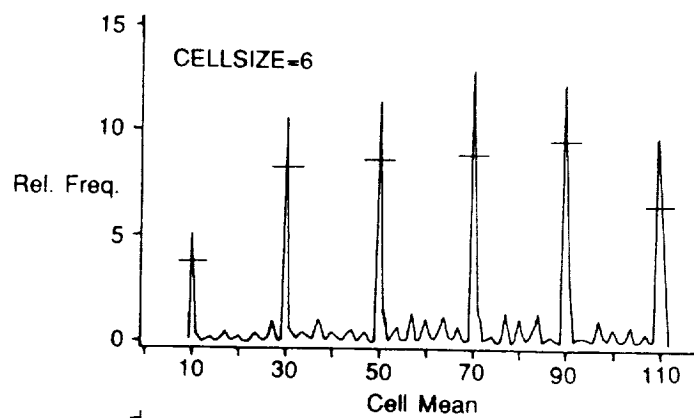


Fig 5

Land/ice cap mask
SMMR 18, 37 GHz ->
Sea Ice Concentration
(7 Days)

SURFACE
IDENTIFICATION
Snow/Land
Ice/Water

AVHRR ch. 1,3,4,3-4 ->
(7 Days)

CLOUD DETECTION
Surface composite
Cloud maps

Cloud-only images
(AVHRR ch. 1,3,4) ->

ANALYSIS OF
CLOUD PATTERNS

GRID CELL
CLOUD DESCRIPTION

(250 km)
e.g., ISCCP-scale

Temp., Albedo
Cloud fraction
at all levels,
Cloud/background
connectivity
Fourier measures

MESOSCALE
CLOUD PATTERN
IDENTIFICATION

Spectral/Textural

TEXTURE
Mean of local
texture (16x16)
for each pixel

GLD Measures

CLASSIFICATION
OF CLOUD PIXELS

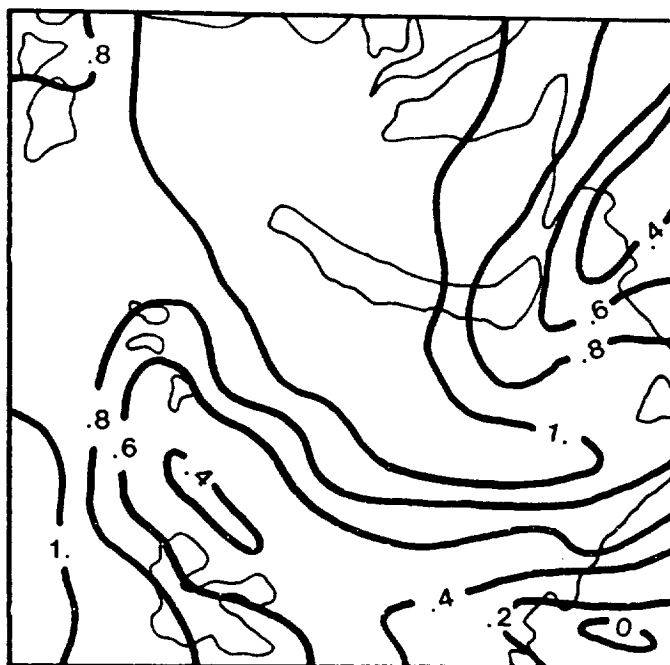
Maximum
Likelihood

Training
Data ->

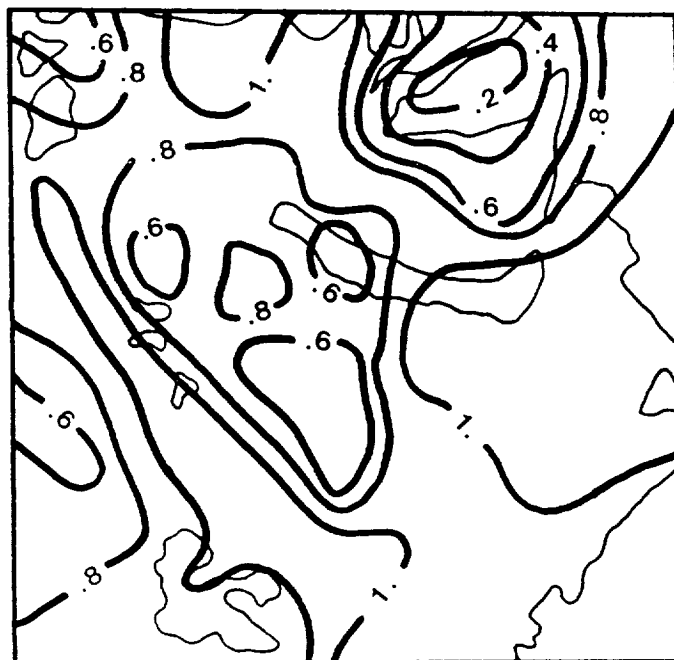
CLOUD
CLIMATOLOGY
(Parameters over
time and space)

RELATIONSHIP TO
SYNOPTIC SYSTEMS

Low Cloud Fraction

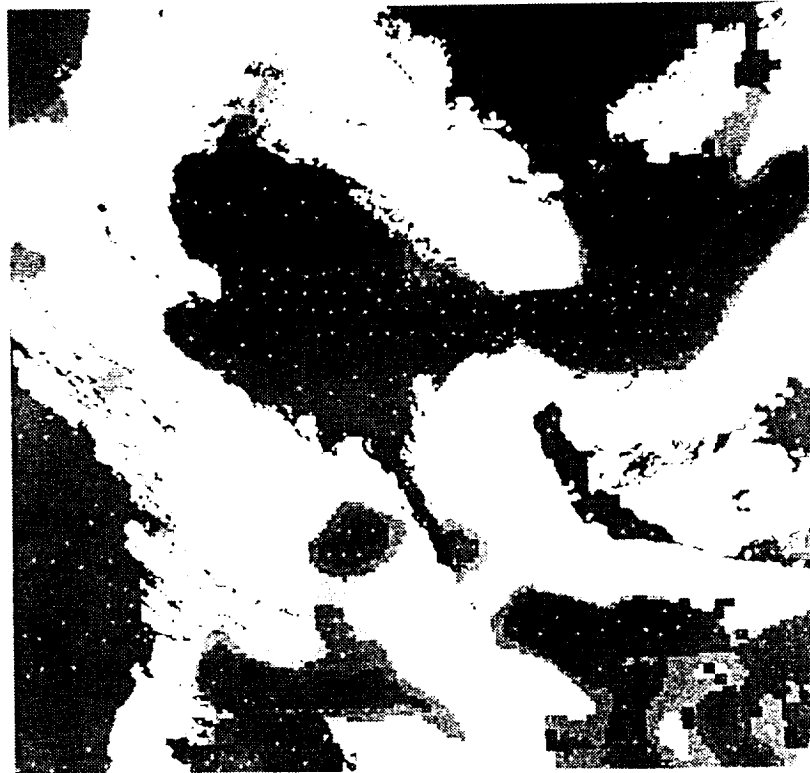


Cloud Connectivity



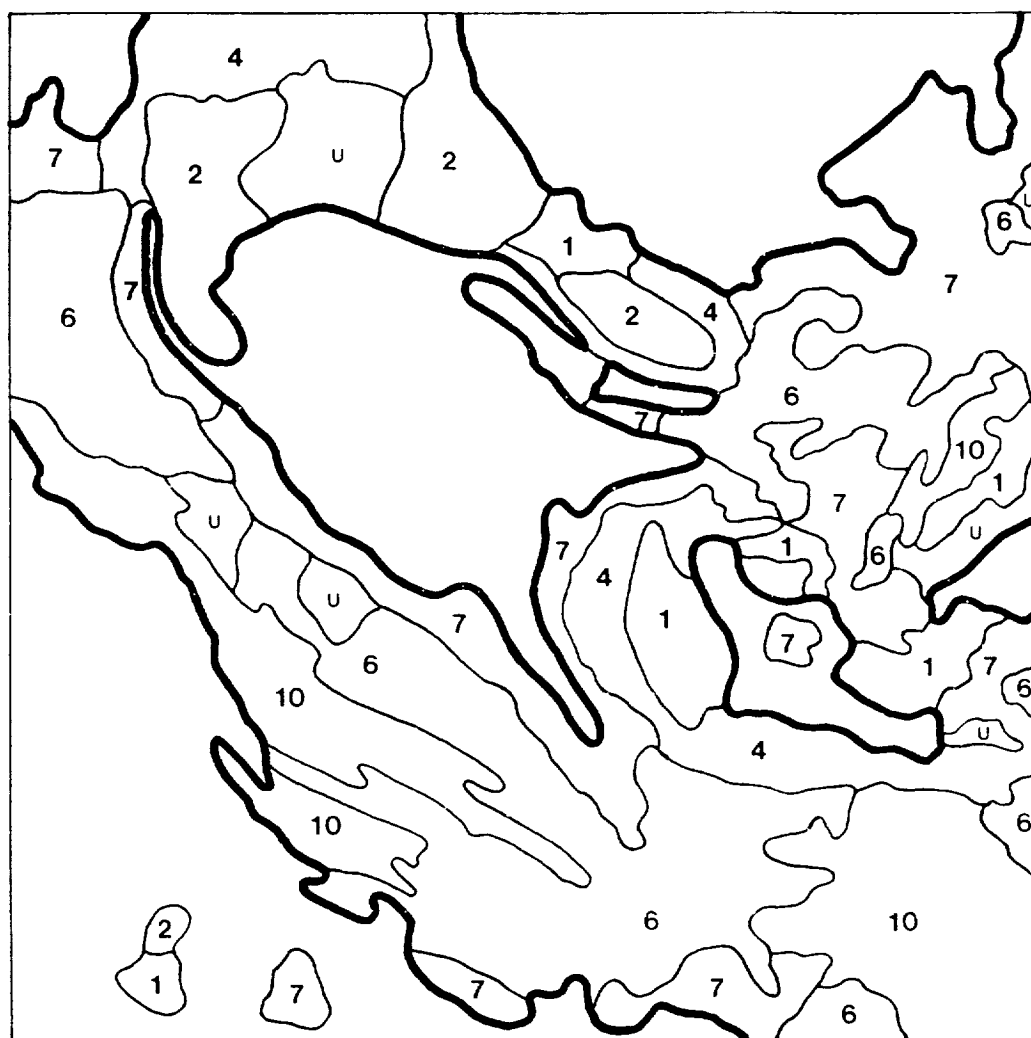
1157

ORIGINAL PAGE
BLACK AND WHITE PHOTOGRAPH



508

Maximum Likelihood Classification



Manual Classification

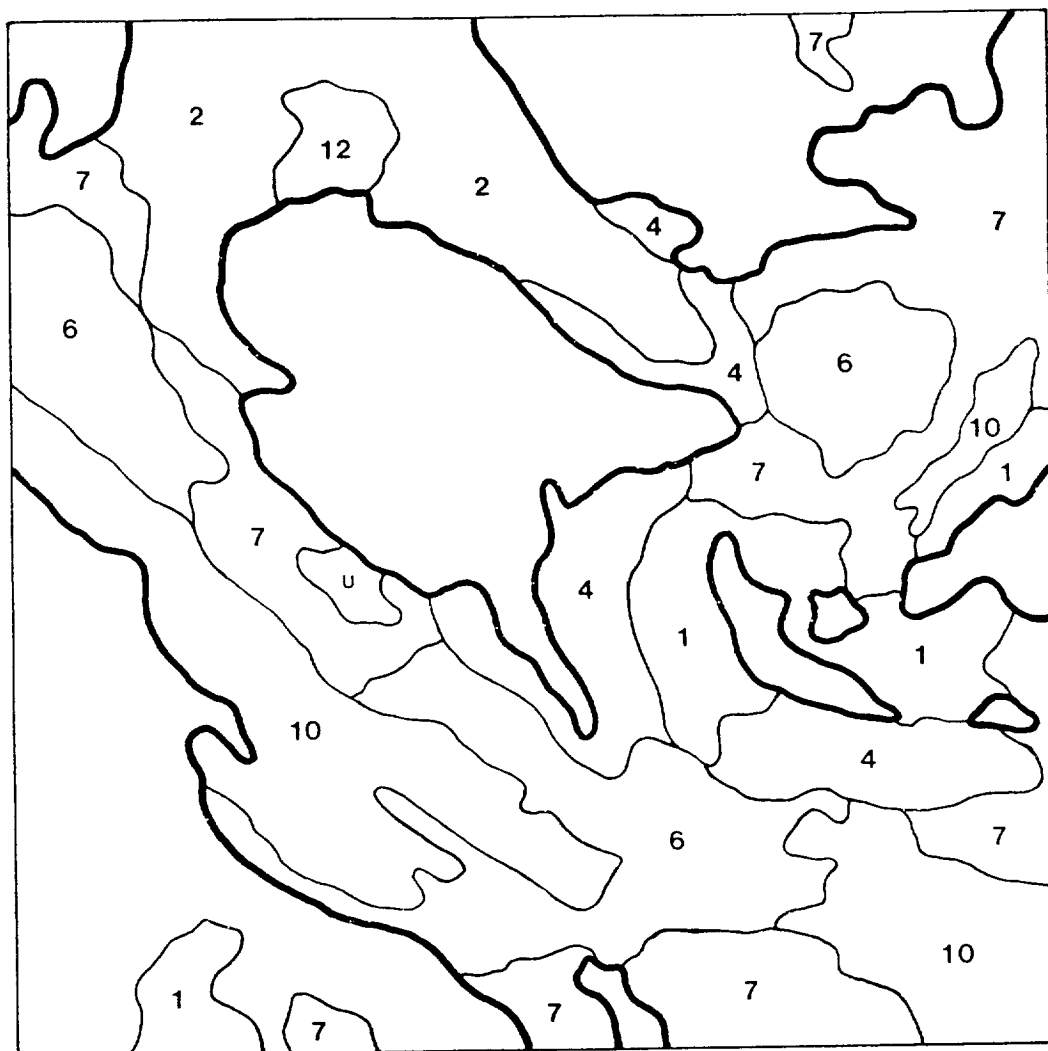
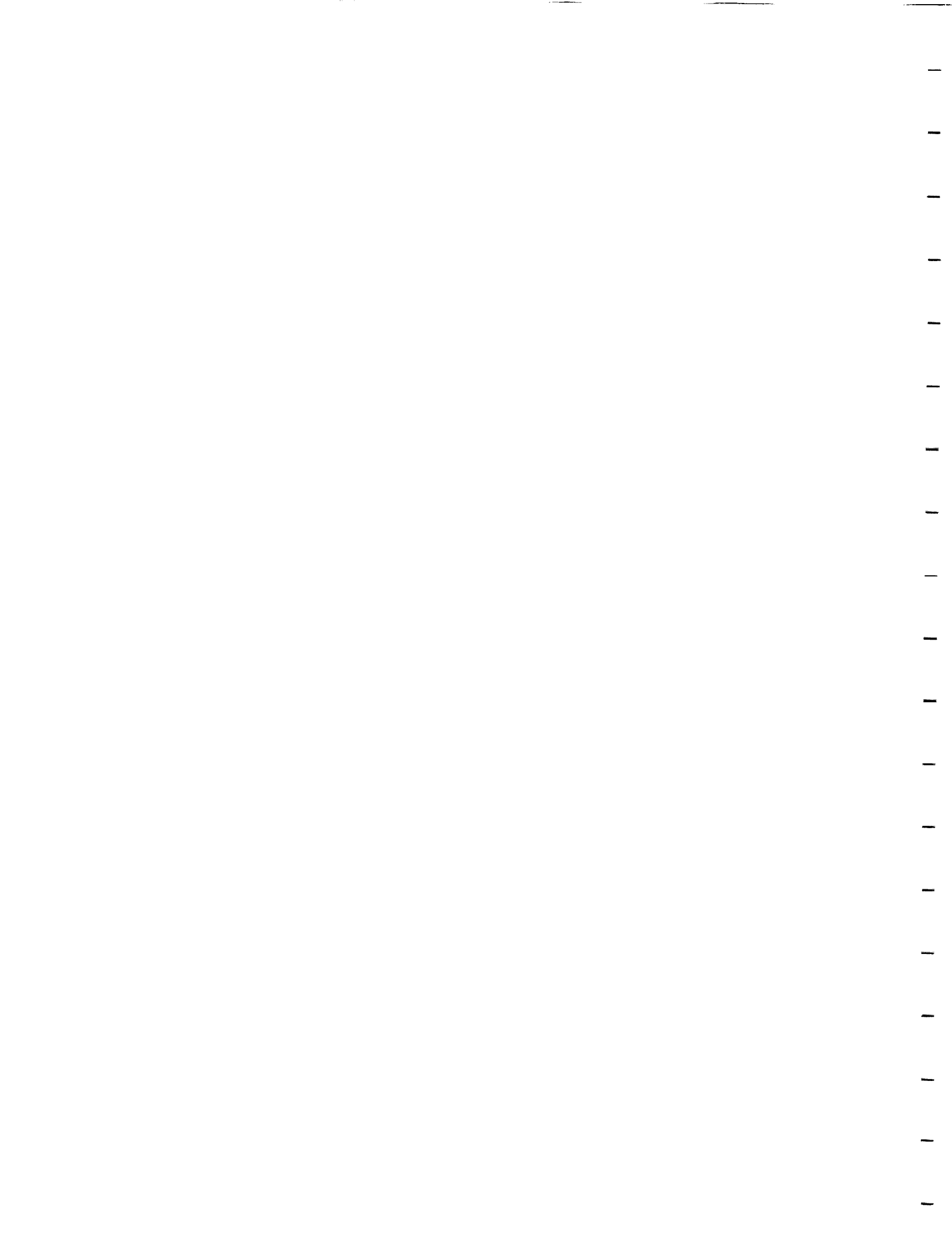


Fig 10

ATTACHMENT 7

INTERCOMPARISON OF SATELLITE-DERIVED CLOUD ANALYSES



Intercomparison of satellite-derived cloud analyses for the Arctic Ocean in spring and summer

K. McGUFFIE†, R. G. BARRY‡, A. SCHWEIGER‡,
D. A. ROBINSON§ and J. NEWELL‡

†Department of Geography, University of Liverpool, Liverpool, England

‡Cooperative Institute for Research in Environmental Sciences and Department of Geography, University of Colorado, Boulder, Colorado, U.S.A.

§Lamont-Doherty Geological Observatory of Columbia University, Palisades, New York, U.S.A.

(Received 5 February 1987; in final form 10 July 1987)

Abstract. Several methods of deriving Arctic cloud information, primarily from satellite imagery, have been intercompared. The comparisons help in establishing what cloud information is most readily determined in polar regions from satellite data analysis. The analyses for spring-summer conditions show broad agreement, but subjective errors affecting some geographical areas and cloud types are apparent. The results suggest that visible and thermal infrared data may be insufficient for adequate cloud mapping over some Arctic surfaces.

1. Introduction

There is wide recognition of the importance of accurate global cloud cover data for climate research (Schiffer and Rossow 1983) and efforts to determine the character of global cloud cover go back many decades (MacDonald 1938). Cloud observations describe the fractional coverage of the sky (as observed from a point or, in the case of satellite data, for a particular area), the appearance of the cloud (stratiform, cumuliform) and height of the cloud base above the surface (see, for example, World Meteorological Organization 1956). Cloud type is determined for three levels, low, middle and high cloud. None of the existing global cloud climatologies provides comprehensive information for the polar regions. Of the 15 distinct global cloud climatologies reviewed by Hughes (1984), only two (Beryland and Strokina 1980, Sherr *et al.* 1968) provide information about both poles while a further four have information for one or other of the poles.

Polar cloud cover may play an influential role in ice-albedo feedback (Barry *et al.* 1984 b), which remains a crucial issue in the concern over CO₂ (and other greenhouse gas) global warming effects. Shine and Crane (1984) used a thermodynamic sea ice model to show that changes in Arctic cloudiness can have a marked effect on sea ice conditions. It is therefore desirable that the character of Arctic cloud be more reliably established. The most comprehensive cloud climatologies for the Arctic, by Vowinckel (1962), Huschke (1969) and Gorshkov (1983), are derived primarily from surface observations. They show a broad agreement over much of the Arctic in regard to the seasonal cycle of total cloud amount, namely a winter minimum and a summer maximum, as illustrated by Huschke's data in figure 1. However, there is less agreement between the climatologies regarding the geographical distribution of cloud cover, particularly in the case of low cloud in winter. As noted by Crane and Barry

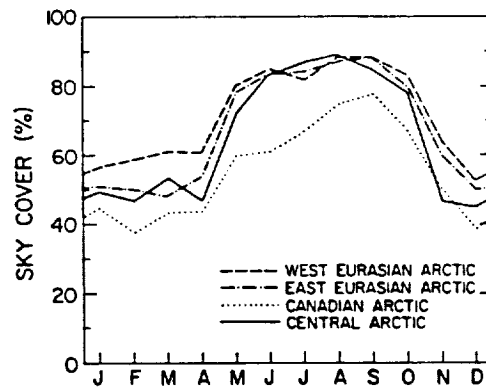


Figure 1. Annual variation of total cloud amount in four sections of the Arctic (from Huschke 1969).

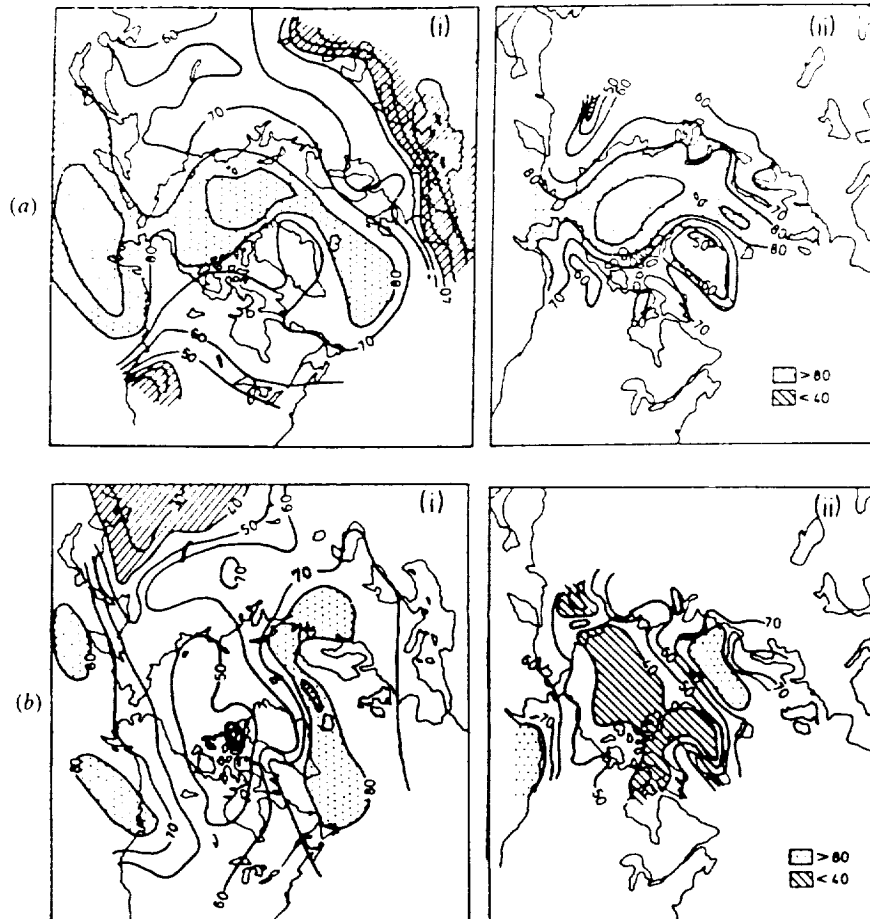


Figure 2. Mean total cloud amount (per cent) over the Arctic in (a) July (b) January according to (i) Beryland and Strokina (1980) and (ii) Vowinckel (1962).

(1984), for example, Voskresenskiy and Chukanin (1959) show a much lower frequency of occurrence of low clouds over the central Arctic Basin than does Vowinckel (1962). There are also considerable differences between the mean maps of total cloud for January and July presented by Vowinckel (1962) and those of Berlyand and Strokina (1980) (figure 2). This may be due in part to the incorporation in the latter source of some satellite observations.

Prior to the advent of satellites there were few observational studies of Arctic cloud. There were no meteorological stations in the Canadian Arctic Archipelago and northern Greenland until the late 1940s and, at most, there are only two or three drifting stations on the pack ice at any one time. Moreover, accurate reporting of cloud in the Arctic presents special problems for the observer. Loewe (1935, cited by Putnins 1970) noted that cloud observations in Greenland were not very precise, especially during the polar night. Ice crystal precipitation may occur even in the absence of cloud (Astapenko 1960). Even with present-day satellite radiance measurements, cloud cover determination in polar regions remains difficult due to the overall similarity of signatures over clouds and snow or ice in both visible and infrared wavelengths.

This study uses the results of three independent satellite-based analyses of Arctic cloud conditions for selected periods in spring and summer. The cloud cover maps were prepared using different techniques to identify and classify cloud, but all of the results were primarily derived from Defense Meteorological Satellite Program (DMSP) images. The scope of the intercomparison is determined by the availability of overlapping time intervals analysed in the various studies. Although somewhat limited, there is sufficient overlap to provide useful intercomparisons.

2. Analysis techniques

In this section we review the techniques used in the individual cloud analyses (termed nephanalyses) as a prelude to the comparison of their results. Of the three techniques which are discussed here, two are manual nephanalyses and the third is a computer-based automatic algorithm. The table summarizes the data sources and mapping techniques.

The automated algorithm is the US Air Force 3D-nephanalysis which has been described by Fye (1978) and more briefly in Hughes and Henderson-Sellers (1985). It categorizes cloud cover fraction and cloud level over the northern hemisphere on a 46×46 km grid. Over areas of snow and ice cover it is largely based on infrared imagery and surface station data. Each 46×46 km grid box contains 64 'pixels' which are reduced statistically to a single output every 3 hours (see Hughes and Henderson-Sellers 1985). Modes are identified in the frequency distribution of infrared counts and used to establish up to four clusters with thermally similar characteristics. An infrared radiance temperature is determined for each cluster and used to decide on the presence of cloud/no cloud based on a threshold method. The number of cloudy elements (5.5 km) over the 46 km grid is then established and an average value assigned to that grid point. Finally, surface and aircraft observations are integrated with the satellite data, together with a continuity field comprising data from the previous analyses, to fill in missing values. McGuffie (1985) uses the full spatial and temporal resolution of the 3D-neph data for the analyses reported here.

Technique 2 uses a manual classification of cloud characteristics for 3-day intervals during April–June in both 1979 and 1980 for areas north of 70°N . The 3-day interval sampling is considered to be sufficient to indicate the overall cloud climatology, given the persistence of Arctic weather systems. Additional dates were also analysed to

Characteristics of the data sources and classification procedures used for the three cloud mapping techniques.

	McGuffie 1985	Barry <i>et al.</i> 1986	Robinson <i>et al.</i> 1985
Data source	3D-neph product from DMSP visible and IR digital data	DMSP visible and IR mosaic images	DMSP visible and IR orbital images
Pixel resolution	5.5 km	5.4 km	2.7 km (supplementary 0.6 km)
Data sampling grid interval	~45 km	~42 km (digitized from analysed cloud maps)	~190 km
Temporal sampling	3-hourly data	~3-day	~3-day
Cloud identification criteria	Cloud/no-cloud threshold set by histogram analysis of visible and IR values over 64 pixels. Grid point cloud fraction is box-averaged value	Visual recognition (1) cloud-free areas, stratiform/cumuliform areas from visible image (2) low/middle/high cloud levels from IR relative grey scale and evidence of cloud shadows	Visual recognition of cloud and surface features
Cloud classification	Total cover (per cent) (3D-neph also gives cloud type and estimated heights of base and top)	Cloud/cloud-free for each level mapped for synoptic and mesoscale features (typically $\geq \frac{1}{2}$ –1° latitude in extent)	Cloud-free, thin/moderate/thick cloud

provide 10-day samples for each of eight mean sea-level pressure patterns identified by a computer classification, as discussed by Barry *et al.* (1986, 1987). Shortwave band (0.4–1.1 μm) DMSP images were used to identify areas of open conditions (largely cloud free), stratiform (flat, featureless) cloud and 'cumuliform' (cells or rolls with some vertical development showing texture on the images). Open conditions were identified particularly on the basis of lead patterns in the ice being visible. The infrared (10.5–12.5 μm) images were used, together with shortwave evidence of cloud shadows, to divide the cloud into low, middle or high categories according to relative grey scale. The 5.4 km resolution computer-rectified and gridded mosaic images allowed cloud covered areas of extent $\geq c. \frac{1}{2}$ –1° latitude to be outlined. These maps were subsequently digitized as cloud covered or cloud free for the three levels at each point on a 42×42 km grid. The cloud type information was not analysed digitally and is not discussed further here. The low cloud amounts for the April monthly average and pressure-pattern average maps are weighted by 0.5 to eliminate an apparent bias in April caused by low Sun angle and Arctic haze effects. This is discussed more fully in Barry *et al.* (1987).

The second manual technique (Robinson *et al.* 1985, 1986a) used available DMSP direct readout images with 0.6 km resolution for the Alaskan sector and 2.7 km resolution orbital strips elsewhere. Clouds were visually differentiated from snow and ice, primarily by the characteristic large-scale features of the pack ice fields identified in shortwave imagery. In addition, certain cloud fields, particularly those located in cyclonic regions, were recognized by their characteristic shapes and patterns. These

were often evident in both shortwave and infrared imagery. Three cloud categories were recognized: thin cloud (surface features clearly recognizable but with reduced contrast from cloud-free skies), moderate cloud (surface features marginally recognizable) and thick cloud. Cloud cover was charted at about 3-day intervals from mid-May to mid-August of 1977 and 1979 and digitized using a standard grid with an approximate grid interval of 190 km.

Specific intercomparisons of the categories used by Robinson *et al.* (1985) and Barry *et al.* (1986) for 24 June and 13 July 1979 suggest that thick corresponds to cloud areas with vertical development (cumuliform) and that moderate cloud would usually be stratiform cloud at the middle level. A check for sample days on the possible differences in interpretation that might arise as a result of using the 5.4 km rather than the 2.7 km resolution imagery suggests little or no effect for the categories of open or cumuliform cloud.

3. Intercomparison of results

We begin by examining the results for the monthly time scale. In general, the analyses show more cloud over the Subarctic than over the Arctic Ocean. McGuffie's data for May 1979 show that cloud decreases towards the pole with a slight increase again near the centre of the basin, a phenomenon which was also reported by Robinson *et al.* (1985). The zonal mean cloud amount determined by R.G. Crane (in Barry *et al.* 1984a) for May 1979 and May 1980, using a manual interpretation of large-scale features on DMSP imagery, also illustrates this tendency (figure 3). Although May 1980 appears to have been slightly more cloudy, the general pattern has remained the same. These results are all much lower than the climatology of Vowinckel (1962) who describes cloud as *increasing* from North America towards the pole in May and the other summer months, reversing the pattern of April. Possible reasons for this contradiction are discussed further below.

Figure 4 shows the geographical distribution from the 3D-nephanalysis and the manual interpretation of Barry *et al.* (1986) for the month of May 1979. The results for the 3D-nephanalysis in figure 4(a) refer only to the common dates available from the manual analysis for May. The 3D-nephanalysis shows substantially less cloud over the Arctic than the manual analysis. In fact, the 3D-nephanalysis agrees better, in terms of

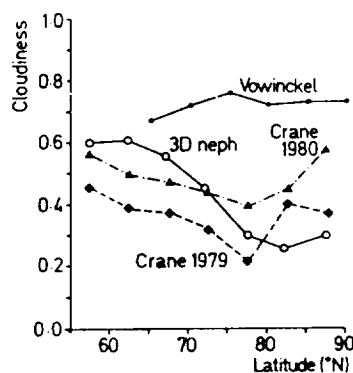


Figure 3. Zonal mean cloud amounts 58°–90°N in May showing mean values (Vowinckel 1962), manual analysis for 1979 and 1980 (Crane in Barry *et al.*, 1984a) and 3D-nephanalysis of 1979 (McGuffie 1985).

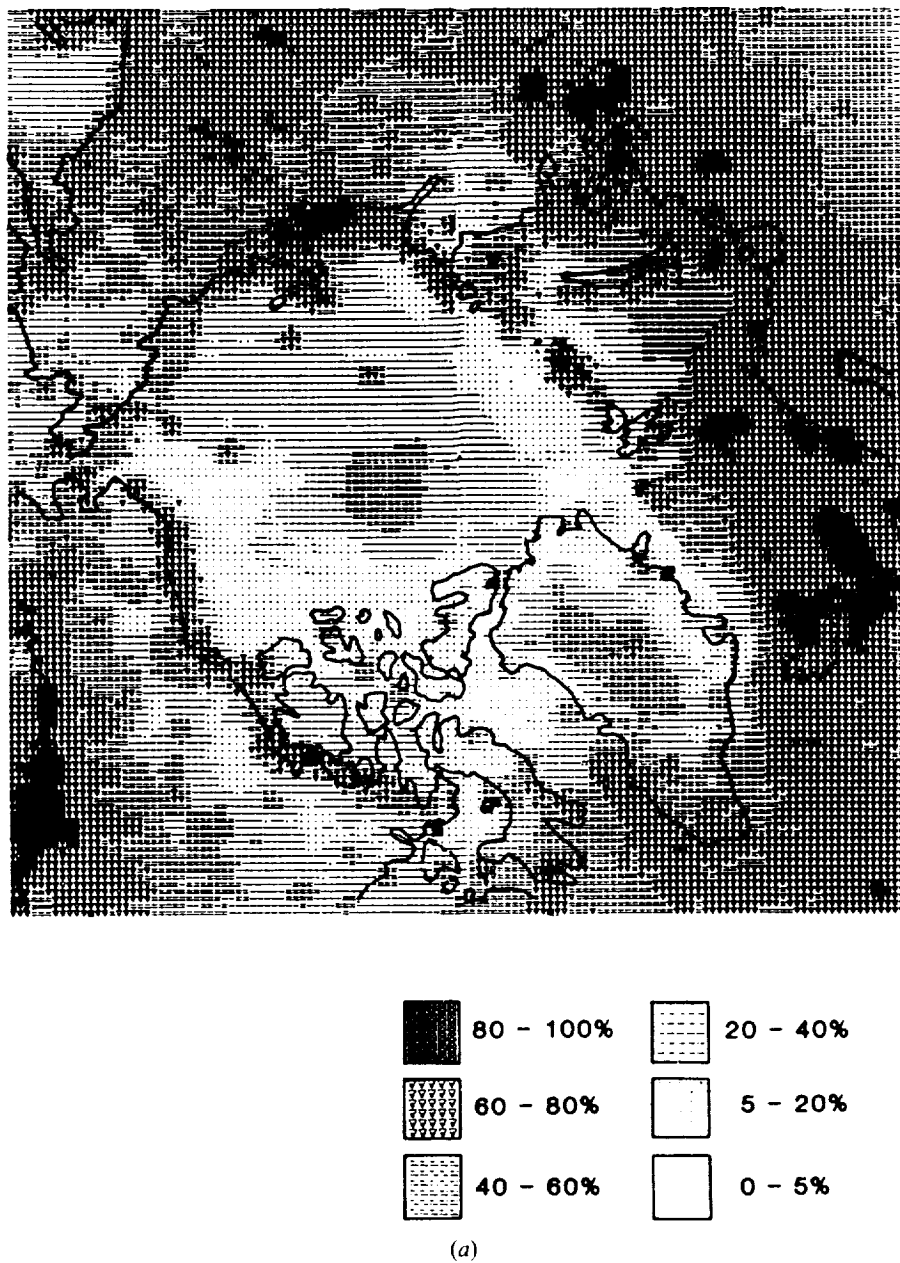
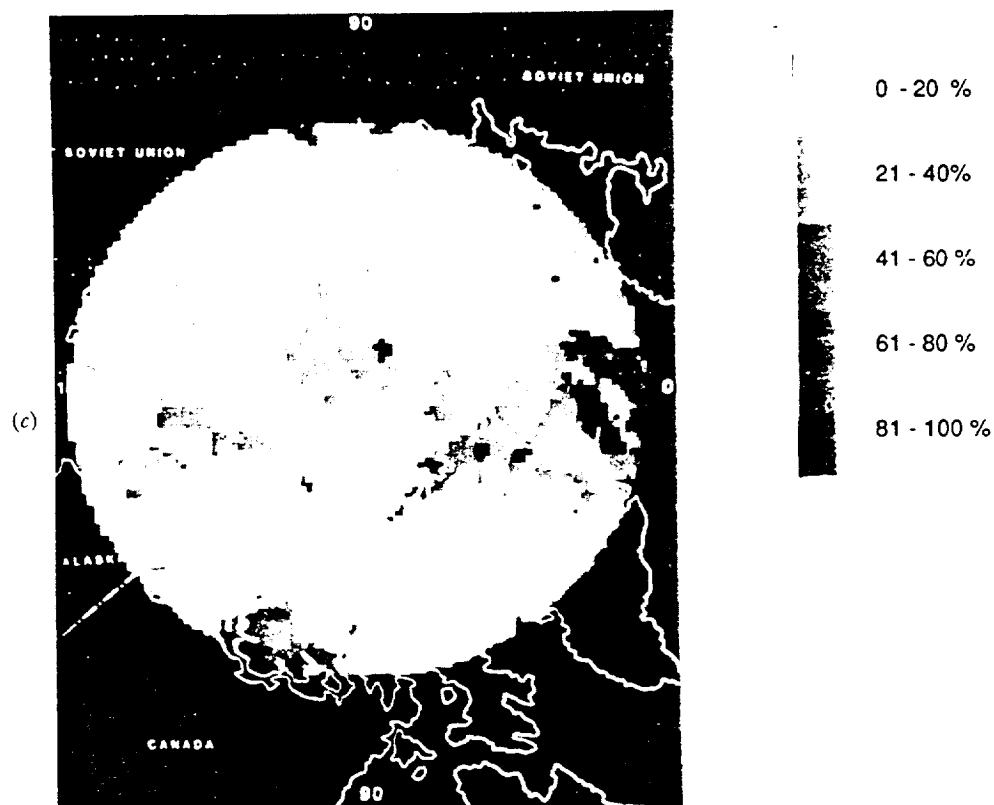
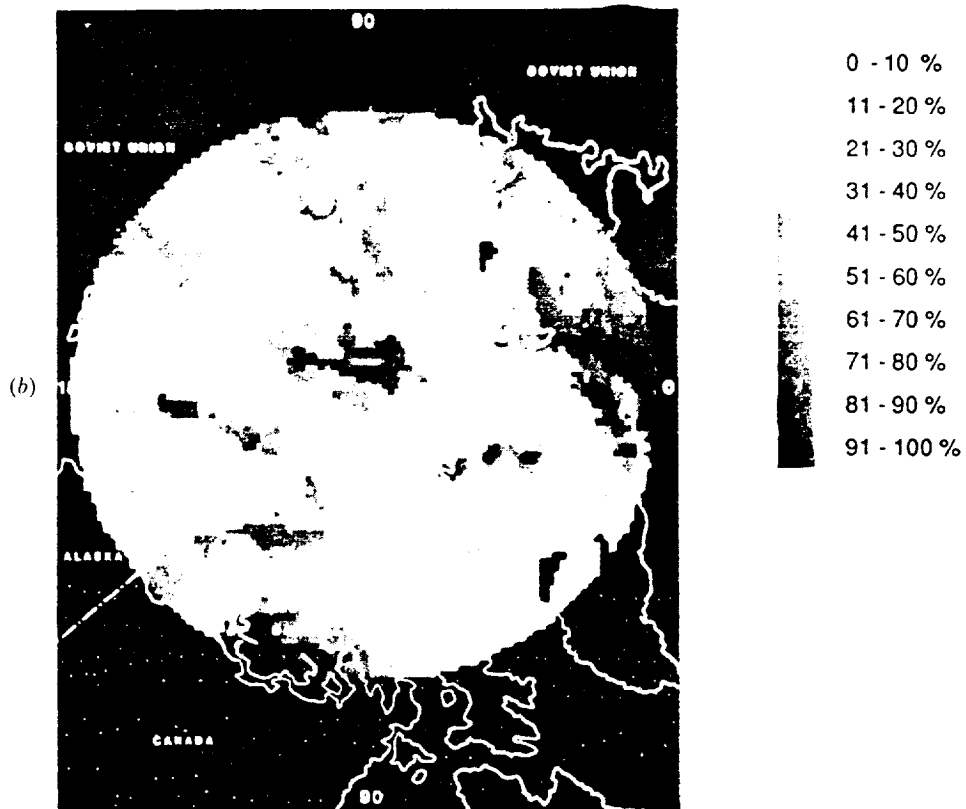


Figure 4. Mean total cloud amount for May 1979 (a) from 3D-nephanalysis data, per cent (McGuffie 1985), sampled at 3-day intervals and (b) from manual analysis of DMSP images at 3-day intervals; per cent (Barry *et al.* 1986), and (c) middle level cloud from the corresponding analysis to (b); per cent.



ORIGINAL PAGE
BLACK AND WHITE PHOTOGRAPH

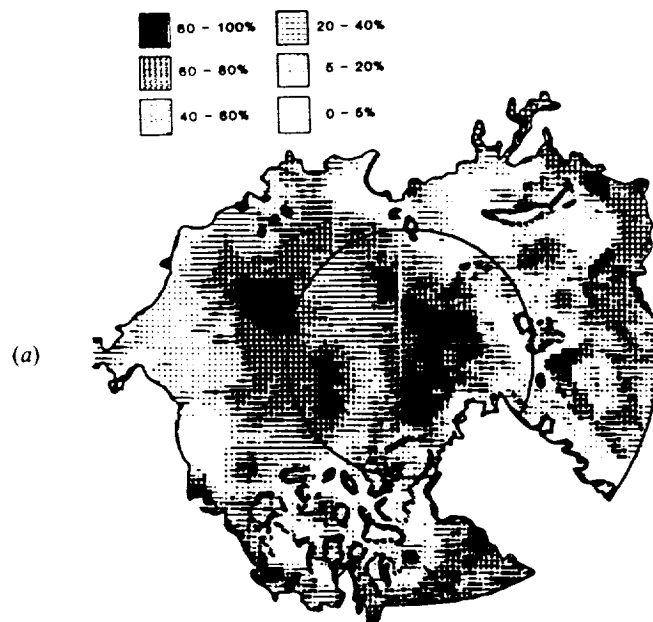
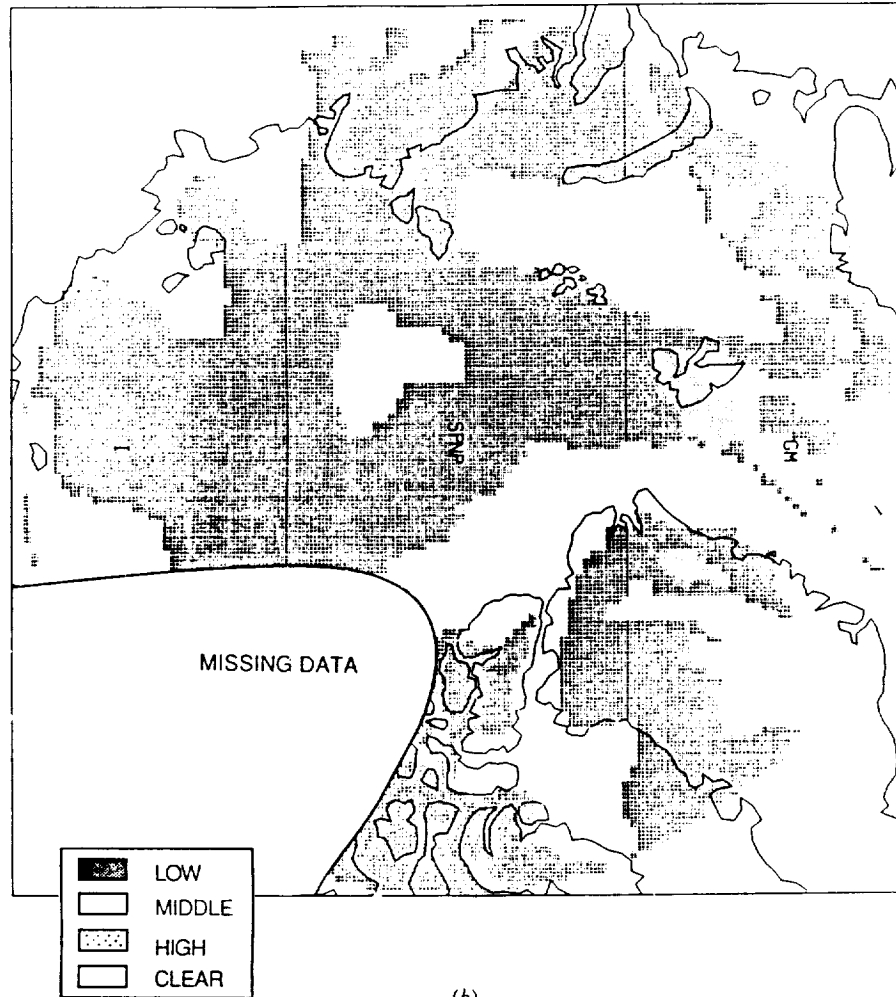


Figure 5. Total cloud amount over the Arctic for 10 April 1979 (a) from 3D-nephanalysis (McGuffie 1985) and (b) from manual analysis (for 9 April) (Barry *et al.* 1986), and (c) mean sea-level pressure analysis (millibars) for 10 April (Thorndike and Colony 1980).

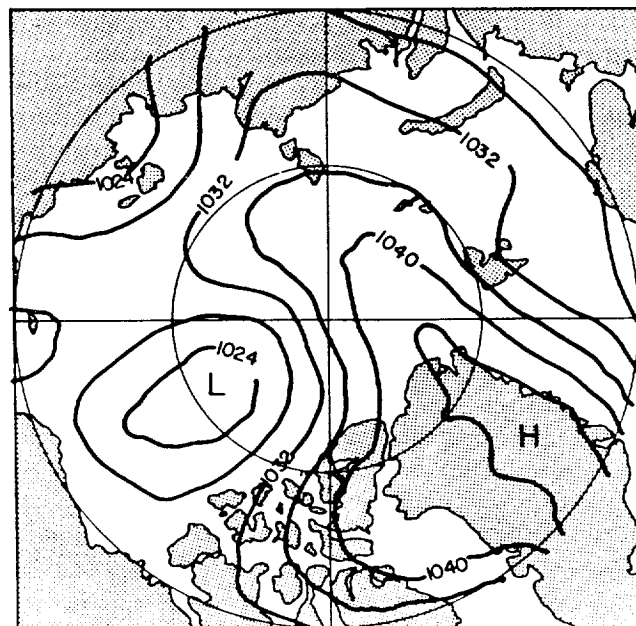
cloud amount over the central Arctic, with the middle level cloud analysis of the manual technique (figure 4 (c)). This result is probably due to the temperature structure of the Arctic atmosphere in summer, when the near-surface layers are almost isothermal and only middle and higher-level clouds may be different enough in temperature to be separable from the ice surface. Both analyses agree that there is a cloudiness maximum over the North Atlantic Ocean, associated with cyclone activity. There is disagreement in the cloud cover over Greenland, where the 3D-nephanalysis reports a cloud maximum in opposition to the other retrieval. This may be due to the misidentification of the high ice plateau as cloud by the automated algorithm. The mean surface pressure map for May 1979 indicates a large anticyclone over northern Greenland which supports the case for a cloud-free area. Both analyses agree on the presence of a relatively cloud-free area between east Greenland and Spitzbergen but, in the Beaufort Sea, the 3D-nephanalysis shows less cloud than the manual technique.

Next, the results of the 3D-nephanalysis for individual daily cloud maps are compared with those of the manual technique of Barry *et al.* (1986) for April. On these maps, cloud data are not included from the 3D-nephanalysis over Greenland. The 12 GMT mean sea-level pressure maps from Thorndike and Colony (1980) incorporate measurements from 16 drifting buoys on the ice and up to 70 coastal and land stations. Figures 5–7 show a generally good agreement in the patterns of total cloud obtained by the 3D-nephanalysis and technique 2. In figure 5 for 10 April, 1979, with high pressure over Greenland and the central Arctic, both analyses show an area of cloud located over the pole and a relatively clear area north of the Arctic coastline, in the Barents Sea and around Greenland. In comparison with figure 5, which resembles the mean cloud pattern for April 1979, there is a very different cloud distribution for 15 April (figure 6 (a) and (b)). The pressure pattern features a high over the East Siberian

ORIGINAL PAGE
BLACK AND WHITE PHOTOGRAPH



(b)



(c)

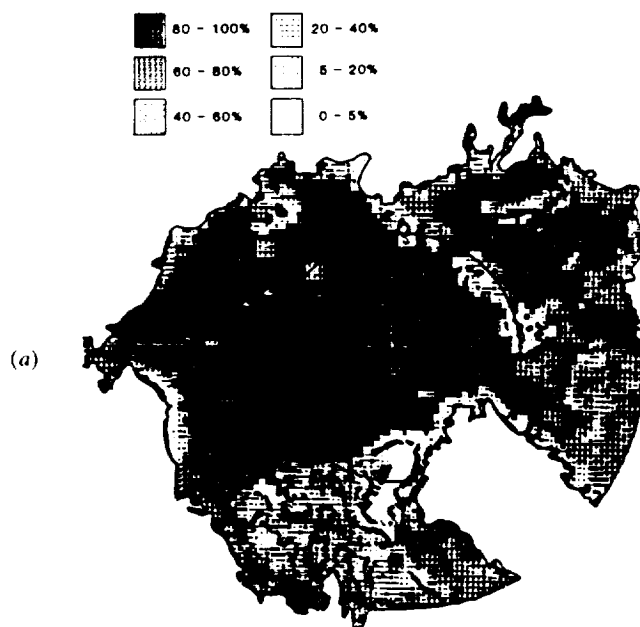


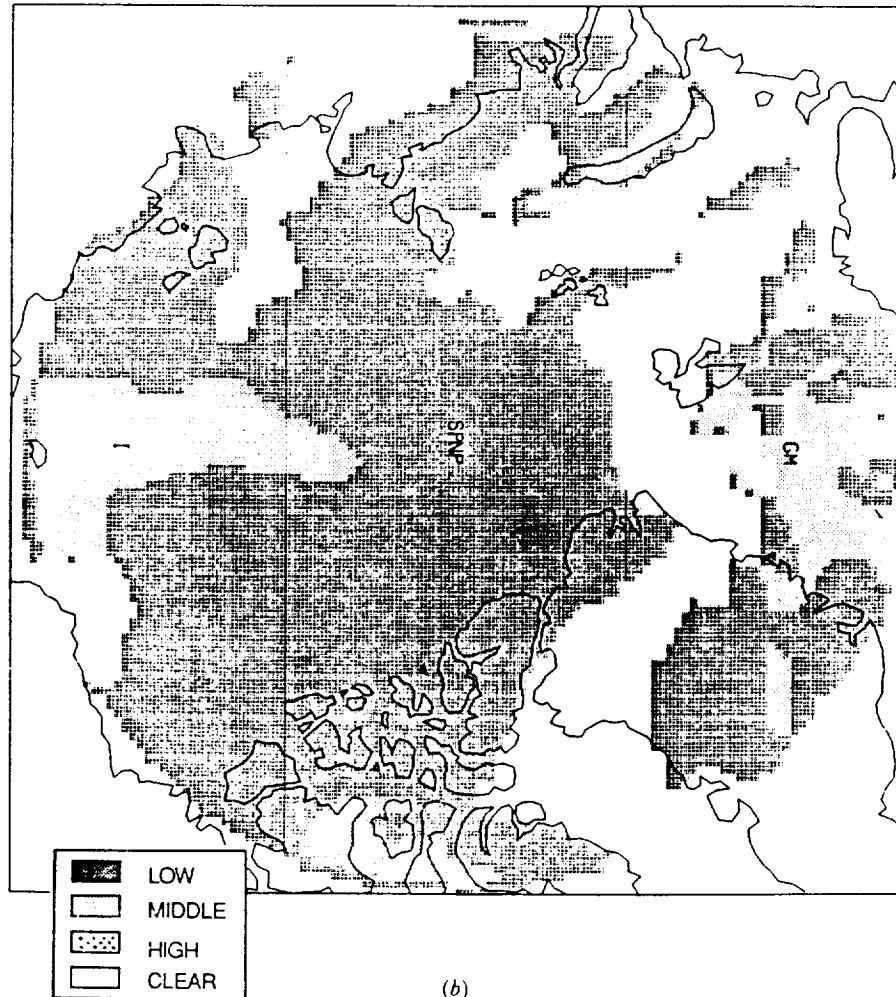
Figure 6. Total cloud amount over the Arctic 15 April 1979 (a) from 3D-nephanalysis (McGuffie 1985) and (b) from manual analysis (Barry *et al.* 1986), and (c) mean sea-level pressure analysis (millibars) for 15 April (Thorndike and Colony 1980).

Sea with easterly flow in the Barents Sea–Greenland sector. The Arctic Ocean has large amounts of cloud on both April maps. In this case most Arctic coastal stations would clearly be unrepresentative of the Arctic Ocean. The agreement between the analyses is weaker in figure 7 (a) and (b), for 25 April, respectively, in part due to the 1-day time difference between them. The low pressure system in the Beaufort Sea is represented by heavier cloud cover in the 3D-nephanalysis and the manual analysis, but there is substantial disagreement over the Siberian sector of the Arctic.

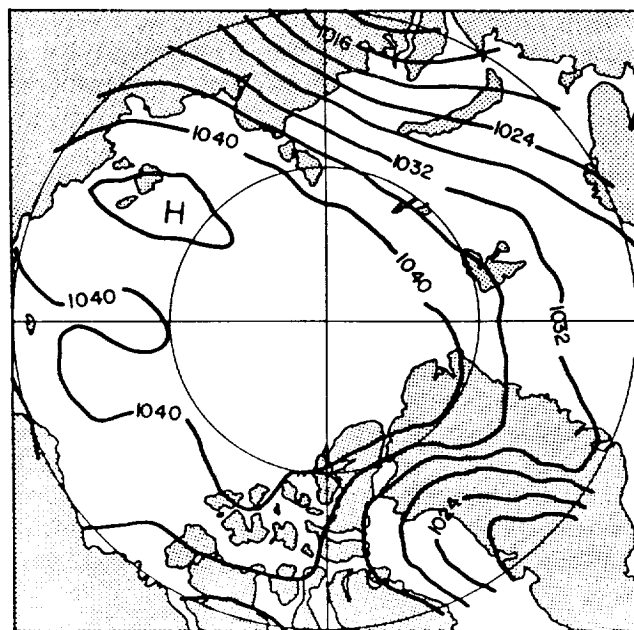
Overall, the cloud charts obtained by manual analysis show a reasonable agreement with the 3D-nephanalysis for the individual dates. One feature that appears to be common to both analyses of mean cloud for the month of April is the presence of a maximum of cloud cover over the central Arctic Ocean. However, the manual technique may exaggerate this due to the bias thought to be caused by pollution layers at a time of very low solar elevation angle (Barry *et al.* 1986).

Finally, comparison is made between the 3D-nephanalysis and the manual techniques of Robinson *et al.* (1985) for three dates in June 1979. Figure 8 for 10 June, characterized by a Kara Sea low and East Siberian–Beaufort Sea high, shows quite close agreement between the patterns obtained by Robinson *et al.* and the 3D-nephanalysis, although the amounts depicted by the latter are not as high as might be expected given the ‘thick’ cloud cover identified manually. Figure 9 for 13 June (East Siberian Sea high, central Arctic low) and figure 10 for 15 June (low over Ellesmere Island) refer to a low pressure system noted by Kukla (1984) that moved across the Pole from the Taymyr Peninsula to the Canadian Arctic Archipelago, and contributed to the onset of the summer snow melt regime on the pack ice. LeDrew (1987) analyses the dynamic properties and vertical motion of this system. Figures 9 and 10 show a considerable difference between the manual analyses and the 3D-nephanalysis. In both cases, the latter shows considerably less cloud over the Arctic Ocean. This probably

ORIGINAL PAGE IS
OF POOR QUALITY.



(b)



(c)

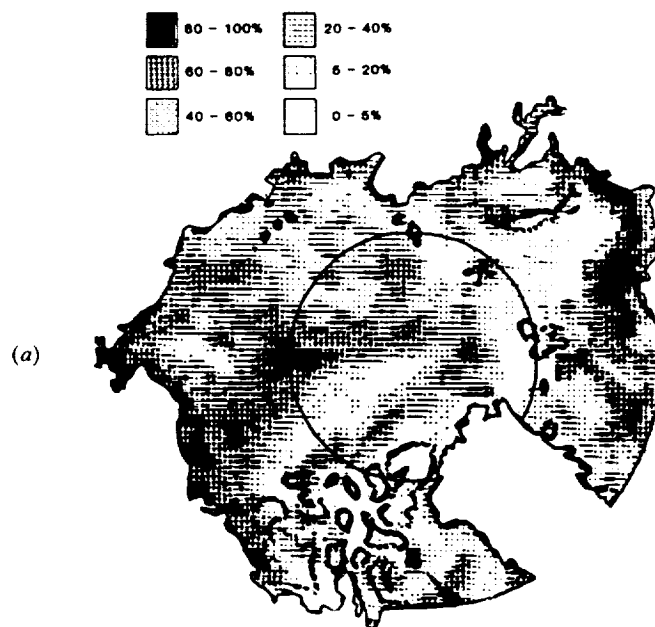


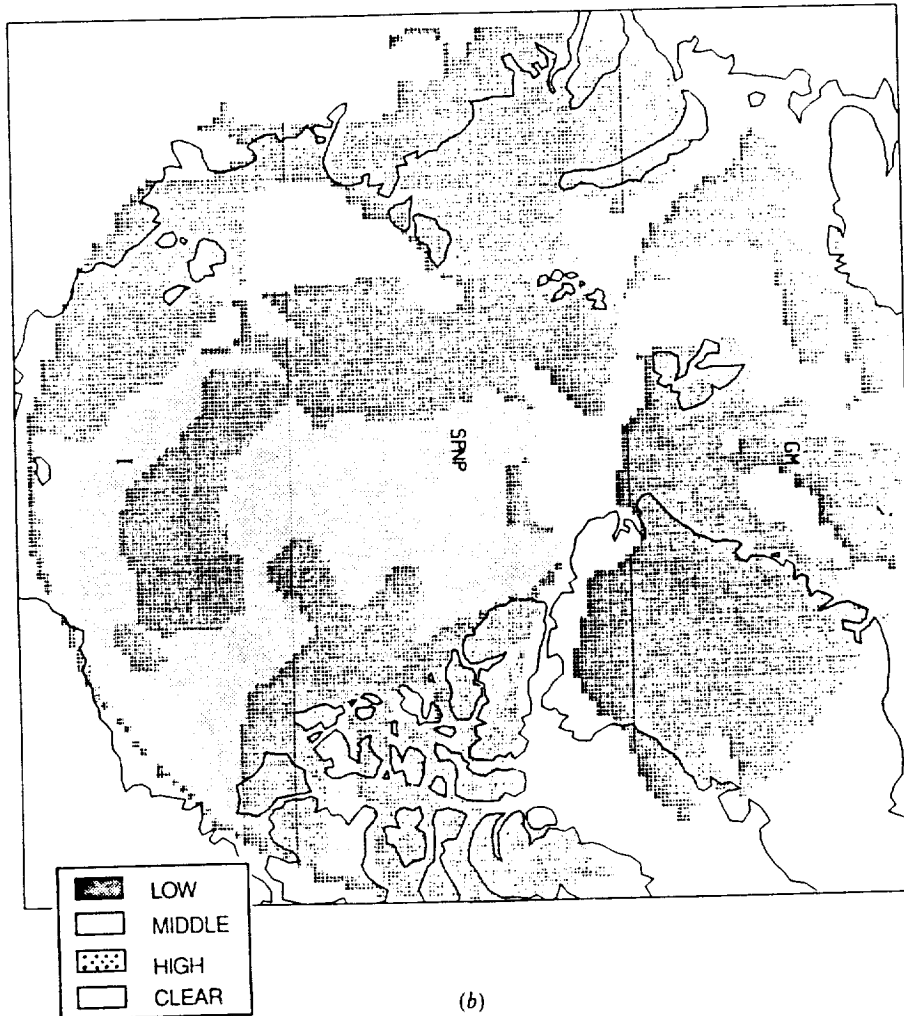
Figure 7. Total cloud amount over the Arctic 25 April 1979 (a) from 3D-nephelometry (McGuffie 1985) and (b) from manual analysis (for 24 April) (Barry *et al.* 1986), and (c) mean sea-level pressure analysis (millibars) for 25 April (Thorndike and Colony 1980).

reflects the influence of the lower tropospheric temperature structure on the 3D-nephelometry retrieval technique noted earlier. The two manual analyses for 15 June are in general in good agreement for the main cloud-covered areas (low or middle on figure 10(c) corresponding with thick or medium on figure 10(b)) and the areas of clear or high cloud (figure 10(c)) and clear or thin cloud (figure 10(b)). The analyses of Robinson *et al.* (1985) for both dates show cloud bands associated with the low pressure systems on figure 10(d). Cloud models have been extensively developed for mid-latitude weather patterns (Carleton 1984, for example), but for the Arctic insufficient data are as yet available to establish reliable synoptic models (Fraser 1973).

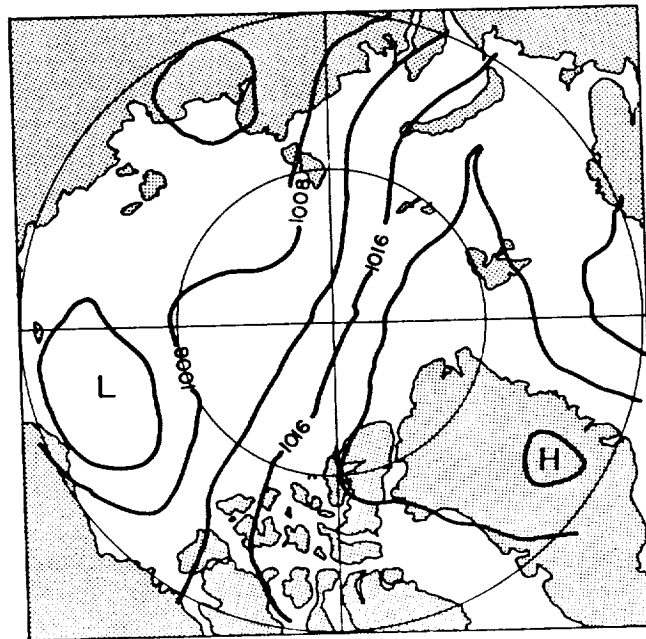
4. Discussion and conclusions

This comparison of satellite-derived Arctic cloud information produced by two manual analysis techniques and 3D-nephelometry (an automated algorithm) shows that these methods are capable of capturing broad climatological features of the cloud cover. However, the spatial patterns are subject to error due to surface effects that may mislead the interpreter or bias the algorithm. This variability makes it difficult to assign reliability estimates. None of the techniques discussed above has been able to portray all of the characteristics of Arctic cloud cover. The automated IR threshold techniques has problems in the Arctic because of the temperature structure of the lower atmosphere, with a persistent surface inversion and warmer low-level clouds in winter and a near-isothermal structure and extensive persistent stratiform clouds in summer. Manual analysis is subjective and depends on the skill of the analyst, with decisions as to the amount and nature of the cloud cover in complex situations inevitably differing between analysts.

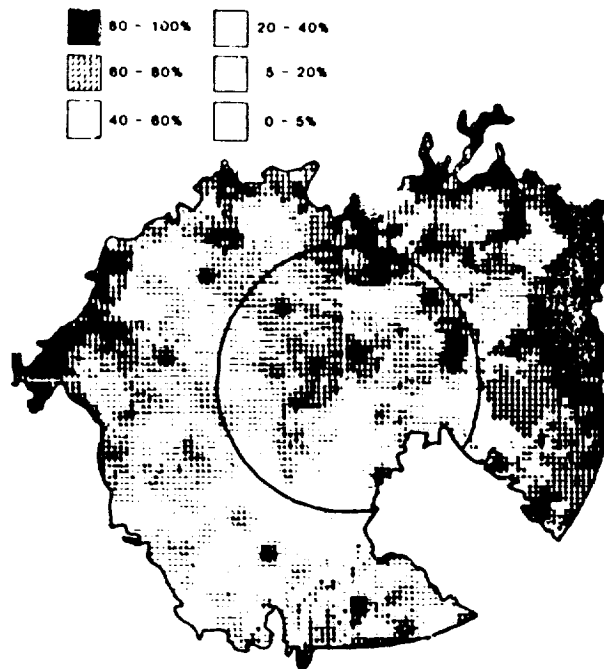
ORIGINAL PAGE IS
OF POOR QUALITY



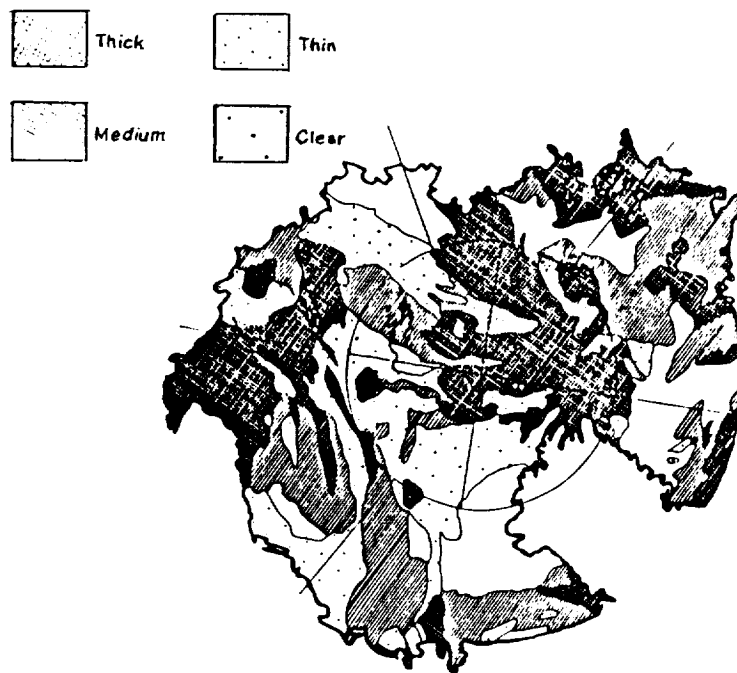
(b)



(c)

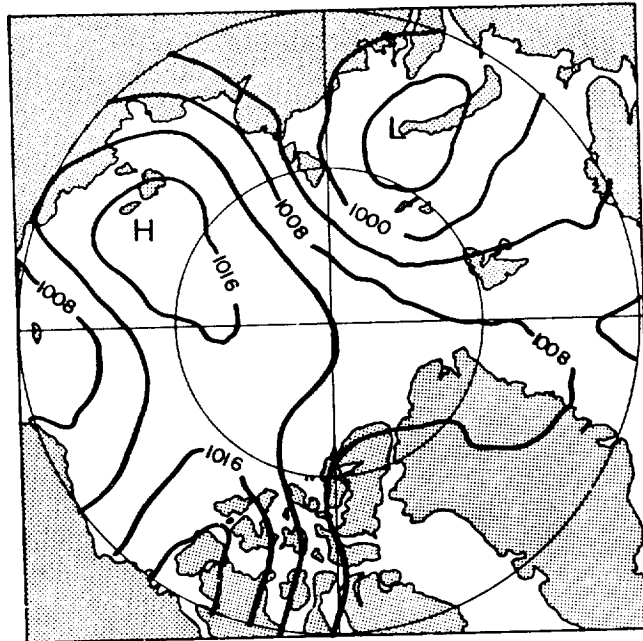


(a)



(b)

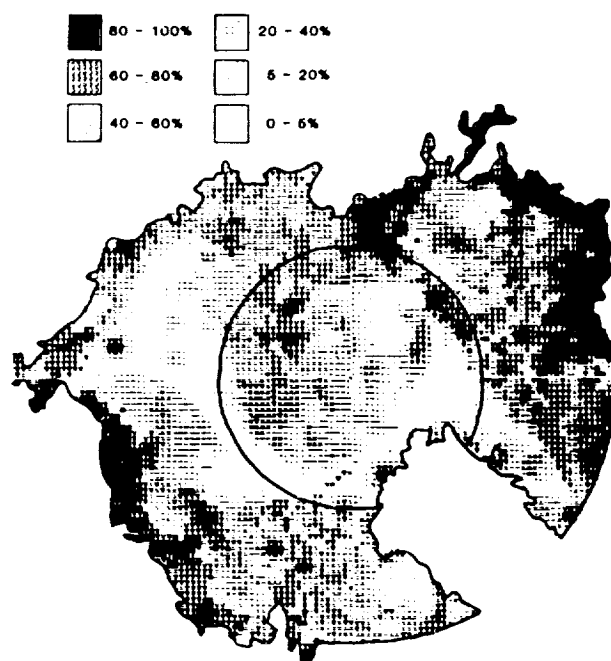
Figure 8. Total cloud amount for 10 June 1979 (a) from 3D-nephelometry (McGuffie, 1985) and (b) from DMSP imagery analysis (Robinson *et al.* 1985), and (c) mean sea-level pressure analysis (millibars) for 10 June (Thorndike and Colony 1980).



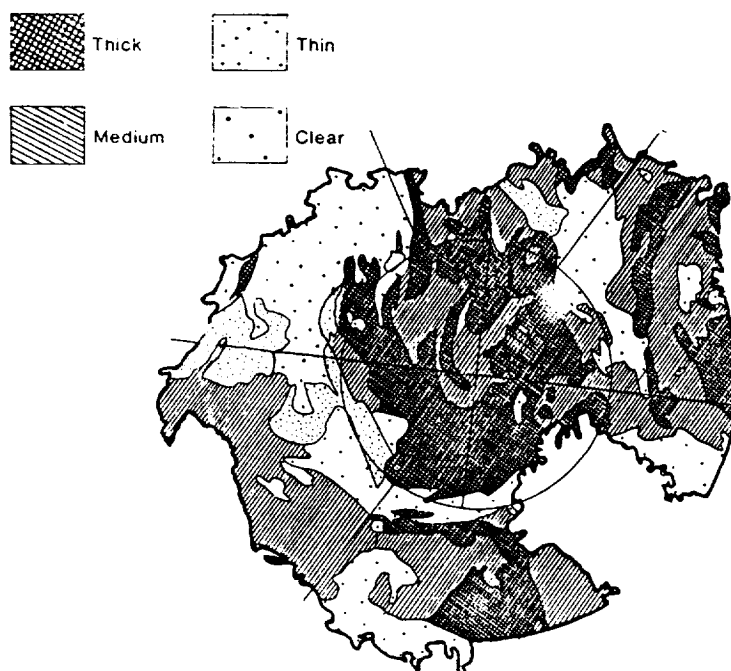
(c)

The estimates of Arctic cloudiness derived manually from satellite imagery are lower than those derived from surface observations, as noted elsewhere by other workers (Tanizer 1968, Malberg 1973). In part this reflects the statistical effect of the scale of resolution of the data (Henderson-Sellers *et al.* 1981). Station observations of cloud amount tend to be bimodal (presence, absence) whereas 5° grid boxes have a J-shaped frequency distribution. This difference also involves the consequences of what is often referred to as the 'observer seeing sides of clouds' problem. This bias may be exaggerated in the Arctic by the high albedo surface. The multiple reflection of shortwave radiation from clouds, and in spring from Arctic haze layers, will make it more difficult for the ground observer to identify breaks in the cloud. It seems likely that some of the difference between surface and satellite observations in the Arctic may be due to the background contrast viewed from the surface and from a satellite. A surface observer views a very low contrast, often milky blue sky, whereas the interpreter of satellite photos is often presented with the high contrast offered by leads in the ice cover. Calculations show that on clear days the presence of an aerosol layer can increase the downward diffuse radiation by up to 60 per cent. Consequently, a thin cloud layer over fractured sea ice may be recorded as broken cloud by a satellite image analyst and yet be reported as 100 per cent cover by an observer at the surface.

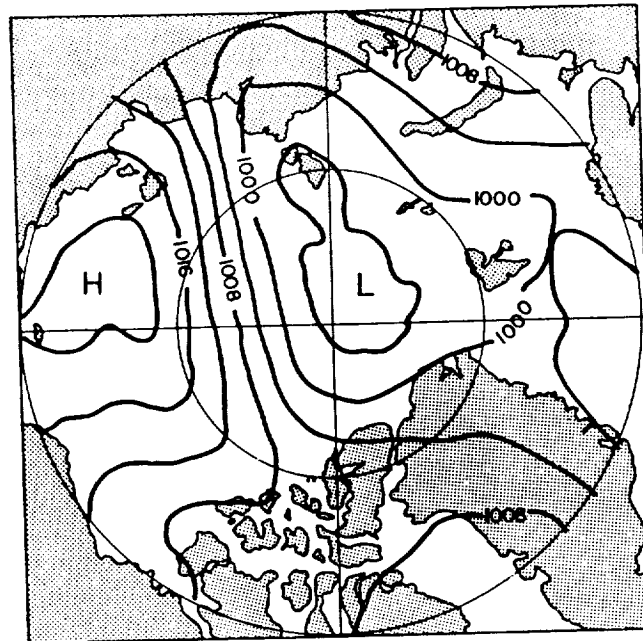
The results of the analyses also suggest that in the early part of the spring-summer season cloudiness is strongly influenced by weather systems. The melting of snow cover on the Arctic sea ice, which is in part initiated during May and June by large-scale warm air advection, is also associated with synoptic weather system activity (Robinson *et al.* 1986 b). This subsequently enables local advection over the melting ice surfaces to contribute to the increase in basin-wide cloudiness, particularly by the production of the widespread summer-time Arctic stratus clouds.



(a)



(b)



(c)

Figure 9. Total cloud amount for 13 June 1979 (a), (b) and (c) as for figure 8.

Changes in the atmospheric circulation and synoptic patterns, which are predicted to occur in response to increasing CO_2 concentrations for example, might be manifested by changes in cloudiness in spring. Such changes would affect the surface energy balance and most likely the timing of melt onset. Consequently, additional data on the occurrence of Arctic clouds and on their optical properties are urgently required if modelling studies of possible climate perturbations in the Arctic are to be successful. Satellites potentially offer the best way of deriving cloud parameters in the polar regions, but it remains for a consistent automatic classification procedure of high latitude clouds to be developed. Our results suggest that this probably cannot be achieved through the use of only visible and thermal infrared data. The manual techniques take into account surface features visually identifiable through thin or transient cloud cover. Over snow and ice, however, the 3D-nephanalysis algorithm scheme relies principally on the infrared channel as noted above. An improved automatic classification may need to incorporate these textural aspects of the scene, as well as employing a 1.6 or $3.7 \mu\text{m}$ channel to help resolve the mapping of low-level stratiform water cloud.

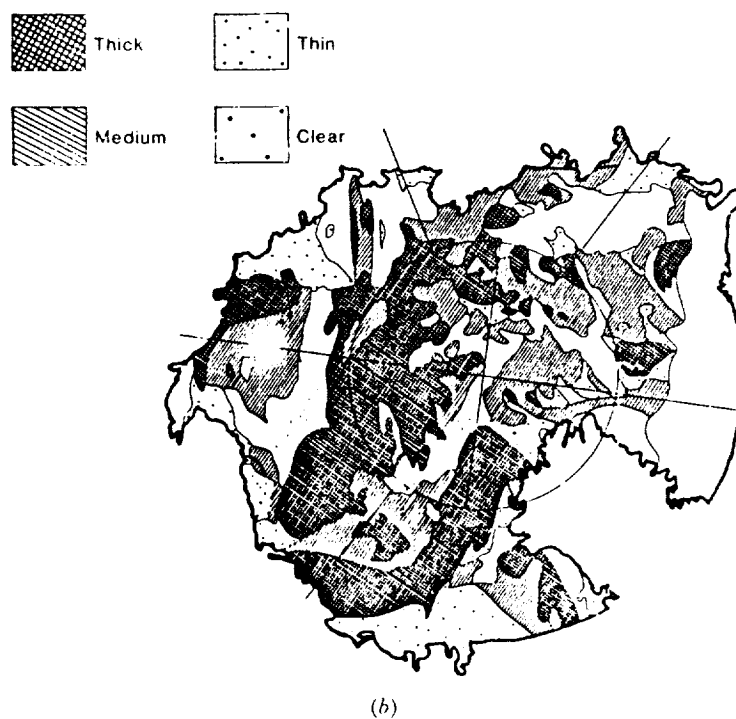
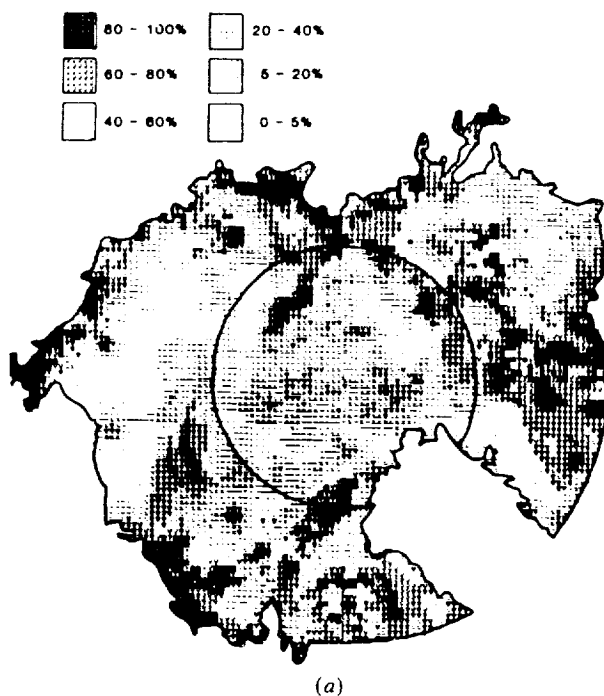
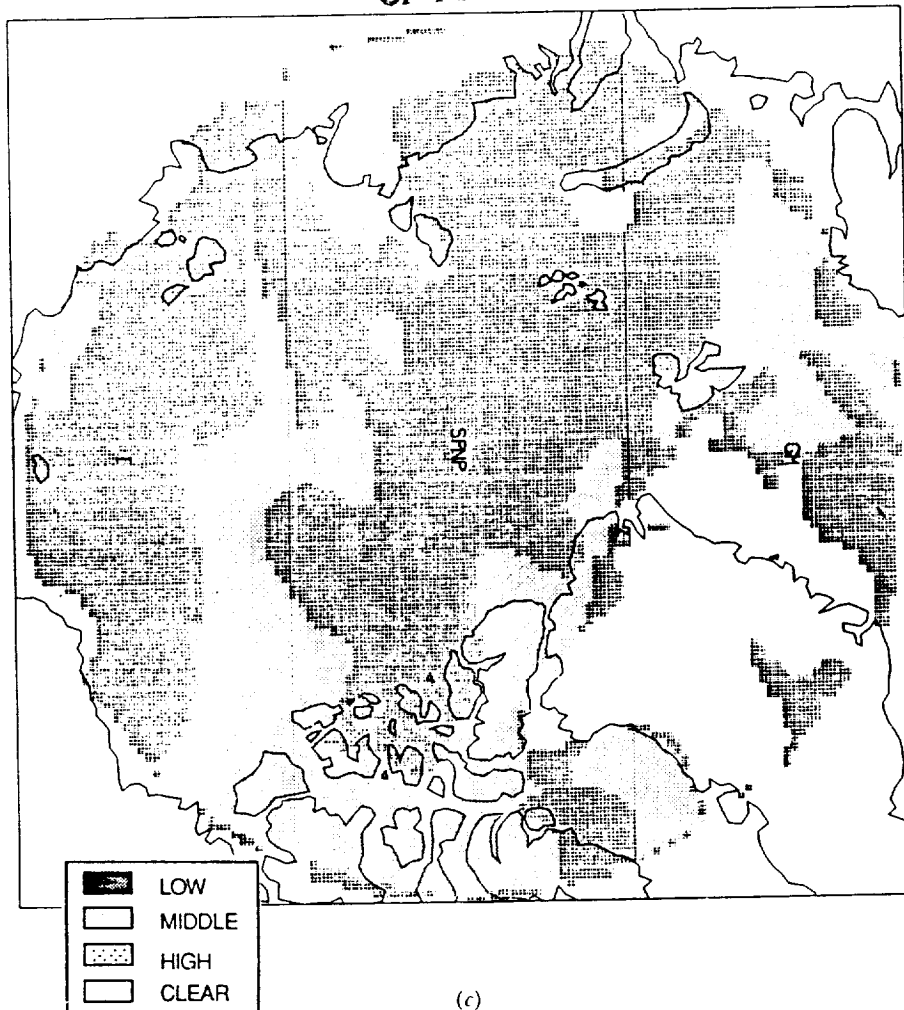
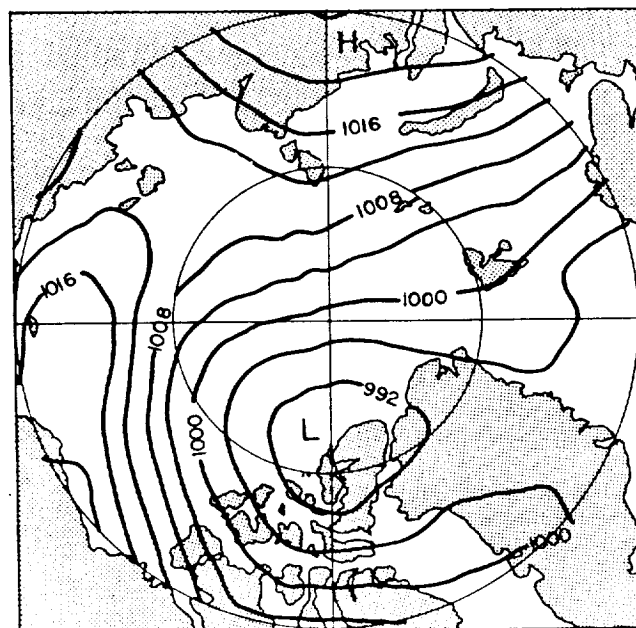


Figure 10. Total cloud amount for 15 June 1979, (a) and (b) as for figure 8 (the blank area in (b) in the North Atlantic represents missing data); (c) manual analysis (Barry *et al.* 1986) and (d) mean sea-level pressure analysis (millibars) for 15 June (Thorndike and Colony 1980).

ORIGINAL PAGE IS
OF POOR QUALITY.



(c)



(d)

Acknowledgments

This work was supported by NASA grants NAG-5-417 and NAG-5-898 to the University of Colorado, Boulder, and by the U.S. Department of Energy, CO₂ Research Division, agreement DE-ACO2-81EV10665 and U.S. Air Force grant 86-0053 to Columbia University, New York. K.McG. wishes to acknowledge the sponsorship of the United States Air Force under grant AFOSR-86-0195. We thank Margaret Strauch for word processing support and Maria Neeri for drafting some of the figures.

References

- ASTAPENKO, P. D., 1960, *Atmospheric Processes in the High Latitude of the Southern Hemisphere*, Section 2 of the IGY Program (Meteorology) 3, Academi Nauk SSSR, (translators Israel Program for Scientific Translations, Jerusalem), p. 286.
- BARRY, R. G., CRANE, R. G., ANDERSON, M. R., CARLETON, A. M., and SCHARFEN, G., 1984 a, Empirical analysis of cryosphere-cloud interactions. In *Cryosphere-Cloud Interactions near the Snow/Ice Limit*, edited by R. G. Barry, K. P. Shine and A. Henderson-Sellers, CIRES, (Boulder: University of Colorado), p. 75.
- BARRY, R. G., CRANE, R. G., NEWELL, J. P., and SCHWEIGER, A., 1986, Empirical and modeled synoptic cloud climatology of the Arctic Ocean. Final Report to NASA, NAG-5-417, Cooperative Institute for Research in Environmental Sciences, University of Colorado, Boulder, p. 103.
- BARRY, R. G., CRANE, R. G., SCHWEIGER, A., and NEWELL, J., 1987, Arctic cloudiness in spring from satellite imagery. *J. Clim.*, 7 (in the press).
- BARRY, R. G., HENDERSON-SELLERS, A., and SHINE, K. P., 1984 B, Climate sensitivity and the marginal cryosphere. In *Climate Processes and Climate Sensitivity* (Geophysics Monograph 29) edited by J. E. Hansen and T. Takahashi, (Washington D.C.: American Geophysical Union), p. 221.
- BERLYAND, T. G., and STOKINA, L. A., 1980, *Global Distribution of Total Cloud Amount* (in Russian) (Leningrad: Gidrometeoizdat), p. 72.
- CARLETON, A. M., 1984, Cloud-cryosphere interactions. In *Satellite Sensing of a Cloudy Atmosphere*, edited by A. Henderson-Sellers (London: Taylor and Francis), p. 289.
- CRANE, R. G., and BARRY, R. G., 1984, The influence of clouds on climate with a focus on high latitude interactions. *J. Clim.*, 4, 71.
- FRASER, D. B., 1973, Synoptic weather patterns over the Arctic. In *Arctic Operational Meteorology*, edited by H. P. Wilson (Edmonton, Alberta: Environment Canada, Arctic Weather Central), p. 348.
- FYE, F. K., 1978, The AFGWC automated cloud analysis mode. AFGWC-TM-100c-1978, Air Force Global Weather Central, Offutt, Nebraska, p. 97.
- GORSHKOV, S. G. (editor), 1983, *World Ocean Atlas*, Vol. 3, *Arctic Ocean*, (Oxford: Pergamon Press).
- HENDERSON-SELLERS, A., HUGHES, N. A., and WILSON, M., 1981, Cloud cover archiving on a global scale: a discussion of principles. *Bull. Am. met. Soc.*, 62, 1300.
- HUGHES, N. A., 1984, Global cloud climatologies: a historical review. *J. Climate appl. Met.*, 23, 724.
- HUGHES, N. A., and HENDERSON-SELLERS, A., 1985, Global 3-D nephanalysis of total cloud amount—climatology for 1979. *J. Climate appl. Met.*, 24, 669.
- HUSCHKE, R. E., 1969, Arctic cloud statistics from 'air-calibrated' surface weather observations. RAND Corporation Memo RM-6173-PR, Santa Monica, California, p. 79.
- KUKLA, G. J., 1984, Variation of Arctic cloud cover during summer 1979, Part 1. Technical Report LDGO-84-2, Lamont-Doherty Geological Observatory of Columbia University.
- LEDREW, E. F., 1987, Q-Vector analysis of five depression systems with the Polar Basin. *J. Clim.*, (submitted).
- LOEWE, F., 1935, Das Klima des Grönlandischen Inlandeises. In *Handbuch der Klimatologie*, edited by W. Köppen and R. Grieger, 2, K., (Berlin: Borntraeger), p. 67.
- MACDONALD, W. F., 1938, *Atlas of Climatic Charts of the Oceans* (Washington, D.C.: Weather Bureau, U.S. Department of Agriculture).

- MCGUFFIE, K., 1985, Cloud and radiation over cryospheric surfaces: climatology and climate sensitivity. Ph.D. thesis, University of Liverpool, Liverpool, England, p. 363.
- MALBERG, H., 1973, Comparison of mean cloud cover obtained by satellite photographs and ground-based observations over Europe and the Atlantic. *Mon. Weath. Rev.*, **101**, 893.
- PUTNINS, P., 1970, The climate of Greenland. In *Climates of the Polar Regions (World Survey of Climatology, Vol. 14)*, edited by S. Orvig. (Amsterdam: Elsevier), p. 3.
- ROBINSON, D. A., KUKLA, G. J., and SERREZE, M., 1985, Arctic cloud cover during the summer of 1977-1979. Technical Report LDGO-85-5, Lamont-Doherty Geological Observatory of Columbia University, Palisades, New York, p. 175.
- ROBINSON, D. A., KUKLA, G. J., and SERREZE, M., 1986a, Arctic summer cloudiness. *Proceedings of the Sixth Conference on Atmospheric Radiation* (Boston: American Meteorological Society), p. 176.
- ROBINSON, D. A., SCHARFEN, G., SERREZE, M. C., KUKLA, G., and BARRY, R. G., 1986b, Snow melt and surface albedo in the Arctic Basin. *Geophys. Res. Lett.*, **13**, 945.
- SCHIFFER, R. A., and ROSSOW, W. A., 1983, The International Satellite Cloud Climatology Project (ISCCP). The first project of the World Climate Research Programme. *Bull. Am. met. Soc.*, **64**, 779.
- SHERR, P. E., GLASSER, A. M., BARNES, J. C., and WILLARD, J. M., 1968, World-wide cloud distribution for use in computer simulations. Final Report Contract NAS-8-21040, Allied Research Associates, Inc., Baltimore, Maryland, p. 272.
- SHINE, K. P., and CRANE, R. G., 1984, The sensitivity of a one-dimensional thermodynamic sea ice model to a change in cloudiness. *J. geophys. Res. C*, **89**, 10,615.
- TANIZER, T., 1968, Differences between cloud coverages observed from ground stations and satellites. *Idöjárás*, **72**, 321.
- THORNDIKE, A. S., and COLONY, R., 1980, Arctic Ocean Buoy Program. Data Report. 19 January 1979-31 December 1979. Polar Science Center, University of Washington, Seattle, p. 131.
- VOSKRESENSKIY, A. T., and CHUKANIN, K. I., 1959, Meteorologicheskie usloviya obledeneniya v oblakov tipa st i sc. *Arkt. Antarkt. Nauch-Issled. Inst., Trudy*, **228**, 124.
- VOWINCKEL, E., 1962, Cloud amount and type over the Arctic. *Publications in Meteorology*, No. 51 (Montreal: Arctic Meteorology Research Group, McGill University), p. 27.
- WORLD METEOROLOGICAL ORGANIZATION, 1956, *International Cloud Atlas* (Geneva: WMO).

ATTACHMENT 8
ARCTIC CLOUDINESS IN SPRING

ARCTIC CLOUDINESS IN SPRING FROM SATELLITE IMAGERY: A RESPONSE

R. G. BARRY¹, R. G. CRANE², A. SCHWEIGER¹, AND J. NEWELL¹

¹CIRES, University of Colorado, Boulder, CO 80309-0449, U.S.A.

²Geography Department, Pennsylvania State University, University Park, PA 16802, U.S.A.

Received 8 March 1988

We welcome Curry's (1988) reconsideration of the possible role of pollution aerosols in causing the springtime obscuration of Arctic surfaces as viewed from space. The need for such further study was called for in our paper, hereafter B87 (Barry *et al.*, 1987). The role of Arctic haze in surface obscuration was also proposed earlier, and sample radiation calculations made, by Shine *et al.* (1984). Curry proposes that ice crystals in the lower troposphere may account for a significant fraction of the obscuration detected in our manual analysis of April cloud cover from DMSP visible wavelength imagery. Several points raised in Curry's note deserve further commentary.

The occurrence of ice crystal precipitation ('diamond dust') from cloudless skies in high latitudes during the cold season is well known, because it is usually associated with optical phenomena (halos, sun pillars). However, its frequency does not seem to be well documented in climate summaries. Wilson (1969, p. 86) states that horizontal or slant visibility during such ice crystal haze is seldom reduced below 3 to 8 km. Curry also notes that the 'Ptarmigan' weather reconnaissance reports over the Beaufort Sea area suggest that the haze in these regions lacked the optical effects of ice.

Boundary-layer information of a different kind is now being provided by airborne lidar measurements in the Arctic. Work in progress (Barry and Miles, 1988) shows that open leads in the sea ice during winter and early spring give rise to large ice crystal plumes that can be detected by 1.06 μm lidar. These subvisible ice crystal plumes appear to spread out extensively, but are also detected by lidar to penetrate the inversion. Moreover, such moisture transfer is probably much more common than Raatz (1984) believes, based on our mapping of lead occurrence. Work on the frequency and extent of such events is in progress, but this source seems likely to be as important for ice crystal generation as large-scale advection of maritime polar air masses proposed by Curry. Such airmasses seldom penetrate into the North American sector of the Arctic, as shown by cyclone tracks (B87, Figure 3a).

Arctic haze is the subject of continued investigation through the Arctic Gas and Aerosol Sampling Program (AGASP), the results of which are not discussed by Curry. The AGASP experiments during March 1983 and April 1986 show tropospheric aerosol optical depths (at 0.5 μm) during aerosol events ranging up to 0.5 and 0.7 (Dutton *et al.*, 1984, 1988). Surface measurements at Barrow for April 1986 give a mean value for the month of 0.235. Hence, our assumed value of 0.3 for τ is not exaggerated as stated by Curry. Shaw's (1982) statement that pollution aerosol is an order of magnitude lower than in mid-latitude source regions is also contradicted by comparison of the AGASP-II results with measurements off the east coast of the United States during pollution episodes (Schnell, 1987). Ruhnke and Schnell (1987) indicate that the haze particles have a typical diameter of 0.3 μm . Graphitic carbon is responsible for most of the absorption in the visible. They also report a high single scattering albedo of 0.86, demonstrating the dominance of scattering in the total extinction coefficient, but note that 'visible range and measured scattering coefficients in Arctic haze are not unambiguously related to each other.' Herbert *et al.* (1987) report that thick haze on 2-3 April 1986 obscured the surface north of Barrow, Alaska, from 2 km altitude. The fraction of ice crystal aerosol in haze layers has not yet been specifically determined; however, the AGASP-II measurements of backscatter relate only to dry

aerosol (Schnell, 1987). The relationship between haze layers and moisture content is shown by the AGASP-II flight data to be highly variable; some haze layers are moist, others dry (Ruhnke and Schnell, 1987; Herbert *et al.*, 1987).

Curry correctly points out that the solar altitude and daylength figures stated in B87 (p. 425) for 80°N are in error. The values of solar altitude given in our paper are in fact for 90°N.

In summary, measurements of Arctic haze support the optical depth value assumed for the radiation calculation reported in B87. We agree, nonetheless, that tropospheric ice crystal clouds during late winter and early spring may on occasion contribute to surface obscuration as viewed from space. If this is the case, such layers might be included in cloud statistics as Curry proposes. A major source of such ice crystals, at least in the western Arctic, appears to be the leads that form repeatedly in Arctic sea ice, rather than large-scale advection of maritime polar air masses. Ice crystal plumes from open leads are detectable from airborne lidar data and statistical analysis of their temporal and spatial occurrence is in progress. Clearly, various aspects of the general problem of cloud detection in polar regions remain to be satisfactorily resolved.

ACKNOWLEDGEMENTS

We thank Ellsworth Dutton and Russ Schnell for helpful discussion supported by NASA NAG5-898.

REFERENCES

- Barry, R. G., Crane, R. G., Schweiger, A. and Newell, J. 1987. 'Arctic cloudiness in spring from satellite imagery'. *J. climatol.*, **7**, 423-451.
- Barry, R. G. and Miles, M. W. 1988. 'Lead patterns in arctic sea ice from remote sensing data: characteristics, controls and atmospheric interactions'. *Preprint Volume Second Conference on Polar Meteorology, 1988*. Am. Meteorol. Soc., Boston, 40.
- Curry, J. A. 1988. 'Arctic cloudiness in spring from satellite imagery: some comments'. *J. climatol.*, **8**, (in press).
- Dutton, E. G., DeLuisi, J. J. and Bodhaine, B. A. 1984. 'Features of aerosol optical depth observed at Barrow, March 10-20, 1983'. *Geophys. Res. Lett.*, **11**, 385.
- Dutton, E. G., DeLuisi, J. J. and Herbert, G. 1988. 'Spectral aerosol optical depth of Arctic haze as measured on board the NOAA WP-3D during AGASP-II, April 1986'. *J. Atmos. Chem.*, in press.
- Herbert, G. A., Bridgman, H. A., Schnell, R. C., Bodhaine, B. A. and Ottmans, S. J. 1987. 'The analysis of meteorological and haze distributions for the second Arctic Gas and Aerosol Sampling Program (AGASP-II), March-April, 1986'. *NOAA Tech. Mem. ERL ARL-158*, U.S. Dept of Commerce, NOAA, Boulder, Colorado.
- Raatz, W. E. 1984. 'Observations of "Arctic haze" during the "Ptarmigan" weather reconnaissance flights, 1948-1961'. *Tellus*, **36B**, 126-136.
- Ruhnke, L. H. and Schnell, R. C. 1987. 'Arctic haze'. In E. Harrison and R. Gomez (eds), *Arctic and Arctic-related Environmental Sciences*. A. Deepak Publishing Co., Washington, DC, 285.
- Schnell, R. C. 1987. 'A "major" Arctic haze event north of Point Barrow, April 1986'. R. C. Schnell and R. M. Rossen (eds), *GMCC Summary Report No. 15*, U.S. Department of Commerce, NOAA Environmental Research Laboratories, Boulder, Colorado, 96.
- Shaw, G. E. 1982. 'Atmospheric turbidity in the polar regions'. *J. Appl. Meteorol.*, **21**, 1080-1088.
- Shine, K. P., Robinson, D. A., Henderson-Sellers, A. and Kukla, G. 1984. 'Evidence of Arctic-wide atmospheric aerosols from DMSP visible imagery'. *J. Clim. Appl. Meteorol.*, **23**, 1459.
- Wilson, C. 1969. 'Climatology of the cold regions. Northern hemisphere II.' *Cold Regions Science and Engineering Monograph I-A 3b*. U.S. Army, Corps of Engineers, Cold Regions Research and Engineering Laboratory, Hanover, NH, 158 pp.

ATTACHMENT 9
COMPARISON OF OBSERVED AND SIMULATED CLOUD COVER

**Arctic Cloud Cover Simulated by the
Goddard Institute for Space Studies
General Circulation Model**

Robert G. Crane

Report
Submitted to Dr. Roger G. Barry
Cooperative Institute for Research in Environmental Sciences
December 1987

1. Introduction

Most General Circulation Model (GCM) sensitivity experiments show a marked high latitude response to external forcing such as changes in the solar constant, changes in atmospheric CO₂, or experiments with glacial boundary conditions. The implication of all of these experiments is that the polar regions may play a significant role in global climate and may also be one of the first places to demonstrate present or future climate change.

Climatic processes in the Arctic are dominated by the presence of sea ice--primarily through the effect on the surface albedo and ocean-atmosphere heat exchange--and by the polar cloud cover. Unfortunately, neither sea ice nor cloud cover are particularly well treated in many GCM's, and in the case of the cloud cover the observational data are also very limited.

The role of cloud cover in climate has been discussed by Crane and Barry (1984) with a particular focus on the polar regions. The Arctic cloud cover is known to have a large seasonal variability increasing from about 40-60% in winter to 80-90% in summer (Huschke, 1969). This large increase in summer is attributed, in part, to a shift in the cyclone tracks with an increase in the number of low pressure systems that enter the Arctic Basin at this time. It is also assumed that the rapid increase in spring/summer cloud cover is partly due to decreasing ice concentration and increased moisture availability. At present, however, we do not have sufficient observational data to fully support these assumptions. The problems of the satellite retrieval of cloud parameters is being examined in related studies as part of this project; it is the purpose of the present report to

concentrate on the Arctic cloud cover simulations in the Goddard Institute for Space Studies' (GISS) GCM.

2. The GISS GCM

The present study examines the Arctic cloud cover simulated by a control run of the GISS Model II. This model, described in detail in Hansen et al. (1983), has a horizontal resolution of 8 degrees latitude by 10 degrees longitude and 9 atmospheric layers (2 in the boundary layer, 5 in the remainder of the troposphere and 2 in the stratosphere). Snow depth, cloud cover and cloud height are computed in addition to the usual atmospheric variables, and the model includes diurnal and seasonal cycles. The ocean temperatures and the sea ice cover, however, are specified climatologically.

A comparison of the observed and modelled synoptic climatology of the Arctic Basin has been made by Crane and Barry (1988) using this model. The observed pressure fields over the Arctic are compared with those obtained from the model using a classification typing procedure developed by Kirchhofer (1973) and a rotated principal components analysis for both data sets. The analysis shows that the GISS model appears to give a quite realistic simulation of both the spatial and temporal characteristics of the sea level pressure field. Using the same synoptic climatology Barry et al. (1987) suggest that synoptic controls may be an important factor determining the observed cloud amount during the spring and early summer of 1979 and 1980. Cloud cover is derived from the model data in such a way that it is unlikely that a similar synoptic scale study would be valid in this case (see below). Some idea of the relative importance of synoptic

scale advection versus local effects can be obtained, however, by an examination of the monthly data at various levels in the model.

3. The GISS CGM Cloud Scheme

The GISS model calculates both large scale and convective cloud cover. The actual cloud amounts are not saved on the 5-hourly output available from the control run, but they can be inferred from the optical depth which is saved for levels 1 to 7.

Convective Cloud

The convective cloud is obtained as a proportion of the mass of saturated moist air rising from one layer to the next. The scheme computes a cloud fraction which, at each time step, is compared to a random number between 0 and 1. If the random number is less than the cloud fraction, a cloud amount of 1 is assigned for that time step; if the random number is greater than the cloud fraction a cloud amount of zero is assigned. The GISS model, therefore, uses a cloud amount of zero or one at each time step and simulates the effects of fractional cover within a grid box by using full cloud cover for a fractional amount of time. This gives similar results to computing separate radiation calculations using fractional cloud for both the clear and cloudy portions of the grid box, but saves computer time (Hansen et al., 1983).

Large-Scale Clouds

The large-scale cloud is given by the saturated fraction of the grid box, assuming uniform absolute humidity and subgrid scale temperature variation. As with the cumulus cloud, the fractional amount of cloud cover is also compared to a random number and either zero or complete cloud

cover assigned for the time step. No distinction is made between convective and large-scale cloud in the present analysis but, in general, large-scale clouds account for about 80% of the global cloud cover generated by the model (Hansen et al., 1983).

Cloud Optical Depth

In place of the fractional cloud cover, the 5-hourly data give the optical depth at each layer of a grid box in the presence of clouds. That is, a cell has an optical depth of zero if no clouds are present and a value greater than zero in the presence of clouds. The actual optical depth is a function of cloud type, temperature and depth in the atmosphere. For large-scale cloud, if the layer temperature is less than 258 K the optical depth is given as .33 to match the observational data of Platt (1975) which indicates that cirrus clouds typically have an optical depth of 0.25 - 0.5. Otherwise the optical depth is proportional to the pressure thickness of the layer containing the cloud. For convective cloud the optical depth is .08 times the pressure thickness giving an optical depth of about 8 per 100 mb of thickness. Where both large-scale and convection clouds are present in a cell, the largest optical depth is used.

Determination of Cloud Cover Fraction

While the optical depth of cloud is obviously the important factor in terms of radiative calculations, this is difficult to compare with observations that are made in the form of fractional cloud cover. For the present study, the fractional cloud cover is obtained from the optical depth data by averaging over time.

The cloud optical depths are used to produce a binary map of cloud cover at each level; that is, for optical depth > 0 , cloud cover = 1, for

optical depth = 0. cloud cover = 0. The binary grids are used to produce low, middle and total cloud cover; low cloud is cloud in levels 1 or 2 (from the surface to about 850 mb), middle cloud is cloud in levels 3 and 4 (about 850 mb to 550 mb), and total cloud includes cloud at any level. The binary grids of low, middle, and total cloud are averaged over 30 days (150 grids). The time average gives a fractional amount which is similar to the original monthly cloud cover fraction calculated by the model (Figures 1 and 2).

4. Results

The monthly average cloud cover fraction for the Arctic north of 72°N is shown in Figure 3a. This shows a seasonal cycle having a summer maximum similar to that of Huschke (1969) (Figure 4), but with much lower values. At the same time, the winter values are much higher in the model showing that the seasonal range in the model cloud cover for the central Arctic is much less than the observations would suggest. Figure 3b shows the seasonal cycle for the area north of about 55°N and in this case the cycle is reversed with less cloud in the summer months. This reversal in the seasonal cycle is also demonstrated on a regional basis although both the western Arctic (135°W - 135°E) and the Canadian Arctic (45°W - 135°W) show very little seasonal variability (Figure 5), and most of the variation occurs in the European sector (45°W - 45°E) and the Kara/Laptev Sea (45°E - 135°E). In these regions the seasonal cycle is again reversed with less cloud in the summer months. These regions extend from approximately 86°N to 55°N and should not, therefore, be compared with the regional data of Huschke. The change in the seasonal cycle reflects the change in cyclone tracks as they move further north in summer; the decrease in the

regional cloud fractions being matched by an increase in the central Arctic fraction (Figures 3a and 5d). This seasonal variability is further illustrated in the cloud maps for January and July (Figures 6 and 7). In January the largest cloud fractions are found in the higher mid-latitudes primarily in the North Pacific region and in the NE Atlantic, while in July the greater cloud cover occurs north of about 70°N. The July distribution of total cloud cover for the Arctic agrees with Gorshkov (1980) in that there is a relative maximum at high latitudes with the largest fractions being in the north Atlantic region. However, there is a major difference in the Central Arctic where Gorshkov shows 90% cloud cover while the model has a relative minimum with less than 60% cloud cover. One should note, however, that the model values for June and August are much higher (Figure 5e) and that we are only examining one year of model output.

Comparing Figures 6a-c it is apparent that the regions of largest low, middle and total cloud cover coincide suggesting that cloud cover is controlled by the large scale processes. We should also note, however, that the low cloud fraction is much higher than either Voskresenskiy and Chukanin (1959) or Vowinckel and Orvig (1970) find for the Eastern Arctic. Figures 7a-c for July, on the other hand, show the higher levels of low, total and middle cloud coinciding in the western Arctic and North Atlantic, but with an area of increased low cloud north and west of the Taymyr Peninsula where ice concentrations have already begun to decrease in the model.

The minimum ice extent in the model occurs in September with low ice concentrations (less than 30%) in the southern Barents/Kara Sea and along the Beaufort Coast. Ice concentrations of less than 50% are found along

the Siberian coast and ice concentrations between 75% and 85% are found in the Beaufort up to about 78°N and the Barents Sea up to about 86°N. The September cloud cover shows a general decrease over the July figures with the largest cloud cover fractions being found further south once more. For the most part there is a general agreement between the low, middle and total cloud, but again there are areas which have a relative maximum in low cloud and a minimum in middle cloud corresponding to the regions of low ice concentration in the Barents/Kara Sea and, to some extent, along the Beaufort Coast. There are extensive areas of low cloud in the Canadian Arctic and the East Siberian Sea, but these also coincide with regions of extensive middle cloud as well.

Although it cannot be demonstrated conclusively, these results do suggest that the decreased ice concentration in the Seasonal Sea Ice Zones of the Eastern Arctic and along the Beaufort Coast do contribute to increased low level cloudiness in the model. For the most part, however, the Arctic cloud cover does appear to be controlled by the larger scale processes.

5. Summary and Conclusions

The GISS model cloudiness in the polar region of the Northern Hemisphere demonstrates the seasonal variability that would be expected from the observational data, but at a much reduced range for the Central Arctic. As with the observational data, the zone of maximum cloud cover moves north in the summer, but actual amounts are less than expected by about 10-20%.

Barry et al. (1987) suggest that there is a strong synoptic control on

cloud cover amounts in the Arctic which is supported by the more detailed microphysical studies of Jayaweera (1982) who also suggests that the lower stratus layers may be formed by the lifting of fog over sea ice, while the upper layers are a response to large-scale southerly flow. In the case of the GISS model, while most of the cloud cover would appear to be due to large-scale processes, there is some evidence that reduced ice concentration in summer does give rise to some increased low level cloud on a limited regional basis. One final consideration is that during the early summer, when the model is already showing too little cloud in the Arctic, there is also a tendency for mid-latitude aerosols to be transported to the Arctic resulting in the presence of optically thick Arctic Haze (Rahn, 1985). This again may have some further effect on the surface and lower tropospheric energy balance in the Arctic.

Acknowledgment

This work was supported under NASA Climate Research Grant NAG 5-898 to Roger G. Barry. We are indebted to Dr. J. Hansen for providing the GISS Model data.

References

- Barry, R. G., Crane, R. G., Schweiger, A. and Newell, J., 1987. Arctic Cloudiness in Spring From Satellite Imagery. *J. Climatology*, 7: 423-451.
- Crane, R. G. and Barry, R. G., 1984. The Influence of Clouds on Climate with a Focus on High Latitude Interactions. *J. Climatology*, 4: 71-93.
- Crane, R. G. and Barry, R. G., 1988. Comparison of the MSL Synoptic Pressure Patterns of the Arctic as Observed and Simulated by the GISS General Circulation Model. Submitted to *Met. and Atmos. Phys.*
- Gorshkov, S. G. (ed) 1980. *World Ocean Atlas. Vol 3, Arctic Ocean.* Dept. of Navigation and Oceanography, Ministry of Defence, USSR (Pergamon Press, Oxford, 1983).
- Hansen, J., Russell, G., Rind, D., Stone, P., Lacis, A., Lebedeff, S., Ruedy, R. and Travis, L., 1983. Efficient Three-Dimensional Global Models for Climate Studies: Models I and II. *Mon. Wea. Rev.*, 111: 609-662.
- Kirchhofer, W., 1973. Classification of 500 mb Patterns. *Arbeit der Schweizer Meteorolo. Zentral.*, 45: 16 pp.
- Platt, C. M. R., 1975. Infrared Emissivity of Cirrus-Simultaneous Satellite, Lidar and Radiometric Observations. *Quart. J. Roy. Met. Soc.*, 101: 119-126.
- Rahn, K. A. (ed) 1985. Arctic Air Chemistry. *Atmos. Environ.*, 19.
- Vowinckel, E. and Orvig, S., 1970. The Climate of the North Polar Basin. In Orvig, S. (ed) *World Survey of Climatology*, 14, 129.
- Voskresenskiy, A. I. and Chukanin, K. I., 1959. Meteorologicheskie Usloviya Obled Eneiia v Oblakov Tipa st is sc. *Trudy Arktichescogo i Antarkticheskogo Nauchno-Issledovatel'skogo Instituta*, 228: 124.

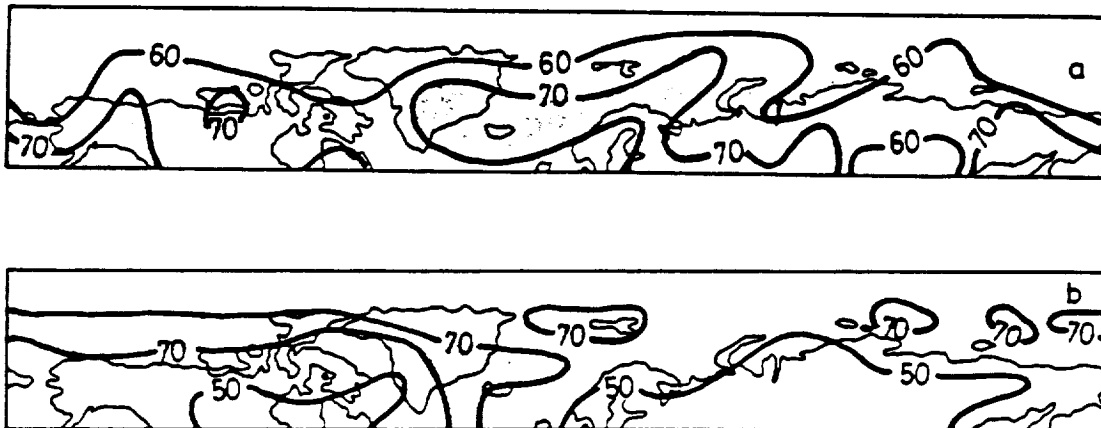


Figure 2. January (a) and July (b) Total Cloud Cover From the Present Study (shaded areas have greater than 70% cloud cover)

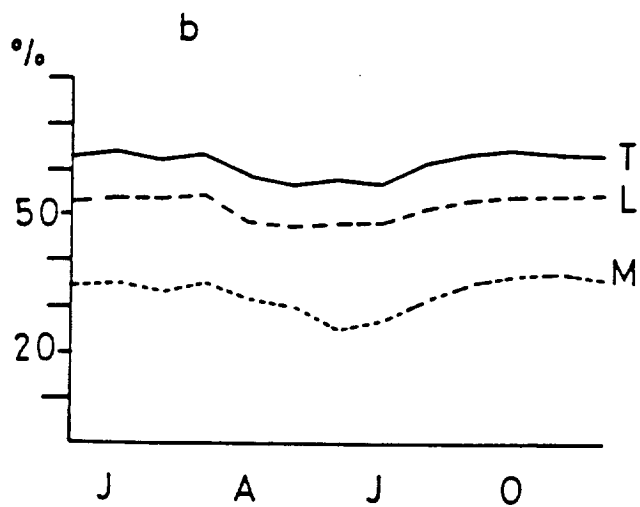
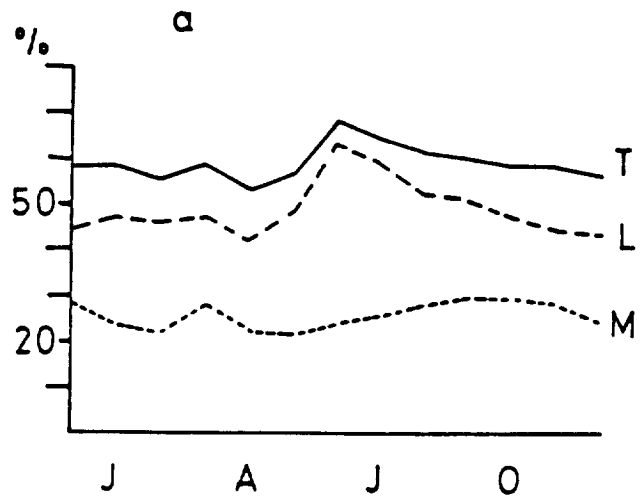


Figure 3. Seasonal Cycle of Cloud Cover for the Arctic North of 72N (a) and North of 65N (b)

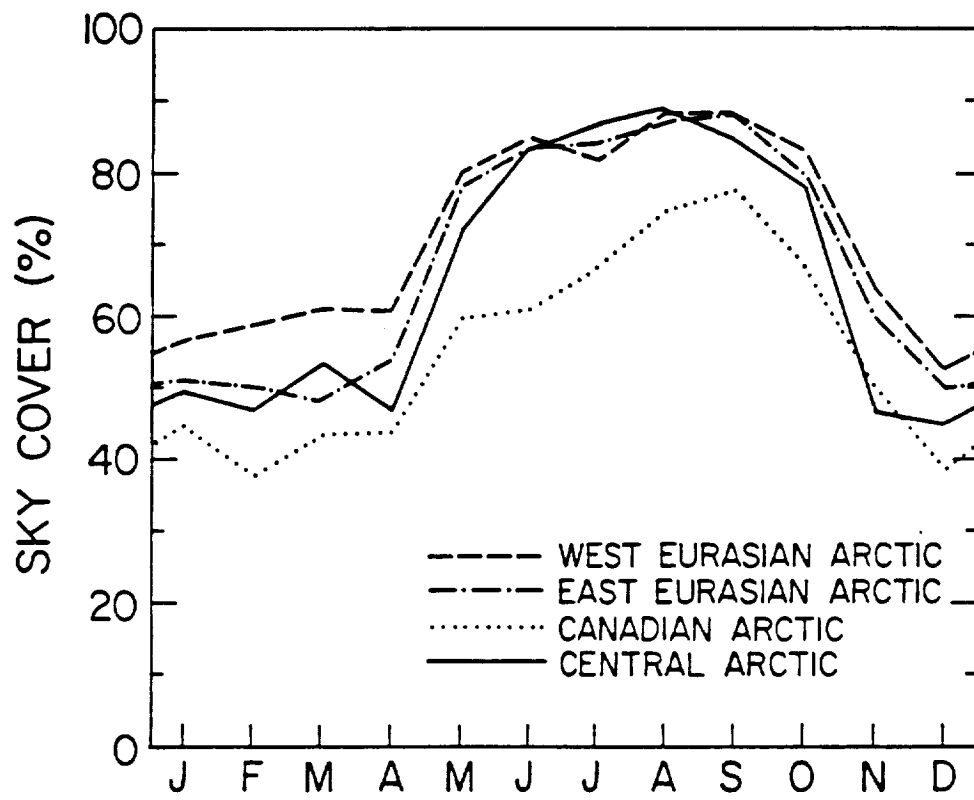


Figure 4. Monthly Cloud Cover For the Arctic (Huschke, 1969)

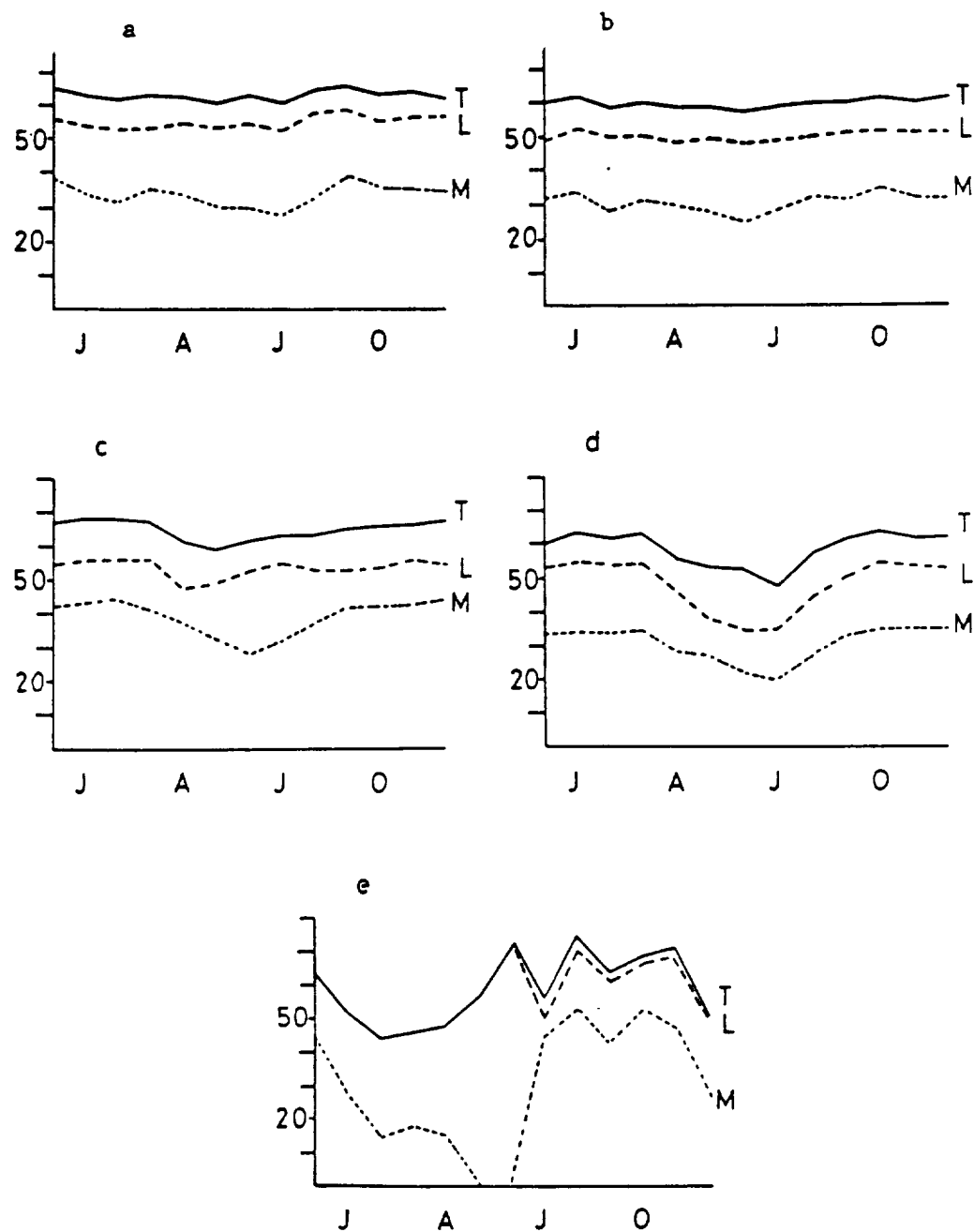


Figure 5. Monthly Cloud Cover (GISS Model) For a) the Western Arctic, b) Canadian Arctic, c) European Arctic, d) Laptev Sea, and e) the North Pole

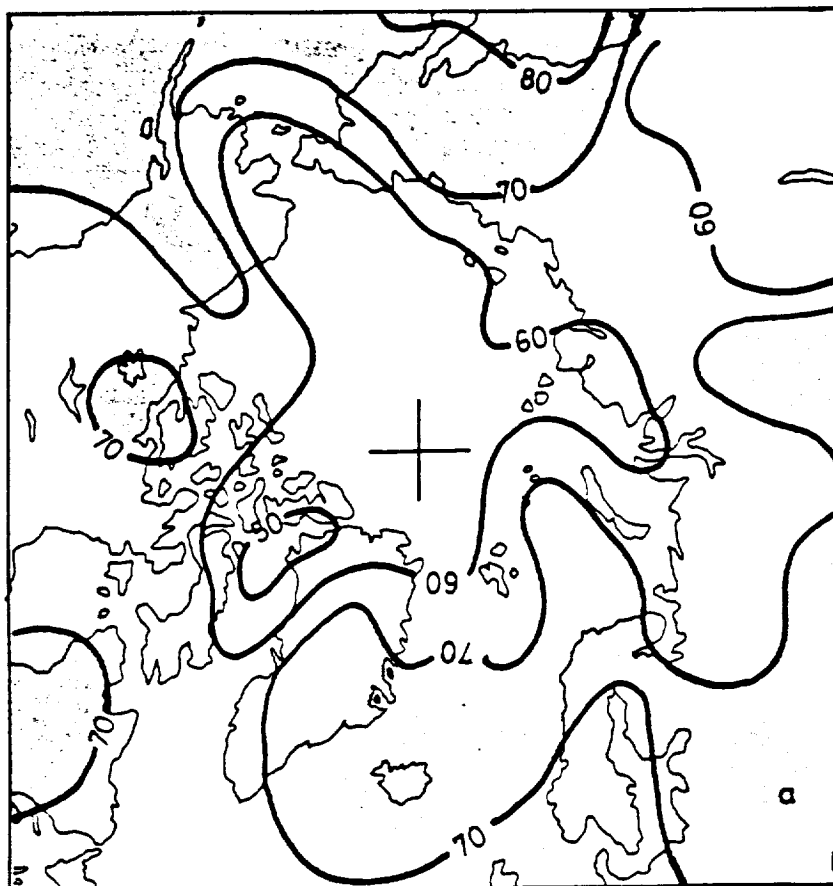


Figure 6. Mean January Cloud Cover From the GISS GCM.
(a) Total Cloud (shaded areas = greater than 70% cloud)
(b) Low Cloud (shaded areas = greater than 60% cloud)
(c) Middle Cloud (shaded areas = greater than 40% cloud)

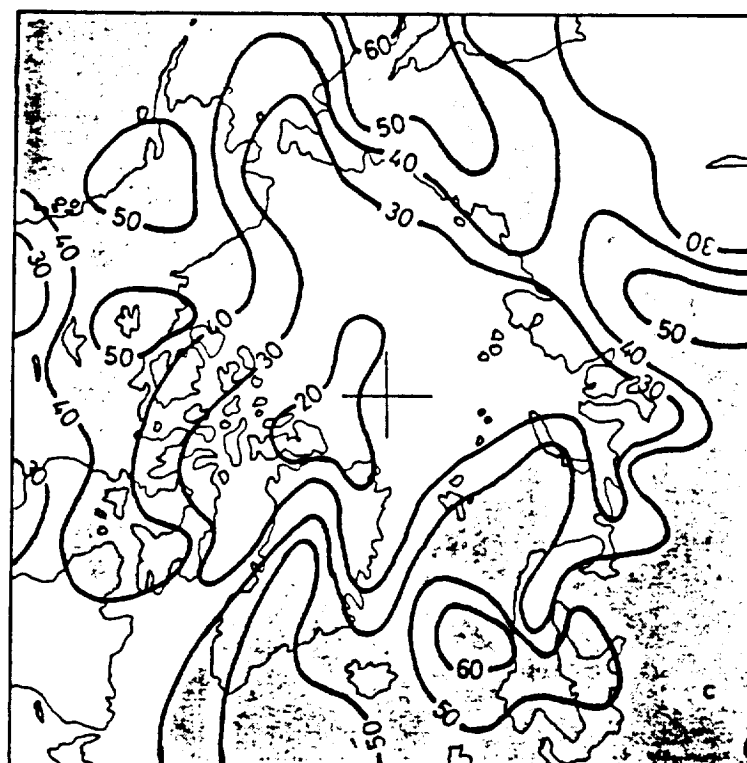
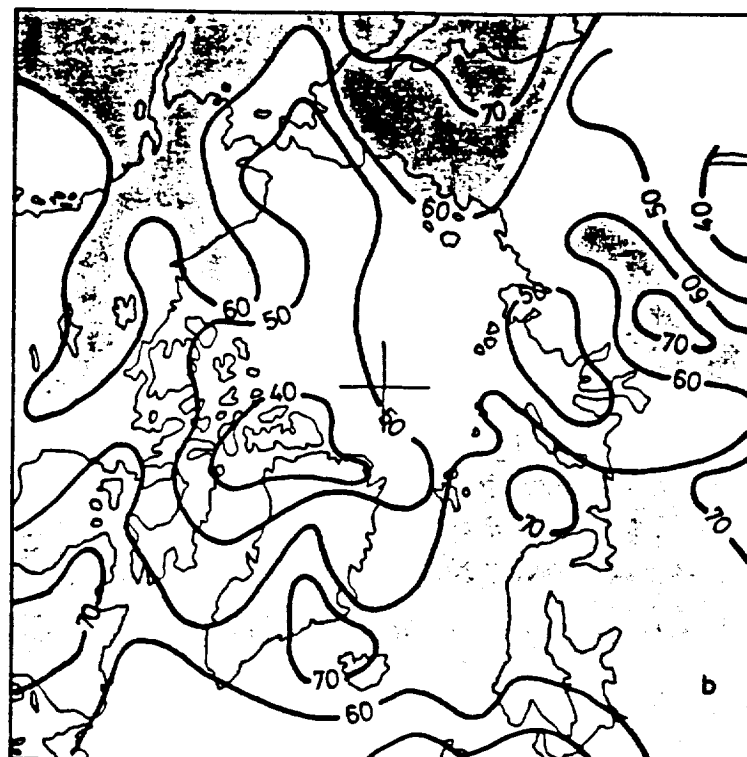


Figure 6. Continued

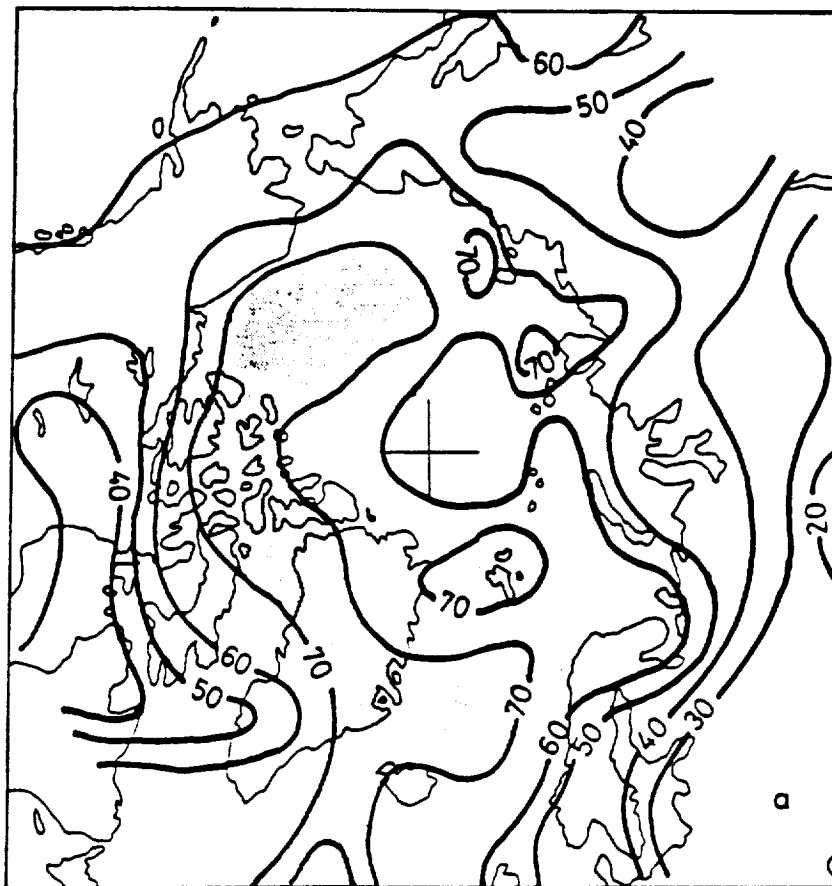


Figure 7. Mean July Cloud Cover From the GISS GCM.
(a) Total Cloud (shaded areas = greater than 70% cloud)
(b) Low Cloud (shaded areas = greater than 60% cloud)
(c) Middle Cloud (shaded areas = greater than 40% cloud)

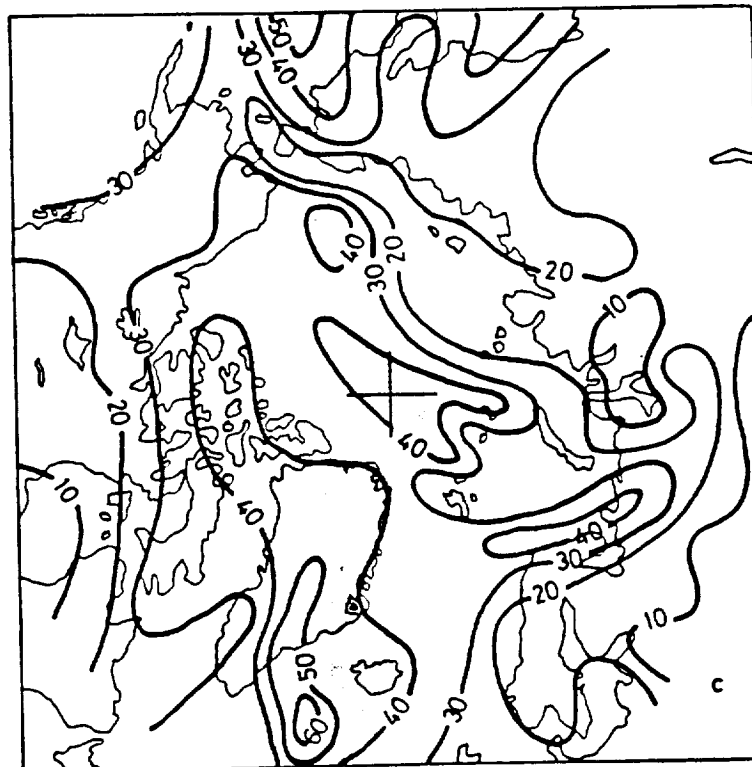
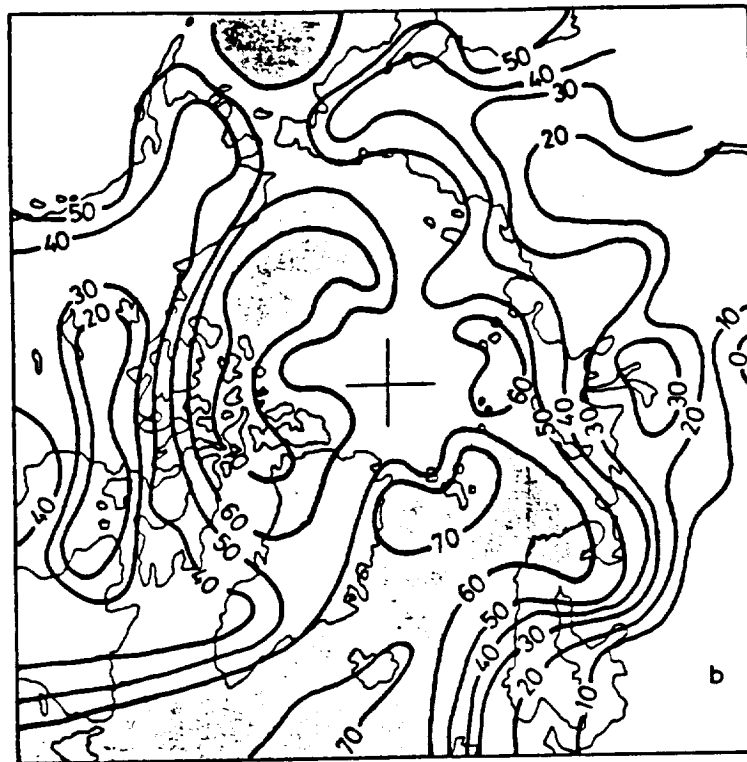


Figure 7. Continued

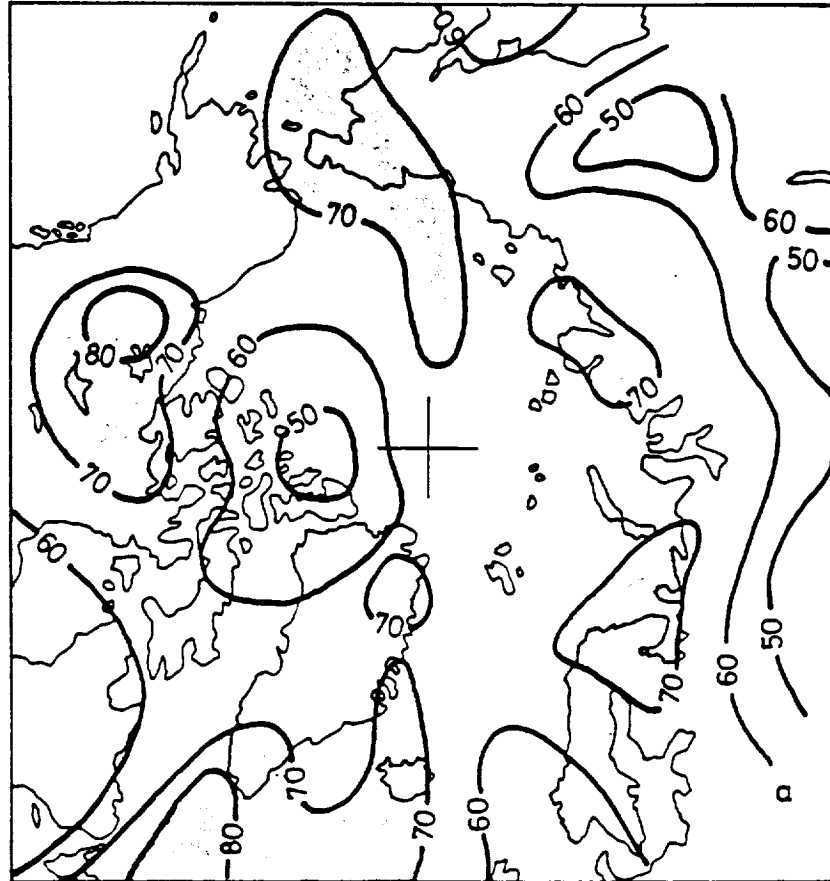


Figure 8. Mean September Cloud Cover From the GISS GCM.
(a) Total Cloud (shaded areas = greater than 70% cloud)
(b) Low Cloud (shaded areas = greater than 60% cloud)
(c) Middle Cloud (shaded areas = greater than 40% cloud)

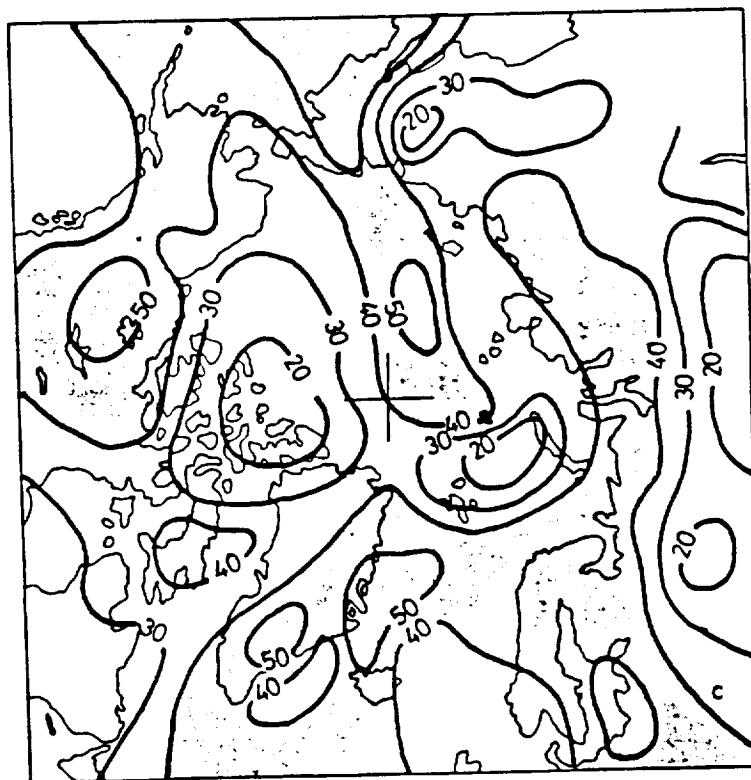


Figure 8. Continued

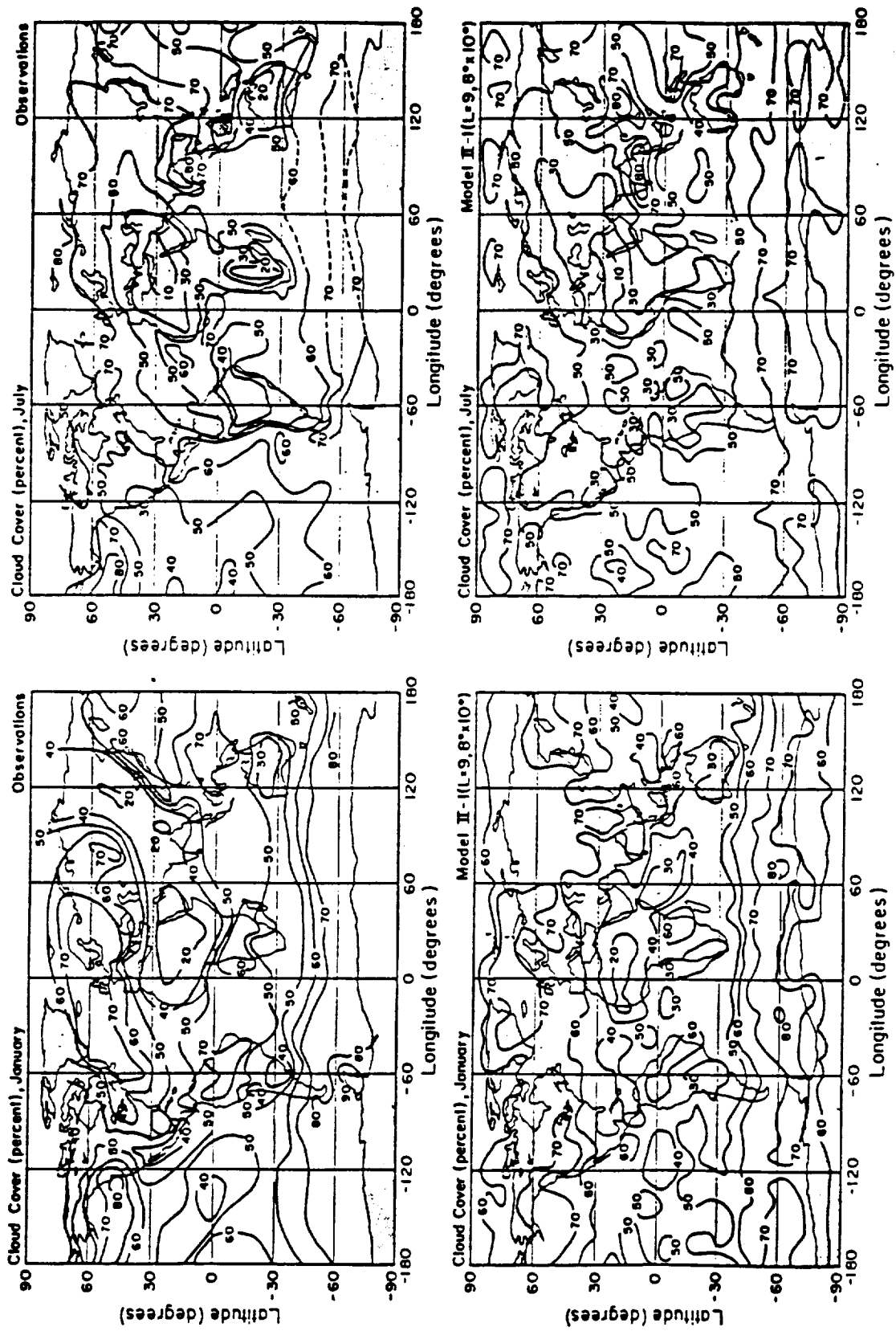


Figure 1. Modelled and Observed Cloud from Hansen et al. (1983)

